Modelling of Heavy Fuel Oil Spray Combustion using Continuous Thermodynamics

by

Vikrambhai Babubhai Garaniya

A dissertation submitted in fulfilment of the requirements for the Degree of Doctor of Philosophy in Engineering

at the

National Centre for Maritime Engineering and Hydrodynamics

Australian Maritime College

University of Tasmania

Dec 2009

Declaration of Originality

I certify that this thesis contains no material which has been accepted for a degree or diploma by the University or any other institution, except by way of background information duly acknowledged in the thesis, and to the best of the my knowledge and belief contains no material previously published or written by another person except where due acknowledgment is made in the text of the thesis, nor does the thesis contain any material that infringes copyright.

Vikrambhai. B. Garaniya……
Date……..

Statement of Authority of Access

This thesis may be made available for loan. Copying of any part of this thesis is prohibited for two years from the date this statement was signed; after that time limited copying is permitted in accordance with the Copyright Act 1968.

Vikrambhai. B. Garaniya……
Date……..

Note: This thesis contains a number of colour photographs and graphs. Reproducing it without colour may affect the quality of the photographs and hinder the identification of the data in the graphs.

Abstract

Commercial liquid petroleum fuels are complex mixtures of various hydrocarbons. In multicomponent fuel modelling, these liquid fuels are represented typically with two components or up to ten discrete components. Even with ten components, there are limitations on the representation of real commercial fuels such as heavy fuel oil (HFO), which contains large numbers of hydrocarbons with a wide range of molecular weights and dissimilar structures. Continuous thermodynamics and pyrolysis chemical kinetics are used to model the behaviour of HFO in diesel spray combustion.

The evaporation model is developed using the principle of continuous thermodynamics rather than discrete component modelling, to accurately cover the entire range of composition. Continuous thermodynamics reduces the computational simulation load compared to conventional discrete thermodynamics, without degrading the quality of prediction of the complex behaviours of such multicomponent fuels. In continuous thermodynamics modelling, liquid mixture compositions are simply represented by probability density functions (PDF). In the present study, HFO is represented by four fuel fractions: n-paraffins, aromatics, naphthenes and heavy residue. Each of these fractions is assigned a separate distribution function. In the evaporation model, both low-pressure and high-pressure formulations for the calculation of vapour-liquid equilibrium (VLE) at the droplet surface are provided. The formulations for high-pressure VLE are developed for a semicontinuous mixture and a generic approach to the equation of state (EOS) is used. Therefore, depending on the mixture compositions (continuous or semicontinuous) these formulations can be applied with any EOS. It is identified that in the high-pressure model, interaction coefficients between the liquid-liquid components and between the liquid component and air plays an important role during evaporation. Interaction coefficients help to improve the evaporation rate of heavy molecules.

HFO is primarily composed of high molecular weight hydrocarbons which cannot evaporate but are pyrolised at high temperatures. Pyrolysis produces volatile gases and polymers through thermal cracking and polymerisation respectively. Baert's pyrolysis model based on chemical kinetics for thermal cracking and polymerisation rate is developed. Results of this pyrolysis model show that polymer formation within a droplet

is dependent on droplet heating rate and composition. Moreover, it is observed in Baert's pyrolysis model results that the process of polymerisation starts prior to the thermal cracking. This order of thermal cracking and polymerisation is contradictory to the experimental evidence. Subsequently, Baert's pyrolysis model parameters are modified. Results of the modified pyrolysis model did not show any significant dependency of polymer formation on droplet heating rate and in addition it showed thermal cracking beginning earlier than the polymerisation.

The low and high-pressure evaporation models along with the modified pyrolysis model are applied to a single HFO droplet in a high pressure environment, showing good agreement with experimental results obtained by other researchers. A comparison of the low-pressure model with the high-pressure model for 100 micron and 30 micron droplets at high pressure and temperature show that evaporation of the volatile hydrocarbons (n-paraffins, aromatics, naphthenes) from HFO occurs at a faster rate for the high-pressure model. However, this faster evaporation does not significantly affect the droplet lifetime because modelled HFO contains only 30% volatile hydrocarbons (cutter stock) by mass. Therefore, droplet lifetime is found to be similar for both models. Thus in sprays where droplets are generally small, the VLE calculation can be obtained with sufficient accuracy by the low-pressure model avoiding the use of the complex high-pressure EOS model.

The low-pressure evaporation and modified pyrolysis models along with a heterogeneous liquid phase soot burnout model are implemented via subroutines in a diesel spray simulation in the CFD package StarCD. This simulation is applied to two different constant volume spray combustion chambers which are used to examine the combustion characteristics of HFO. The models are tested for two representative fuel samples; one with the good combustion quality and the other poor. Good qualitative agreement is shown between the computer simulations and the published experimental data.

A sample of HFO is characterised in the laboratory using chemical characterisation procedures such as; sequential elution solvent chromatography (SESC), gas-chromatography (GC), mass spectrometry (MS) and elemental analysis, to obtain the composition and mean molecular weights of HFO fractions required for continuous thermodynamics modelling. A CFD simulation of the characterised HFO is performed using the developed low-pressure evaporation and modified pyrolysis models.

Acknowledgements

First of all, I would like to take an opportunity to express heaps of thanks to my supervisors; Dr Laurie Goldsworthy, Assoc. Prof. Don McWilliam and Assoc. Prof. Norman Lawrence. I am really grateful to Dr Laurie Goldsworthy for giving me the chance to do this research work, for all his assistance, valuable guidance, patience and financial support. He has been an excellent mentor and helpful hand when called upon. It has been a great privilege to work under him and benefiting from his expert knowledge. I must acknowledge the contribution of Assoc. Prof. Don McWilliam whose extensive knowledge in chemistry has been a valuable source while planning experiments. I am also thankful to Assoc. Prof. Norman Lawrence for quick and careful editing of the manuscript, his comments add significantly to the quality of this thesis.

I wish to acknowledge the important discussions with Lou Mason, his comments have always helped me in implementing the models. I owe thanks to Prof. William Hallett from University of Ottawa for helping me in understanding the theory of continuous thermodynamics at the initial stage of the present study. I also owe thanks to the Australian Maritime College (AMC) for providing me the IPRS and John Bicknell scholarships. I would like to acknowledge the help of the AMC library and UTAS international office staff.

It would have been extremely difficult without my loving and caring wife Trupti (Mamta), she has always encourage me to keep going. I would like to express my deepest and personal thank to my family and in-law's family back home in India for their love, unconditional support and encouragement. Further, I would like to thank my friends and colleagues; Harshil, Paramjeet, Ameya, Thaila, Nafisa, Vineet, Karamjit, Paramjit, Jignesh, Darshna, Milan, Bong, Shinsuke, Saut, Indika, Alan and Ben for sharing their time and making my life enjoyable.

A special thanks to the God for giving me the courage and energy to complete this thesis. Finally, I would like to acknowledge one and all those who helped me directly or indirectly in making this thesis possible. If someone feels left out I apologise for my poor memory.

Table of Contents

List of Figures

List of Tables

Nomenclature

AR	Aromaticity
A	Surface area of the droplet, m^2
B	Mass transfer number
B_{TH}	Thermal transfer number
D	Average diffusivity, m^2/s
E	Activation energy, kJ/kmol
I	Distribution variable (Molecular weight), kg/kmol
J	Number of distribution functions
H	Number of discrete species
N	Evaporating molar flux, $kmol/m^2s$
P	Pressure, kPa
R	Radius of the droplet, m
$\mathcal{R}$	Universal gas constant, 8.314 kJ/kmol K
T	Temperature, K
V	Droplet volume, m^3
X	Liquid mass fraction
C_p	Specific heat, kJ/kmol K
Nu_o	Nusselt number at zero mass transfer rate
Sh_o	Sherwood number at zero mass transfer rate
c	Molar density, $kmol/m^3$
d	Droplet diameter, m
i	Species
k	Pre-exponential for the reaction rate, 1/s
m	Mass, kg
r	Radial coordinate beyond droplet surface, m
t	Time, s
v	Molar volume
x	Liquid phase mole fraction
y	Vapour phase mole fraction

$f(I)$ Distribution function

h_{fg} Evaporation Enthalpy, J/kmol

h_{dec} Decomposition enthalpy, J/kmol

S_{fg} Entropy of vaporization, kJ/kmol K

v^* Average velocity, m/s

Greek Symbols

α Γ-Distribution shape variable

β Γ-Distribution shape variable

γ Γ-Distribution variable (Origin shift)

θ Mean (first moment) of distribution = Molecular weight, kg/kmol

ψ Second central moment of distribution ($\psi = \theta^2 + \sigma^2$)

$\Gamma(\alpha)$ Gamma function of variable α

λ Thermal conductivity, W/mK

ρ Mass density, kg/m^3

σ Distribution standard deviation, kg/kmol

ξ_j Molar flux fraction = N_j / N

ξ_G Molar flux fraction of pyrolysis gas = N_G / N

Φ_D Temperature dependence

Subscripts and Superscripts

ATM Atmospheric

A Air

B Bubble or boiling point

F Fuel

G Pyrolysis Gas/Gas phase

L Liquid

P Polymer

R At droplet surface

V	Vapour phase
cr	Critical
j	Index for a fuel fraction (1 to 4)
0	Initial conditions
∞	Ambient condition

Chapter 1. Introduction

1.1 Background

Since the invention of the wheel, the transport industry has greatly evolved with mankind and in today's world, it has become one of the basic requirements for man's survival. This transport requirement is commonly satisfied by three means; land, air and sea (marine) transport, but each of these has its own advantages and disadvantages. However, the marine transport industry is still dominant as the main means of transport because it is economical, energy efficient, emits less pollutants per tonne-km of goods displacement and is regarded as the safest means of transport compared to other available transport options [3, 4].

Marine engines employ the process of combustion to convert the chemical energy of heavy fuel oil into other usable forms of energy. The marine transport industry uses Heavy Fuel Oil (HFO) as the primary source of energy generation. Heavy fuel oil is less expensive when compared to petrol, diesel and other aviation fuels because it is a residue of the vacuum distillation unit of a petroleum refinery [2]. Generally, vacuum residue has high viscosity and contains large heavy hydrocarbons. Therefore, before vacuum residue can be used as a fuel, cutter stock is blended with it to lower the viscosity of the residue. Cutter stock may have high aromatic content but it has lower molecular weight than residue [2]. Heavy fuel oil contains a large amount of stable and/or unstable hydrocarbons and has a high carbon to hydrogen ratio.

Current global environmental legislation and the steady increase in emission regulations have forced the transport industry to develop higher performing and more efficient engines. [5]. The modern on road transport engine industries demand has forced the oil refining industry to produce lighter oil (gasoline, diesel, etc.) in greater quantity. Subsequently large marine engines are using more and more carbon rich and higher aromatic content fuel [6, 7]. As a result of this poor quality aromatic contained fuel, engines are facing problems [8] because aromatics are very stable and difficult to ignite. Some of the major issues are piston ring wear (see Figure 1-1), cylinder liner scuffing and exhaust valve

sticking [6]. Moreover, the awareness of limited fuel resources and considerable interest from the industry has supported the mathematical modelling for large marine diesel engines. In order to develop an efficient engine, an understanding of the detailed process of engine combustion and chemistry of such multipart fuels is essential [5].

Figure 1-1: Damaged piston due to poor quality of fuel [9].

The various physical and chemical processes occurring during the combustion of fuels within the engines are extremely complex. These processes include fuel injection, fuel atomisation, wall impingement, evaporation, fuel ignition, combustion and pollutant formation. Each of these individual processes plays its own important role in the overall efficiency and performance of real engines. In order to develop and design efficient engines, an in-depth understanding of these processes and their controlling factors is required. The computation model is built on existing mathematical descriptions available about these processes in various papers and reference books.

Computational Fluid Dynamics (CFD) has become an essential part of various engineering fields, such as hydrodynamics, aerodynamic, engine modelling etc. In CFD, computers are used to calculate the many parameters required in simulating the interaction of the two phases (generally the gas phase and the liquid phase) in complex geometry. The CFD

simulations can provide the approximate solution of unknown problems in an acceptable timescale [10]. To apply this modern tool to engine development, it is vitally necessary to include the spray process and various chemical processes which occur during the combustion of the liquid droplets inside a real engine chamber.

When a fuel is injected into a hot engine chamber many mass transfer (e.g. evaporation and pyrolysis) processes occur. These mass transfer processes convert fuel (liquid) into volatile vapour and gases, which later on burns in oxidising environment and generate the energy to drive the engine shafts. Therefore, an understanding of these mass transfer processes plays a crucial role in engine design and development.

1.2 Motivation

For many reasons, research on the combustion of fossil fuels is highly necessary. The first and most obvious reason is to increase the efficiency of the combustion process. The second reason is to optimise the process of combustion to reduce emissions. This research can be improved by computer simulations and/or by experimental measurements.

Throughout the past couple of decades, computer simulation has become an extremely powerful tool in the design of engines. In addition, usage of the computer is increasing rapidly due to advancements in software and the low cost of computer simulation compared to expensive experiments [10]. This computer simulation trend will continue with more and more applications in future engine development.

Although heavy fuel oil is the most important source of fuel for the marine transport industry, because of difficulties in combined handling of preferential evaporation and pyrolysis mathematically, to date very little effort has been made to model the behaviour of such multicomponent fuels [11, 12]. Even in the literature, very little research work has been found on evaporation of multicomponent fuels and most of this work is based on binary component mixtures or up to ten discrete components [13-16]. In the discrete multicomponent fuel model, each component has its individual mole fraction and it requires a separate transport equation. During the evaporation process modelling, these transport equations need to be solved at each time step for every individual component.

Hence, it requires considerable computation power to solve multicomponent fuels. Therefore, this kind of approach is inadequate to represent fuel such as HFO, which contains thousands of different components. An alternative approach is required to treat these types of multicomponent fuels. There are three different techniques used to represent evaporation modelling: pseudo component technique, continuous thermodynamics technique, and semi continuous thermodynamics technique.

In the pseudo component technique, individual components with similar properties are lumped together to form one group. This technique is good to represent the binary or small component mixture but it is not superior to represent the multicomponent fuels. Continuous thermodynamics technique represents the fuel components as a series of multi distribution Probability Density Functions (PDF) rather than a series of discrete components. Hence, it reduces computational simulation load compared to discrete component modelling without much degradation of the prediction quality of the complex combustion behaviours of such multicomponent fuels. The semicontinuous thermodynamics technique is a summation of the first two techniques. In this technique some components of a fuel are represented as a discrete component and others are represented using probability density functions.

1.3 Objectives

Increased application of catalytic cracking and/or thermal cracking techniques during the refining process of petroleum, has caused the quality of heavy fuel oil to deteriorate [13]. Compared to years ago, heavy fuel oil has become more and more carbon rich and aromatic in content. This deteriorating quality of heavy fuel oil has provided impetus for researchers to understand the spray combustion of these fuels [14]. The effect of fuel composition during the combustion of droplets within spray and its pollutant formation tendency currently provide the areas for research work. Most of the research is aimed at understanding the basic process of the combustion occurring in large diesel engines. In particular, the main interest is towards the environmental aspect of the combustion of heavy fuel oil.

The present work is a development step towards studying the evaporation and pyrolysis process of a single droplet and liquid spray combustion of heavy fuel oil in the context of large marine diesel engines. It will help in the modelling of chemical and physical processes of complex fuel mixtures. The present model builds on the previous semi-empirical model developed by Goldsworthy [2], which was validated using limited experimental data for the overall combustion process outcomes. The current work aims to describe the evaporation and pyrolysis process from first principles. Generally, data on the behaviour of heavy fuel oil in diesel spray is hard to obtain directly. The droplets in spray are much smaller than droplets which have been analysed in laboratories and the heating rate is much higher than that can be achieved in single droplet measurements. Thus, the use of a model with detailed physics should give much needed insight into the mass transfer processes within the droplet in a marine diesel spray context. The models are ultimately validated against the same data as the semi-empirical model of Goldsworthy [2]. One of the objectives of this work is to apply the principle of continuous thermodynamics to represent the evaporation process of heavy fuel oil and develop various models for the individual droplets and spray as outlined below:

- Development of a model for mass transfer rate into vapour phase from the individual droplets
- Development of a model of heat transfer rate to individual droplets from the surrounding environment
- Development of a model for mass transfer rate from a single HFO droplet in a high pressure environment.
- Development of a chemical kinetics model for the thermal cracking and polymerisation rate within the droplets in a burning fuel spray
- CFD modelling of the processes of evaporation and pyrolysis of heavy fuel oil in the context of large marine diesel engines
- Development of a liquid phase soot burnout model and study its formation tendency in heavy fuel oil spray combustion. Higher proportion of liquid phase soot potentially could increase the possibility in damaging the engine piston ring.
- Validation of the above mentioned developed models (kinetics, mass transfer rate and heat transfer rate) with available experimental data.

A recent article by Ramanathan & Carmichael [15] pointed out that Black Carbon (BC) is one of the largest contributor to the rising global temperatures. Black Carbon absorbs solar energy in the atmosphere and reduces the albedo of snow (reflectivity). According to a report [16] from International Maritime Organisation (IMO), this effect on the snow albedo may be particularly important in the Arctic where rapid climate change is occurring and shipping access to the area will increase due to retreating sea ice. The present model accounts for the formation and burnout of liquid phase soot in diesel engines, this soot will be emitted as Black Carbon if unburnt. While soot which originates in the vapour phase is well studied, studies of soot which originates in the liquid phase for combustion of HFO in diesel engines are not reported in the literature.

1.4 Methodology

Different characterisation methods are studied to understand the chemistry of heavy fuel oil. These include separation of heavy fuel oil into small factions and their analysis through various available instrumentation techniques.

In most of the multidimensional modelling, fuels have been represented by a single component such as tetradecane for diesel and/or isooctane for gasoline [17]. In some of the literature, studies have been reported using the concept of binary mixtures, but the fact is there are still limitations in representing the actual commercial fuels such as heavy fuel oil. Heavy fuel oil consists of many components having different molecular weight ranges and dissimilar structures. The present study uses a principle of continuous thermodynamics to represent the fuel effectively. Continuous thermodynamics allows the use of far-reaching range of fuel compositions, which can have a range of molecular weights and dissimilar structures.

The continuous thermodynamics idea was first studied 70 years ago, but a decade ago Tamim & Hallett [18] applied this idea in studying the evaporation process of various commercial fuels. The scope of that paper has broadened the application of continuous thermodynamics in the evaporation of fuels. The limitation of their work was that it uses a single distribution function to represent the fuel composition. Hence, it only allowed one group of hydrocarbons, whereas commercial fuel contains more than one group of

hydrocarbons having different structures. Recently, Hallett et al. [19-21] resolved this limitation and developed a mathematical model which used multiple distribution functions to represent the fuel.

1.5 Thesis Outline

The present thesis is comprised of eight chapters in total. Chapters 1 and 2 mainly consist of an introduction to the problems and provide a detailed literature review. Chapter 3 contains the methodology and experimental procedure to obtain the chemical information required for continuous thermodynamics modelling of heavy fuel oil. It mainly includes the procedure for separation of heavy fuel oil into small fractions and characterisation of all of them individually. Chapter 4 discusses the numerical procedure of continuous thermodynamics and pyrolysis chemical kinetics modelling of a single droplet. This chapter also includes the continuous thermodynamics modelling of a single droplet in high pressure environment using a non-linear equation of state for vapour-liquid equilibrium. The model developed in Chapter 4 is compared with the available experimental data in Chapter 5. The main discussion in Chapter 4 and Chapter 5 includes a published article by Garaniya & Goldsworthy [22].

Chapter 6 explains the extended study of heavy fuel oil spray using the CFD software StarCD. Descriptions of specifically developed subroutines of mass transfer of the burning spray are contained in this chapter. Main content described in this chapter uses the methodology and chemical information discussed and developed in previous chapters. The model outlined in Chapter 4 is developed solely for a single droplet which does not include the effect of aerodynamic forces from the ambient environment to a droplet and the effect of the combustion. Consequently, Chapter 6 provides the comprehensive discussion about developed models for the combustion process of burning spray. Chapter 7 explores the theoretical spray model validation against available experimental data, which includes two different sets of experimental result validations of burning heavy fuel oil spray. Chapter 8 provides the overall conclusions from the current research and recommendations for future research based on the present study. A summary of the present thesis is outlined in Figure 1-2.

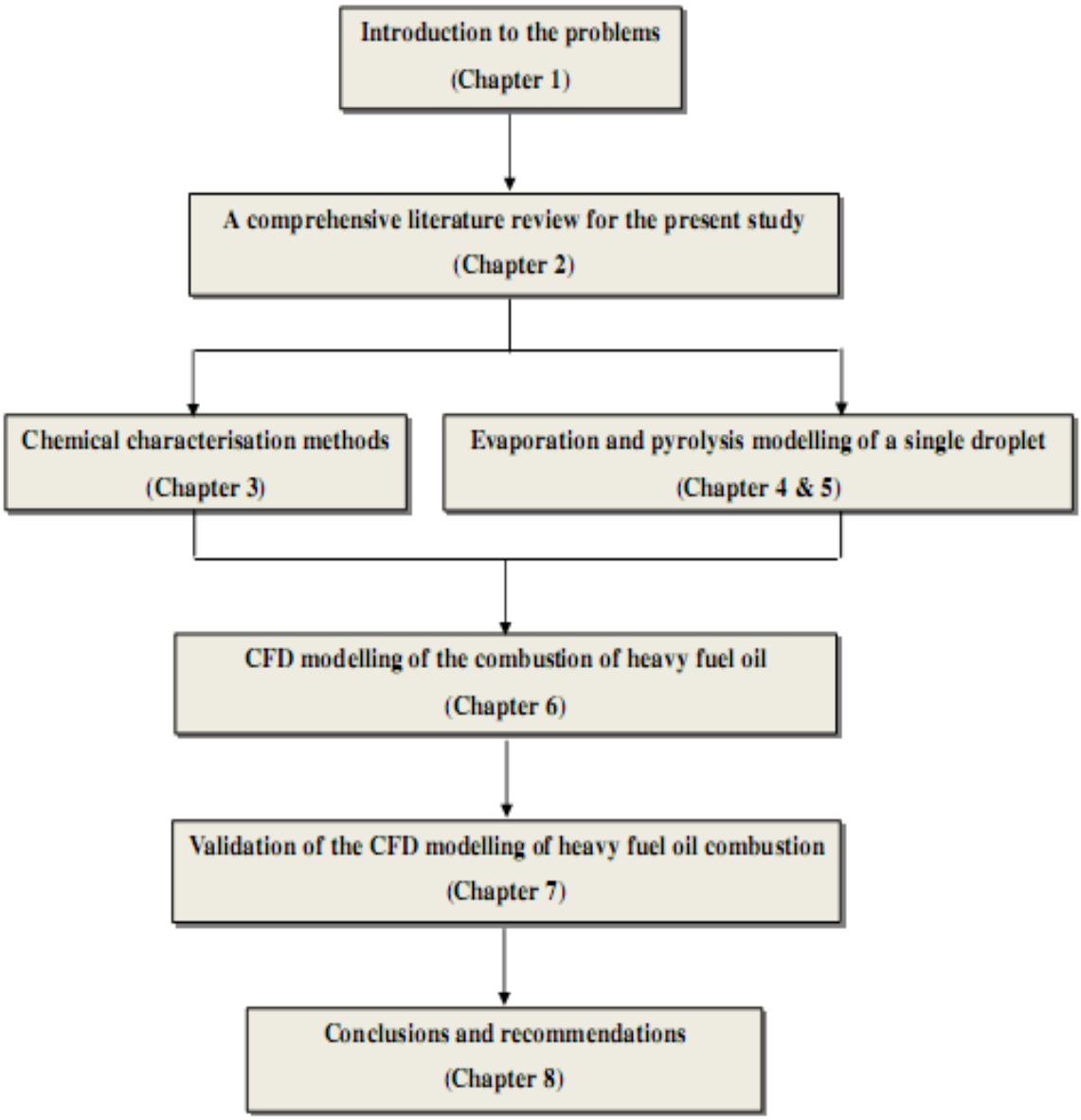

Figure 1-2: Thesis structure.

Chapter 2. Literature Review

2.1 Introduction

This chapter covers the basic review on critical points of the present study. The second section of the present chapter covers the basic description of heavy fuel oil and its complex composition. The third section provides literature review on the previous studies of the combustion process. A broad review on the evaporation process and different areas of research on evaporation is presented in section four. A comprehensive overview on the technique of continuous thermodynamics and its practical usage in research is given in section five. An overview of spray combustion related studies is described in section six. A brief literature review associated with the experimental measurement of heavy fuel oil's combustion characteristics is described in the final section of the present chapter.

2.2 Heavy Fuel Oil

Heavy fuel oil is the most common fuel used in the marine transport industry. Due to daily rises in fuel cost, fuel economy has become a major part of the operational cost for the transport industries. Greater demand of the gasoline and diesel as well as advancement in the petroleum refinery operations has a direct impact on the quality of heavy fuel oil. That is why currently most marine diesel engines use low cost and poor quality fuels [8]. The combustion process of this kind of fuel is very complex. It is found that the combustion of heavy fuel oil involves not only burning of volatile components but also burnout of coke residue. This indicates that it is necessary to understand the detail combustion process of the heavy fuel oil [23].

As discussed in the previous chapter, heavy fuel oil is a blended product of the cutter stock and the residue of petroleum refining and cracking processes. The residue is material that remains after distillation and cracking which consists of high molecular weight and low volatility hydrocarbons. Cutter stock may have high aromatic content but it is of lower molecular weight than the residue. Some common processes of heavy fuel oil blending are shown in Figure 2-1 and Figure 2-2. Due to increased regulations, two factors are very

important during the blending of a heavy fuel oil (HFO). Firstly the overall sulphur (S) content of the HFO, and secondly the viscosity of the HFO. Figure 2-1 illustrates blending of HFO in which sulphur content is the control factor [24], while Figure 2-2 shows the production of HFO where the viscosity is the control factor [24]. In both figures, general unit operations such as distillation, vacuum distillation, hydrocracker, visbreaker etc. of petroleum refinery are shown. Mostly these unit operations are aimed to extract lighter fuels (gasoline, kerosene, gas oil) to a greater extent to meet the global demand. Lastly, when it is not possible to produce these lighter fuels by any of the available processes then that residue is utilised in making HFO. To compensate the viscosity and content, cutter stock is added. Therefore, heavy fuel oil (HFO) is chemically very complex consisting of many different hydrocarbons having dissimilar structures. In the maritime industry heavy fuel oil is also known as Bunker Fuel Oil (BFO) or Residual Fuel Oil (IFO) and some lighter forms are knows as Intermediate Fuel oil (IFO).

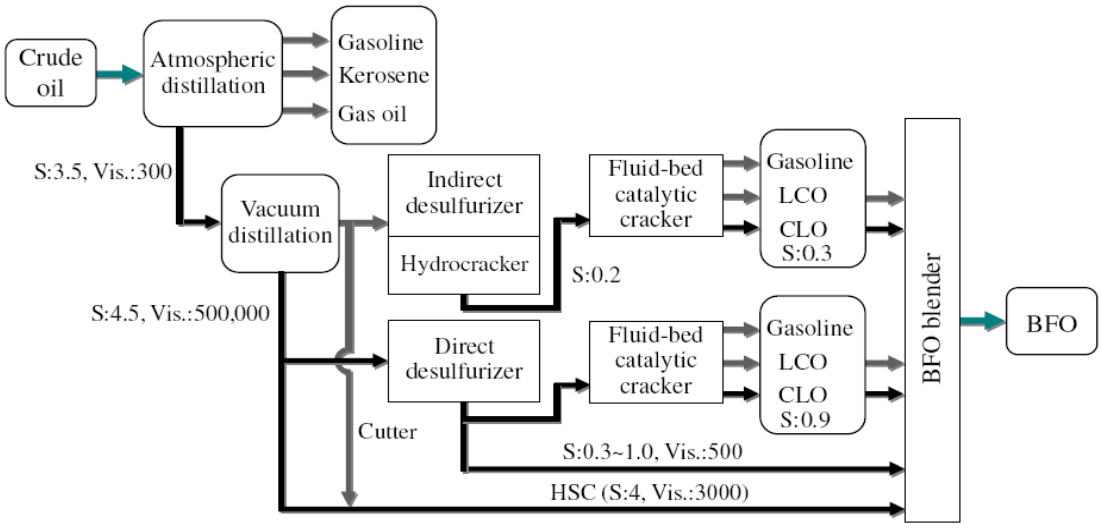

Figure 2-1: Blending of HFO where S content is the control factor (courtesy of Assoc. Prof Hiroshi Tajima [24]).

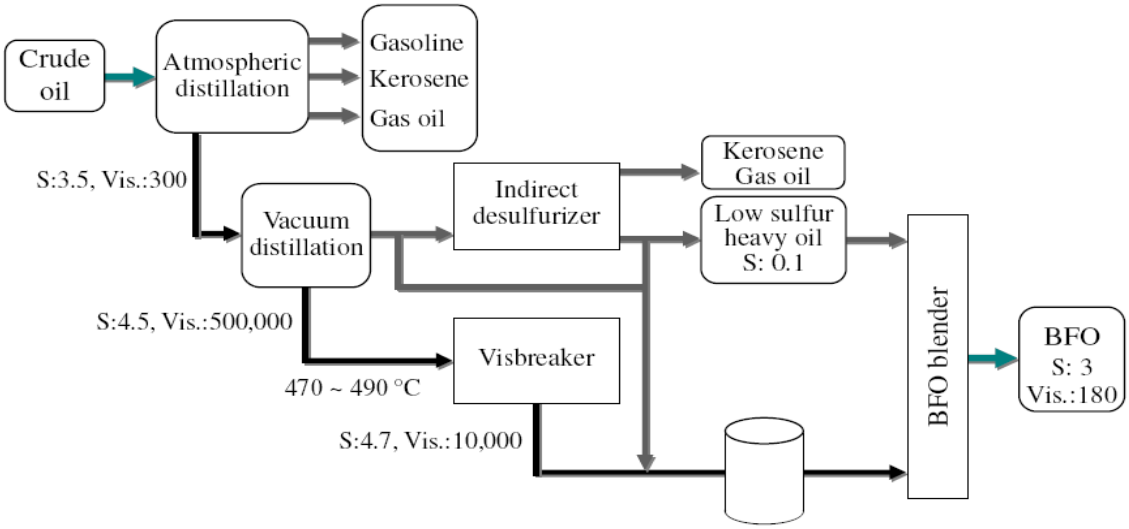

Figure 2-2: Blending of HFO where viscosity is the control factor (courtesy of Assoc. Prof Hiroshi Tajima [24]).

Heavy fuel oil consists of a large number of hydrocarbons having a very high molecular weight range and dissimilar structures [14], but the smallest molecules belong to any one of the following main four types of hydrocarbons: paraffins, olefins, naphthenes and aromatics. According to Baert [14], the presence of olefins is negligible in HFO, therefore apart from the olefins, the remaining three compounds define the basic structure. Heavy fuel oil can be classified into two hydrocarbon groups as follows [14];

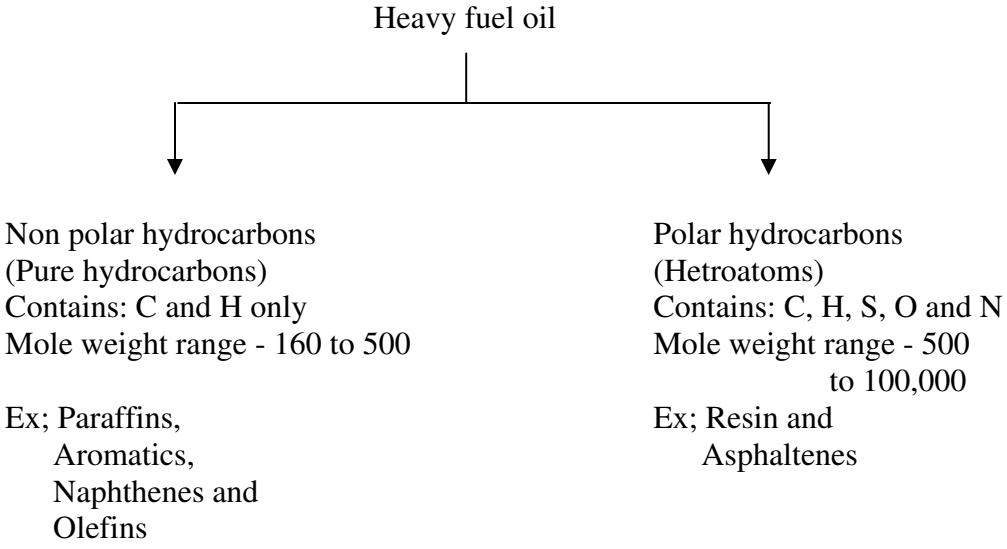

Figure 2-3: Classifications of hydrocarbons in heavy fuel oil.

Chemical structures and molecular weights both are necessary to determine the behaviour of heavy fuel oil during evaporation and pyrolysis. In general, heavy fuel oil has a

molecular weight range from 160 to 100000, but depending upon the molecular weight range, it has different structures [14]. In other words, a complete description of the chemical structure of molecules present in a heavy fuel oil is impossible due to the large range of molecular weights and different types, but it can be described by different group contribution methods [14]. The average structures of the four main components (fractions) of HFO are shown in Figure 2-4.

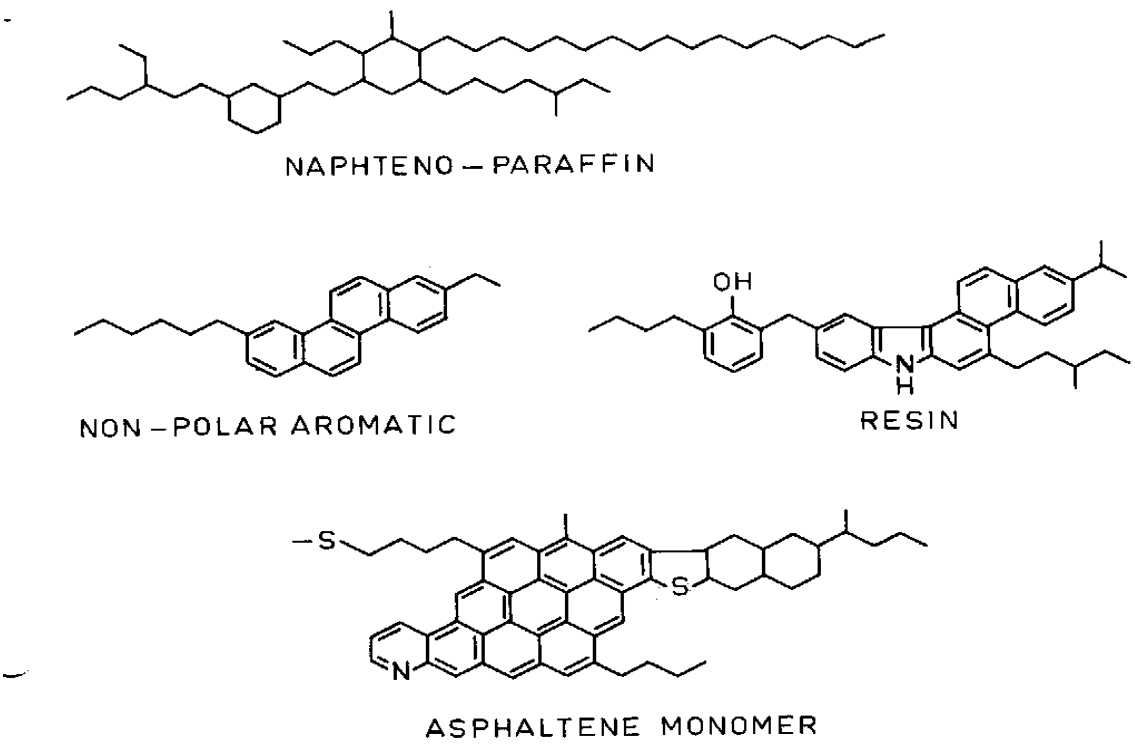

Figure 2-4: Average structures of heavy fuel oil components (from Baert [14]).

Hydrocarbons in HFO that have molecular weight below 500 are generally pure hydrocarbons as illustrated in Figure 2-3, whereas hydrocarbons with a molecular weight above 500 contain small amount of O, N and S, which are known as heteroatoms. Generally, these heteroatoms give polar characteristics to the compound. Aromaticity and polarity (number of heteroatoms) of the molecule increases with the increase in molecular weight. These polar molecules can be separated into two fractions;

1) Asphaltenes and
2) Resins (Non-asphaltene)

The asphaltenes are the polar compounds which are insoluble in n-heptane [25-27] and contain up to 15 aromatic rings. Asphaltenes are also known as the 'cholesterol of

petroleum' [28] while non-asphaltene compounds are known as resin compounds. The molecular weight of asphaltenes reported in the literature is from 1000 to $2*10^6$, but it also depends on the method and conditions of measurements [29]. However, Badre et al.[30] noted that the molecular weight and the structure of asphaltenes is a most controversial issue and there is no definite molecular weight. Resin have a smaller number of aromatic rings (2 to 7) and lower polarity [14]. With the increase in molecular weight, the complexity of hydrocarbons increases.

2.3 Basic Process of Combustion

Combustion is the oldest technology for energy production. In fact today, most of the world's energy requirements are directly or indirectly satisfied through combustion. That is why it is worthwhile to study this process in detail and develop a mathematical model for it. Fuel combustion is a combined process of many sub-processes. According to Ikegami et al.[23] the combustion process of heavy fuel oil is divided into two main phases;

1. Liquid droplet phase
2. Solid coke phase

The liquid droplet phase is complicated and it includes many heat and mass transfer processes and some chemical reactions. Solid coke phase is the heterogeneous oxidation of polymer residue. Liquid phase combustion can be further subdivided into four successive stages;

1) Pre-ignition heating
2) Evaporation
3) Thermal decomposition
4) Polymerisation

Williams [11] also divided the entire combustion course as summation of five different phases;

I. Heating up and vaporization of low boiling point fraction.
II. Self ignition with little thermal decomposition and continued vaporization of the droplet's light components.

III. Disruptive boiling that can occur due to boiling of the low boiling point component within the droplet and swelling together with thermal decomposition.
IV. Formation of carbonaceous residue.
V. Heterogeneous combustion of carbonaceous residue.

Similarly, Chen & EI-Wakil [31] summarised the combustion history of burning the droplet in a flowchart which is shown in Figure 2-5.

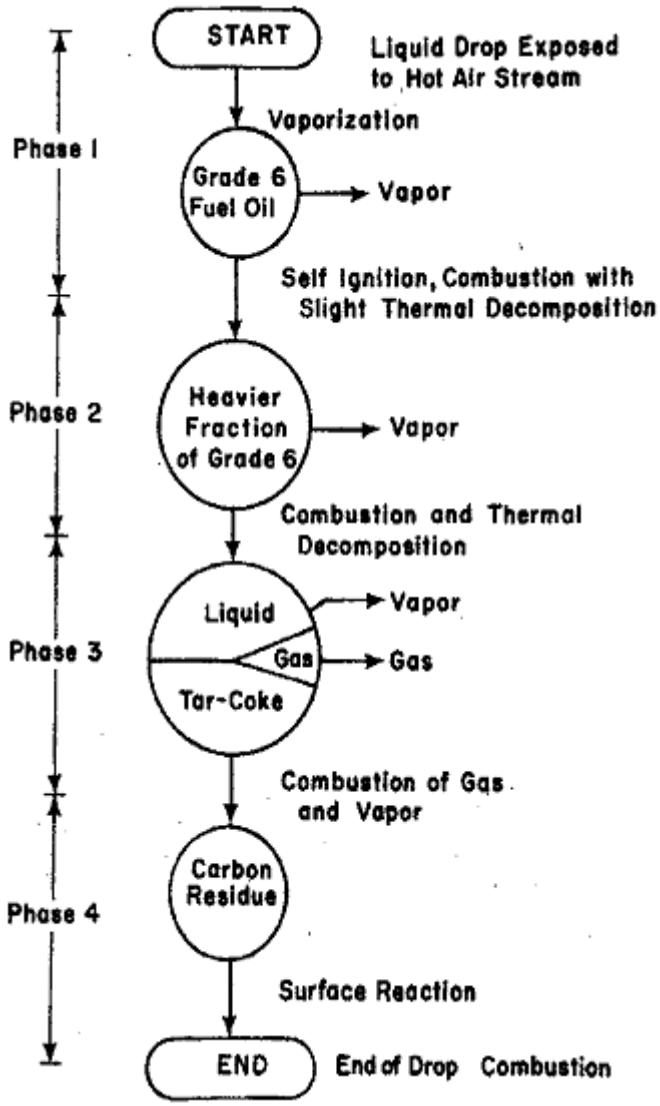

Figure 2-5: The combustion history of a burning droplet (from Chen & EI-Wakil [31]).

Furthermore, according to Goldsworthy [2] combustion of heavy fuel oil also involves some complex phenomenon like,

- Viscous shell formation due to evaporation of lighter components from the surface and high viscous residue,
- Liquid pyrolysis (includes thermal decomposition and polymerisation) due to convective and radiative heating,
- And also the disruptive boiling.

2.3.1 Overview of Combustion Studies

In the late 1950's, pioneering researchers of combustion modelling behaviour, Hottel et al.[32] and Godsave [33], made efforts to understand the combustion behaviour of fuel droplets. Hottel et al.[32] proposed three stages of the burning process of droplets of heavy oil. First, the pre heat stage, second evaporation and third the combustion of volatile matter. In 1960, Wood et al.[34] studied the heterogeneous combustion of multicomponent fuels. Their result showed that during combustion, the composition of multicomponent fuel changes by a simple process of batch distillation. In 1967, Michael & EI-Wakil [35] divided the burning process into liquid and residue phases. They further divided the liquid phase into an evaporation and thermal decomposition phase. Chen & EI-Wakil [31] and Shyu et al. [36] proposed a mathematical model for the evaporation and combustion of heavy fuel oil droplets, they treated fuel as a single component liquid with variable boiling points. Lightman & Street [37], and Marrone et al.[38] studied detailed combustion behaviour of various fuel components and their tendency to form coke residue. Urban and Dryer [39] had concerns about the coke oxidation process and they studied the structure of cenospheres. It has been recognised that the residual portion of the oil is the major source of the coke formation. Generally, the residual portion of heavy fuel oil is characterised by a high content of large, stable hydrocarbon molecules, including aromatics and asphaltenes. The contribution of asphaltenes to the formation of coke is still a controversial issue.

In 1993, Baert [14] divided the liquid phase (droplet) into four components and using the block type distribution to represent each of them, developed a simple evaporation and pyrolysis mathematical model of heavy fuel oil which predicts coke formation and evaluation of gases from the fuel. Baert [14] demonstrated that asphaltenes is the main source of coke formation. The present work has drawn having on Baert's pyrolysis

chemical kinetics, but has taken the more rigorous approach to evaporation modelling as described in later chapters. In that simple evaporation model, Baert assumed that fuel components remain in the liquid phase until the droplet temperature reaches 90% of its boiling point (BP). This assumption is quite adequate for the representation of highly volatile component's evaporation, if boiling points of the components are known. Baert [14] used a block type molecular weight distribution instead of an actual gamma type distribution of the molecular weight. A block type distribution requires four parameters to represent the fuel compositions in evaporation and pyrolysis modelling.

Takasaki et al.[1] studied the combustion characteristics of marine fuel oil. They used two different fuels BFO-S and BFO-A. Results of composition analysis of both fuels showed that BFO-A (poor fuel) contains 24% saturated hydrocarbon, which is lower than good fuel BFO-S (31%). The percentage of aromatic hydrocarbon is very high (67%) in BFO-A compared to BFO-S (47%). Both these fuels contain residue of more than 50% by weight and its properties have not been verified [1]. As mentioned in other literature, there is no uniformity in the composition of HFO since it depends on the crude oil source and also on the type of vacuum residue and cutter stock used [40]. Chromatographic analysis of cutter stock shows that in trouble free BFOs sharp peaks of n-paraffins are observed while in trouble making BFOs naphthalene peaks are found [1].

Recently, Goldsworthy [2] proposed a basic combustion and ignition model of heavy fuel oil. According to Goldsworthy [2], the cutter stock's properties determine the ignition quality of the heavy fuel oil because it is the first component to evaporate. The combustion process of heavy fuel oil is very complex due to large range of the molecular weights and molecule types. Higher aromatic content can lead to late ignition and poor combustion of fuel [2]. The purpose of the addition of cutter stock in HFO is not only to reduce the viscosity for convenience in handling, but it also helps the residue to complete the combustion. The role of cutter stock is to evaporate and ignite first, and then it forms the flame surrounding the unevaporated residual portion. Though the residual portion is heavy, it can burn perfectly. Hence, the role of cutter stock is more important when the residue is heavy [1]. Formation of the carbonaceous residue (cenospheres) is a function of the aromatic content of the heavy fuel oil. It is a characteristic of the high asphaltene content of the fuel [41]. To some extent, Organo-sulfur and nitrogen compound are also responsible for the formation of carbonaceous compound. This is contradictory to the

findings of Bomo et al.[42] that the formation of cenospheres are not correlated to the asphaltenes content but to the chemical structure of molecular units of asphaltenes. Similarly, Whitehead et al.[43] also ruled out any relationship between the fuel properties and corresponding particulate emission.

2.4 Evaporation

2.4.1 General Observations

Fuel vapour and air must be intimately mixed to allow the combustion. For the purpose of better mixing of fuel vapour with air and to burn low volatile liquid, spray combustion is used in most diesel engines, turbines and furnaces. Calculation of the overall evaporation rate of the spray can be achieved by calculating the evaporation history of each droplet in the spray [44]. Research on evaporation is a major element of the engine modelling and in order to understand the process of spray combustion, a good knowledge of the evaporation process is indeed necessary. A comprehensive review of the published literature in the past and present is given in this section. The aim is to introduce the reader to the details of evaporation.

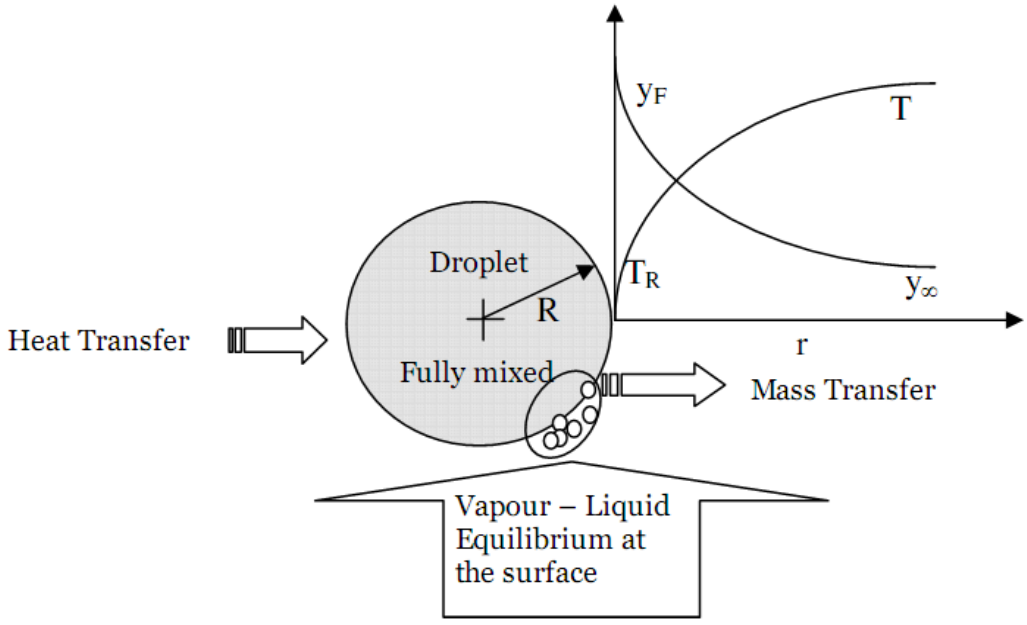

Figure 2-6: Evaporation process of a droplet in hot environment.

A physical feature of droplet evaporation in a hot environment is shown in Figure 2-6. Since the temperature at the droplet surface is lower than ambient, heat is transferred to the droplet through conduction. All heat transfer related processes are transient in nature. The heat transferred to the droplet affects in two ways; (1) it heats up the liquid known as sensible heat and (2) it helps to evaporate the liquid at the surface known as latent heat. Initially in the droplet lifetime, most of the transferred energy is utilised to heat-up the liquid until it reaches to the steady-state level; at that level all the energy transferred to the droplet goes into evaporation. The temperature at this steady-state level is known as pseudo wet-bulb temperature [45] and it may not exist when the droplet lifetime is shorter than the heat-up time. Under certain conditions, condensation may occur on the droplet surface due to high ambient pressure. The liquid phase within the droplet itself may not be uniform. There may be difference in terms of concentration and temperature within the droplet. Investigation on this topic is given in a later section.

The liquid phase and vapour phase interface establishes the concentration of the vapour at the droplet surface and can be achieved by assuming vapour-liquid equilibrium (VLE). The concentration of the vapour at the droplet surface equilibrium can be achieved either by *Raoult's law* and Clausius-Claypeyron equation at low pressure, or by an equation of state at high pressure. The classical fuel droplet evaporation theory was derived by Godsave [33] in 1953 with the following main assumptions;

- Spherical Symmetry: forced and natural convection is ignored.
- Constant gas phase properties evaluated at some reference temperature.
- Constant vapour phase pressure.
- Isolated droplet (no spray effect).
- Ideal vapour-liquid behaviour.
- No chemical reactions.
- Quasi-steady gas phase: Due to density difference between the liquid phase and the gas phase the properties of liquid phase changes at a slower rate than the gas phase. Therefore, the properties of the gas phase can be assumed constant. In other words, it assumes that the gas flow field adjusts more rapidly than the droplet surface regression rate.

- Liquid phase temperature and concentration are uniform throughout the droplet lifetime but they vary with time.

Advanced modelling techniques attempt to overcome all these assumptions. For example, the transient effect cannot be ignored. However, this basic theory provides the starting point for the development of an analytical model for evaporating droplet. Using the fuel species equation together with the overall continuity equation and integrating the transport at droplet surface, the mass flux at the droplet surface can be obtained as [46];

$$\frac{\dot{m}_F}{4\pi R^2} = \frac{\rho_G D}{R} \ln(1+B) \qquad wh,\ B = \frac{y_{FR} - y_{F\infty}}{1 - y_{FR}} \tag{1}$$

Where B is the Spalding number, R is the radius of the droplet, D is the binary mass diffusion coefficient, $\dot{m}$ is the mass flow flux (evaporation rate), y is the vapour phase mass fraction, and ρ_G is the gas phase density. The subscripts F, R and ∞ stand for fuel, condition at the droplet surface and at infinity respectively. By assuming constant droplet density, the rate of change of droplet diameter can be defined as;

$$\frac{dD_d}{dt} = -4 \frac{\rho_G D}{\rho_L D_d} \ln(1+B) \tag{2}$$

The above can be integrated to yield the d^2-*law* [33]. The d^2-*law* predicts linear decrease in droplet surface area with time as [47];

$$D_{d,0}^2 - D_d^2 = K_D \cdot t \qquad wh,\ K_D = 8 \frac{\rho_G D}{\rho_L} \ln(1+B) \tag{3}$$

In order to solve the complete problem of the evaporation of a droplet, the droplet temperature needs to be solved as well. The heat transfer effect to the droplet can be obtained in a same way as the mass flux as [46];

$$\frac{\dot{m}_F}{4\pi R^2} = \frac{\lambda}{C_{P,F} R} \ln(1 + B_T) \qquad wh,\ B_T = \frac{C_{P,F}(T_\infty - T_R)}{h_{fg} + q_L \dfrac{4\pi R^2}{\dot{m}_F}} \tag{4}$$

Where λ is the thermal conductivity, B_T is the thermal transfer number, q_L is the heat conducted to the droplet, h_{fg} is the evaporation enthalpy and $C_{P.F}$ is the specific heat of vapour. The *d^2-law* can be written as;

$$D_{d,0}^2 - D_d^2 = K_\lambda \cdot t \qquad wh,\ K_\lambda = 8 \frac{\lambda}{\rho_L C_{P,F}} \ln(1 + B_T) \tag{5}$$

At the pseudo-wet bulb temperature, when all the heat transferred to the droplet goes to the evaporation enthalpy, the evaporation rate constants of mass and heat transfer become equal, meaning $K_D = K_\lambda$. Miller et al.[48] compared the many different existing evaporation models. The equations for droplet mass transfer and heat transfer of those models are rewritten and presented here. By considering two phase flow where the dispersed phase is in the form of a single component spherical liquid droplet with density higher than the surrounding gas, the rate of temperature and the mass of the droplet can be obtained as [48];

$$\frac{dT_d}{dt} = f_{corr} \left(\frac{Nu}{\mathrm{P}_{r,G}} \right) \left(\frac{\theta_1}{\tau_d} \right) (T_\infty - T_d) + \left(\frac{h_{fg}}{C_{P,L}} \right) \left(\frac{\dot{m}_d}{m_d} \right) - H_{\Delta T} \tag{6}$$

$$\dot{m}_d = \frac{dm_d}{dt} = -\left(\frac{Sh}{3 S_{C,G}} \right) \left(\frac{m_d}{\tau_d} \right) H_M \tag{7}$$

Where, Nu is the Nusselt number, Sh is the Sherwood number, $\theta_1 = C_{p,G} / C_{p,L}$ is the ratio of gas phase and liquid phase specific heat. m_d is the mass of the droplet, $S_{C,G} = \mu_G / (\rho_G \Gamma_G)$ is the Schmidt number with ρ_G , μ_G and Γ_G are the gas phase density, viscosity and binary diffusion coefficient respectively. $\mathrm{P}_{r,G} = \mu_G C_{p,G} / \lambda_G$ is the Prandtl

number with λ_G is the thermal conductivity. f_{corr} is the correction factor to heat transfer due to mass transfer, $\tau_d = \rho_L D_d^2 / (18\mu_G)$ is the particle time constant for Stokes flow. H_M is the mass transfer driving potential (similar to $(T_\infty - T_d)$ for heat transfer and $H_{\Delta T}$ represents the any additional terms used to incorporate non-temperature internal effects (i.e. finite thermal conductivity).

After rewriting all these equations, the different models can be compared by comparing the models parameters (H_M , $H_{\Delta T}$ and f_{corr}). The comparison is shown in Table 2-1.

Table 2-1: Comparisons of different evaporation models (by Miller et al.[48]).

Model	Name	f_{corr}	$H_{\Delta T}$	H_M
1	Classical	1	0	$\ln(1+B_M)$
2	Abramzon and Sirignano [49]	$\frac{\dot{m}_d}{m_d B_T^{'}}\left(\frac{3P_{rG}\tau_d}{Nu}\right)$	0	$\ln(1+B_M)$
3	Heat-transfer analogy	$(1+B_T)^{-1}$	0	B_M
4	Renksizbulet and Yuen	$(1+B_T)^{-0.7}$	0	$\ln(1+B_M)$
5	Lage et al.	$(1+B_T)^2 \Delta_h^b \exp\left[c \cdot \ln^2(1+B_T)\right]$	0	$\ln(1+B_M)$
6	Langmuir-Knusden	$G = \frac{\beta}{e^\beta - 1}$	$\frac{2\beta}{3\mathrm{P}_{\mathrm{r}G}}\left(\frac{\theta_1}{\tau_d}\right)\Delta_s$	$\ln(1+B_{M,neq})$

The classical model (Model number 1) is already presented in the present section. Abramzon & Sirignano [49] developed the model number 2 to include the effect of Stefan flow (blowing) in heat and mass transfer processes. This model was proposed with modified *Nu* and *Sh* numbers and it requires an iteration process which can be costly for spray simulations [48]. Model number 3, is a simple model derived from species transport equations in the gas phase, and substituting the mass fraction gradient in terms of *Sh* number and mass fraction difference [48]. Model number 4 incorporates the effect of mass transfer in the heat transfer process and does not require any iteration [48]. Model number

5 was derived on the basis of series solution, by investigating the effect of blowing on the heat and mass transfer over a spherical droplet. In Miller et al.'s paper [48], model number 6 showed better results than the other models. It includes the non-equilibrium effect using the non-equilibrium transfer number ($B_{M,neq}$) and non-equilibrium temperature. It also includes the correction factor based on quasi-steady solution of gas phase.

2.4.2 Convective and Distortion Effect during Evaporation

The heat transfer effect to a spherical evaporating droplet by classical theory, which assumes unity Lewis number, can be rewritten as [50];

$$Nu \text{ and / or } Sh = 2\frac{\ln(1+B_M)}{B_M} \tag{8}$$

The effect of convection can be accounted for by correcting the $Nu \text{ and / or } Sh$ [51] as;

$$Nu \text{ or } Sh = (2 + f(\mathrm{Re}, \mathrm{Pr} \text{ or } Sc))\frac{\ln(1+B_M)}{B_M} \tag{9}$$

A paper by Arcoumanis [52] found in the literature includes the effect of distortion during the evaporation. Distortion means the effect of relative motion of the droplet, i.e. aerodynamics forces are taken into account during the evaporation. Arcoumanis [52] included the effect of distortion in diesel spray calculation. The corrections for Nu and Sh are similar to Ranz and Marshall's correction [51, 53] as;

$$\begin{aligned} Nu &= (2.0 + 0.085\,\mathrm{Pr}^{1/3}\,\mathrm{Re}^{0.804})\frac{\ln(1+B)}{B} \\ Sh &= (2.0 + 0.085 Sc^{1/3}\,\mathrm{Re}^{0.804})\frac{\ln(1+B)}{B} \end{aligned} \tag{10}$$

2.4.3 Liquid Phase Phenomenon

Circulation within the liquid phase is one of the most critical issues during the liquid droplet modelling. Droplets are generally injected into a hot pressurised environment though an injector. The deceleration of the small droplets is proportional to the drag. The drag is a function of droplet diameter squared divided by its inertia, therefore, the droplet velocity varies inversely to its diameter. Due to the high relative velocity, shear at the droplet causes internal motion within the liquid droplets as shown in Figure 2-7 (a).

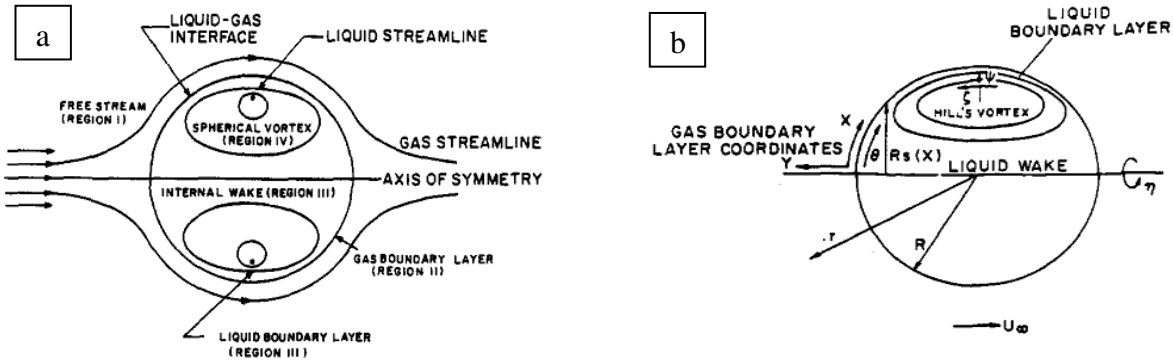

Figure 2-7: (a) Flow region inside and outside the droplet moving with high velocity. (b) Hill's vortex analysis of the droplet (Both figures from Sirignano [54]).

In 1983, Sirignano [54] explained this liquid motion phenomena using Hill's vortex analysis as shown in Figure 2-7 (b). This figure is in ideal condition; in reality the liquid core breaks up due to secondary atomisation of the droplet which causes disruption to the droplet. According to Sirignano [54], the internal circulation improves the heat and mass transfer rates and decreases the droplet lifetime. Sirignano also noted that the fully mixed droplet assumption is not valid. Sirignano's argument is that internal circulation still maintains the gradient within the droplet, no matter how strong Hill's vortex is. Opinions of different researchers on the mixing within the liquid are discussed in a later section.

2.4.4 Multicomponent Liquid Evaporation

Considerable amount of research has been done on the evaporation and combustion of a single pure component fuel. These studies provide the basic understanding and approximations. Most of the commercial fuels (e.g. diesel, gasoline, heavy fuel oil) are multicomponent and possess a large range of boiling points [55]. The modelling of such fuel is not straightforward because describing its physics is more complex compared to a

single component fuel. This complexity involves mass transfer processes within the droplet, vapour-liquid equilibrium at the droplet surface and gas phase representations.

Previous theoretical and experimental studies showed that evaporation and combustion characteristics of multicomponent fuel have two main characteristics different from single component fuel as:

(1) The phase change process at the fuel surface and the transport of the fuel vapour in the vapour phase is different from that of single component, and
(2) The evaporation is time varying due to continuous changes in the composition and the temperature of the droplet as evaporation proceeds, therefore, a better understanding of heat and mass transfer within the droplet is required [55].

The importance of multicomponent evaporation in heavy fuel oil combustion has been discussed in the previous sections. Many researchers focused on the two-component or multicomponent evaporation, ignition and combustion using the classical theory or with some modifications. The examples of such studies are Kneer et al.[56], Law [55, 57], Law and Law [58], Bergeron and Hallett [59], Mawid & Aggarwal [60], Hallett & Ricard [61] etc. Most of the studies listed above were for two components except a study by Hallett & Ricard [61] who applied a well-mixed model to the ignition of a seven component fuel droplet. Further, results obtained by Law [55] showed that no single component or bicomponent mixture can effectively represent the evaporation of the real commercial multicomponent fuel.

The major factors noted from the literature which should be considered in understanding the evaporation of multicomponent fuel are summarised as follows [62];

- Different components evaporate at different rates. The more volatile components evaporate at a faster rate than the low volatile components. This difference in evaporation rates creates concentration gradients in the liquid droplet.
- The amount of mixing within the droplet because miscibility of different components also controls the rate at which the components are exposed to the droplet surface.

- Simultaneous solution of liquid phase species continuity equations are required for, (1) multicomponent vapour-liquid equilibrium, (2) gas phase multicomponent energy and species continuity equations.

2.4.5 Liquid Mixing in Evaporation of the Droplet

It is accepted that the liquid evaporates only when it is exposed to the surface. Therefore, mixing within the liquid droplet has become an important subject of research. In the literature two kinds of limiting cases for the transport of the mass and heat within the liquid are found:

(1) Well mixed model (Infinite diffusivity model)
(2) Diffusion limited model

2.4.5.1 Well Mixed Model (Infinite Diffusivity Model)

This model is applicable for low viscosity mixtures in which the internal circulation within the liquid is fast enough so that the droplet concentrations and temperature remain uniform, but varying with time. In this model, the evaporation of the entire droplet is controlled by the relative volatilities of the components. In other words, the more volatile components are continuously brought to the surface where they evaporate in order of their volatility, leaving the less volatile components in the droplet. This kind of evaporation is similar to batch distillation. The motion within the liquid droplet can be caused by the buoyant motion of the air or evaporated vapour in the surrounding [55].

Law [55] presented this kind of well mixed model (spatially uniform droplet properties but temporarily varying). A binary mixture of octane and heptane was used. In the results two separate slopes were observed for the prediction of d^2-*law,* Dominant evaporating species evaporates in order of their relative volatility. Both regions follow the d^2 *law* behaviour and showed the preferential type of evaporation. Law et al.[63] developed a model by assuming a uniform liquid temperature. Their results showed that the intensity of mixing increases as the viscosity decreases. As noted earlier, Hallett & Ricard [61] assumed a well-mixed droplet and developed a model for the droplet evaporation and ignition using

seven different components to accurately model the distillation curve. They pointed out that the distillation curve is not a good indicator of the ignition behaviour but overall ignition is governed by the chemical nature and boiling point of the most volatile species in the mixture.

In 1995, Tamim & Hallett [18] developed a new approach for the evaporation of multicomponent fuels using a Probability Density Function (PDF) for the fuel composition. This approach is called the theory of continuous thermodynamics and will be described in great detail in the next section. They assumed a well-mixed droplet behaviour in their approach, their result showed good agreement with the experimental observations. Moreover, Law [58] has pointed out that the theoretical analysis showed the diffusion limited type behaviour of the multicomponent droplet but experimental evidence supported the batch type distillation behaviour. Baert [14] pointed out that HFO evaporation process is different from multicomponent droplet evaporation. Opinions of different researchers about evaporation behaviour of heavy fuel oil droplet are given in Chapter 4.

2.4.5.2 Diffusion Limited Model

This model is relevant for the high viscosity mixtures where internal circulation within the liquid does not exist and transport within the liquid phase is only governed by molecular diffusion. Molecular diffusion is extremely slow compared to the liquid surface regression rate. The concentration changes at the droplet surface very rapidly but the core of the droplet remains unaffected. Therefore, the relative volatility of the liquid does not affect the overall process of the evaporation [18, 55].

Landis & Mills [64] studied the effect of internal diffusional resistance on the evaporation of binary droplets. Their result showed that internal concentration approaches a constant profile after a short initial transient period and it remains there till the end of droplet lifetime. They concluded that the liquid phase diffusion is a slow process and it controls the surface composition.

Law & Law [58] presented the d^2-*law* behaviour of a single component and multicomponent fuel. They assumed the gas phase as quasi-steady and Lewis number as unity in the gas phase. Their derived equations showed that multicomponent equations are closely related to single component equations; except their values were replaced by mixture mass fraction weighted values. The droplet surface temperature in a single component model can be derived from the liquid boiling point but in the case of multicomponent mixture it needs an iteration procedure to obtain it (refer Law & Law [58] for detailed expressions). Their result showed that due to the extremely slow rate of diffusion, an approximately constant concentration profile exists for a significant portion of the droplet lifetime, with a sharp concentration gradient near the droplet surface. They also suggested that the quasi-steady gas phase assumption can be used to simplify the complex multicomponent modelling.

Mawid & Aggarwal [60] studied the transient combustion of a multicomponent fuel mixture droplet and they showed that at the surface of the droplet a boundary layer exists. Sirignano [62] studied both cases of the internal mixing (well mixed model and diffusion limited model) of the droplet and They result shows the considerable amount of difference with both models.

Jin & Borman [65] proposed a model with internal circulation by means of an effective molecular diffusivity. This model includes the effect of high pressure to calculate the vapour-liquid equilibrium at the droplet surface by means of the Redlich-Kwong equation of state. It also utilises an intermediate approach between the well-mixed and the diffusion limited model. The model of Jin & Borman [65] showed a linear slope of the d^2-*law* for the steady evaporation beyond the initial droplet heating. Preferential evaporation was observed to a lesser extent, when the ambient pressure is close to critical pressure. Abraham & Magi [66] developed a model for the multicomponent droplet evaporation in sprays. They weighted the molar vapour fraction at the droplet surface by the molecular diffusivity of each component. This model was limited to theoretical study only, no experimental results were found.

Kneer et al.[56] studied the importance of variable properties in diffusion controlled evaporation of a multicomponent fuel. Their result showed that the diffusion resistance of the droplet can be altered by varying the properties of liquids (density, viscosity, binary

diffusion coefficient and thermal conductivity) which are dependent on liquid concentrations and temperature. It was also shown that the sharp increase in vapour concentration at the initial stage of droplet lifetime caused by high volatile components is important for ignition.

2.4.5.3 Droplet with Internal Circulation

Sirignano et al. (Lara-Urneja & Sirignano [67], Prakash & Sirignano [68, 69], Sirignano [54], Tong & Sirignano [70]) have conducted detailed studies on the effect of circulation in the convective environment which is summarised in ref [62]. Parkash and Sirignano [68, 69] developed a model for the temperature distribution of a droplet. Later, Lara-Urneja & Sirignano [67] extended that model to mass transfer of a multicomponent droplet. Furthermore, Tong & Sirignano [70] simplified the complex model developed by earlier researchers and implemented a so called vortex model for spray calculations. Their model accounted for liquid phase internal circulation, transient droplet diffusion, and asymmetric gas phase convection. However, they noted that due to large scattering in the results with experimental comparison, a concrete conclusion was not drawn. Abdel-Qader & Hallett [71, 72] investigated the role of internal mixing in the evaporation of droplets of mixture containing many components using continuous thermodynamics. Their results showed that internal mixing has a smaller influence on the droplet containing many components than the binary component droplet.

In general, many papers are found in the literature concerning heat and mass transfer models of a multicomponent droplet. The models have varying levels of complexity in terms of computational cost. Sirignano has categorised liquid phase models into different levels of complexity in his book [62]. In increasing order of the complexity these models are summarised in Table 2-2.

Table 2-2: Levels of liquid phase modelling complexity (Sirignano [62]).

Level	Liquid Phase Modelling
1	Constant droplet temperature model (d^2 *law*)
2	Infinite liquid conductivity model (uniform droplet temperature but varying with time)
3	Finite liquid conductivity, droplet divided into 2 regions (shell or skin and core region)
4	Spherically symmetric droplet heating (conduction limited or finite conductivity)
5	Vortex model for droplet heating (using Hill's vortex in the modelling)
6	Navier-Stokes solution of the droplet internal flow

2.4.6 High Pressure Effects on Evaporation

The high-pressure evaporation models are different from low-pressure models on a number of levels. These differences are summarised as [47, 73, 74];

- Lewis number is not unity.
- Ambient gas may dissolve in the liquid at the droplet surface.
- *Raoult's law* cannot be assumed since neither the liquid nor the gas are ideal.
- The transient heating time is longer than the low-pressure model due to high pseudo wet bulb temperature.

Furthermore, to include the effect of high pressure the thermodynamics and transport properties of the liquid and vapour phase need to be adjusted. Droplets may reach the critical temperature at high pressures which does not occur at low pressures. Therefore, some of the transport properties which need to be adjusted at high pressure are given as [47, 73, 74];

- The evaporation enthalpy decreases with an increase in the temperature and at the critical temperature it completely vanishes [75]. Moreover, it also diminishes with increase in pressure, and is can be represented by ideal latent heat of evaporation.

- The surface tension of the liquid also decreases as the temperature approaches the critical temperature and it completely vanishes at the critical point. In order to allow the effect of high pressure by allowing the ambient gas to dissolve into liquid surface, the surface tension needs to be taken into consideration during the modelling.
- The specific heat is a function of pressure and needs to be corrected at high pressure.
- The viscosity of a mixture is a function of temperature, which may enhanced at critical point therefore it needs to be adjusted for high pressure calculations.

The vapour flux from the evaporating droplet can be written as [74];

$$\dot{W}_F = y_F(\dot{W}_F + \dot{W}_N) - (\rho D_{FN})_G \frac{dy_F}{dr} \tag{11}$$

Where $\dot{W}_F = \dot{m}_F / (4\pi R^2)$ is the mass flux of fuel species, subscript N stands for surrounding gas nitrogen and $(\rho D_{FN})_G$ is the product of the gas phase density and the binary diffusion coefficient of the fuel vapour in nitrogen. $\dot{W}_N$ is the rate of gas diffusion into the liquid. For slow evaporation and no gas diffusion into the liquid, the above equation can be simplified to;

$$\dot{W}_{F,R} = (\rho D_{FN})_G \left.\frac{dy_F}{dr}\right|_R \left(\frac{1}{1-y_F}\right) \tag{12}$$

For high rates of surface regression and diffusion of many species, the above equation can be modified to;

$$\dot{W}_{F,R} = (\rho D_{FN})_G \left.\frac{dy_F}{dr}\right|_R \left(\frac{1}{x_F - y_F\left(1-\frac{\rho_G}{\rho_L}\right)}\right) \tag{13}$$

Where, x and y stand for the liquid and vapour phase mass fractions. Kodota & Hiroyasu [76] included the surface regression effect on convectional evaporation rate which can be given as;

$$\frac{\dot{m}_F}{4\pi R^2} = \frac{(\rho D)_G}{R}(Sh^o \cdot \xi_M)B^* \quad wh, B^* = \frac{y_{F,R} - y_{F,\infty}}{1-(1+\varsigma)y_{F,R}} \tag{14}$$

Where, Sh^o is the Sherwood number without evaporation effect, ξ_M is the correction factor for evaporation (in low pressure this correction is given as $\ln(1+B_M)/B_M$), B^* is the modified transfer number, which includes the surface correction due to pressure as;

$$\varsigma = \frac{\dot{W}_F}{\dot{W}_N} = -\frac{\rho_G(1-y_{F,R})}{\rho_L + \frac{R}{3}\frac{d\rho_L}{dt}\Big/\frac{dR}{dt}} \tag{15}$$

Similar to the mass transfer correction factor the correction to the heat transfer also is found in Kodota & Hiroyasu's paper [76]. They included the non-ideality of liquid and gas by using the Redlich-Kwong EOS. Their results showed the difference between low-pressure and high-pressure models and also the importance of high pressure model.

Givler & Abraham [47] presented a very good paper on the evaporation and the combustion of droplets at supercritical conditions. They used many numerical and experimental studies and therefore it is worthwhile to note their findings here. Their results which are summarised in the form of figures are shown in Figure 2-8. As shown in Figure 2-8(a), if the reduced pressure and temperature exceeds 2, pure evaporation and unsteady evaporation exists throughout the droplet lifetime. The evaporation rate increases with increase in the pressure. Moreover, it increases strongly for the subcritical pressures but for the supercritical condition it may decrease. The droplet temperature may be transient for the droplet lifetime but evaporation rate can follow quasi-steady behaviour.

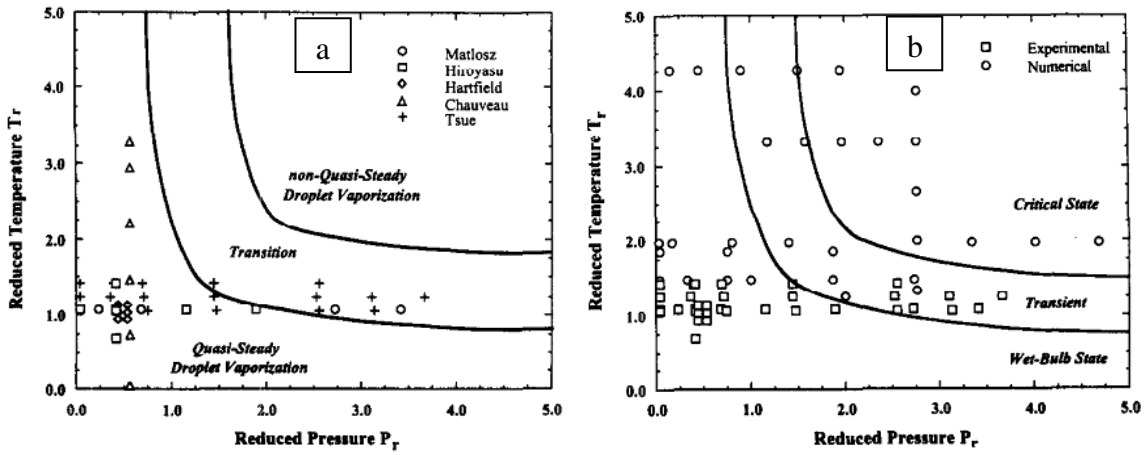

Figure 2-8: (a) Qualitative representation for quasi-steady and non-quasi-steady evaporation as a function of experimental reduced temperature and pressures. (b) Qualitative representation of the droplet temperature over a range of ambient temperatures and pressures (from Givler and Abraham [47]).

Furthermore, as shown in Figure 2-8 (b), Givler & Abraham also defined three regions for droplet temperature, namely pseudo wet bulb temperature, transient temperature and critical temperature region. The first region (pseudo wet bulb temperature) is the steady temperature the droplet reaches under higher pressure and temperature. The second region is the transient temperature which is observed throughout the droplet lifetime. The third region is the critical temperature region, when the reduced pressure and temperature are greater than 2 then the droplet may reach critical state in the liquid phase.

Most recently, Yan & Aggarwal [77] developed a high-pressure droplet model for spray simulations of a single component fuel. They compared the model for quasi-steady and transient effects. Their result showed good engagement between the quasi-steady and the transient model for the wide range of pressures at low ambient temperature, and also for the high temperature but at pressures only up to the critical pressure of the liquid.

In the literature, many papers are found that dealt with the evaporation of multicomponent fuels at high pressure and use the equation of state to describe the vapour-liquid equilibrium, and they are summarised in the present section. Pedersen et al.[78-80] published three papers which described the thermodynamics of the petroleum mixtures containing heavy hydrocarbons. Pedersen et al.[79] showed that the critical temperature and pressure of each of the carbon number fractions heavier than the C_6 should be determined by Cavett and Lee-Kesler relations (refer Pedersen et al.[79] for details of

these relations). They reported that the most suitable method to determine the liquid phase density is Alani-Kennedy equation and Standing-Katz method [80].

Zhu & Aggarwal [75, 81, 82] reported a numerical investigation of droplet evaporation in a supercritical environment. The physical-numerical model was developed to simulate the trans-critical and supercritical evaporation based on time dependent conservation equations for liquid and vapour phases and pressure dependent thermo-physical properties. They have used three different equations of state; Redlich-Kwong (RK), Soave-Redlich-Kwong (SRK) and Peng-Robinson (PR). Their result showed variations with all three EOS. Moreover, their results also indicated that at low to moderate temperature, droplet lifetime first increases then decreases with increase in pressure. On the other hand, at high temperatures droplet lifetime continuously decreases with pressure.

Zhang [83] developed a numerical model and studied the evaporation of a suspended droplet in forced convective high-pressure conditions. The model included liquid phase internal circulation, real gas effect, gas-liquid transient effect and solubility of gas into liquid phase. The results showed good agreement with the microgravity experimental results. Further, the result also showed that droplet lifetime decreases with increase in pressure and temperature. This result confirms the findings of Zhu & Aggarwal [75, 81, 82] described in the previous paragraph. Zhang [83] also noted that solubility of nitrogen in liquid (n-heptane) can be neglected at low ambient pressure but it cannot be neglected at higher pressure.

Kim & Sung [84] studied the effect of ambient pressure on the evaporation of a single droplet and the spray. The developed model considered the fugacities of the liquid and gas phases for the calculation of VLE. Their result showed that the droplet lifetime decreases with increase in the ambient pressure. The evaporation of the spray was enhanced at high pressure and temperature. At high pressure, the atomisation and the evaporation rate from a single droplet was increased compared to low pressure.

In the above section, the literature based on the evaporation of single and multicomponent liquids at high-pressure are reviewed. In the following section literature based on the theory of continuous thermodynamics used for high pressure evaporation are reviewed. In 1985, Cotterman & Prausnitz [85] introduced the equation of state to calculate the phase

equilibrium of a mixture containing many components. Around the same time, they [86] also introduced the equation of state for the flash calculation (calculation of bubble points and dew points) of the semi-continuous mixture. In that paper they introduced two different methods; (1) method of moment and (2) quadrature method to determine the flash calculations. This paper is found to be very useful in later studies where continuous thermodynamics is applied to complex hydrocarbons. Based on Cotterman & Prausnitz's work [86], Baer et al.[87] developed a method for the prediction of vapour-liquid equilibrium of a complex multicomponent mixture based on a two parameter equation of state using the method of continuous thermodynamics. They used a continuous version of the Wong-Sandler mixing rule and RK EOS. Their result showed good agreement with the experimental data.

Zhu & Reitz [75, 88] developed a comprehensive model for the transient evaporation process of real engine fuels at high pressure using continuous thermodynamics. They derived transport equations for a semi-continuous mixture for both the gas phase and also the liquid phase. Moreover, their approach to the equation of state was generic; hence vapour-liquid equilibrium can be obtained for any EOS. Their result showed that at high pressure, light species evaporation is inhibited compared to heavy species. Their result of the comparison of multi-component with the single-component droplets also emphasizes the importance of considering multi-component fuels.

In the literature a paper [89] is found where researchers used the continuous thermodynamics for modelling of practical diesel engine spray combustion at high-pressures. Yi et al.[89] developed a model for the spray combustion of diesel at high pressures by assuming a well-mixed droplet composition and temperature. The model predicted the liquid length in an evaporating spray and showed a good match with experimental results. Yi et al.[89] noted that the high pressure model provides better mixing in the spray region because it considers the effect of temperature and pressure in the calculation of physical properties. The comparison of Sauter Mean Diameter (SMD) as a function of axial distance from the nozzle exit by low-pressure and high-pressure model showed similar results.

2.5 Overview of Continuous Thermodynamics

The representation of the composition of any multicomponent fuel is always difficult in engineering applications such as distillation and other separation techniques. Some examples of commonly used multicomponent mixtures in engineering are; petroleum fractions, coal derived chemicals, acids and aldehydes in biomass oil. The representation of two or three components is easy and can be represented by mole fractions, but when they contain more than hundreds or thousands of different components, their representation is extremely difficult. In addition, mole fractions of most of the components in multicomponent mixtures are unknown. Hence, there should be some technique that can be applied to accurately represent these fuels. In the literature, three techniques are found, namely; (1) pseudo component technique, (2) continuous thermodynamics and (3) semi continuous thermodynamics. Sometimes the continuous thermodynamics technique is also called thermodynamics of continuous mixture.

In the pseudo component technique, individual components with similar properties are lumped together to form one group, then their representation is carried out by a block or bar type distribution (see Figure 2-9). This technique is useful for representing the binary mixture or mixture with small component numbers but it is not adequate for representing multicomponent fuels. Generally, this technique is adopted to avoid mathematical complexity in phase equilibrium calculations, but it has a disadvantage of distortion in expressing composition accurately [90].

The second technique (continuous thermodynamics technique) uses a simple continuous mathematical distribution function (probability density function (PDF)) to represent one of the physical properties of the fuel instead of the mole fractions of individual components, as shown in Figure 2-9. The third technique is can be summarised as summation of the first two techniques. In other words, a few components of fuel are represented as discrete components and others are represented by probability density functions. This technique is very useful when some the components of the mixture are discrete (such as nitrogen in nitrogen-fuel vapour mixture) which are represented as the discrete components, while the other continuous components (fuel vapour) are represented by PDFs.

Generally, fuel is composed of many homologous chemical components and each these components are comprised of many species. For example, heavy fuel oil is comprised of n-paraffins, aromatics and naphthenes etc, yet in that mixture n-paraffins itself is comprised of many different spices such as octane, nonane, decane etc.

In continuous thermodynamics, the distribution function represents some physical properties of homologous chemical components of multicomponent mixture, such as boiling point of component, molecular weight of the component or carbon number of the component. These homologous components can be paraffins, naphthenes, aromatics etc. Figure 2-9 shows the comparison between conventional discrete (classical thermodynamics) and continuous thermodynamics representation of multicomponent fuel mixtures. As shown in Figure 2-9, in discrete modelling mole fractions of the species of homologous components are used to represent the composition of that particular component, while in continuous thermodynamic modelling these mole fractions are simply replaced by an appropriate distribution function. And depending upon the number of homologous hydrocarbons groups, the number of distributions can be used.

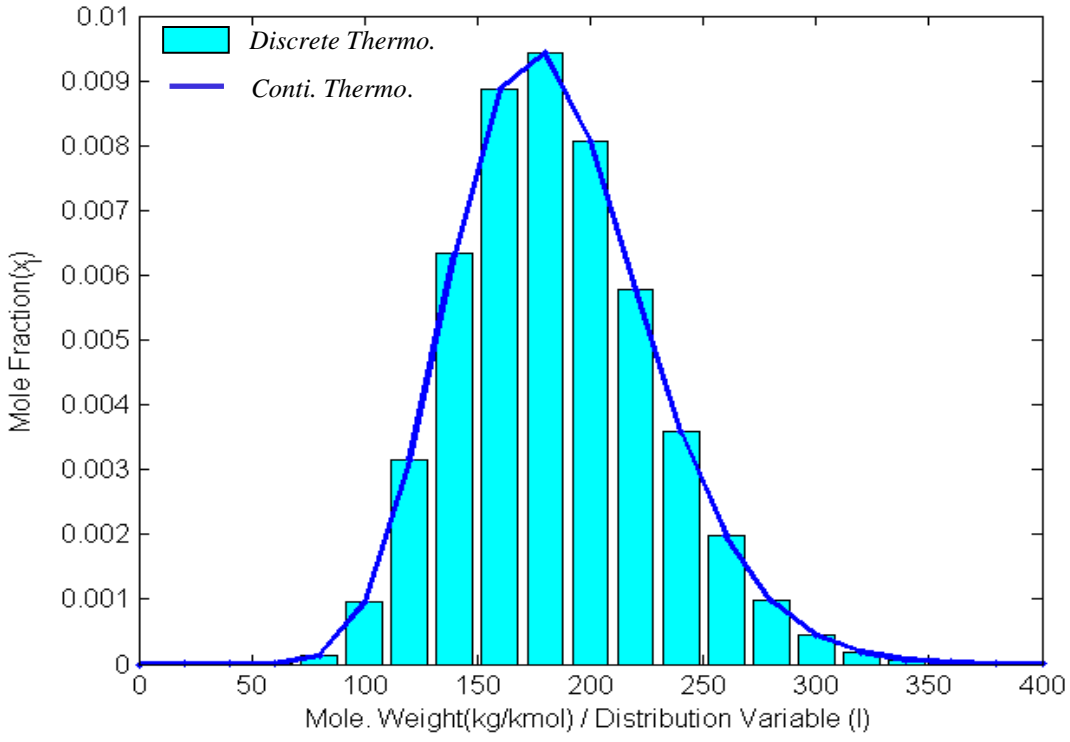

Figure 2-9: Discrete and continuous representation of multicomponent mixture

In discrete modelling summation of all individual components mole fractions are given by unity as;

$$\sum_{i=1}^{H} x_i = 1. \tag{16}$$

While in continuous thermodynamics the above equation for individual phase is given as [17];

$$\sum_{j=1}^{J} x_j \int_I f_j(I)dI = 1. \quad where \int_I f_j(I)dI = 1. \tag{17}$$

In continuous thermodynamics, each individual component in the fuel mixture is characterised by the characterising variable I. As mentioned earlier this characterising variable can be any physical property. Therefore, the total molar concentration of fuel mixture with distribution function is given as [91];

$$n(I_1, I_2) = \int_{I_1}^{I_2} f(I)dI \tag{18}$$

Where, n is the molar concentration of the property I and is between I_1 and I_2.

Representation of the semi continuous thermodynamics for H family of discrete species and J family of continuous distribution is given as the summation of the above two approaches [17];

$$\sum_{i=1}^{H} x_i + \sum_{j=1}^{J} x_j \int_I f_j(I)dI = 1. \quad where \int_I f_j(I)dI = 1. \tag{19}$$

The concept of continuous thermodynamics was first introduced by Katz & Brown [92] approximately 70 years ago. They introduced an adapted method of calculating vapour

pressure of petroleum fractions. They assumed that properties of a continuous mixture vary continuously in the composition range. Subsequently, this technique was not often used for some time, but over the past two decades many researchers have used it. The majority of work using this technique has been found is in the petroleum industry, where mixtures contain large numbers of different and dissimilar components.

Some of the major areas of science and engineering found in literature, where the continuous thermodynamics technique has been successfully applied are;

- Gas condensate mixtures simulation [93]
- Natural gas dew points calculations [94, 95]
- Petroleum mixture phase equilibrium [18, 90, 96-99]
- Petroleum mixtures flash calculation [85, 86, 90, 100-102]
- Distillation and absorption of petroleum mixtures [103-105]
- Liquid –liquid phase equilibrium of polymers [85]
- Homogeneous nucleation of multicomponent vapour [106]

From the above literature three main points are found to be important for continuous thermodynamics modelling [18];

1. The choice of proper distribution function to represent the mixture
2. The choice of proper characterising variable
3. The choice of phase equilibrium

To represent the fuel, the distribution function is one of the basic requirements of continuous thermodynamics. It can be any suitable mathematical distribution function that represents the mixture accurately, but its choice depends on convenient handling throughout the model execution. In many papers [103, 107-109] a Gaussian distribution has been used as the distribution function to represent the mixture. The only limitation of this distribution is that it is unbound at both ends. Therefore, it cannot be used in practical calculations where the characterising variable requires a lower bound. Some common examples of such characterising variable are molecular weight of petroleum fractions, carbon number etc. This limitation of the Gaussian distribution can be overcome by

selecting the gamma distribution function. The gamma distribution function is simple and it has a lower bound therefore it more accurately represents petroleum fractions. Many researchers such as Cotterrman & Prausnitz [85, 86, 100], Peng et al.[99], Chou & Prausnitz [104], Hallett et al. [18-21, 61, 71, 72, 110, 111], Lippert et al. [91, 112, 113], Zhu & Reitz [75, 88], Ra & Reitz [114, 115], Harstad et al. [116, 117], Rakowski et al.[17] used the gamma distribution in their modelling. Other distribution functions found in the literature are; a bivariate log-normal distribution by Teja & William [118], a β-distribution function by Radosz [119] and a general distribution function by Vakili-Nezhaad et al.[120].

After the choice of distribution function, the choice of characterising variable is important. This characterising variable can be any physical properties of the multicomponent mixture. Some examples of such characterising variables found in the literature are;

- Molecular weight of the component, used by Cotterman & Prausnitz [85], Peng et al.[99], Hallett et al. [18-21, 61, 71, 72, 110, 111], Lippert et al. [91, 112, 113], Zhu & Reitz [75, 88], Ra & Reitz [114, 115] and Rakowski et al.[17]
- Component's boiling point, used by Kehlen & Ratzsch [108].
- Component's carbon number, used by Willman & Teja [94].

The third important point to be considered for continuous thermodynamics is vapour-liquid equilibrium. Vapour-liquid equilibrium is extremely important; it provides the relationship between vapour phase and liquid phase molecules at the liquid surface and when dealing with equilibrium of hundreds and thousands of different molecules its importance is high. Two main approaches are found in the literature of continuous thermodynamics for vapour-liquid equilibrium: 1, ideal solution and 2, non-ideal solution approach. Most of the researchers, Kehlen & Ratzsch [107], Hallett et al. [18-21, 61, 71, 72, 110, 111], Lippert at al. [91, 112, 113], Zhu & Reitz [75, 88], Ra & Reitz [114, 115], Harstad at al. [116, 117], Doue at al. [121-123] used an ideal solution assumption in their respective study. In those studies, *Raoult's law* was used to obtain the mole fraction (which is part of the vapour-liquid equilibrium) of different components of multicomponent mixture along with Clasious-Clapeyron equation and Trouton's rule to

give the component's vapour pressure. These basic assumptions yield the relationship between liquid phase and vapour phase at low pressure. However, at elevated pressure an appropriate equation of state yields the VLE. An equation of state provides the relationship between state variable (temperature, pressure, mass, enthalpy etc) of liquid and vapour phase under given physical condition. Many researchers used different types of equation of state to describe the relations between state variables which are;

- Viral equation of state [94]
- Peng-Robinson equation of state [96, 99, 124]
- Van der Wales equation of state [98]
- Redlich-Kwong or Soave-Redlich-Kwong equation of state [85, 104].

Continuous thermodynamics gained popularity since a successful mathematical model for the evaporation of multicomponent fuel developed by Tamin & Hallete [18] in 1995. Thereafter a large amount of research work [17, 19, 20, 71, 72, 75, 110, 111, 114, 115, 117, 121, 123, 125] has been done on the fuel evaporation process using this technique. The continuous thermodynamics technique also has potential to describe the behaviour of a multicomponent fuel in a spray model. This was demonstrated by Lippert at al. [91, 112, 113]. Recently, Hallett & Clark [21] developed a continuous thermodynamics model of biomass evaporation and pyrolysis which shows good agreement with the experimental results.

In summary, continuous thermodynamics modelling has proved successful for dealing with multicomponent mixtures.

2.6 Spray Combustion

Most engines use fuel in liquid form and many processes are involved which affect engine efficiency, performance and emissions. Spray modelling of the liquid is one of the most studied areas of engine modelling. Spray combustion modelling involves many complicated models of turbulence, chemical reactions and two phase flow interactions.

In spray combustion, fuel enters into a combustion chamber of the engine through an injector at high velocity and breaks up through atomisation. As the fuel droplets travels, the size of the droplets and their composition changes due to aerodynamic forces and effect of ambient temperature and pressure on the droplet. The size history of the droplet is part of the turbulence modelling liquid spray, while composition changes due to temperature and pressure are covered in mass and heat transfer modelling of the liquid. Spray combustion modelling employs basic concepts of fluid dynamics, heat and mass transfer engineering along with a statistical approach.

In 1953, Godsave [33] studied the theory of combustion of droplets in spray and the burning of droplets. However, from Godsave's literature it was clear that actual studies commenced earlier. In 1952, Hottel et al.[32] also studied the combustion of droplets. Then after almost three decades the well known d^2-*law* for multicomponent fuel developed by CK Law [58] enhanced the studies. During the 1990's some researchers [126-128] studied the structure of evaporating sprays. In addition, during the same period Manuel et al.[129] developed the simulation of a vaporising spray with particular focus on heat transfer during the compression stroke, spray development, vaporization and fuel/air mixture formation and ignition.

During 1998-99, Siebers [130, 131] studied the evaporation and multicomponent behaviours of diesel spray using MIE scattering imaging. The author investigated the penetration of liquid (liquid length) in evaporating spray and observed that liquid length decreases with the decrease in orifice diameter, while injection pressure does not affect the penetration. Liquid length of a multicomponent fuel is controlled by its lower volatility fractions. Evaporation of diesel spray is controlled by turbulent mixing while other processes such as atomization of liquid, do not affect the liquid evaporation rate. Evaporation of diesel spray is a batch distillation type process, in which low volatile components evaporate early, while the high volatile components control the liquid length. These conclusions drawn by the authors have been found useful in the context of the present study.

2.7 Experimental Procedures

There are four different types of experimental setup found in the literature [1, 13], which are used to measure the combustion data of HFO;

1. Fuel Ignition Analyser
2. Visual Combustion Chamber
3. Visual Engines and
4. Thermogravimetry differential thermal analysis (TG-DTA).

2.7.1 Fuel Ignition Analyser (FIA)

The FIA is an instrument developed in Norway by joint effort from the Norwegian Institute of Technology and the Norwegian Marine Technology Research Institute – MARINTEK [132]. The FIA measures the ignition quality of fuels based on ignition delay. It works on the same principle as the constant volume combustion rig (discussed in section 2.7.2). In the FIA, the fuel sample is injected from the top into the highly pressurised and heated air constant volume chamber. The ignition delay of the fuel provides the measurement about the quality of fuel.

Generally, injection in FIA is attained by plunger piston with the help of springs in an injection pump. At the pre-defined chamber temperature and pressure, fuel is injected through a 0.35 mm diameter nozzle. The ignition delay of the fuel is defined as the time between start of injection (injection needle lift detected) to the time of first combustion. The first combustion is generally measured as the increase in 0.2 bar pressure from the initial chamber pressure. The ignition delay is measured in milliseconds. The chamber condition can be set at any chamber condition (temperature and pressure) but for marine and/or heavy fuel oil it is set as 450 ^{o}C and 45 bar, whereas for the light and distillate fuel it should be set as 450 ^{o}C and 20 bar. A schematic of the apparatus of FIA version 4 obtained from Takeda et al.[133] is shown in Figure 2-10. The complete testing procedure is controlled by computer, which allows the required parameters to be set, depending upon testing fuels.

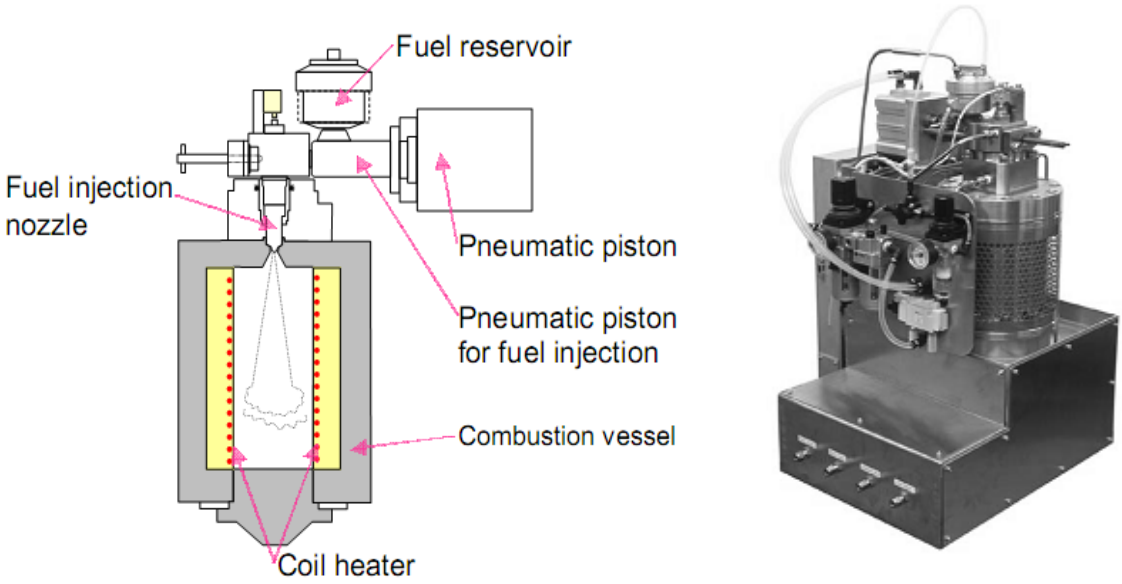

Figure 2-10: FIA version 4 (from Takeda et al.[133]).

2.7.2 Visual Combustion Chamber

The visual combustion chamber is a large cylindrical chamber developed by Takasaki et al. [1] at Kyushu University in Japan. It is used to visualise the spray/flame and study the combustion. A typical setup of the visual combustion chamber along with the upper and lower windows is shown in Figure 2-11.

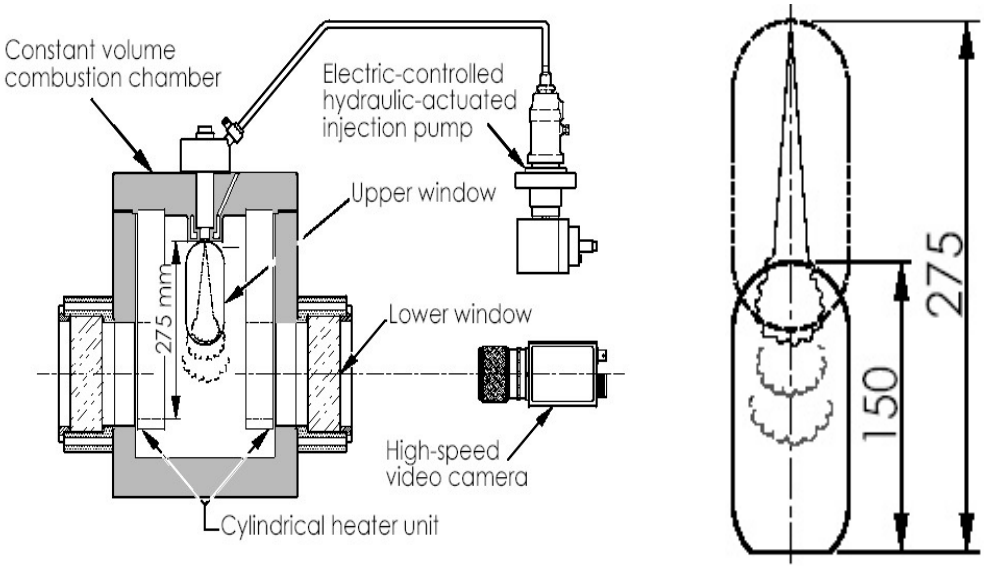

Figure 2-11: Visual combustion chamber along with configuration of windows (courtesy of Takasaki et al.[1]).

As shown in Figure 2-11, the visual chamber has 150 mm bore, greater than 275 mm length and it is electrically heated. The fuel spray is injected through an injector into the chamber, where air is kept at 2.5 MPa pressure and 600 ^{o}C. Windows of the chamber allow optical access to the full length of the spray. Since the distance between nozzle and the bottom of the chamber is around 300 mm, the interaction between wall and spray can be avoided. Hence, relatively long free sprays can be observed. The special design fuel injector system for bunker fuel oil is electronically controlled. In CVCC, injection proceeds beyond the ignition, while in FIA injection ceases before the start of the combustion.

The results obtained from the FIA and visual CVCC measurements of heavy fuel oil are given in Chapter 7 (section 7.2) where the actual comparison between experiments and simulations are illustrated.

2.7.3 Visual Engine

As described by Takasaki et al.[1], visual engine is used to visualise the combustion in the combustion chamber. A visual engine is two-stroke single cylinder engine with a 190 mm bore. It has 15-16 bar IMEP (Indicated Mean Effective Pressure) and 400 rpm engine speed. More detail about the visual engine setup can be found in Takasaki et al.[134].

2.7.4 Thermogravimetry Differential Thermal Analysis (TG-DTA)

Thermogravimetry Differential Thermal Analysis (TG-DTA) is a commercial instrument which is used to measured the combustion performances of fuel [13]. TG-DTA combines the high flexibility of the differential temperature analysis (DTA) feature with proven capabilities of the Thermogravimetry (TG) measurement technology. In TG-DTA experiment, a fuel sample is heated at a constant rate in oxidising environment.

In TG, change in the mass of the sample is continuously recorded with respect to time or temperature. In DTA, the sample and an inert reference are made to undergo identical thermal cycles, difference between sample and inert reference temperature are recorded.

This differential temperature is then plotted against time. Changes in the sample, either exothermic or endothermic, can be detected relative to the inert reference.

Uehara et al.[13] applied the TG-DTA technique to 28 samples of marine fuel oil by using the Rigaku TAS-300 thermal analysis system. In their experiment, temperatures ranged from room temp to 1000 ^{o}C and carrier gases were nitrogen and air. Moreover, air flow rate used was 100 mL/min and heating rate was 100 ^{o}C/min which is close to real combustion heating rate. Typical outcome of the experiment is shown in Figure 2-12.

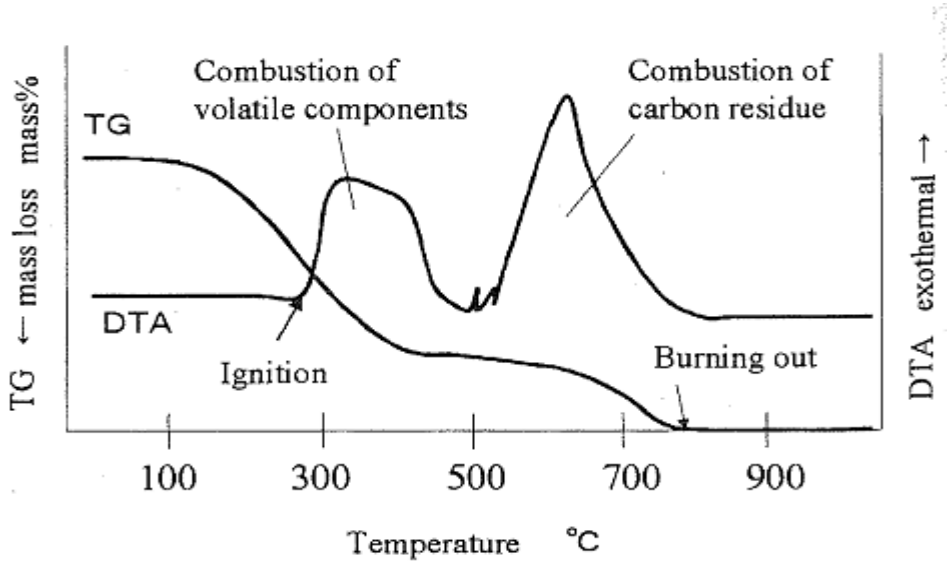

Figure 2-12: TG-DTA results of marine fuel oil (from Uehara et al.[13]).

It can be observed in Figure 2-12 that mass loss due to evaporation and combustion (TG curve) begins at around 150-200 ^{o}C and continuously decreases till the sample reaches burnout point. The increase in DTA curve shows the exothermic reaction. Two DTA peaks are apparent in above figure, the first peak appeared at around 300 ^{o}C is due to the combustion of cutter stock and thermal cracking gases, and the second peak appeared at around 600 ^{o}C is due to the combustion of carbonaceous residue (polymer).

The ignitability and combustibility of the fuel is estimated from the ignition and the burnout points respectively. Uehara et al.[13] studied the ignition and combustion quality of the good (normal) and the poor fuels. They found that the ignition and burnout points of the poor fuel are higher than the good fuel. Completion of combustion of poor fuel occurs

at a higher temperature compared to good fuel. They [13] also pointed out that high asphaltene content fuel has more combustion failure tendency.

Chapter 3. Chemical Characterisation of Heavy Fuel Oil

3.1 Introduction

Commercial petroleum fuels are complex mixtures of various hydrocarbons. Their physical and chemical properties differ according to their location of origin, depth, and age of source. The chemical composition of these multicomponent fuels is important in many engineering applications including the optimising of process parameters during refining, product and quality predictions, structure property correlations, product efficiency and performance, and fuel combustion modelling. Hence, characterisation of a multicomponent fuel is an essential tool for understanding its behaviour during transportation and processing. Some of the common problems encountered are solid deposition, clogging and choking of the filters, and cylinder liner wear. Solutions to these serious problems can be facilitated by a detailed understanding of the multi-phase behaviour of various constituents. Moreover, the combustion characteristics of a multicomponent fuel are directly related to its composition [135]. Consequently, it is necessary to understand the interaction of the various components in the context of their combustion characteristics. The present chapter outlines a method of determining the chemical composition of heavy fuel oil by separating the heavy fuel oil into fractions that differ in their chemical composition and physical properties, and by analysing each fraction. The chemical information obtained from the separated fractions can be directly used in the detailed spray combustion modelling of heavy fuel oil using continuous thermodynamics.

As discussed in earlier chapters, heavy fuel oil (HFO) is chemically very complex consisting of many different hydrocarbons having dissimilar structure and related compounds. Complete characterisation of HFO is impractical if not impossible [136]. However, there are some methods reported in the literature by which the overall composition can be determined by analysing groups of components. Rahimi & Gentzis [136] have reported methods for separating heavy fuel oil into different fractions based on solubility and adsorption. A commonly employed method of fractionating heavy oil into smaller fractions involves separation by column chromatographic techniques, and a

compound class characterisation commonly used is SARA, where SARA stands for Saturates, Aromatics, Resins and Asphaltenes fractions.

The saturates fraction consists of saturated hydrocarbons, which are either linear or branched chain hydrocarbons known as paraffins (alkanes), or contain one or more rings known as cycloparaffins (naphthenes). Generally, carbon (C) and hydrogen (H) are linked through single covalent bonds in these types of hydrocarbons. The boiling point and the stability of these compounds increase with the increasing number of carbon atoms. Aromatics are hydrocarbons containing one or more aromatic rings in their structure. They may also contain attached naphthenic rings or linear chain hydrocarbons in their structures. Both the saturates and the aromatics classes contain non-polar hydrocarbons. The resins fraction is the second least volatile fraction of heavy fuel oil after the asphaltenes, while the asphaltenes have the highest molecular weight and polarity. The asphaltenes and resins fractions contain sulphur, nitrogen and oxygen in addition to carbon and hydrogen and are the polar components of the heavy fuel oil. The polarity of resins and asphaltenes is mainly responsible for their low volatility. Characterisation using the SARA technique can be helpful for modelling the evaporation and pyrolysis stage of the combustion as the asphaltenes fraction is frequently found to be the component responsible for coke formation during combustion [14].

Often the asphaltenes fraction is initially precipitated from the heavy fuel oil by treatment with a non polar hydrocarbon solvent. The remaining fractions (saturates, aromatics and resins) commonly known as maltenes, are then separated by sequential elution solvent chromatography (SESC). In this technique, progressively more powerful solvents are employed to elute progressively more polar fractions from an adsorbent. A column filled with adsorbent media is employed, and a sample of maltenes is introduced at the top of the column. Different fractions of the maltenes are removed by passing different solvents through the column and collecting the eluent as it emerges from the column. Clearly, both the choice of solvents and adsorbent is important. Most researchers prefer to remove asphaltenes from the samples prior to chromatography because asphaltenes contain most polar compounds which are likely to be irreversibly adsorbed by the adsorbent. Once the fractions are separated, they can be analysed by various methods as outlined later in this chapter.

Many researchers such as Yasar et al.[137], Vazquez & Mansoori [138], and Farcasiu [139] have used silica gel as the adsorbent media for sequential elution solvent chromatography of petroleum. Liu et al.[140], Schiller & Mathlason [141] and Marquez et al.[142] used alumina. Burke et al.[143] have used glass beads for the analytical column for the analysis of petroleum products.

In addition to different adsorbent media, many different solvents have been used for the elution of the fractions. The following tables lists the solvents used by various researchers for precipitation of asphaltenes from heavy fuel oils (Table 3-1) and give a brief summary of the solvents and adsorbents used for the SESC chromatography (Table 3-2).

Table 3-1: Solvents used for precipitation of asphaltenes from the heavy fuel oil.

Solvents	**References**
n-heptane	[137, 140]
benzene/toluene	[143]
n-pentane/n-heptane/n-nonane	[138, 144]

Table 3-2: Solvents and adsorbent used for the SESC chromatography.

Fractions	**Solvents**	**Adsorbent**	**Ref-erences**
Saturates	n-heptane	Silica gel (40-140 mesh)	[137]
		Alumina (1% water)	[140]
	hexane	Neutral alumina	[141]
	hexane/cyclohexane	Neutral alumina	[142]
	n-pentane	Activated silica	[138]
Aromatics	toluene/ heptane (50/50% by vol)	Silica gel (40-140 mesh)	[137]
	toluene	Activated silica	[138]
		Neutral alumina	[141]
	benzene	Alumina (1% water)	[140]
	toluene/ pentane (50/50% by vol)	Neutral alumina	[136]
	hexane/toluene (70/30% by vol)	Neutral alumina (80-200 mesh)	[142]

Resins	methanol/toluene/petroleum ether (50/25/25% by vol)	Silica gel (40-140 mesh)	[137]
	benzene/ethanol (50/50 % by vol)	Alumina with 1% water	[140]
	$CCl_4/CHCl_3$ (70/30% vol)	Neutral alumina (80-200 mesh)	[142]
	toluene/methanol (90/10 % by wt)	Activated silica	[138]

3.2 Experimental

3.2.1 Chemicals

A sample of marine heavy fuel oil was collected from the port of Sydney, New South Wales, Australia. All other chemicals used for the experiment were standard laboratory chemicals. Their details are as follows;

- **Adsorbent**: - Silica gel grade 922, mesh size 200-325 (AJAX Chemical Ltd.).
- **Solvents** :-
    - n-pentane (UNILAB, LR grade)
    - Toluene (BDH, AR grade)
    - Methanol (MERCK, AR grade) and
    - Chloroform (UNILAB, LR grade).

All solvents were purified by fractional distillation prior to their use. Normal-pentane was distilled by a single plate conventional distillation apparatus at 37 ^{o}C. Toluene was similarly also distilled and collected at 110 ^{o}C. This precaution was taken to avoid contamination of the original sample by high boiling point impurities in the solvent, which could be concentrated on evaporation of the solvents after fractions were collected. Gas chromatography was used to check the quality of the solvents before and after fractional distillation.

3.2.2 Procedure

A flowchart of the current experimental procedure used for HFO separation is shown in Figure 3-1.

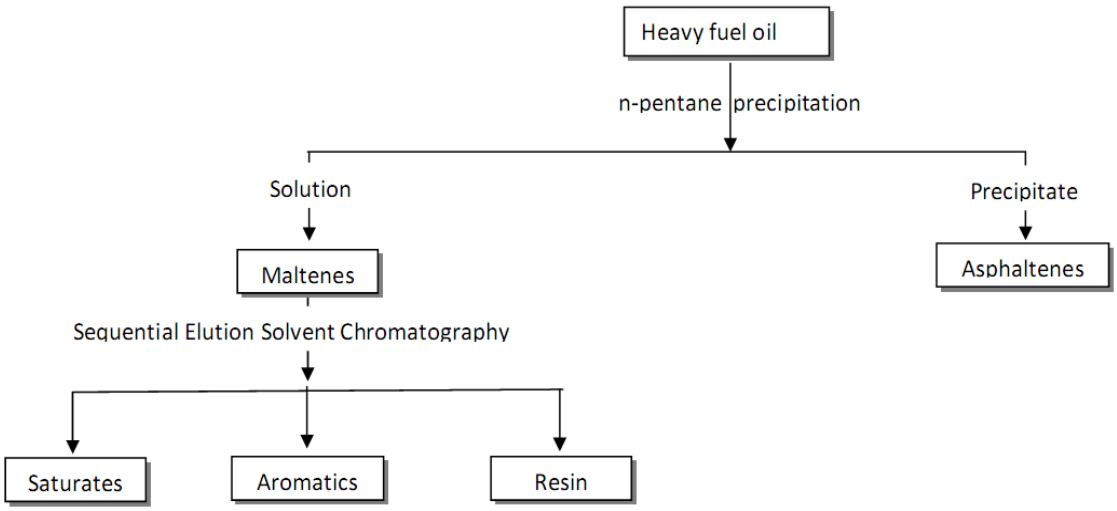

Figure 3-1: Flowchart of the experimental procedure of separation of HFO into different fractions.

3.2.2.1 Precipitation of Asphaltenes

As shown in Figure 3-1, the asphaltenes fraction was initially separated from the heavy fuel oil because it can cause adverse effects on the adsorbent by becoming irreversibly adsorbed. Asphaltenes are also known as 'bad actors' in refineries as they promote coke and sludge formation as well as causing catalyst deactivation during the processes.

As used in the literature [139, 145], a 40:1 ratio of solvent to sample was used. An accurately weighed 2.557 g sample of heavy fuel oil was mixed with 100 mL of purified n-pentane. This mixture (heavy fuel oil + n-pentane) was stirred for 24 hours at room temperature and allowed to settle for approximately 3 hours. The precipitated asphaltene fraction was separated from the mixture by vacuum filtration, the most common method reported for the separation of asphaltenes from maltenes. For filtration, a 0.2 micron, 47 mm size Nylon filter paper and a laboratory scale Buchner vacuum filtration apparatus, employing 150 mmHg vacuum at room temperature was used. Precipitated asphaltenes were collected on the filter paper and the solvent was allowed to evaporate from the filter paper at room temperature in a vacuum dessicator for approximately 24 hours. Further, the small amount of asphaltenes which was deposited on the surface of the glass vessel during stirring and which could not be removed by washing with n-pentane was collected by dissolving in chloroform. The chloroform was also allowed to evaporate off for at least 24 hours. Finally, the dried asphaltenes which were collected on the filter paper and also via

chloroform were collected and weighed separately. The total weight of asphaltenes in heavy fuel oil is given by the summation of the weights collected on both the filter paper and by chloroform dissolution.

3.2.2.2 Separation of Maltenes into Saturates, Aromatics and Resins

Maltenes in pentane solution were isolated from asphaltenes by vacuum filtration and collected as a filtrate as described above. During vacuum filtration some solvent loss occurred due to the low boiling point of n-pentane (37 ^{o}C). Additional solvent was added to make up the volume of the solution of maltenes to 50 mL. From this solution of maltenes, 10 mL (20% by vol) was taken and mixed with 15-20 g silica gel, which had been previously activated by heating for 24 hours at 115 ^{o}C. Precautions were taken to ensure uniform mixing of the solution of maltenes with the silica gel by using a vacuum rotary evaporator to remove the solvent during the mixing of silica gel and maltenes, over a period of approximately 3 hours. This uniform mixing technique was found very efficient and useful later during the experiment in terms of column development for the separation of the fractions.

A glass column with an internal diameter of 2 cm and a height of 35 cm was used for the sequential elution solvent chromatography (SESC). This column was filled with slurry of pre activated silica gel (grade 1) in pentane up to 23 cm, while the top 5 cm of the column was filled with the mixture of maltenes and silica gel mixture prepared earlier.

Once the column had been prepared, separation was commenced. The saturates fraction was eluted by passing 125 mL of n-pentane through the column and the eluate was collected in 10 mL test tubes in sequence. All test tubes were later examined by gas chromatography to ensure the elution of saturates was complete. Afterwards, only those test tubes which contained significant amounts of saturates were mixed to form a composite solution of saturates in n-pentane. As expected, it was found that of all the test tubes, only the middle set of test tubes in the sequence contained appreciable amount of saturates. Some initial and final tubes were free from saturates. This proved that the amount of solvent used was sufficient to elute all saturates from the maltenes. In this way,

saturates were removed from the maltenes and the next step was to separate the aromatics and resins.

Aromatics were eluted similarly to saturates, using 125 mL of toluene as eluent and the eluted fractions were collected in 10 mL test tubes. The presence of aromatics in all test tubes was detected by gas chromatographic analysis. Thereafter, a composite sample of aromatics in toluene was prepared. Once saturates and aromatics had been removed, it proved a difficult task to remove the entire resins fraction from the column due to their polar characteristics similar to asphaltenes.

Initially a mixture of 110 mL of toluene and 15 mL (12% by vol) of methanol was used to elute the resins fraction. However, this was not found to be effective in completely removing the resins from the column. Hence, a second volume of 40 mL of toluene and 10 mL (20% by vol) of methanol mixture was applied, which eluted most of the resins from the column. Finally a 25 mL toluene and 25 mL (50% by vol) methanol mixture was applied to ensure that all the resins had been removed. In this way, all resins were eluted and a composite sample was prepared. Thus, all three fractions of maltenes (saturates, aromatics and resins) were separated by the sequential elution solvent chromatography and collected in different containers. The next task was to analyse all the separated fractions.

After the separation of the three fractions, the solvents were removed by employing a rotary evaporator operating at around 150 mmHg vacuum and 90 ^{o}C. However, this was found to be incapable of removing all the toluene from the aromatics and resins fractions. Consequently, a vacuum oven was used to remove the last traces of toluene from the aromatics and resins fractions. The vacuum oven was operated for 4 hours at 50 ^{o}C and 10 mmHg. Finally, the dried saturates, aromatics and resin were collected and weighed accurately. The amounts and yields of these fractions are discussed in a later section of this chapter.

3.2.2.3 Gas Chromatography

After the separation of heavy fuel oil into four fractions, gas chromatography (GC) was performed on the light fractions to characterise the fractions. Prior to GC analysis the separated saturates fraction was mixed with pentane and a 25 mL solution was prepared. Similarly, a 10 mL solution of the separated aromatics in toluene was prepared. GC analysis was conducted on a HEWLETT PACKARD-5890 gas chromatography instrument equipped with a 30m length, 0.25 mm id, 0.5 micron thickness BPX5 column, and flame ionisation detector (FID). The GC column temperature was programmed in the following manner: 40 ^{o}C for the first 4 minutes, then from 40 ^{o}C to 300 ^{o}C at a rate of 7 ^{o}C /min and finally the temperature was held constant at 300 ^{o}C for 15 minutes. During GC analysis injection volumes of 2 microlitre of saturates and aromatics fractions were employed using a hot needle injection technique. The results of GC analysis are discussed later in section 3.3.2.

3.2.2.4 Mass Spectrometry

To understand the chemistry of fuel it is important to know the molecular weight distribution of its fractions. The mean molecular weight helps to assign the physical and chemical properties correlations of hydrocarbons. In the present work it is very important to know the mean molecular weight of each fraction and its range, to fit the Γ-distribution function parameters which are the basic requirement of any continuous thermodynamics modelling. Mass spectrometric (MS) analysis was conducted on a KRATOS CONCEPT ISQ high resolution magnetic sector mass spectrometer. Mass spectrometric analysis was performed to try to determine the mean molecular weights and the molecular weight ranges of the separated SARA fractions of heavy fuel oil. Electron ionisation at 70 eV was employed with a Desorption Chemical Ionisation (DCI) probe heated from 40 ^{o}C to 500 ^{o}C at 2 ^{o}C/sec. Each fraction (Saturates, Aromatics, Resins and Asphaltenes) was scanned between charge/mass ratio (m/z) 50 to 1800 molecular weight ranges at 1 second per decade. The accelerating voltage and source temperature used for this analysis was 4 kV and 200 ^{o}C respectively. All data of this analysis were acquired in “raw” profile mode. Prior to analysis the instrument was calibrated between m/z 50 to 1300. The results obtained by this analysis are discussed in a later section (Section 3.3.4) of this chapter.

3.3 Results and Discussion

3.3.1 SARA

The sequential elution solvent chromatography (SESC) technique was employed for the separation of heavy fuel oil's complex mixture into basic hydrocarbon groups, namely saturates, aromatics, resins and asphaltenes. The sequence of solvents was chosen in this separation such that it should elute only one hydrocarbon group and leave the remainder on the column. The results obtained from this analysis of heavy fuel oil were found to be very useful in the thermodynamic modelling of heavy fuel oil, and also in the prediction of the behaviour of each individual fraction during its combustion. In addition, the separated fraction such as asphaltenes can be studied individually for the further effect of these fractions on solid deposition issues of heavy fuel oil.

As discussed at the beginning of this chapter, a large number of solvent and adsorbent media combinations were studied before making the final selection of solvents and adsorbents for the SARA technique. Ali Mansoori et al.[144] states that the properties of saturates and aromatics fractions are independent of the solvent used for their elution, whereas the same statement is not true for the composition and properties of asphaltenes and resins. Generally, the properties of resin and asphaltenes fractions vary according to the solvent used for their separation. The authors also mentioned that some amount of resins is always mixed with asphaltenes, while some high molecular weight paraffin wax may also precipitate with the resins and asphaltenes.

The results obtained on the fractionation of the heavy fuel oil sample by SARA technique are summarised in Table 3-3.

Table 3-3: Result obtained by SARA analysis

Components	**Weight %**
Saturates	24.08%
Aromatics	55.81%
Resins	6.66%
Asphaltenes	7.86%
Loss + Unknowns	5.59%

Furthermore, some preliminary observations of samples were made by visual inspection. The original HFO sample was dark black in colour but its separated fractions were found to vary from a transparent light colour to a dark colour. Saturates contained viscous compounds of a whitish colour. Aromatics contained yellowish viscous hydrocarbons, while the resins fraction had a reddish colour, and as expected, asphaltenes contained black solids.

3.3.2 Gas Chromatography

Following the separation of heavy fuel oil into saturates, aromatics, resins and asphaltenes, gas chromatography was employed to provide a more detailed characterisation of some fractions. The first two fractions (saturates and aromatics), which were thought to contain lighter molecular weight compounds, were analysed by this technique. The lighter components which can be analysed by GC are assumed to be from the cutter stock. In particular, gas chromatography was used to determine two characteristics of the separated fractions as;

(1) Concentration of the saturates and aromatics fractions which originated from pure cutter stock, since not all saturates and aromatics fractionated by SARA are necessarily from cutter stock, they may have originated from residue. (2) The mean molecular weight of the saturates and aromatics fractions originating from cutter stock.

3.3.2.1 Concentration of Saturates in Cutter stock

Figure 3-2 shows the gas chromatogram peaks obtained on analysis of the pentane solution of the saturates fraction. In all chromatograms in the present section the abscissa represents the retention time duration of analysis and the ordinate shows the output millivolt (mV) from the FID detector.

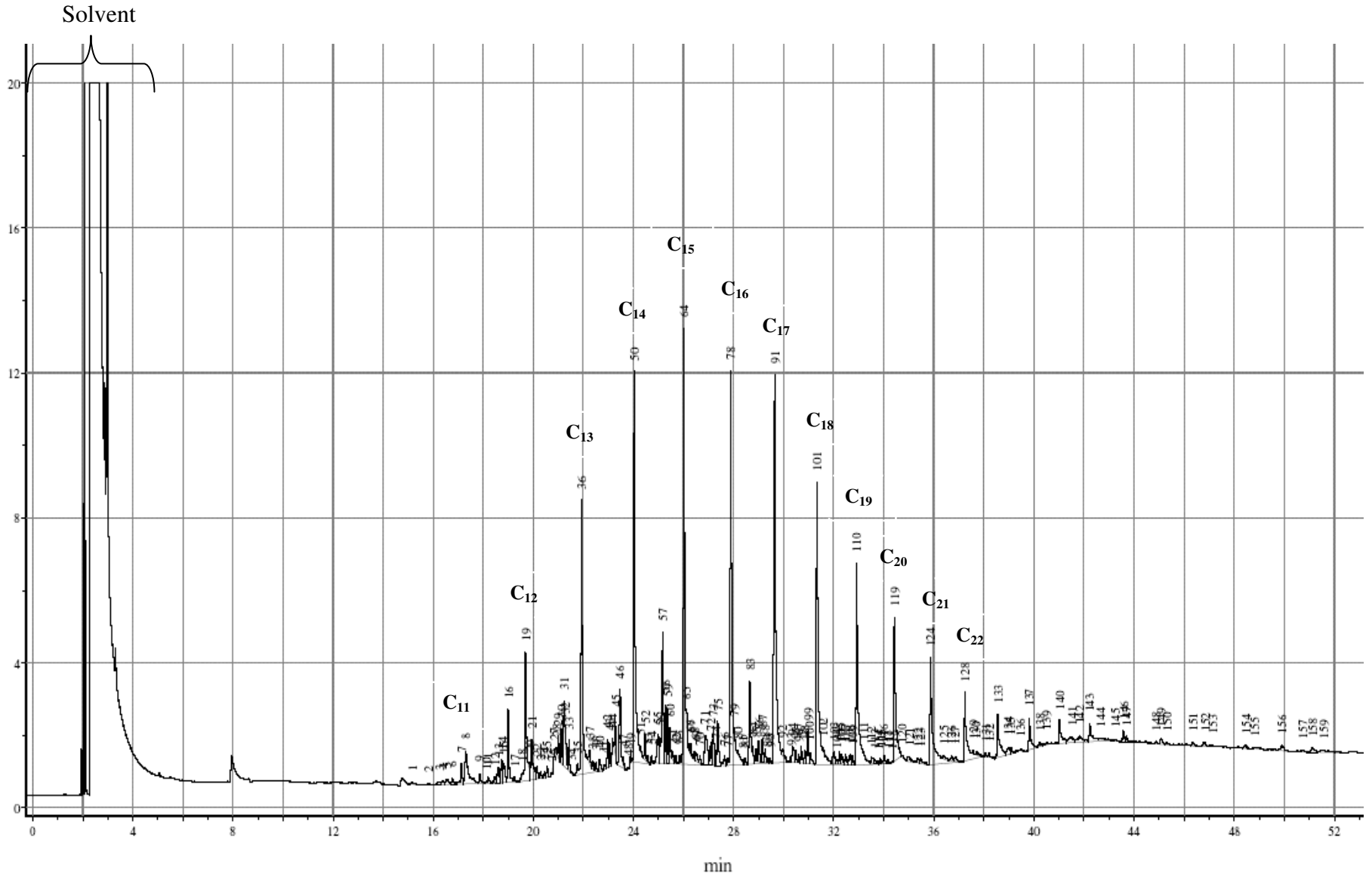

Figure 3-2: GC-FID chromatogram of fractionated saturates of HFO.

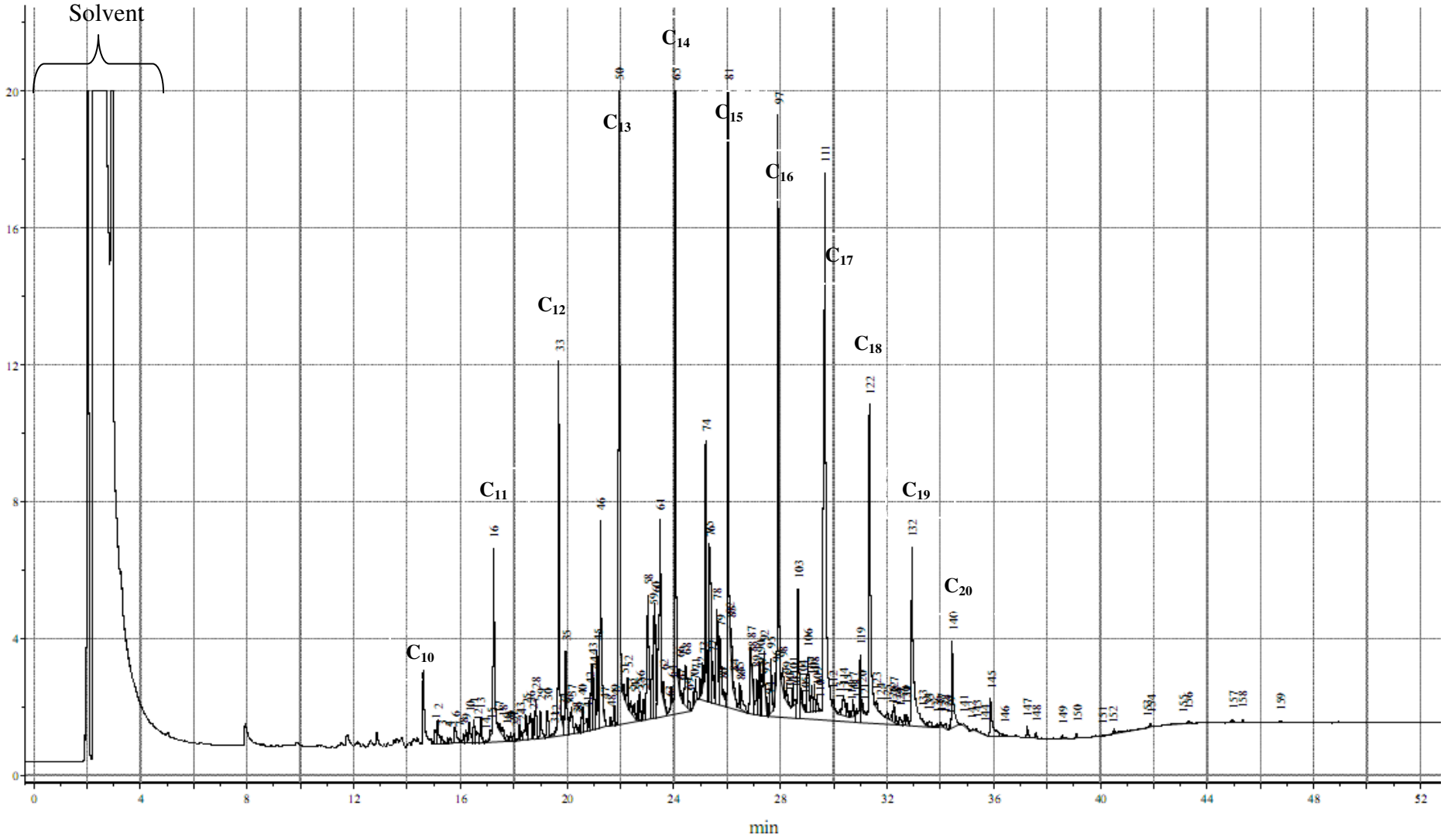

Figure 3-3: GC-FID chromatogram of standard saturates solution (diesel).

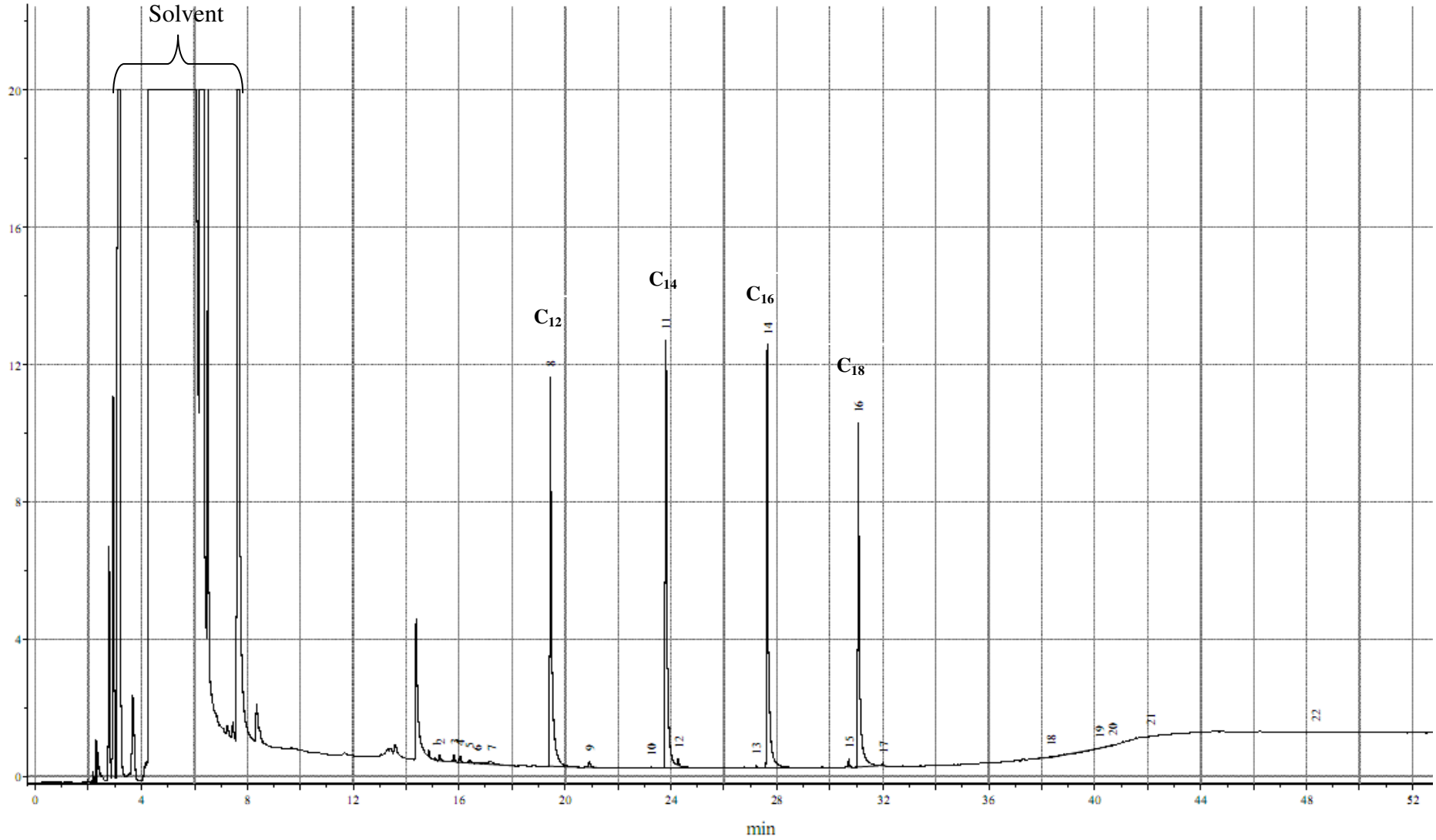

Figure 3-4: GC-FID chromatogram of standard C_{12}-C_{18} alkane solution.

As expected, pentane was eluted early, while the volatile compounds of the saturates fraction eluted in the order of their decreasing volatility and increasing molecular weights. To determine the concentration of saturates in cutter stock through GC-FID, comparison with a known concentration standard saturates solution is essential. In the present experimental study diesel is used as a standard saturates solution. Figure 3-3 shows the chromatogram of the standard saturates solution (diesel) of known concentration. Nevertheless, diesel itself is a mixture of light hydrocarbons and in order to compare it with the fractionated saturates, the compounds in diesel first need to be identified by comparison with a standard solution of C_{12}, $C_{14,}$ C_{16} and C_{18} straight chain alkanes. Figure 3-4 shows the chromatogram of the standard C_{12}-C_{18} alkanes solution under the same conditions.

In Figure 3-4 the C_{12}, $C_{14,}$ C_{16} and C_{18} peaks were clearly identified. Figure 3-3 (chromatogram of diesel) was compared with Figure 3-4 (chromatogram of C_{12}-C_{18}) in order to identify the carbon numbers (shown on the top) of the peaks in the diesel fraction. Through precise comparison of the retention times in both figures the C_{12}, C_{14}, C_{16} and C_{18} alkanes in diesel could be identified. Both solutions were prepared with the identical solvent (n-pentane), and the gas chromatographic conditions were the same for both the analyses. By interpolation and extrapolation the carbon numbers shown on top of the remaining peaks in diesel have been identified and assigned. This information was then used to identify individual compounds in the fractionated saturates from the HFO.

Similar comparisons of retention times were done between Figure 3-3 (diesel) and Figure 3-2 (fractionated saturates) to identify the peaks in the saturates fraction. The saturates were found to contain long carbon chain alkanes ranging in length from C_{11} to C_{29} as identified in the Figure 3-2. All the identified components are designated on the top of each individual peak. The results obtained from the comparison of retention times in the chromatograms were within the range of expected experimental variations. These results also agree with similar results obtained by Takasaki et al.[1]. The heavy fuel oil which they analysed contained alkanes with the carbon numbers ranging from C_9-C_{28}. It would also be useful to identify unidentified peaks in the chromatogram (Figure 3-2), but because of the limited resources further analysis of these saturates was restricted.

The chemical structure characterisations of the separated fractions by gas chromatography are limited by their volatility complexity. From Figure 3-2 it has been shown that the majority of the volatile compounds of the saturates contained the linear chain hydrocarbons. Subsequently, an external standard comparison method was employed to determine the concentration of volatile saturates and aromatics in the heavy fuel oil. In the external standard method the area under the curve from the chromatogram of known concentration solution is compared with the area under the curve from the chromatogram of unknown concentration solution. As a result the concentration of the unknown solution is obtained as;

$$Conc_{unknown} = Conc_{known} \cdot \frac{Area_{unknown}}{Area_{known}}$$

In the present study, by mixing 0.1229 g of diesel with 50 mL of pentane, a known concentration solution was prepared. The chromatogram of this solution is shown in Figure 3-3. The concentration of known (diesel) solution is given as;

$$= \frac{0.1229}{50} \cdot 100$$
$$= 0.246\,\%$$

The area under the curve excluding the solvent obtained from Figure 3-3 is 920 mV*min.

As mentioned earlier (section 3.2.2.2), after the separation of asphaltenes, only 20% by vol (or $1/5^{th}$) of the original sample (2.557g) was used for the rest of the experiment. Hence, the weight of HFO in this small sample is given as;

$$= \frac{2.557}{5}$$

$$= 0.5114\,\text{g}$$

Prior to GC analysis the separated saturates fraction was mixed with pentane and a 25 mL solution was prepared. The summary of areas under the curves obtained from the

chromatograms of diesel (Figure 3-3) and saturates (Figure 3-2) and their respective concentration is given in Table 3-4.

Table 3-4: Area under the curve and concentration of diesel and saturates

Solutions	**Diesel**	**Saturates**
Concentration	0.246%	*Calculated below as: 10.3%*
Area under the curve	920 mV*min	793 mV*min
Figure reference	Figure 3-3	Figure 3-2

$$\text{Conc. of volatile saturates in 25 mL of pentane} = \frac{793}{920} * (0.246)$$

$$= 0.212\%$$

$$\text{The amount of volatile saturates in 25 mL of pentane} = 0.212 * \frac{25}{100}$$

$$= 0.053\,\text{g}$$

$$\text{Hence, the \% of saturates in HFO as cutter stock} = \frac{0.053}{0.5114} \cdot 100$$

$$= 10.3\%$$

The amount of volatile saturates calculated by the external standard method was found to be 10.3% of the original HFO sample.

3.3.2.2 Concentration of Aromatics in Cutter stock

The aromatics fraction was also analysed by an external standard method. For external standard comparison, naphthalene solution in toluene was used as a standard aromatics solution. The following figures show the chromatograms of fractionated aromatics (Figure 3-5) and a standard solution of naphthalene (Figure 3-6).

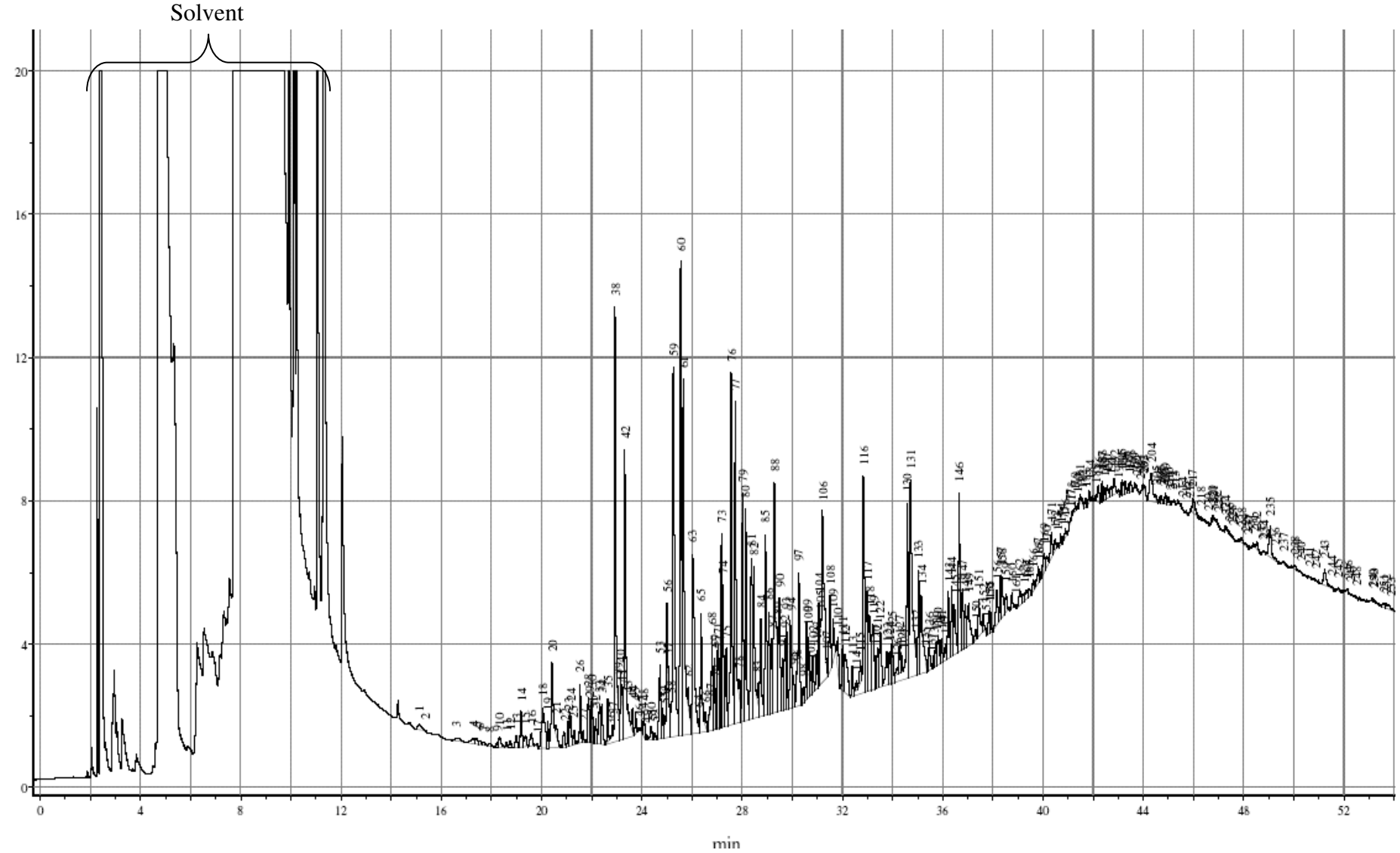

Figure 3-5: GC-FID chromatogram of fractionated aromatics.

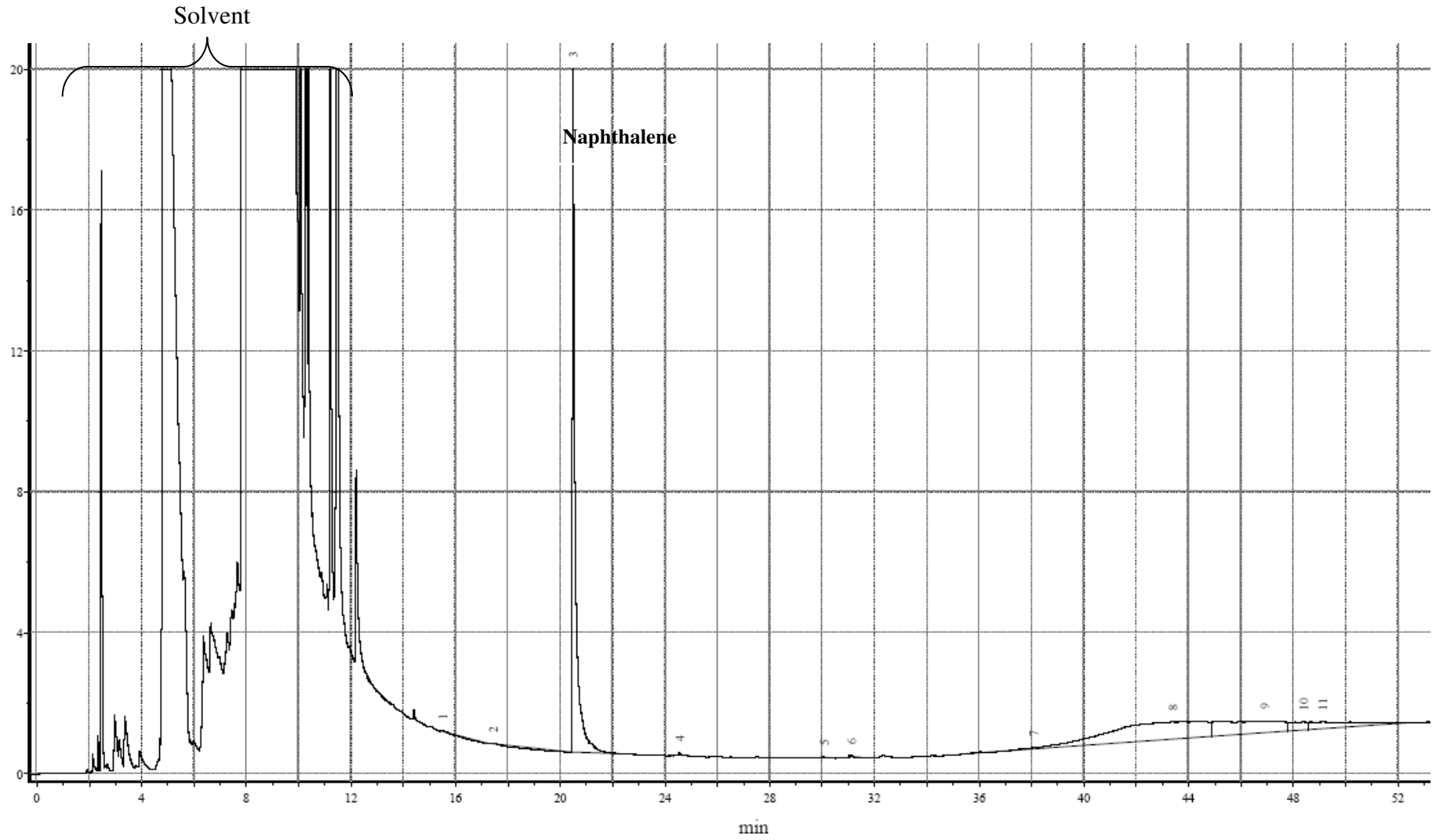

Figure 3-6: GC-FID chromatogram of standard aromatic solution.

As similar to saturates, prior to GC analysis, a 10 mL solution of the separated aromatics in toluene was prepared. And, by mixing 2.04mg of naphthalene in 10 mL of toluene, a standard aromatic solution was prepared, whose concentration can be given as;

$$= \frac{2.04 \times 10^{-3}}{10} \cdot 100$$
$$= 0.0204\ \%$$

Table 3-5 summarises the area under the curves (excluding the solvent), obtained from both the chromatograms (Figure 3-5 and Figure 3-6) and the concentrations of standard naphthalene and fractionated aromatics.

Table 3-5: Area under the curve and concentrations of naphthalene and fractionated aromatics.

Components	**Naphthalene**	**Aromatics**
Concentration	0.0204%	*Calculated below as: 5.9%*
Area under the curve	126.5 mV*min	1873 mV*min
Figure reference	Figure 3-5	Figure 3-6

Conc. of aromatics in 10 mL of toluene $= \frac{1873}{126.5} * (0.0204)$

$= 0.302\%$

The amount of volatile of aromatics in 10 mL of toluene $= 0.302 \cdot \frac{10}{100}$

$= 0.0302\ \text{g}$

Hence, the % of aromatics in HFO as cutter stock $= \frac{0.0302}{0.5114} \cdot 100$

$= 5.9\ \%$

3.3.2.3 Cutter stock

It is clear by comparison of the results obtained by SESC analysis and subsequent GC-FID analysis that not all compounds present in the separated fractions are able to be analysed by GC. The SESC analysis showed that the original HFO sample contained 24.08%

saturates by weight, however only 42.77% of this fraction (10.3%), was detected by GC. Consequently the remaining 57.23% of this fraction probably consists of very long chain alkanes which were not volatile enough to be analysed by gas chromatography.

The GC analysis of the aromatic fraction also showed that only a small amount of the aromatic fraction of HFO can be analysed by GC. Only 10.5% of the 55.81% by weight aromatics in the original sample separated through SESC analysis was able to be analysed by GC. The reason for this is that HFO contains large amounts of high molecular weight saturates and aromatics but GC is only able to analyse light and medium molecular weight components which have sufficient volatility to pass through the column. Hence, the majority of high molecular weight saturates and aromatics were unable to be analysed by GC. However, the precise concentrations of these fractions were determined through SESC analysis.

The sum of volatile saturates (10.3%) and volatile aromatics (5.9%) analysed by GC are considered as the cutter stock of the present HFO sample, which is calculated in this study as 16.2% of the original sample.

The mean molecular weight of the volatile saturates fraction calculated by normalisation of the data in Figure 3-2 is found to be 237. This means the majority of this fraction consists of C_{17} compounds. This result can be confirmed by the findings of Ciajolo & Barbella [146]. Their sample of fractionated paraffins from HFO showed the compound range between C_{10}-C_{30} with a majority of C_{18} compounds. Using a similar approach to saturates, comparison was carried out to determine the mean molecular weight of aromatics fractions, but the large shifting of the baseline in the chromatogram of aromatics (see Figure 3-5) at the end of the run, created difficulties in calculating the mean molecular weight. However, it was approximated as 165, which is in between naphthalene and anthracene/phenanthrene (see Figure 3-7). Figure 3-7 shows the chromatogram of standard naphthalene, anthracene and phenanthrene solution, whose molecular weights are 128, 178 and 178 respectively.

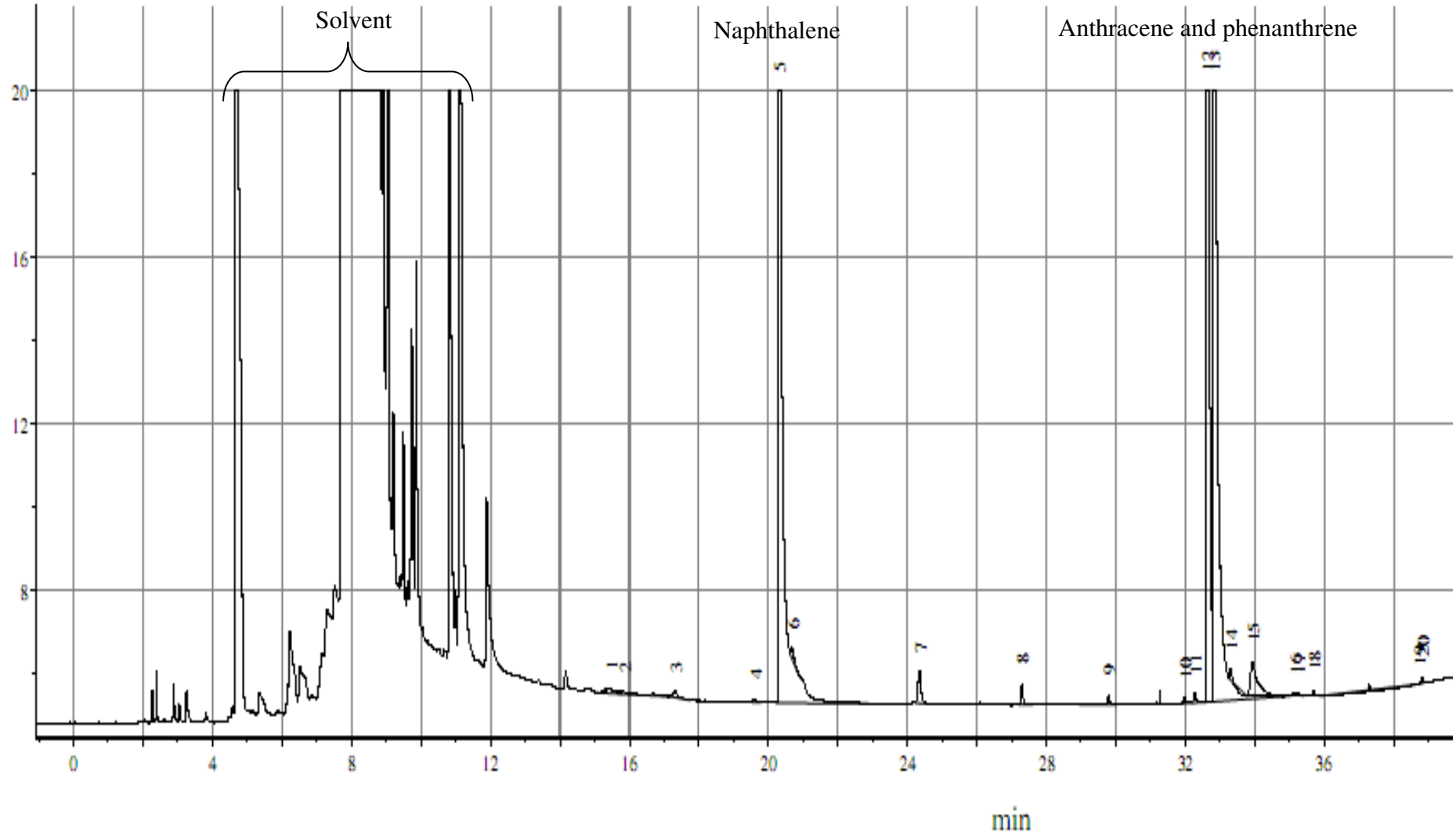

Figure 3-7:GC-FID chromatogram of standard naphthalene, anthracene and phenanthrene solution.

3.3.3 Elemental Analysis

Elemental analysis of this complex mixture of hydrocarbons provides a meaningful method to estimate the heteroatom content of the complex components. Elemental analyses of the HFO sample, as well as all the separated fractions were conducted and the results are given in Table 3-6. Elemental analyses showed that the resins and asphaltenes fractions contained the majority of heteroatoms (S and N) and are the polar components of heavy fuel oil, whereas the saturates contain the least amount of heteroatom. This result concurs with the discussion by Baert [14] that nafteno-paraffins and nafteno-aromatics contain only carbon and hydrogen in their structure with very little or no polarity. The saturates and aromatics fractions contains small amounts of nitrogen and some amounts of sulphur. The sulphur in aromatics fraction could be due to thiophenic aromatics as stated by McKay et al.[147]. The higher percentage of hydrogen in saturates confirms that this fraction is free from aromatics and heteroatom compounds. The hydrogen to carbon ratio (H/C) obtained from this analysis is 1.852 and 1.420 for saturates and aromatics respectively. The total amount of C, H, S and N in the original sample is found to be equal to the summation of all individual fractions with minor errors. The low H/C ratio for asphaltenes (1.154) shows that it has high aromaticity due to condensed ring aromatic structure.

Table 3-6: Elemental analysis of HFO and its fractions.

Sample Name	C%	H%	S%	N%	Total Yield	H/C ratio
Saturates	85.32	13.17	0.48	0.05	99.02	1.852
Aromatics	83.83	9.92	4.28	0.20	98.23	1.420
Resins	80.03	10.55	2.78	0.82	94.18	1.581
Asphaltenes	83.49	8.03	7.07	0.75	99.34	1.154
HFO	85.17	9.16	4.42	0.24	98.99	1.290

3.3.4 Mass Spectrometry

The mass spectrometric results obtained are discussed in this section. The mass spectrum of the saturates was difficult to interpret (see Figure 3-8 (a)) due to the high instability of

the molecular ions of linear alkanes and the extensive fragmentation as evidenced by the predominance of odd molecular weight ions detected below 400. Even numbers for mass (ignoring the number after the decimal point) in Figure 3-8 (b) represent the molecular ions, whereas odd numbers for mass (see Figure 3-8 (a)) show the presence of fragment ions in the saturate fraction. Ions shown below 400 in Figure 3-8 (a) are most probably the fragment ions and were neglected during the normalisation calculation.

GC analysis of the saturates fractions showed the presence of alkanes with molecular weights less than 394 (C_{30}), which corresponds to only 43% of the total separated saturates fraction. The remaining 57% of this fraction is thought to contain very long chain alkanes and cycloalkanes with molecular weights well in excess of 394. There is some evidence of molecular ions in the range 200-1100 in the mass spectrum, but it is very difficult to accurately estimate the mean molecular weight of these longer chain alkanes.

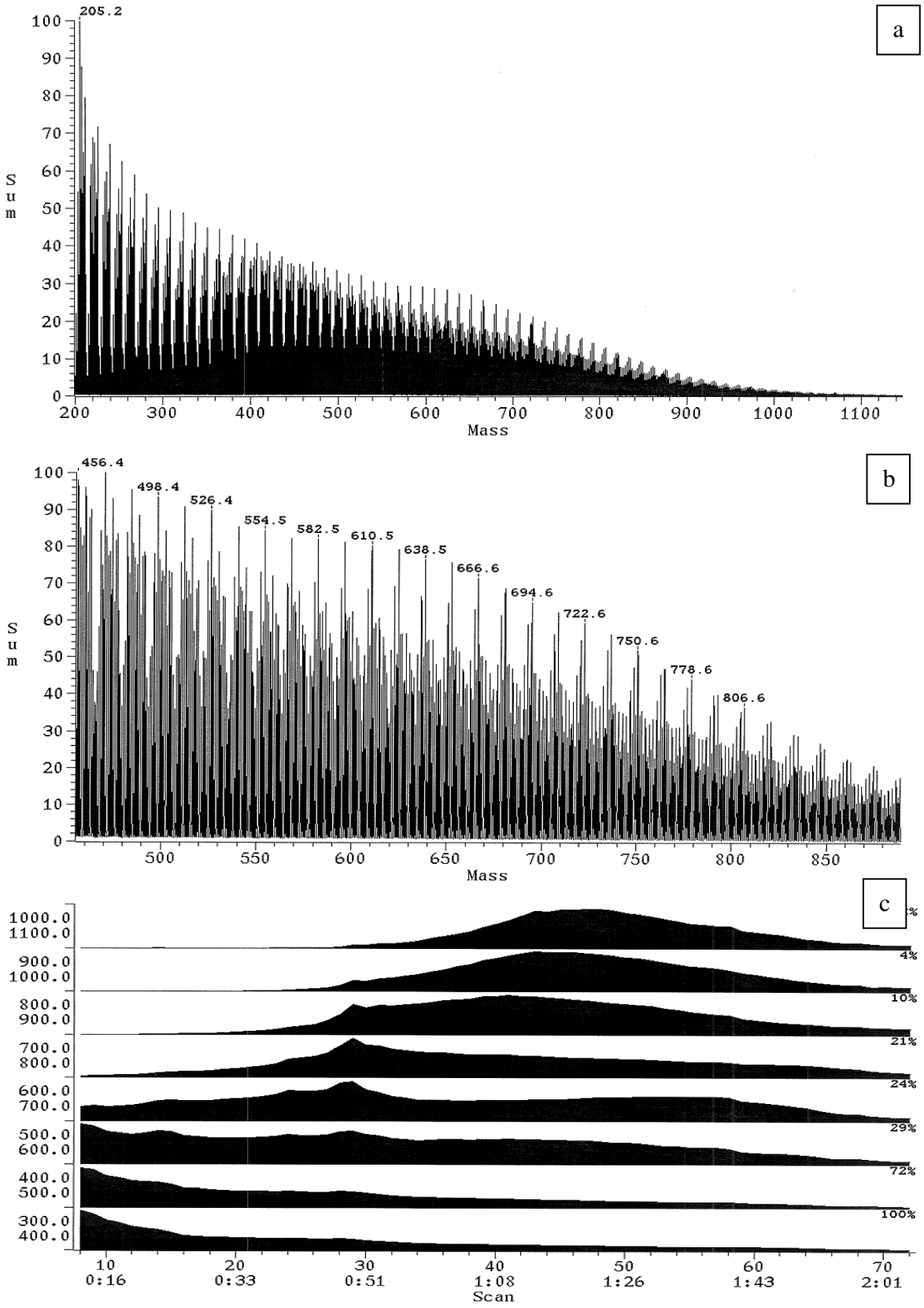

Figure 3-8: Mass spectrum of saturates fraction of HFO. Sub-figure (a) represents the entire scan of the saturates fraction, (b) shows a zoom view of a selected range of molecular weight of sub-figure (a), and (c) provides the statistical measure of the molecular weights with time.

In Figure 3-8 (b), the difference between two successive molecular ions was observed as 14, due to a -CH_2- unit. The first molecular ion shown in Figure 3-8 (b) is at 456.4. If this molecule is a straight chain alkane (C_nH_{2n+2}) then the number of carbons it contains is equal to 454/14=32.43. This means its molecular formula is close to $C_{33}H_{68}$, which corresponds to molecular weight 464. Nevertheless, the peak at 456.4 has a shortage of (464-456) 8 hydrogen atoms. One way this is possible, is if this molecule contains four cyclic structures along with side chain(s) and is based on steroid residue such as;

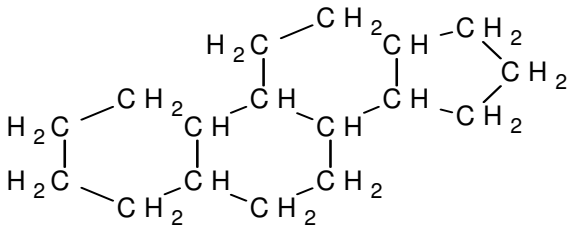

The molecular weight of this parent cyclic structure ($C_{17}H_{28}$) is 232.

That means a representative structure of saturates fraction can be a summation of: x tetracyclic compound (x=1) as shown in figure above plus y -CH_2- units attached as side chains.

Hence, the number of –CH_2- molecules (y) = (456-232)/14 = 16. The hydrogen to carbon ratio for this representative structure obtained is 1.818, which is very close to the experimental result (1.852).

Hence a structure which is consistent with the first molecular ion shown in Figure 3-8 (b) at 456.4 contains a tetracyclic ($C_{17}H_{28}$) ring structure along with the 16 –CH_2- units attached in their structure. These 16 –CH_2- units could be attached randomly to the structure. Moreover, the remaining molecular ions shown in Figure 3-8 (b) are also believed to contain the same cyclic structure but with additional –CH_2- units attached. These tetracyclic molecules with many -CH_2- side chains would be expected to form more stable molecular ions than linear alkanes as fission of a carbon-carbon bond in the ring does not result in fragmentation. However, it is possible that these results may not be really representative of the heavy alkane components as the long linear alkanes are likely to be undetected. The mean molecular weight calculated for saturates in Table 3-7 is 580.

This result confirms that the average structure and the mean molecular weight obtained for the saturates fraction are closely related.

Figure 3-9 shows the mass spectra obtained for the separated aromatics fraction, but again it is difficult to estimate the average molecular weight of aromatics from the current figure. Presumably the lighter peaks in the beginning of the spectrum of Figure 3-9 (a) are mainly odd weight (ignoring the number after decimal point) ions resulting from fragmentation, while the even weight ions are due to the molecular ions of aromatics.

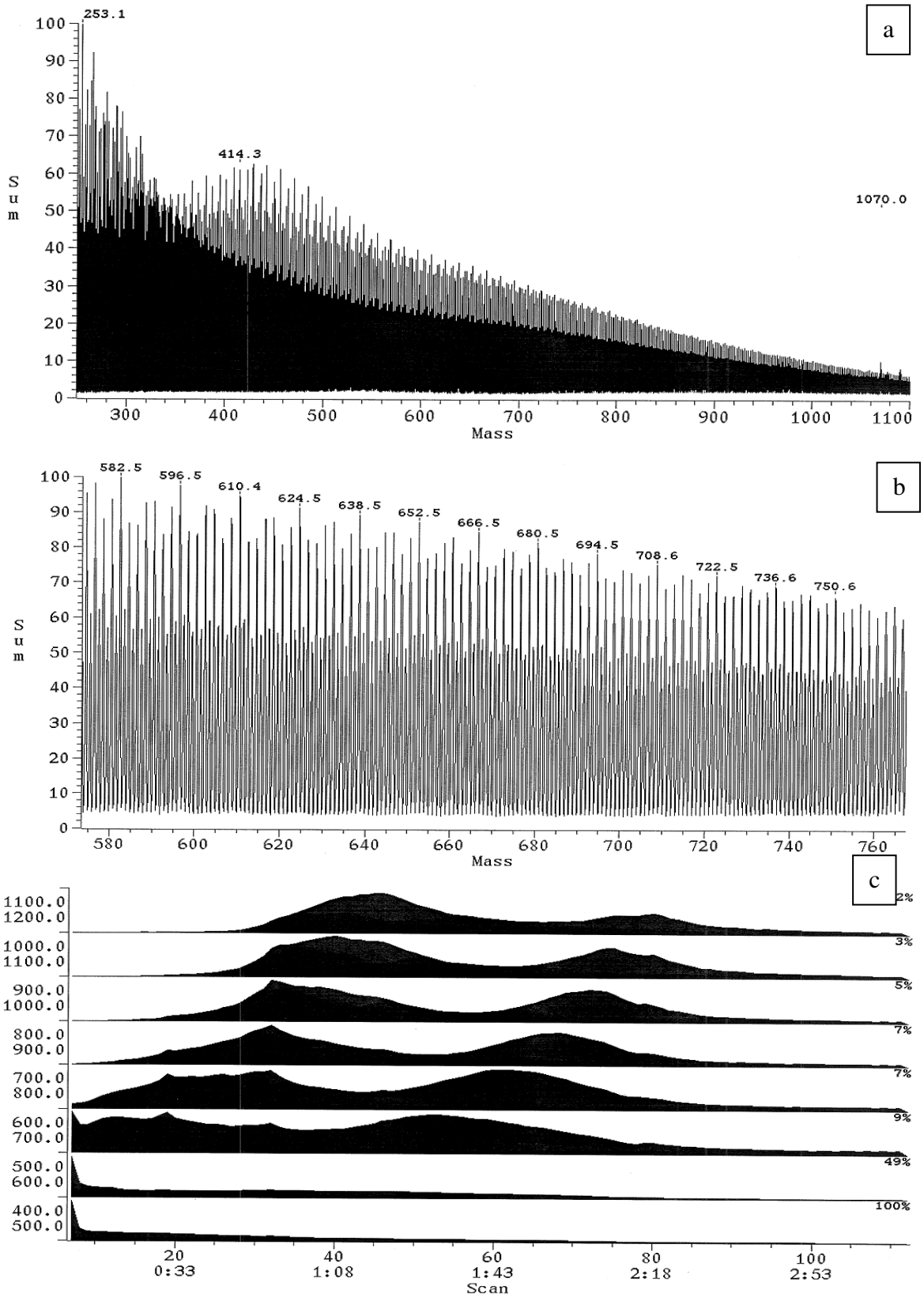

Figure 3-9: Mass spectrum of aromatics fraction of HFO. Sub-figure (a) represents the entire scan of the aromatics fraction, (b) shows a zoom view of a selected range of molecular weight of sub-figure (a), and (c) provides the statistical measure of the molecular weights with time.

The hydrogen to carbon ratio for the simplest aromatic (benzene) is 1 and as the number of fused aromatic rings increases hydrogen to carbon ratio decreases, whereas the hydrogen to carbon ratio for simple alkane (-CH_2-) is 2. The hydrogen to carbon ratio obtained for the separated aromatics fraction is 1.42, which is higher than 1 and lower than 2 indicating the presence of aliphatic side chains attached to the aromatic structures. This information helps to determine the average possible structure of the aromatics fraction.

The first molecular ion shown in Figure 3-9(b) is at 582.5. A possible structure for this compound is an aromatic ring structure containing sulphur ($C_{20}H_{16}S$) as shown in figure below with 21 –CH_2- units as side chain attachments.

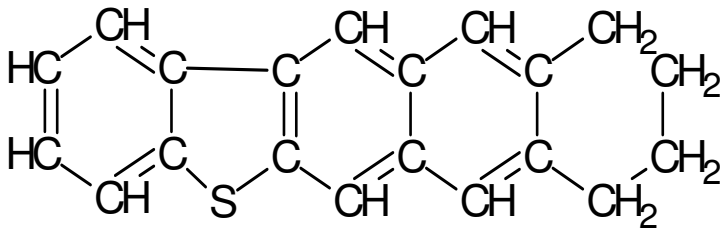

The molecular weight of the above aromatic structure ($C_{20}H_{16}S$) is 288.

Molecular formula of representative aromatics structure is a summation of $C_{20}H_{16}S$ and $C_{21}H_{42}$, which results as $C_{41}H_{58}S$ (MW=582). The hydrogen to carbon ratio for this structure obtained is 1.415, which is very close to the analytical result (1.42) and the S content of 5.5% is close to the analytical result (4.28) too. Mean molecular weight calculated for aromatics in Table 3-7 is 545. This result confirms that the average structure and the mean molecular weight obtained for the saturates fraction are closely related.

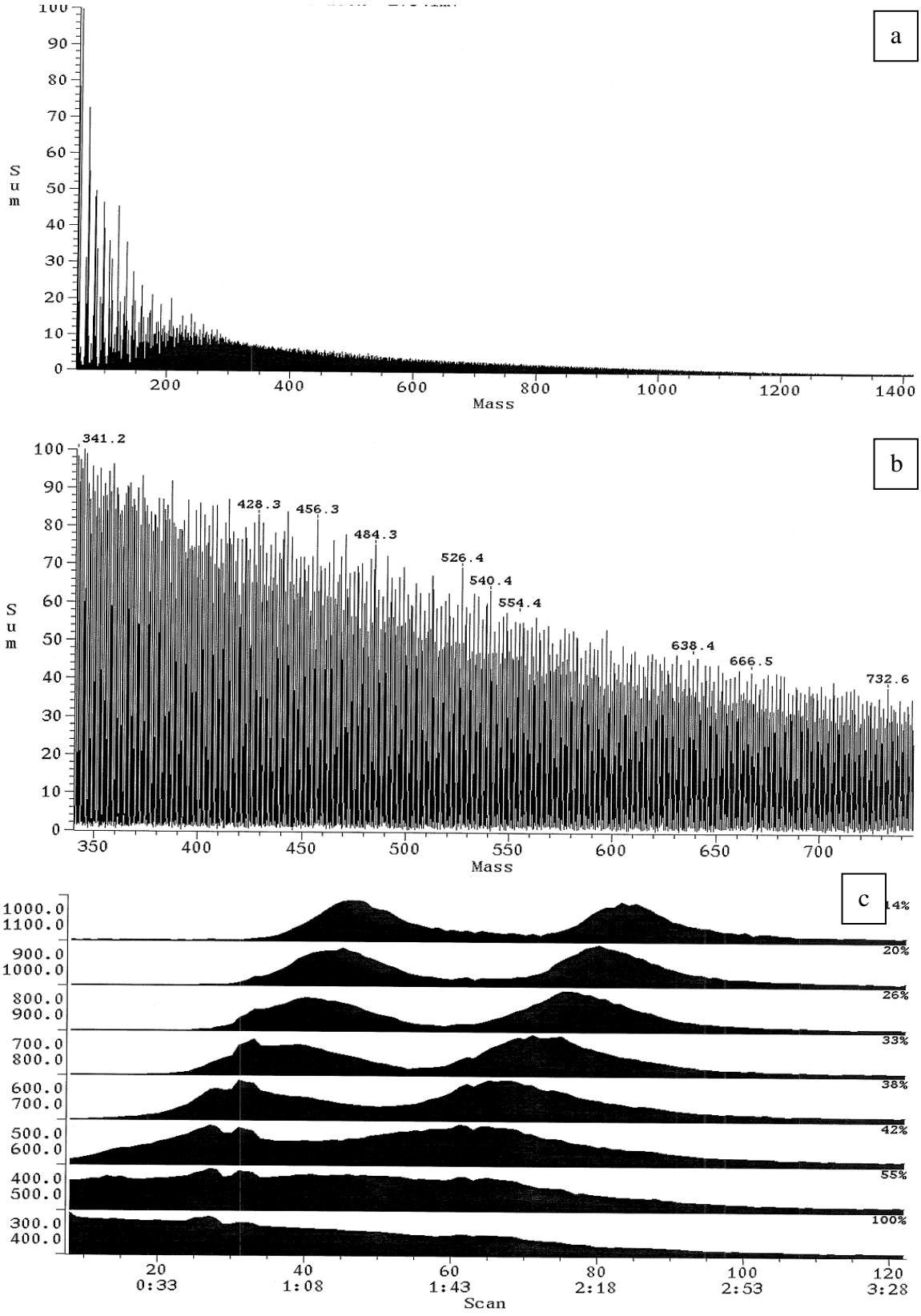

Figure 3-10: Mass spectrum of resins fraction of HFO. Sub-figure (a) represents the entire scan of the resins fraction, (b) shows a zoom view of a selected range of molecular weight of sub-figure (a), and (c) provides the statistical measure of the molecular weights with time.

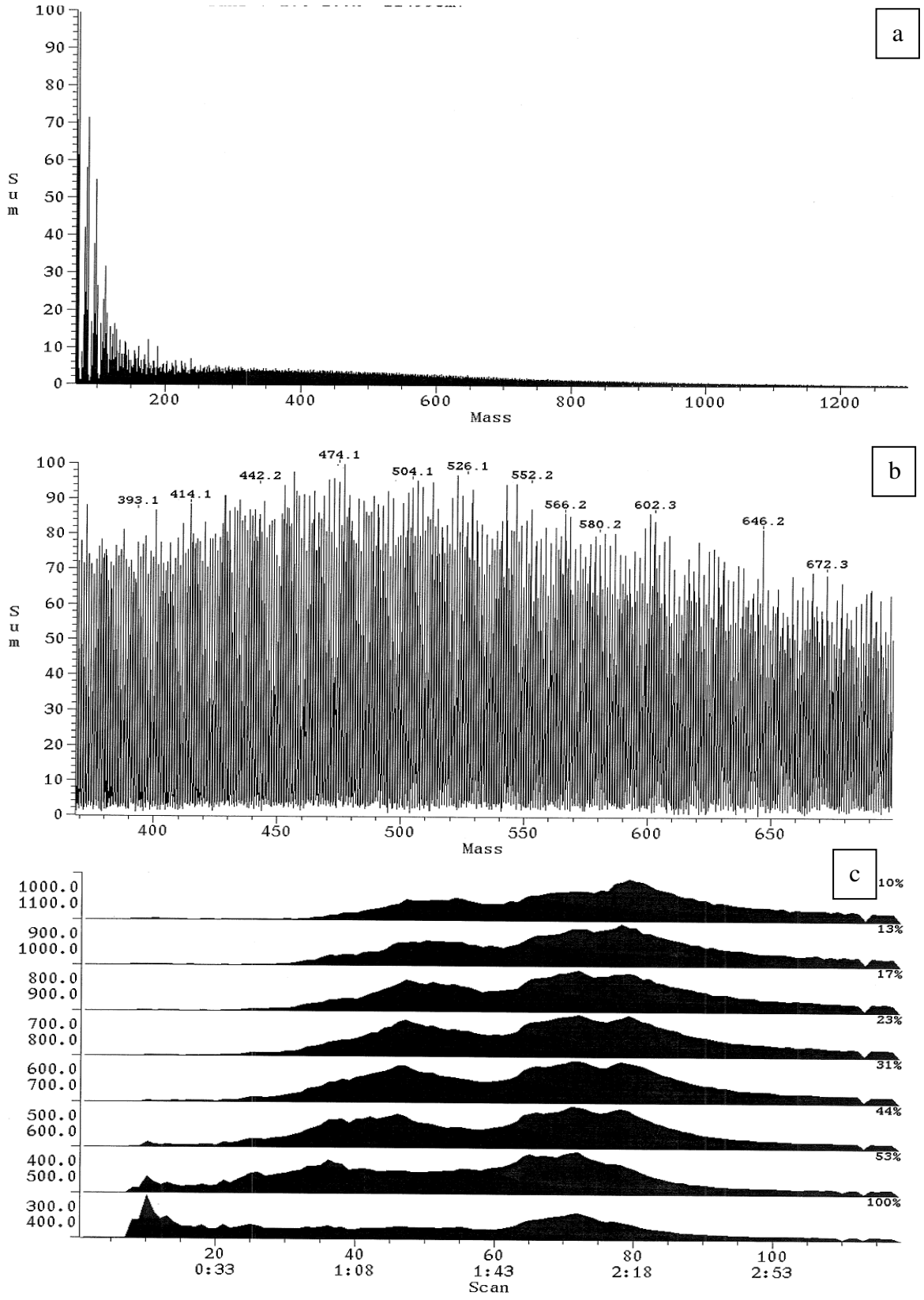

Figure 3-11: Mass spectrum of asphaltenes fraction of HFO. Sub-figure (a) represents the entire scan of the asphaltenes fraction, (b) shows a zoom view of a selected range of molecular weight of sub-figure (a), and (c) provides the statistical measure of the molecular weights with time.

Figure 3-10 and Figure 3-11 shows the mass spectra obtained for the resins and asphaltenes fractions respectively. Resins and asphaltenes have very complex molecular structures; therefore determination of molecular structures of these compounds is restricted. Here again, it is very difficult to estimate the mean molecular weight of these separated fractions. However, through the normalisation of the available data in all above sub–figures (c) the mean molecular weights were calculated as;

Table 3-7: Mean molecular weights of the SARA fractions

Sample Name	Mean Molecular weight
Saturates	580
Aromatics	545
Resins	573
Asphaltenes	542

The molecular weight of the asphaltenes reported here is lower than that mentioned by Rahimi et al.[136]. This could be due to decomposition of the large polar molecules with low volatility as the probe is heated. In sub-figure (c) of all four spectra, double humps of molecular ions were observed. This could be an artefact of the instrument, which is most likely to be due to temperature variations in the different regions of the heated probe. The mean molecular weight of saturates or aromatics shown in Table 3-7 looks heavy though the heavy asphaltenes was separated early on. There are possibilities that the high molecular weight species of saturates or aromatics still remain in the maltenes due to their saturatic or aromatic nature. These high molecular weight species of saturates or aromatics are responsible for polymerisation. Further explanation about the molecular weights and compositions used for the spray combustion (includes evaporation, thermal cracking, polymerisation and polymer burnout) of the present characterised fuel is discussed in Chapter 7.

3.4 Summary

In summary, the outlined experimental procedure enables the separation of heavy fuel oil fractions by sequential elution solvent chromatography (SESC) based on chemical functionality groups using a silica gel column. The present procedure also provides

detailed information on the amounts and chemical characteristics of the separated fractions. The extended study including gas chromatography, mass spectrometry and elemental analysis provided further chemical characterisation of heavy fuel oil. SARA analysis provided compositional analysis of saturates, aromatics, resins and asphaltenes in the heavy fuel oil. Estimation of the mean molecular weight and molecular weight range of each separated fraction were obtained by gas chromatography and mass spectrometry.

Based on the results obtained from the sequential elution solvent chromatography (SESC) and gas chromatography, it was clear that gas chromatographic analysis alone is not sufficient to determine the overall composition of heavy fuel oil, because only the medium molecular weight compounds (light compounds) were able to be analysed by gas chromatography and most of the heavy compounds were not sufficiently volatile to pass through the column and be detected.

Mass spectrometric analysis provided far more detail of all separated fractions than conventional gas chromatography. With the mass spectrometer mean molecular weight, molecular weight range and the possible representative structure of the SARA fractions were obtained. When the mass spectra of all separated fractions were compared with each other significant differences were noted, though they were difficult to interpret due to fragmentations of odd molecular weight ions. The indicated results showed that saturates include cyclic structures with attached aliphatic hydrocarbons, whereas aromatics fraction contain tetracyclic aromatics rings along with aliphatic side chains. The separated fractions of HFO possess very broad molecular weight distributions with differing volatility. Interrelations of all separated fraction can have insightful consequences on the nature of HFO that must be understood and modelled.

The polarity of the components is indeed a very important factor for the separation of complex structure multicomponent fuels. The composition information obtained by separating the fractions of HFO is highly important and can be used directly in continuous thermodynamics modelling. Continuous thermodynamics modelling of multicomponent fuel requires composition, molecular weight range and mean molecular weight of individual fractions. In addition, the present developed method can also be found useful in determining the characteristics of asphaltenes in heavy petroleum ends and its troublesome effect during transportation process. In other words, the effect of asphaltenes

concentration during transportation process can be studied separately for different HFO samples. The present chapter outlines the criteria for choosing the condition and sequence of solvents to characterise heavy fuel oil and other analytical methods to obtain the required information for modelling. Only a CFD simulation of the present characterised HFO is performed using the developed evaporation and pyrolysis model which is given in Chapter 7.

Chapter 4. Evaporation and Pyrolysis Modelling of a Single Droplet

4.1 Introduction

The droplet evaporation is one of the controlling processes for the performance and combustion characteristics of the liquid fuels. Studying and understating the evaporation process of an isolated droplet may help to improve the spray combustion models. The present chapter provides the demonstration of model development for the calculation of evaporation and pyrolysis of a single heavy fuel oil droplet in a hot environment. The chapter is comprised of the combined modelling using the continuous thermodynamic technique for evaporation and chemical kinetics modelling for the pyrolysis process. Two different vapour-liquid equilibrium approaches are employed for low-pressure and high-pressure conditions.

In the literature on fuel modelling, model fuel is sometimes treated as a single component fuel with the same properties as a typical hydrocarbon such as tetradecane. This assumption is quite valid to represent the evaporation in diesel engines under normal conditions (fuel droplets are relatively small and temperature is sufficiently high to evaporate the droplet rapidly). However, in some conditions, such as in a cold start of the diesel engine, differences in the evaporation rates of different components may result in stratification of these components species. Therefore, it is necessary to account for this stratification process during modelling [66]. Heavy fuel oil comprises of large range of components and molecules (low to high molecular weights) and thus large variations in component evaporation rates are predicted.

It is always desirable and advantageous that a developed model should be fast and accurate. Therefore, in the current model the gas phase is considered as quasi-steady and its properties vary with time. The advantage of the quasi-steady model over the full transient model is that the transient model is very complicated and requires a lot of computational power. This quasi-steady assumption was first made by Law & Law [58] and they derived an analytical model for multicomponent fuel. Quasi-steady state means

that at any time, the field of concentration and temperature is assumed to be in quasi-steady state so that d/dt terms from the transport equations can be neglected. All the variables are assumed to adjust to a new steady state instantly. Comparisons between quasi-steady and full transient models proved that the quasi-steady model has a close ability to represent the fuel evaporation process without loss of much accuracy [110, 148]. To simplify the present single droplet model the following assumptions have been made;

- *Fick's* and *Fourier's laws* for mass and energy diffusion are used in the gas phase.
- Homogeneous liquid phase (fully mixed droplet)
- Energy terms arising from viscous dissipation and radiation heat transfer are neglected.
- Soret and Dufour effects are neglected.
- Droplet evaporation is spherically symmetric.
- *Raoult's law* is valid at vapour-liquid equilibrium for low-pressure model.
- A constant pressure exists throughout the process.
- Surface regression is neglected.
- Absorption of ambient gas into liquid surface is neglected.

In this work, the present model describes evaporation and pyrolysis of a single droplet of HFO at high temperatures and variable pressures. As discussed in earlier chapters, the structural and composition chemistry of HFO is very complex, but the continuous thermodynamics technique used in the present modelling uses the multi-distribution function to represent each fuel component with a simple Probably Density Function (PDF). Continuous thermodynamics modelling requires composition of HFO and its relevant transport properties, so based on the information available in the literature, composition and properties are chosen.

As shown in Table 4-1, HFO is assumed to contain four different chemical components: n-paraffins, aromatics, naphthenes and residue. Each component consists of a range of hydrocarbon species with different molecular weight that is represented by a distribution function. Among the above four, properties of n-paraffins, aromatics and naphthenes are known, while the properties of residue are not known experimentally. Residue of the

heavy fuel oil may contain higher molecular weight than as taken in this modelling because it consists of mainly asphaltenes and large aromatics. Yet to use an accurate distribution function for residue is less important because it evaporates very little. Therefore, appropriate values for residue are chosen based on the discussion available in ref [30] and also described in the literature review (Chapter 2). Overall, the present HFO sample is assumed to comprise of 30% cutter stock and 70% residue. The composition and distribution parameters used here are representative only. It does not pretend to be accurate for any HFO sample.

Table 4-1: Distribution function parameters for the composition of heavy fuel oil.

Components	**Mass Fraction**	**Distribution Origin (γ)**	**Distribution mean (θ) (Mean Molecular weight)**	**Standard Deviation (σ)**
n-Paraffins	0.1	160	340.00	43.69
Aromatics	0.1	160	300.00	45.75
Naphthenes	0.1	160	370.00	45.47
Residue	0.7	500	850.00	320.15

The mean molecular weight and the mass mean molecular weight of the present modelled heavy fuel oil are 581 and 696 respectively. In HFO, the residue is considered to have large hydrocarbons and also have some polar compounds, so it evaporates very poorly but it produces polymer (coke) and volatile gas thorough pyrolysis. This assumption is also supported by the experimental observations of Xu et al.[149], which suggest that heavy oil residual components only are responsible for coke formation through pyrolysis.

The pyrolysis model (described later) of heavy fuel oil is considered to follow a first order simple *Arrhenius law* equations. These *Arrhenius law* equations require kinetics rate parameters for the pyrolysis. The literature [150-152] gives a vast range of activation energy and pre-exponential factor, but values of these coefficients in the present chapter are chosen as suggested by Baert [14]. However, the pyrolysis model is studied in more detail in Chapter 5. The pyrolysis model also requires aromaticity of the components; in the present case the initial aromaticity is taken as 0.4. Typical values of aromaticity of non-cracked vacuum residue found in ref [14] for various hydrocarbons are 0.5, 0.35 and 0.3 for asphaltenes, resins and non-polar aromatics respectively.

4.2 Distribution Function

The distribution function is any suitable function, which can describe the distribution of a property of a multi-component fluid mixture accurately. Here, the Γ-distribution function (Schultz or Pearson type III function) is chosen. It is also used by many other researchers [18-21, 71, 72, 75, 91, 111, 112, 115, 121-123, 153] and has the ability to represent petroleum fractions. In the evaporation and pyrolysis modelling of HFO, Baert [14] used a block type distribution function for the representation of molecular weights of HFO fractions, however, in Baert's paper [14] actual emphasis was given to a gamma type distribution function.

After the selection of distribution function, the choice of distribution characterising variable is also very important. It can be any physical property like the component's molecular weight, the component's boiling point, the carbon number etc. In the present modelling, the component's molecular weight is chosen as the characterising variable. The Γ-distribution can be given as [122, 123];

$$f_j(I) = \frac{(I-\gamma_j)^{\alpha_j-1}}{\beta_j^{\alpha_j}\Gamma(\alpha_j)} \exp\left[-\left(\frac{I-\gamma_j}{\beta_j}\right)\right] \tag{20}$$

Where, α_j and β_j are the parameters to determine the shape of the distribution and γ_j determines the origin of the distribution. The shape parameters α_j and β_j are different for the liquid and vapour phase but γ_j is assumed to be the same for both the phases. The mean and variance of this function for the liquid phase are given as [122, 123];

$$\theta_{Lj} = \alpha_{Lj}\beta_{Lj} + \gamma_{Lj}, \qquad \sigma_{Lj}^2 = \alpha_{Lj}\beta_{Lj}^2 \tag{21}$$

The distribution functions for the pure hydrocarbons (n-paraffins, naphthenes and aromatics) and residue are shown in Figure 4-1 and Figure 4-2 respectively. Figure 4-1 shows molecular weight distribution of pure hydrocarbons, ranging from 160 to 500 kg/kmol. In the same way, Figure 4-2 represents continuation of the molecular weight

distribution beyond 500 until 1500 kg/kmol. The distribution parameters are chosen such that they cover the range of molecular weight as suggested by Baert [14] for a representative HFO sample. In Figure 4-2, the distribution function of the residue is fitted to cover the range of molecular weight from 500 to 1500.

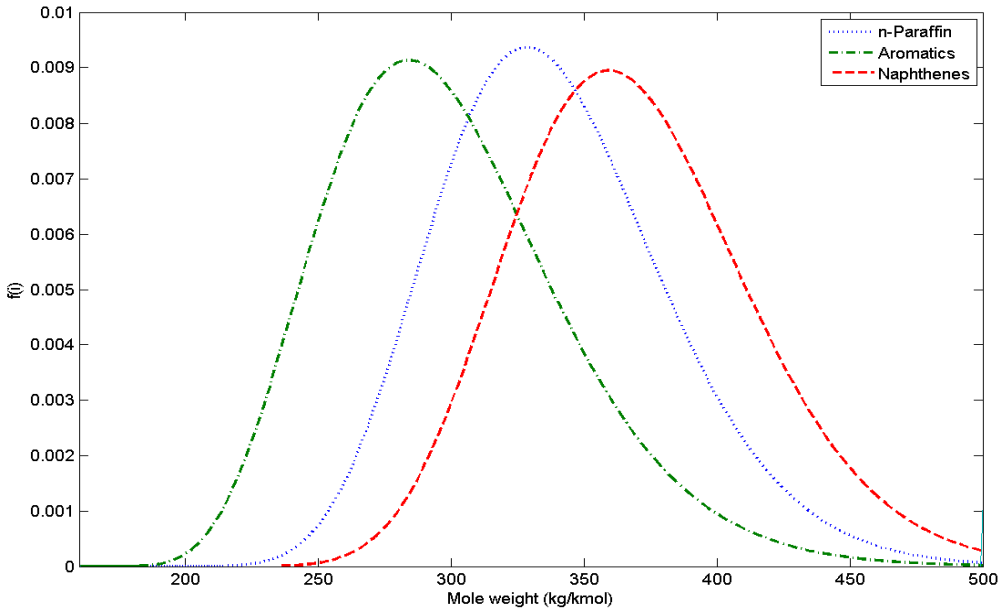

Figure 4-1: Distribution function used for pure hydrocarbons of HFO.

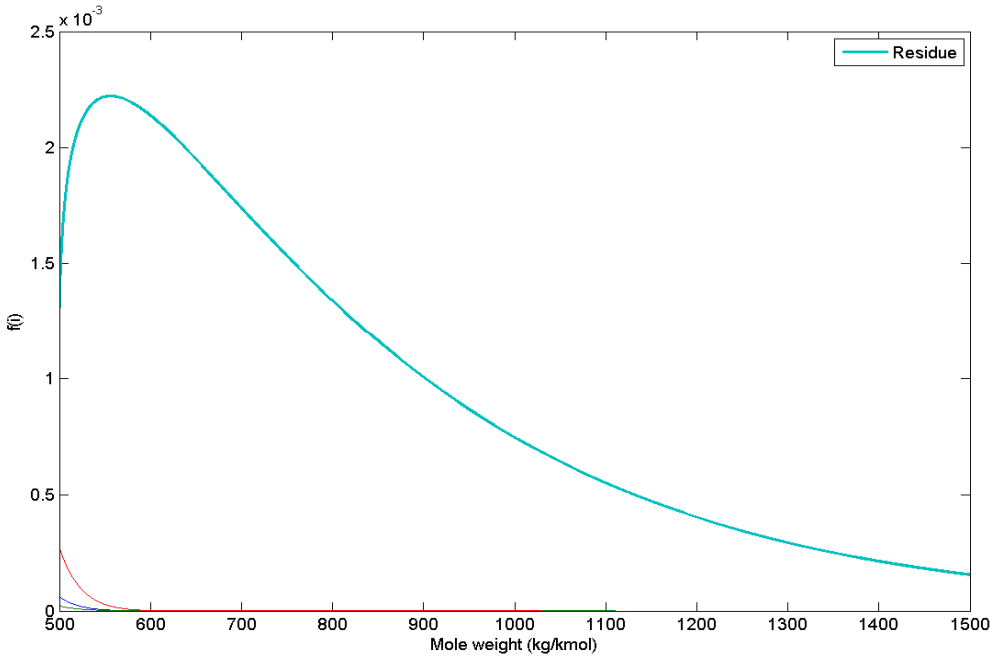

Figure 4-2: Distribution function used for residual portion of HFO.

4.3 Vapour Phase

In the present model, the liquid droplet contains J ($J=4$) hydrocarbon components (fractions) and is initially at temperature T_{L0} . Suddenly it is exposed to surrounding temperature T_{∞} . Here, each hydrocarbon component has been assigned with a separate distribution function $f_{Lj}(I)$ along with two distribution parameters; mean θ_{Lj} and variance as σ_{Lj}^2 . In continuous thermodynamics modelling, these two distribution parameters are sufficient for accurate representation of the composition of each group of hydrocarbon. Vapour is being produced by evaporation. Hence, the corresponding vapour phase distribution is given by $f_{Vj}(I)$. The distribution variable (I) can be any physical property, but here it represents the molecular weight of each hydrocarbon component. The molar concentration of species i of molecular weight I and component j is given by $f_j(I)$. A component of HFO in the present modelling comprise of many species, for example n-paraffin may comprises of C_{10} to C_{35} molecules. Therefore, the vapour and liquid mole fraction of species i are respectively given by [21];

$$y_i = y_{Fj}\ f_{Vj}(I)\,dI, \qquad x_i = x_{Lj}\ f_{Lj}(I)\,dI. \tag{22}$$

Where, y_{Fj} and x_{Lj} are the overall mole fraction of component (fraction/distribution) j in vapour and liquid phase respectively. The overall mole fraction of vapour phase y_{Fj} , together with mole fraction of ambient air and pyrolysis volatile gases sum to unity.

$$\sum_{j=1}^{J} y_{Fj} + y_A + y_G = 1 \tag{23}$$

Now, substituting y_i from equation (22) into the vapour phase species diffusion equation and integrating with I^n (where n = 0, 1 and 2) as a weighting function and dI as interval as described in [21], the transport equations of each component in the vapour phase are derived as follows [21];

$$r^2 cv^* \left(\frac{\partial y_{Fj}}{\partial r} \right) = c\bar{D}_j \frac{\partial}{\partial r} \left(r^2 \frac{\partial y_{Fj}}{\partial r} \right) \tag{24}$$

$$r^2 cv^* \left(\frac{\partial (y_{Fj}\theta_j)}{\partial r} \right) = c\bar{D}_j \frac{\partial}{\partial r} \left(r^2 \frac{\partial (y_{Fj}\theta_j)}{\partial r} \right) \tag{25}$$

$$r^2 cv^* \left(\frac{\partial (y_{Fj}\psi_j)}{\partial r} \right) = c\bar{D}_j \frac{\partial}{\partial r} \left(r^2 \frac{\partial (y_{Fj}\psi_j)}{\partial r} \right) \tag{26}$$

The above equations, describe the transport of fuel vapour composition y_{Fj}, distribution mean θ_j and second central moment of the distribution ψ_j ($\psi_j = \theta_j^2 + \sigma_j^2$). In these above three equations, c is molar density, v^* is average velocity, $\bar{D}_j$ is average diffusivity. To avoid the complexity, molar densities and mole fractions are used in the above equations throughout instead of mass. There are three $\bar{D}_j$ arising from the above equations because average diffusivities are calculated with respect to mole fraction, mean of the distribution and the standard deviation of the distribution. However, as mentioned by Tamim & Hallett [18], their values are almost indistinguishable [111]. Therefore, in the present model they ($\bar{D}_j$) are assumed equal. The molar flux (N) leaving the droplet surface with molar average velocity is represented by [21];

$$cv^* r^2 = NR^2 \tag{27}$$

Spherical symmetry has been assumed and the boundary conditions at the droplet surface and ambient are given as follows;

At the droplet surface (r = R); $y_{Fj} = y_{FjR}$; $y_{Fj}\theta = y_{FjR}\theta_{jR}$; $y_{Fj}\psi = y_{FjR}\psi_{jR}$; and $T = T_R$.

At the ambient (r = ∞); $y_{Fj} = y_{Fj\infty}$; $y_{Fj}\theta = y_{Fj\infty}\theta_{j\infty}$; $y_{Fj}\psi = y_{Fj\infty}\psi_{j\infty}$; and $T = T_\infty$.

Here it is assumed that; $y_{Fj\infty} = 0$; so $(y_{Fj}\theta)_\infty = (y_{Fj}\psi_j)_\infty = 0$.

It is been postulated that from the beginning the residue in the liquid phase contains high molecular weight and during evaporation it evaporates very little, but it produces volatile gas and polymer (coke) through pyrolysis. Therefore, total molar flux N should include this volatile gas along with the fuel vapour. The molar flux fraction of each component (j) and pyrolysis gas (G) are given by;

$$\xi_j = N_j / N \text{ and } \xi_G = N_G / N \tag{28}$$

The total evaporating molar flux can be given as;

$$N = \sum_{j=1}^{J} N_j + N_G \tag{29}$$

The solution of equation; (24) and (27) is given as [19];

$$N = \frac{c\bar{D}_j}{R}\ln(1+B_j) \qquad where, \quad B_j = \frac{y_{FjR} - y_{Fj\infty}}{\xi_j - y_{FjR}}, \tag{30}$$

The above theory can be extended to include the effect of convection using Sherwood number (Sh_o)[1] at low mass transfer rates [21]. The Sherwood number is held constant as $Sh_o = 2$, because the droplet is stationary during the calculation of a single droplet;

$$N = Sh_o \frac{c\bar{D}_j}{2R}\ln(1+B_j) \tag{31}$$

The ξ_j 's used in the above equation may be found by equating equation (31) for $j = 1$ and $j = j$

[1] For a stationary droplet (at zero velocity) Sherwood number is symbolised as Sh_o and for a moving droplet Sherwood number can be symbolised as Sh only.

$$\xi_j = \frac{y_{FjR} - y_{Fj\infty}}{\exp(2NR / c\bar{D}_j Sh_o) - 1} \tag{32}$$

Here, equations (31) and (32) give a set of simultaneous equations and they must be solved simultaneously to calculate the ξ_j, N and N_G. Now, equations (24), (25) and (26) can be solved for the variation of y_{Fj}, $y_{Fj}\theta_j$ and $y_{Fj}\psi_j$ in space (beyond the droplet surface) as follows [21];

$$y_{Fj}(r) = \xi_j - (\xi_j - y_{Fj\infty})(1 + B_j)^{-Z} \tag{33}$$

$$y_{Fj}\theta_j(r) = y_{FjR}\theta_{jR} - \frac{1}{B_j}(y_{FjR}\theta_{jR} - y_{Fj\infty}\theta_{j\infty})[(1 + B_j)^{(1-Z)} - 1] \tag{34}$$

$$y_{Fj}\psi_j(r) = y_{FjR}\psi_{jR} - \frac{1}{B_j}(y_{FjR}\psi_{jR} - y_{Fj\infty}\psi_{j\infty})[(1 + B_j)^{(1-Z)} - 1] \tag{35}$$

Where,

$$Z = 1 + \frac{Sh_o}{2}[\left(\frac{R}{r}\right) - 1] \tag{36}$$

In order to solve the above mentioned vapour phase transport equations during modelling, it requires vapour phase properties. Vapour phase properties are calculated using the one third rule of reference state as suggested by Hallett [111]. More details of property relations used in the present model are given in the appendix of transport properties.

4.4 Liquid Phase (Droplet)

The numbers of mass transfer processes occur during the combustion of heavy fuel oil are described in the literature survey (Chapter 2). The combustion process of heavy fuel oil is divided into two main phases;

1. Liquid droplet phase
2. Solid coke phase

Liquid droplet phase is complicated and it includes heat and mass transfer processes and also some chemical reactions. Solid coke phase is the heterogeneous oxidation of carbonaceous polymer. Liquid phase can be further subdivided into four successive stages;

1) Pre-ignition heating
2) Evaporation
3) Thermal cracking
4) Polymerisation

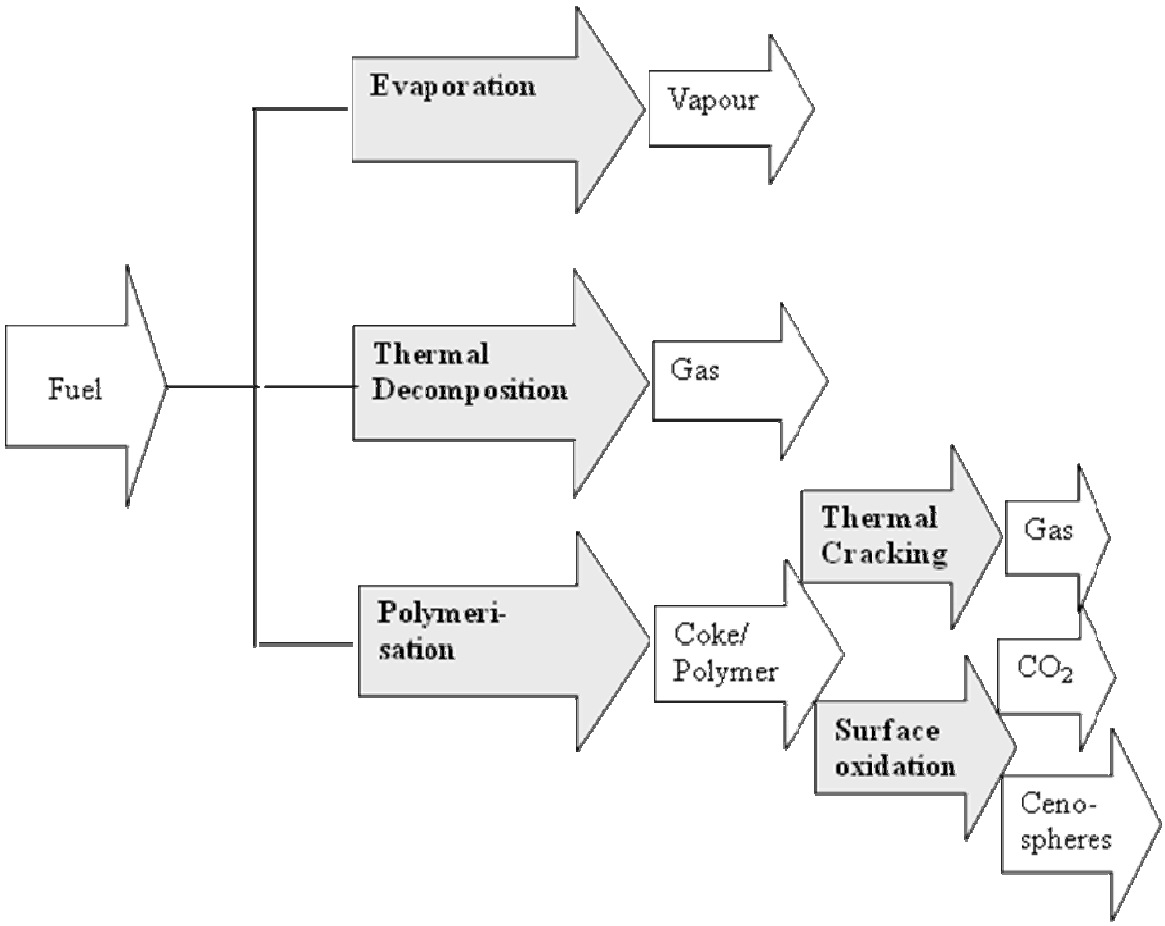

Figure 4-3: The number of mass transfer processes used to describe the mass transfer of a burning droplet in HFO spray.

Figure 4-3 (above chart) summarises the liquid phase mass transfer processes which occur in the liquid phase during the combustion of a heavy fuel oil droplet. The mass transfer processes are represented with grey colour in background whereas their products and fuel

are represented with white background colour. All processes represented in Figure 4-3 are modelled in Matlab code. Details and significance of the various processes and products in the chart are explained in the latter sections. The present chapter only includes the evaporation and pyrolysis (thermal cracking + polymerisation) of a single droplet. Modelling of droplets in a spray, and heterogeneous oxidation of the polymer is given in Chapter 6.

4.4.1 Pre-ignition and Evaporation

In many engineering applications, evaporation of droplets is a major issue of interest. A substantial effort has been made to predict the behaviour of droplets during the combustion of heavy fuel oil. During the evaporation stage of combustion, swelling occurs due to the rapid formation of volatiles within the droplet and slow outer diffusion rate. As evaporation continues liquid temperature increases due to heat transfer between droplets and a hot ambient environment. Consequently, increase in droplet temperature leads to decrease in liquid viscosity. Thus, low viscosity of liquid facilitates diffusion of the formed volatile and helps it to come out, so the droplets contract. Generally, during the evaporation stage, when a droplet of 0.06 inch (1524-micron) diameter is exposed 1145 K, droplets rise to temperature around 700 K[31].

As discussed in the literature survey, the degree of internal mixing within the liquid droplet is also a debatable question, because so far in the literature there are two techniques that have been described [50, 67, 71, 72, 154]. The first technique is commonly used in engineering evaporation modelling, which postulates that a droplet is fully mixed so concentration and temperature are uniform. This technique is also known as “rapid mixing”. The second technique is diffusion limited modelling [50, 67, 71, 72, 154].

In the case of multicomponent fuels such as heavy fuel oil, according to Baert [14], vaporisation of a droplet occurs on the droplet’s surface, but the core of the droplet remains with no vaporization. This surface vaporisation is more similar to droplet distillation vaporization. In that case, light species vaporize rapidly from the surface in the order of their relative volatility and heavier species remain creating a viscous shell. This shell plays an important role for the droplet burning behaviour. As discussed by Ikegami

et al.[23], depending upon the viscosity of liquid the burning time is different for different liquid droplets. In other words, more volatile and less viscous components vaporize earlier from the surface than the low volatile components [67].

Further, according to Williams [11] during the combustion of the heavy fuel oil droplets, composition of the liquid is changing due to fractional distillation on the surface with micro- explosions and splashing. The high boiling point components, which are initially present, can reach high temperature, so that liquid cracking can occur. In other words, the combustion of heavy fuel oil is a non steady state process except for a few initial stages [11].

Baert [14] demonstrated that when a droplet with initial diameter up to 200 micron passes through high temperature gas it possesses uniform temperature and distillation like vaporization behaviour. In other terms, different components deplete in order of their relative volatilities from the liquid phase. This uniform temperature assumption is also supported by other researchers [71, 72].

Over the past decade, numerous research studies have been done on evaporation modelling of multicomponent fuels using the continuous thermodynamics technique. The advantage of continuous thermodynamics over discrete modelling is that it requires less computational power than discrete component modelling. Recently, Abdel-Qader & Hallett [71, 72] developed a continuous thermodynamics model for the role of liquid mixing in the evaporation and demonstrated that internal mixing has less influence when the droplet has a large number of components, whose molecular weight and boiling point ranges are very wide. Furthermore, they concluded that the well-mixed model is a reasonable model for practical spray calculations [72]. Based on experimental results Ikegami et al.[23] concluded that during the evaporation and pyrolysis process of HFO droplets, disruptive boiling occurs in the droplet, which causes very rapid mass transport process within the droplets. Ikegami et al.[23] argued that micro-explosions and swelling occur during the most of the droplet lifetime which leads to considerable amount of internal circulation inside the fuel droplets. Hence, this faster internal circulation causes the droplet to be fully mixed. The experimental results of MIE scattering imaging with rainbow refractometry by Wilms & Weigand [155] also favours the rapid-mixing model over the diffusion–limit model for the binary liquid droplets. Therefore, based on this

information, in the present study, a droplet is considered as “well-mixed”. This approach is justified by numerous other researchers [18-21, 66, 75, 91, 110, 111, 117] in their studies as well.

4.4.2 Pyrolysis

Thermal cracking of the residue has gained more research interest because high molecular weight compounds which cannot evaporate easily crack at a high temperature and convert into gas or soot particles. These thermal cracking reactions are very complex and require a considerable amount of study. Due to increasing fuel prices, petroleum refineries have started producing heavier molecular weight residues. The cracking process of this kind of residue has attracted more researchers to try to understand the cracking during combustion.

Pyrolysis is a process in which chemical changes of organic compounds are caused by heating in the absence of oxygen. Thermal stability of any hydrocarbon molecules increases with an increase in the number of C-C and C-H bond, but when temperature becomes sufficiently high any bond can be broken and these molecules start decomposing into radicals. These radicals can either decompose through cracking or recombine through polymerisation. Pyrolysis reactions convert the higher molecules into low molecular weight gases and coke residue. This combined process of cracking and polymerisation is called pyrolysis [14]. The combined modelling of thermal cracking and polymerisation is termed as the pyrolysis model of the combustion part of the modelling. The chemical kinetics model of the pyrolysis provides the composition and the rate of production of gases and soot particles from the heavy hydrocarbons of HFO during combustion

The pyrolysis process can be sub-divided into three groups (1) Thermal cracking, (2) Low Temperature (LT) polymerisation and (3) High Temperature (HT) polymerisation. Thermal cracking produces light gaseous volatiles, LT polymerisation produces toluene insolubles and HT polymerisation produces high temperature insolubles [14]. Morrone et al.[38] pointed out that pyrolysis rate is an exponentially dependent on droplet temperature.

4.4.2.1 Thermal Cracking

In HFO, the weakest bonds start breaking around 625 K [14]. Therefore, when the temperature of a droplet reaches close to 625 K, the asphaltene molecules of the residual portion of liquid which have a boiling point higher than 625 K, start decomposing into monomer. Furthermore, as the temperature of a droplet approaches to 650 K, C-C and C-H bonds of the paraffinic and naphthenic molecules which have originated from the non-polar aromatics and cannot evaporate can crack into low molecular weight gases [14]. However, to have substantial effect of thermal cracking on liquid, a temperature of 800 K or more is needed. According to Baert [14] cracking gases could be paraffinic or olefinic molecules containing up to 10 carbon atoms along with H_2, H_2O and CO_2. Similarly, Doolan et al.[156] noted that flash pyrolysis of coal produces light gases such as CH_4, C_2H_4, C_3H_6, C_6H_6, CO and CO_2.

The observation made by Chen & EI-Wakil [31] showed that, for a single and bigger droplet (1524-micron diameter) thermal decomposition (cracking) also occurs during the initial phase (evaporation) but it becomes important when a droplet reaches 700 K. Around this temperature, heavy molecules in the liquid phase start decomposing to volatile gases, heavier and lighter liquid and coke. The evaporation of formed heavier and lighter liquid from liquid also takes place simultaneously due to the high temperature. Droplets usually reach almost 977 K during the thermal decomposition (cracking) phase of the combustion [31]

Thermal cracking is an endothermic process; it requires a high amount of energy to begin the process. Therefore, there is a higher tendency for the droplet temperature to plateau for a heavier fuel [23]. In the liquid phase, thermal cracking results in a decrease in the molecular weight of fuel, but only the non-aromatic $(1-AR)$ part of the molecules produces volatiles through cracking. Here, AR is the aromaticity of the compound and '$1-AR$' represent the non-aromatic part of the compounds. The rate of cracking depends exponentially on the temperature (T) [14]. Wallace et al.[157] studied the characterisation of petroleum feedstock for coal-oil co-processing. Their findings showed that under low severity conditions the aliphatic side chains are removed by cracking from the feedstocks, while at high severity conditions condensation of aromatics in the feedstocks occurs.

Hence, it can be accepted that thermal cracking only affects the non-aromatic molecules in the liquid.

4.4.2.2 Polymerisation

Generally, heavy fuel oil polymerisation starts at 840 K [23]. Thermal cracking also takes place simultaneously with polymerisation [23]. In the liquid phase, polymerisation results in a decrease in the number of monomers from the fuel, but only the aromatic part of the monomers combines and produces polymers. This polymerisation rate also depends exponentially on temperature and is independent of molecular weight [14].

Thermal cracking reduces the monomers from the fuel to their aromatic nucleus. These nuclei are very stable and they start breaking at 1000 K. Most of these nuclei either evaporate or form polymers. These polymers are formed from the residual portion of the liquid fuel and since they were formed at a high temperature they are called High Temperature (HT) polymer [14]. Polymers formed at a low temperature are known as Low Temperature (LT) polymer.

From the above discussion, a pyrolysis model similar to Baert's pyrolysis model [14] is hypothesized in the present work based on following assumptions.

1. Initially the mass of all the fuel component is given by m_{Lj}, which converts to volatile gas (m_{Gj}) through cracking and into polymer (m_{Pj}) through polymerisation.
2. Residue is initially present in the fuel.
3. Most of the pure hydrocarbons evaporate before thermal cracking occurs.
4. Once the volatile products of cracking are formed, they disappear from the liquid phase immediately.
5. The tendency to polymerisation increases with aromaticity.

During liquid pyrolysis, polymer formation occurs continuously, but at the same time, the non-aromatic part of the polymer undergoes further cracking due to high liquid temperature. This polymer formation rate shows dependence on temperature (T) and

aromaticity (AR). Hence, the combined rate of volatile gas production by thermal cracking of liquid and cracking of the polymer for a single fraction of is given as [14];

$$\frac{dm_{Gj}}{dt} = (m_{Lj} + m_{Pj})\left\{k_1 \exp\left(\frac{-E_1}{\mathcal{R}T}\right)(1 - AR_j)\right\} \tag{37}$$

The combined rate of polymer (LT and HT polymer) formation through polymerisation of a single fraction of the liquid is given by[14];

$$\frac{dm_{Pj}}{dt} = -m_{Pj}\left\{k_1 \exp\left(\frac{-E_1}{\mathcal{R}T}\right)(1 - AR_j)\right\} + m_{Lj}\left\{\left[k_2 \exp\left(\frac{-E_2}{\mathcal{R}T}\right) + k_3 \exp\left(\frac{-E_3}{\mathcal{R}T}\right)\right] AR_j\right\} \tag{38}$$

The first term on the RHS represents the loss of polymer due thermal cracking and second term represents LT and HT polymer formation.

Where;

Table 4-2: *Arrhenius law* parameters for the pyrolysis of heavy fuel oil (Baert [14]).

Activation Energy (E)	**Reaction rate pre-exponential factor** (k)
$E_1 = 125 * 10^3$ kJ/kmol	$k_1 = 2 * 10^7$ 1/s
$E_2 = 100 * 10^3$ kJ /kmol	$k_2 = 8 * 10^6$ 1/s
$E_3 = 270 * 10^3$ kJ /kmol.	$k_3 = 10^{13}$ 1/s

When non-aromatic molecules leave the liquid phase through cracking, only aromatic molecules are left behind. These aromatic molecules recombine through polymerisation and later burn through heterogeneous surface oxidation. Hence, the residue (cenospheres) found at the end of heterogeneous surface oxidation is found to be highly aromatic. Aromaticity (AR_j) of the components provides an indication of the relative amounts of aromatic and non-aromatic molecules in the liquid phase. Modelling the aromaticity facilitates determination of the end of polymerisation and the beginning of the surface oxidation. The heterogeneous surface oxidation is a later process after the evaporation and

pyrolysis. More details about heterogeneous surface oxidation and its modelling are given in the spray combustion chapter (Chapter 6).

The rate of change of aromaticity is given as;

$$\frac{dAR}{dt} = k_1 \exp\left(\frac{-E_1}{\mathcal{R}T}\right)(1-AR)(AR) \tag{39}$$

Where k_1 and E_1 are the same as given in Table 4-2.

The aromaticity increases as the thermal cracking progresses, while polymerisation does not affect the aromaticity because polymerisation just combines the small molecules and converts them into big molecules but within the liquid phase only.

4.4.3 Theoretical Formulation for the Liquid Phase

A molar flux balance on the surface gives the change of composition of the liquid phase during evaporation and pyrolysis. In this modelling, it has been assumed that all species of residue pyrolise at the same rate. Thus, no molecular weight change of the residue (fraction four) occurs due to pyrolysis. Hence, the change in mean molecular weight of liquid through evaporation and pyrolysis in terms of continuous thermodynamics of any fraction can be given as [19];

$$\frac{d\theta_{Lj}}{dt} = \frac{3N}{x_{Lj}c_L R}\left[\theta_{Lj}\xi_j + \frac{\theta_{j\infty}y_{Fj\infty} - \theta_{jR}y_{FjR}(1+B_j)}{B_j}\right] \tag{40}$$

An analogous equation can be obtained for $\frac{d\psi}{dt}$ as;

$$\frac{d\psi_{Lj}}{dt} = \frac{3N}{x_{Lj}c_L R}\left[\psi_{Lj}\xi_j + \frac{\psi_{j\infty}y_{Fj\infty} - \psi_{jR}y_{FjR}(1+B_j)}{B_j}\right] \tag{41}$$

As evaporation progresses, low molecular weight species (high volatile) of the component leave the liquid phase and only high molecular weight species (low volatile) are remain as left behind. Thus, the mean molecular weight of the distribution increases and its variance decreases. A mass balance on the droplet surface for a single fraction (component) yields;

$$dm_{Lj} + dm_{Vj} + dm_{Gj} + dm_{Pj} = 0 \tag{42}$$

Hence, mass of a single component in the liquid phase at any time can be given as;

$$m_{Lj} = m_{Lj(t=0)} - m_{Vj} - m_{Gj} - m_{Pj} \tag{43}$$

In the present model, components no. 1, 2 and 3 are assumed to follow evaporation only. The fourth component (residue) will mainly form volatile gases and polymer, with negligible evaporation, unless the lighter components (1, 2 and 3) promote the evaporation of component no. 4. The effect of the light molecules promoting the evaporation of heavy molecules is described in the high-pressure model (section 4.5.2)

4.5 Vapour-Liquid Equilibrium (VLE)

The Vapour-Liquid Equilibrium (VLE) determines the concentration of vapour at the droplet surface. Therefore, VLE is a very important correlation for the evaporation of a fuel mixture, in which the liquid mixture contains thousands of different hydrocarbons and their composition are not known discretely. Generally, it is assumed that the chemical potential (μ) at the boundary between two phases is same in each phase [158]. It means;

$$\begin{aligned} &\textit{Discrete components}: \quad \mu_i^G = \mu_i^L \quad \textit{for} \quad i = 1,2,3.....s \\ &\textit{Continuous Thermo.}: \quad \mu^G(I) = \mu^L(I) \quad \textit{for} \quad I_1 < I < I_2 \end{aligned} \tag{44}$$

Where *s* is the total number of species.

As shown in the above relationship, in discrete modelling, the number of chemical potential equations required is the same as the number of species, but in continuous thermodynamics modelling this requirement is satisfied by only one equation per component class. This relation helps in reducing the computing cost during complex simulations.

4.5.1 Low-Pressure (Linear) VLE Model Formulation

In this approach, the liquid is assumed to be an ideal solution whose vapour phase can be approximated as an ideal gas mixture. The VLE comparison for discrete (conventional) modelling and continuous thermodynamics modelling using *Raoult's law* is shown in the following equations;

$$\begin{aligned} &Discrete: \quad y_i P = x_i P_i^{sat}(T) \\ &Continuous: \quad y_{Fj} f_{Vj}(I) P = x_{Lj} f_{Lj}(I) P_j^{sat}(T, I) \end{aligned} \tag{45}$$

Where x_i and y_i are the liquid and vapour phase mole fractions of discrete species respectively, x_{Lj} and y_{Fj} are the liquid and vapour phase mole fractions of the fuel component (fraction) j respectively. P_j^{sat} is the vapour pressure of the fuel component. This VLE can be expressed in terms of continuous thermodynamics for the mole fraction of liquid at the droplet surface as;

$$y_{FjR} = x_{LjR} \int_0^\infty f_{Lj}(I) \frac{P_j^{sat}(I)}{P} dI \tag{46}$$

Integrating the above equation with using I and $(I-\theta)^2$ as a weighing function, the vapour phase mean and variance are obtained as follows;

$$y_{FjR} \theta_{jR} = x_{LjR} \int_0^\infty f_{Lj}(I) \frac{P_j^{sat}(I)}{P} I dI \tag{47}$$

$$y_{FjR}\sigma_{jR}^2 = x_{LjR}\int_0^\infty f_{Lj}(I)\frac{P_j^{sat}(I)}{P}(I-\theta)^2 dI \tag{48}$$

In this VLE correlation the Clausius-Clapeyron equation is used to determine the vapour pressure of a component as [18];

$$P^{sat}(I) = P_{ATM}\exp[\left(\frac{S_{fg}}{\mathcal{R}T}\right)(T - T_b(I))] \tag{49}$$

Where S_{fg} is the entropy of evaporation and $T_b(I)$ is the component's boiling point at atmospheric pressure.

Now, substituting the distribution function (eqn. (20)) into equation (46) and integrating with I^n (n = 0,1 and 2) as a weighting factor, the vapour phase mole fraction and other distribution parameters at the droplet surface are obtained for a single component as [18, 91, 111];

$$y_{FjR} = \frac{P_{ATM}}{P_\infty}\frac{\exp\left[\left(\frac{S_{fgj}}{\mathcal{R}T_R}\right)(T_R - a_B - \gamma_j b_B)\right]}{\left[1+\left(\frac{S_{fgj}}{\mathcal{R}T_R}\right)b_B\beta_{Lj}\right]^{\alpha_{Lj}}} \tag{50}$$

$$\theta_{jR} = \gamma_j + \frac{\theta_{Lj} - \gamma_j}{1+\left(\left(\frac{S_{fgj}b_B}{\mathcal{R}T_R}\right)\frac{\sigma_{Lj}^2}{(\theta_{Lj}-\gamma_j)}\right)} \tag{51}$$

And,

$$\sigma_{jR}^2 = \sigma_{Lj}^2\left(\frac{\theta_{jR}-\gamma_j}{\theta_{Lj}-\gamma_j}\right)^2 \tag{52}$$

4.5.2 High-Pressure (Non-Linear) VLE Model Formulation

At low pressure, usually ideal gas and ideal liquid are assumed and VLE is expressed by *Raoult's law*. However, at elevated pressure compressibility of liquid appears and the solubility of ambient gas into liquid surface may become significant. In addition, interaction between individual components may also become important. Therefore, in order to include the compressibility of liquid and solubility of ambient gas into liquid, an appropriate equation of state (EOS) is needed to obtain the chemical potential of both phases. An equation of state provides relations between state variables (temperature, pressure, mass enthalpy etc.) under given set of physical conditions.

At any given temperature and pressure, the requirement for phase equilibrium of a mixture is that the fugacities of the species in both phases must be the same [73];

$$\hat{f}_{Vi} = \hat{f}_{Li} \tag{53}$$

Where $\hat{f}_{Vi}$ and $\hat{f}_{Li}$ are the fugacities of i th species of a mixture in vapour phase and liquid phase respectively. The fugacity can be defined as;

$$\hat{f}_{Li} = x_i \hat{\phi}_i^L P \quad and \quad \hat{f}_{Vi} = y_i \hat{\phi}_i^v P \tag{54}$$

Where $\hat{\phi}_i^L$ and $\hat{\phi}_i^V$ are the fugacity coefficients of the species of a mixture in vapour phase and liquid phase respectively. Hence, equation (53) can be written for discrete components as [77, 82];

$$y_i \hat{\phi}_i^V = x_i \hat{\phi}_i^L \tag{55}$$

A similar relationship can be derived for continuous fractions as;

$$y_j f_j^V(I) \hat{\phi}_j^V = x_j f_j^L(I) \hat{\phi}_j^L \tag{56}$$

The fugacity coefficients in the above equation are derived from the chemical potential equation of continuous species given by Cotterman et al.[85, 86] as ;

$$\mu(I) = \int_V^{\infty} \left\{ \left[\frac{\delta P}{\delta n_\tau f(I^+)} \right]_{T,V,I^+=I} - \frac{\mathcal{R}T}{V} \right\} dV - \mathcal{R}T \ln\left(\frac{P^o V}{n_\tau f(I^+) \mathcal{R}T} \right) + \mathcal{R}T + \mu^o(T, I) \quad (57)$$

Where n_τ is the total number of moles of substance, μ^o is the pure component ideal gas chemical potential at temperature T and reference pressure P^o .

A cubic equation of state is required to obtain the VLE at high pressure [159]. In the present section a generic approach to the EOS is presented, so that in subsequent calculation any type of EOS can be applied. The general form of EOS can be written as [75, 81, 88];

$$P = \frac{\mathcal{R}T}{v} - \frac{a}{v^2 + ubv + wb^2} \quad (58)$$

Where, v is the molar volume of the system, and u and w are EOS constants. The following table lists the u and w values for a choice of equation of states as [75, 81];

Table 4-3: Constants for various equations of state.

Equation of State (EOS)	u	w
Peng-Robinson (PR EOS)	2	-1
Soave-Redlich-Kwong (SRK EOS)	1	0
Redlich-Kwong (RK EOS)	1	0

Parameters a and b in equation (58) are mixture values obtained by mixing rules. For a semicontinuous mixture of H family of discrete species and J family of continuous distribution, a and b are obtained as;

$$b = \sum_{i=1}^{H} x_i b(i) + \sum_{j=1}^{J} x_{Lj} \int_I f_j^L(I) b(I) dI \quad (59)$$

$$a = \sum_{i=1}^{H}\sum_{j=1}^{H} x_i x_j a(i,j) + 2\sum_{i=1}^{H}\sum_{j=1}^{J} x_i x_{Lj} \int_I f_j^L(I) a(i,I) dI + \sum_{i=1}^{J}\sum_{j=1}^{J} x_{Li} x_{Lj} \int_I \int_{I^+} f_i^L(I) f_j^L(I) a(I,I^+) dI dI^+ \quad (60)$$

The above two equations are generic and given for a semicontinuous mixture. Hence, in order to apply for a continuous mixture, discrete components should be ignored. Similar expressions for a and b also stand for the vapour phase. For different families of hydrocarbons (paraffins, aromatics and naphthenic) $a(I,I)$ and $b(I)$ are given as a function of molecular weight as [86];

$$a^{0.5}(I,I) = a_0(T) + a_1(T) I$$
$$b(I) = b_0 + b_1 I \quad (61)$$

Where b_0 and b_1 are linear fit for b, and are considered constant for a given component. The temperature dependence terms in calculation of $a^{0.5}(I,I)$ are obtained from a quadratic fit as [85, 86];

$$a_0(T) = a_{00} + a_{01} T + a_{02} T^2$$
$$a_1(T) = a_{10} + a_{11} T + a_{12} T^2 \quad (62)$$

In the present modelling, Soave-Redlich-Kwong (SRK EOS) has been chosen because all coefficients required for paraffins, aromatics and naphthenes to use in this EOS are available in the literature. All coefficients for $a(I,I)$ and $b(I)$ used for SRK EOS are listed in the following tables (Table 4-4 and Table 4-5) for paraffins, aromatics and naphthenes. The coefficients for paraffins are obtained from Zhu & Reitz [75], whereas those for aromatics and napthenes are obtained from Cotterman & Prausnitz [86]. The coefficients for component number four (residue) are not available in the literature but realistic values are assumed.

Table 4-4: Constant a for SRK EOS for various hydrocarbon groups of HFO.

Components	a_0 **(bar-cm^6/mol^2)**		
	a_{00}	a_{01}	a_{02}
n-Paraffins	-359.26	0.76707	-1.6114E-4
Aromatics	933.28	-4.9650	9.0332E-3
Naphthenes	434.99	-4.9395	10.065E-3
Residue	1000.0	0.0000	0.0000
	a_1 **(bar-cm^6/mol^2)**		
n-Paraffins	93.905	-0.0781	1.6399E-5
Aromatics	85.466	-0.0677	6.9715E-7
Naphthenes	91.903	-0.0787	5.7932E-6
Residue	50.000	0.0000	0.0000

Table 4-5: Constant b for SRK EOS for various hydrocarbon groups of HFO.

Components	b **(cm^3/mol)**	
	b_0	b_1
n-Paraffins	-31.734	1.8094
Aromatics	-30.848	1.4547
Naphthenes	-37.145	1.6013
Residue	-100.00	1.5000

For accurate predictions of mixture thermodynamics properties using the EOS, a suitable mixing rule is required [160]. A quadratic mixing rule is used here. The cross terms (For ex. $a(i,j)$) in this mixing rule are given by the geometric mean corrected by the binary interaction parameter (k_{ij}) as [78];

$$\begin{aligned} a(i,j) &= \sqrt{a(i,i)a(j,j)}\,(1-k_{ij}) \\ a(i,I) &= \sqrt{a(i,i)a(I,I)}\,(1-k_{iI}) \\ a(I,I^+) &= \sqrt{a(I,I)a(I^+,I^+)}\,(1-k_{II^+}) \end{aligned} \tag{63}$$

In the above equations, k_{ij} represents the interaction between discrete-discrete components, k_{iI} represents the interaction between discrete-continuous components and k_{II^+} represents the interaction between continuous-continuous fractions. For continuous fractions, all k_{ij} are assumed constant and independent of molecular weight for each distribution function.

Now substituting the general form of EOS (58) into the equation of chemical potential (57) the fugacity coefficient for a discrete component in each phase can be obtained as [75];

$$\ln\hat{\phi}_i = \frac{b(i)}{b}(z-1) - \ln(z-B^*) + A_{EOS}\left(\frac{b(i)}{b} - \frac{2}{a}\left[\sum_{j=1}^{H} x_j a(i,j) + \sum_{j=1}^{J} x_{Lj}\int_I f_j(I)a(i,I)dI\right]\right) \tag{64}$$

Where , z is the compressibility factor given as [87, 94] ; $z = \frac{Pv}{\mathcal{R}T}$.

Similar to discrete, the fugacity coefficient for a continuous fraction can be obtained as [75, 89];

$$\ln\hat{\phi}_j(I) = \frac{b(I)}{b}(z-1) - \ln(z-B^*) + A_{EOS}\left(\frac{b(I)}{b} - \frac{2}{a}\left[\sum_{j=1}^{H} x_j a(I,j) + \sum_{j=1}^{J} x_{Lj}\int_I f_j(I)a(I,I^+)dI^+\right]\right) \tag{65}$$

Where, $A_{EOS} = \frac{A^*}{B^*\sqrt{u^2-4w}}\ln\frac{2z+B^*(u+\sqrt{u^2-4w}}{2z+B^*(u-\sqrt{u^2-4w}}$, $A^* = \frac{aP}{(\mathcal{R}T)^2}$, $B^* = \frac{bP}{\mathcal{R}T}$.

The parameters with double subscripts ($a(I,j)$ and $a(I,I^+)$) in equation (65) are cross terms and can be calculated by a mixing rule as shown in equation (63), whereas calculation for a and b are shown in equation (61). The fugacity coefficient for a continuous fraction can be written as an explicit function of molecular weight as [75, 88];

$$\ln \hat{\phi}_j(I) = c_1 + c_2 I \tag{66}$$

Where, c_1 and c_2 are derived for the liquid phase as;

$$\begin{aligned} c_1^L &= \frac{b_0}{b}(z-1) - \ln(z - B^*) + \\ &A_{EOS}\left(\frac{b_0}{b} - \frac{2a_0}{a}\left[\sum_{j=1}^{H} x_j a^{0.5}(j,j)(1-k_{Ij}) + \sum_{j=1}^{J} x_{Lj}(a_0 + a_1\theta)_{I^+}(1-k_{II^+})\right]\right) \\ c_2^L &= \frac{b_1}{b}(z-1) + \\ &A_{EOS}\left(\frac{b_1}{b} - \frac{2a_1}{a}\left[\sum_{j=1}^{H} x_j a^{0.5}(j,j)(1-k_{Ij}) + \sum_{j=1}^{J} x_{Lj}(a_0 + a_1\theta)_{I^+}(1-k_{II^+})\right]\right) \end{aligned} \tag{67}$$

Similar to equation (67), an analogous equation stands for the vapour phase with the properties of the vapour phase. Now integrating over the distribution function, the fugacity coefficient for a continuous fraction can be obtained as;

$$\hat{\phi}_j = \int_I f_j(I) \cdot \exp(c_1 + c_2 I) dI = \frac{\exp(c_1 + c_2\gamma)}{(1 - c_2\beta)^{\alpha}} \tag{68}$$

Therefore, the vapour mole fraction from equation (56) can be obtained as;

$$\frac{y_{FjR}}{x_{Lj}} = \frac{\hat{\phi}_j^L}{\hat{\phi}_j^v} = \frac{\exp(C_1 + C_2 \cdot \gamma_{Lj})}{(1 - C_2\beta_{Lj})^{\alpha_{Lj}}} \tag{69}$$

Where, $C_1 = c_1^L - c_1^V, C_2 = c_2^L - c_2^V$. All the distribution parameters in the vapour phase can be obtained as;

$$\gamma_{Vj} = \gamma_{Lj}, \quad \alpha_{Vj} = \alpha_{Lj}, \quad \beta_{Vj} = \frac{\beta_{Lj}}{1 - C_2\beta_{Lj}}. \tag{70}$$

The first moment (mean molecular weight) and the second moment of distribution (width of the distribution) for a single component at the droplet surface can be written as;

$$\theta_{jR} = \alpha_{Vj}\left(\frac{\beta_{Lj}}{1-C_2\beta_{Lj}}\right)+\gamma_{Vj} \tag{71}$$

And,

$$\sigma_{jR}^2 = \alpha_{Vj}\left(\frac{\beta_{Lj}}{1-C_2\beta_{Lj}}\right)^2 \tag{72}$$

4.6 Energy Balance Equation

The energy equation of a continuous mixture is given by assuming quasi-steady evaporation as given in [111];

$$cv * C_{pV}\frac{\partial T}{\partial r} = \frac{\lambda}{r^2}\frac{\partial}{\partial r}\left(r^2\frac{\partial T}{\partial r}\right) \tag{73}$$

The vapour phase energy equation is solved to give heat transfer to the droplet as [22];

$$q = \left(\frac{Nu_o\lambda\ln(1+B_{TH})}{2RB_{TH}}\right)(T_\infty - T_R) \tag{74}$$

Where,

$$B_{TH} = \exp\left(\frac{2NC_{pV}}{\lambda Nu_o}\right)-1 \tag{75}$$

In the above equation, C_{pV} is the specific heat of the vapour phase, which includes fuel vapour and pyrolysis volatile gas. Nu_o is the Nusselt number (Nu_o =2 for stationary droplet).

Hence, the droplet heating rate can be given for uniform liquid temperature as [22];

$$\frac{dT_R}{dt} = \frac{3}{C_{pL} c_L R}(q - Nh_{fg}) \tag{76}$$

Where, q is the conduction heat flux. Radiation heat transfer is neglected here. If substitute $\rho_L = c_L \theta_L$, then the above equation becomes [22];

$$\frac{dT_R}{dt} = \frac{\theta_L A}{m_L C_{pL}}(q - Nh_{fg}) \tag{77}$$

Now, considering the decomposition enthalpy for pyrolysis and the specific heat of polymer formed in the droplet, the rate of change of droplet temperature (T_R) can be given as follows [22];

$$\frac{dT_R}{dt} = \frac{\theta_L A}{(m_L C_{pL} + m_P C_{pP})}(q - Nh_{fg} - N_G h_{dec}) \tag{78}$$

4.7 Summary

The equations for mass transfer from a droplet and heat transfer to a droplet in the hot and pressurised environment are provided in the above section. Equation (78) provides the rate of change of temperature of a droplet due to the combined effect of the evaporation and the pyrolysis. Three types of mass transfer processes (evaporation, cracking and polymerisation) are illustrated. The rate of cracking and the rate of polymerisation are given by equations (37) and (38) respectively, while the rate of evaporation can be given as [22] ;

$$\frac{dm_{Vj}}{dt} = -N\xi_j A\theta_{jR} \tag{79}$$

The evaporation rate of a single component is given by the evaporation mass flux of a component times the surface area of the droplet. Further, depending upon the low-pressure

and the high-pressure model, evaporation mass flux varies. The evaporation mass flux parameters for the low-pressure model and the high-pressure model are given by equations (51) and (71) respectively. All physical properties required for the mass transfer and heat transfer rates are given in the Appendix.

In summary, in the present chapter, a model for the evaporation and pyrolysis of a single heavy fuel oil into the high pressure and temperature environment is developed with two different VLE approaches and Baert's chemical kinetics pyrolysis model. The models are derived with special emphasis on the fuel compositions and how they change with droplet lifetime. The results of the present developed models are shown in the next chapter (Chapter 5). Also in Chapter 5, the pyrolysis model is modified to reflect alternative values for kinetics constants. Further potential of the model developed in the present chapter is comprehensively shown in Chapter 6 and 7, where calculations for burning spray of heavy fuel oil (HFO) are executed.

Chapter 5. Results and Discussions of Evaporation and Pyrolysis Models for a Single Droplet

5.1 Introduction

In the previous chapter, theoretical studies related to the evaporation and pyrolysis models for a single droplet are described. The present chapter provides results of these developed models and modification of the pyrolysis model to match the experimental results. To illustrate the models, sample calculations are presented for 100-micron and 30-micron diameter stationary droplets of HFO. The initial temperature (T_{L0}) of a droplet is 400 K and it is exposed to surrounding temperature (T_{∞}) and pressure (P_{∞}). For the present calculations, the required parameters of fuel composition for continuous thermodynamics are as given in Table 4-1. This fuel composition is representative only. This was chosen because it allowed the features and abilities of the present developed model, to be demonstrated.

The present models have some initial and boundary conditions. The Ordinary Differential Equations (ODE) in these models are solved using the Fourth Order Runge-Kutta method [161] with variable interval size and accuracy level up to 10^{-5}. The Fourth Order Runge-Kutta method uses more points in the interval (time step) than the simple predictor-corrector method (Euler's method) to predict the next time step. It improves the quality of the solution of ordinary differential equations [161]. Thus, it is the default choice for many researchers; such as Baert [14], Zhu & Reitz [75] etc.

5.2 Low-Pressure Evaporation Model along with Baert's Pyrolysis Model

5.2.1 100-micron droplet

As the liquid droplet enters into hot ambient surroundings, heat transfer between the droplet and the hot ambient surroundings occurs. Consequently, the droplet warms up and

starts losing mass into the surroundings through different processes of mass transfer. The mass history of a 100-micron droplet expressed as fractions of initial droplet mass is shown in Figure 5-1. As shown in Figure 5-1, when a 100-micron single stationary droplet is exposed to 1200 K ambient temperature and at 1 atmospheric pressure, it evaporates and produces vapour. Alternatively, those high molecular weight hydrocarbons in a droplet which cannot evaporate, pyrolise due to high liquid (droplet) temperature. Pyrolysis produces volatile gases and polymers through thermal cracking and polymerisation respectively. Here, as shown in Figure 5-1 around 30% of the initial mass of a droplet produces vapour and the rest becomes volatile pyrolysis gas and polymer. All vapour is mainly produced from the pure hydrocarbons; components 1, 2 and 3, which represent 30% of the initial droplet mass (refer to Table 4-1 for details), whereas, the residue evaporates very little. However, the volatile pyrolysis gas and the polymer are produced from the residual portion of the HFO. Formed polymer remains in the droplet until it burns through surface oxidation (which is not modelled in the present chapter) therefore the mass of the droplet shown in Figure 5-1 includes polymer. The evaporation of light constituents is completed before the temperature of the droplet reaches 800 K. This result concurs with a remark made by Baert [14] that most of the paraffins and naphthenes in HFO evaporate off before 790 K. Moreover, one thing to be noted from Figure 5-1 is that the amount of polymer at the end of the droplet lifetime is a little less than that produced during pyrolysis (see at 0.1 s). The reason for this is that the formed polymer also partially decomposes (cracks) at high temperature by means of thermal cracking and produces volatile gas [22].

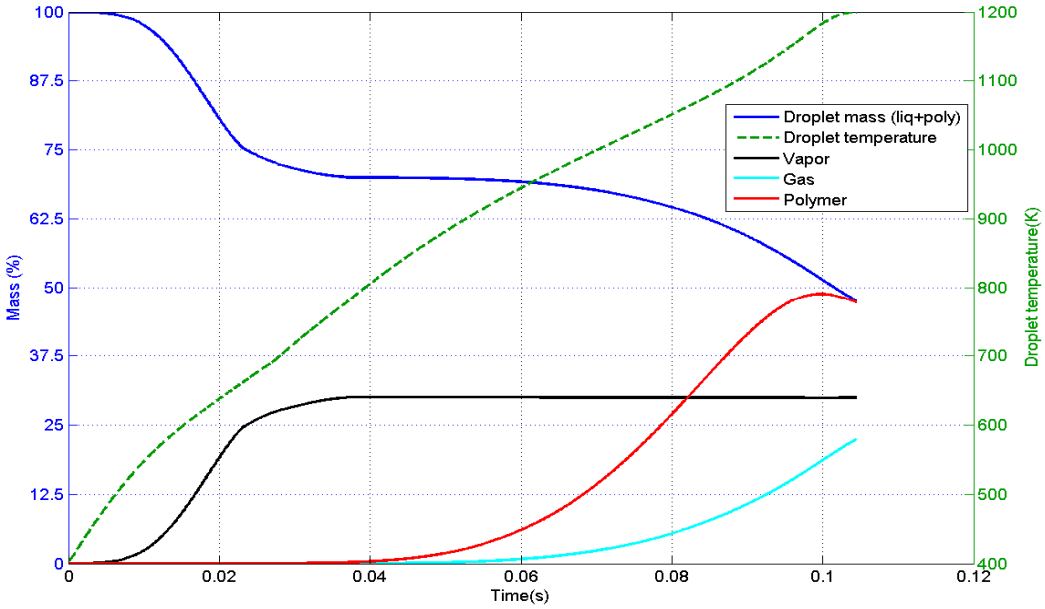

Figure 5-1: Predicted mass percentage history of a 100-micron HFO droplet along with the droplet temperature for the low-pressure evaporation and Baert's pyrolysis models (Ambient condition: T_∞ = 1200 K and P_∞ = 1 atm).

In the previous figure mass percentage history of a 100-micron droplet and its products are shown. A complete and detailed mass balance of the same droplet is shown in Figure 5-2. Figure 5-2 shows the total amount of vapour, total amount of polymer and the total amount of gas produced. The gas produced by the cracking of original liquid residue and by the cracking of polymer is shown separately. The initial mass of a 100-micron spherical droplet is given as;

$$\rho \cdot (4/3)\pi R^3 = 995.29 \cdot (4/3)\pi (50\times10^{-6})^3 = 5.2111\times10^{-10}\ \text{kg}$$

The total amount of vapour produced is 1.5632×10^{-10} kg which is around 30% of the droplet initial mass. The total amount of polymer produced is 2.4604×10^{-10} kg which is around 47.2% of the droplet initial mass. The total amount of gas produced by pyrolysis is 1.1668×10^{-10} kg which is the summation of gas produced by cracking of original liquid (0.4098×10^{-10} kg) and of polymer (0.7569×10^{-10} kg). The total amount of gas produced by pyrolysis is around 22.4% of the droplet initial mass. Of this 22.4% gas, the major contribution, around 14.5% of the droplet initial mass is of the cracking of formed polymer, and only 7.9% is of the cracking of liquid. Hence, cracking of polymer is also important because it plays a major role during pyrolysis.

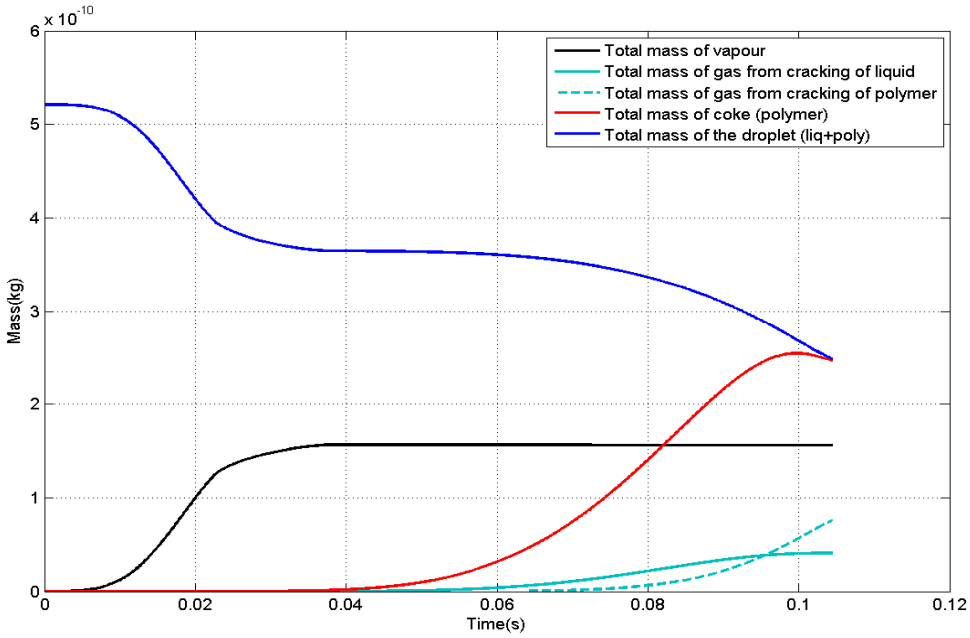

Figure 5-2: Mass balance of a 100-micron HFO droplet for the low-pressure evaporation and Baert's pyrolysis models (Ambient condition: T_∞ = 1200 K and P_∞ = 1 atm).

The mean molecular weight histories of all four components of a 100-micron HFO droplet along with the droplet temperature are shown in Figure 5-3. As shown in Figure 5-3, the mean molecular weight (θ_{Lj}) of pure hydrocarbons (n-paraffins, aromatics and naphthenes) increases and their standard deviation (σ_{Lj}) decreases (not shown in figure). The reason behind this is that the low molecular weight species from the components evaporate early from the droplet while heavy molecular weight species evaporate late. In other words, pure hydrocarbon component's species are evaporating in order of their volatility. This means that evaporation shown here favours the fractional distillation of the light and more volatile hydrocarbons. The mean molecular weight of the residue remains almost unchanged because it evaporates very little during evaporation and later on during pyrolysis it is assumed constant. The present modelling results accord with experimental results given by Ikegami et al.[23] for HFO, which show preferential distillation like evaporation mechanism of the light components from HFO droplet. It is clearly observed from Figure 5-3 that evaporation of all light hydrocarbons (n-paraffins, aromatics and naphthenes) finishes before the temperature of the droplet reaches 800 K. Here, diffusivities of the various pure hydrocarbons in air are in the order of 10^{-8} to 10^{-9} m^2/s [22].

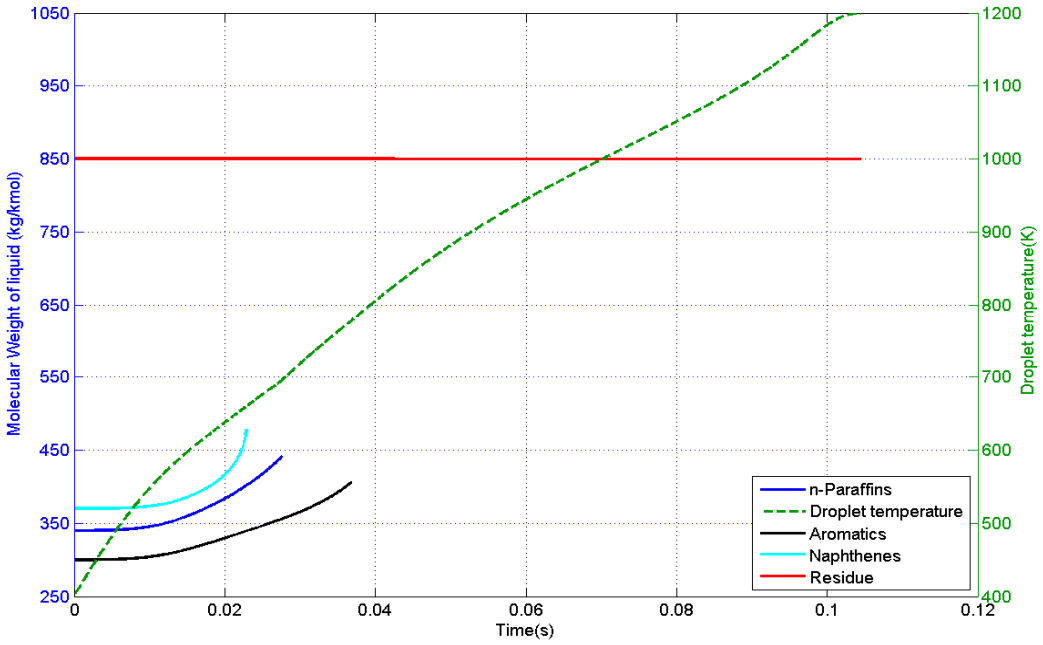

Figure 5-3: The mean molecular weights of all four components of a 100-micron HFO droplet along with the droplet temperature for the low-pressure evaporation and Baert's pyrolysis models (Ambient condition: T_∞ = 1200 K and P_∞ = 1 atm).

Furthermore, Figure 5-3 shows the history of the liquid temperature (T_R). The temperature of the liquid steadily increases with the lifetime of the droplet. In the present case, the droplet may have acquired equilibrium temperature as soon as it completes evaporation, which can be observed from the results of the multicomponent evaporation modelling of Abraham & Givler [162]. However, in the present modelling, the droplet energy balance model is developed with a high accuracy, which included the effect of pyrolysis along with the evaporation process. The present developed energy balance model includes the enthalpy of decomposition and the specific heat of formed polymer in the calculation of droplet temperature. These properties of pyrolysis products allowed accurate prediction of the droplet temperature. Because of this, the liquid temperature steadily increases with time which coincides with the observations of Shyu et al.[36]. Chen & EI-Wakil's experimental observation [31] also confirms that droplet temperature increases linearly with time. In the present study, the enthalpy of decomposition is taken from Baert [14] as $4.589*10^8$ J/kmol ($790*10^8$ kJ/kg). The liquid temperature equation (78) also requires the specific heat of polymer formed due to pyrolysis which was determined as suggested by Merrick [163].

Figure 5-4 shows normalised droplet surface area (normalised square of droplet diameter) and aromaticity of the residue, plotted against droplet lifetime. During the initial period (from 0 to 0.04 sec) of the droplet's lifetime, the normalised square of a droplet diameter decreases very fast due to preferential evaporation of the most volatile components. Later on, it continues to decrease as the pyrolysis of the liquid progresses. As evaporation of the light components from the liquid finishes, the overall rate of evaporation and pyrolysis progresses slowly. The formed polymer remains in the droplet. Therefore, normalised droplet surface area at the end of pyrolysis does not go to zero completely. The linear d^2 behaviour is not reproduced here for a single heavy fuel oil droplet. This type of non-linear d^2 behaviour is expected for the heavy fuel oil droplets as they go through pyrolysis during the combustion [11].

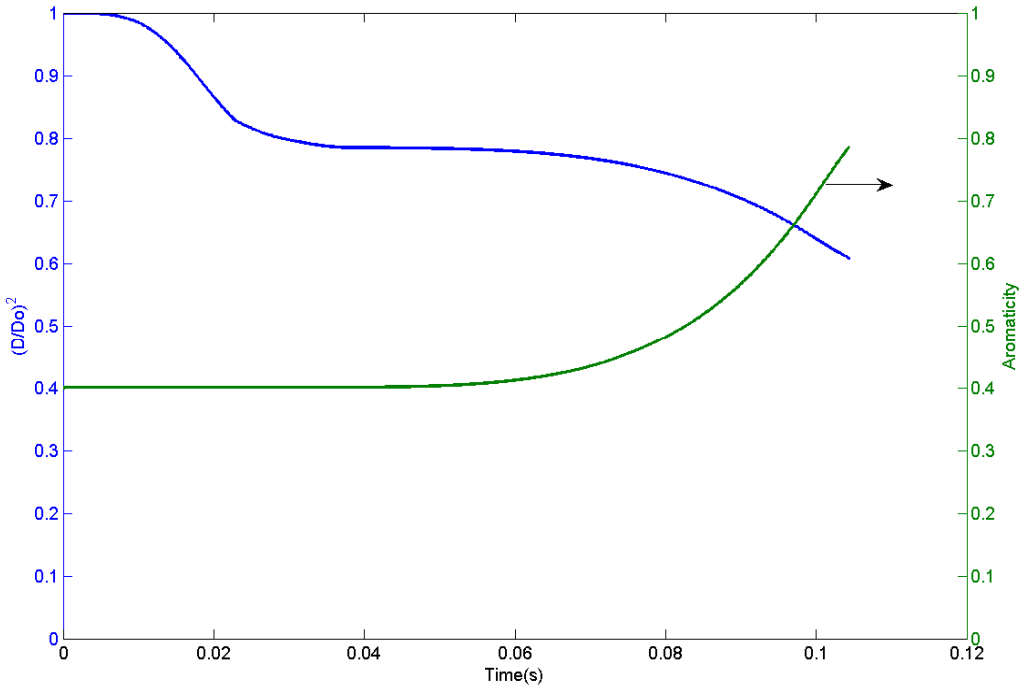

Figure 5-4: Predicted normalised droplet surface area and aromaticity of a 100-micron HFO droplet for the low-pressure evaporation and Baert's pyrolysis models (Ambient condition: T_∞ = 1200 K and P_∞ = 1 atm).

Furthermore, the modelled aromaticity of the heaviest component (residue) is shown in Figure 5-4. As the non-aromatic molecules leave the liquid phase (droplet) through thermal cracking, they leave the aromatic molecules behind, thus the concentration of the aromatic molecules increases within the droplet. Therefore, the aromaticity which

provides the concentration of aromatic molecules, increases as pyrolysis progresses. The initial aromaticity of the residue is 0.4 but increases mainly due to the thermal cracking.

Liquid phase composition is given in Figure 5-5 where mole fractions of the components in the droplet are plotted as a function of droplet lifetime. Mole fractions of the pure hydrocarbons in the droplet decrease as they evaporate. At the same time, the mole fraction of the residue increases to 1 because it is the only component remaining in the droplet. The mole fraction of residue shown here includes the mole fraction of polymer too.

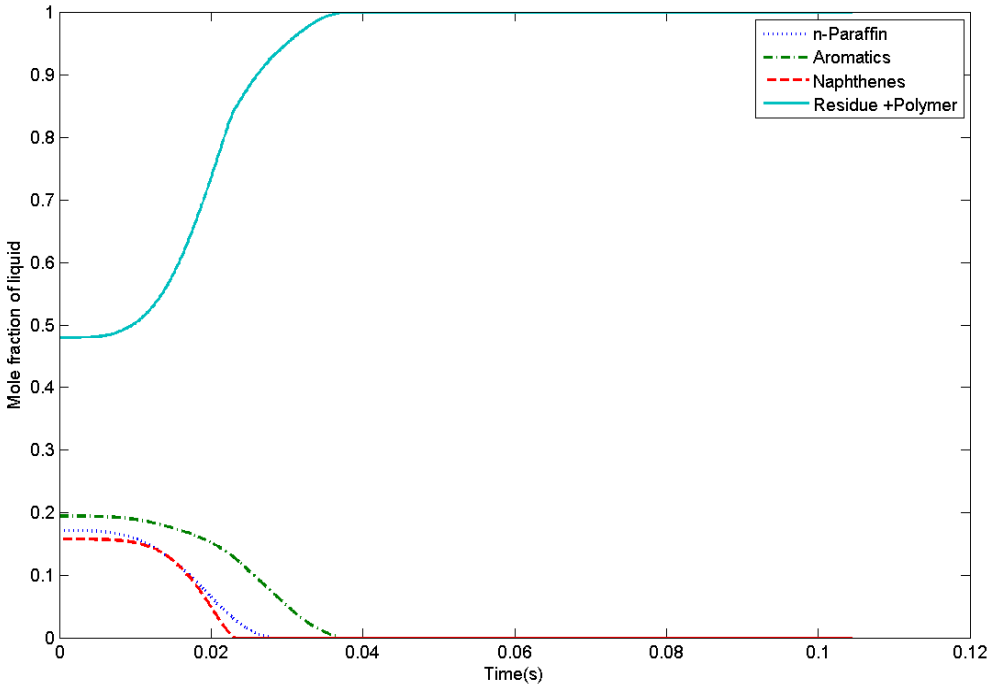

Figure 5-5: Predicted liquid mole fractions of components of a 100-micron HFO droplet for the low-pressure evaporation and Baert's pyrolysis models (Ambient condition: T_∞ = 1200 K and P_∞ = 1 atm).

The present model also calculates the bubble point and the critical temperature of the pure hydrocarbons of an HFO droplet at atmospheric pressure as given in Figure 5-6. The bubble point of any component of the HFO mixture can be obtained by setting the vapour pressure of the component equal to 1 atm and solving equation (50) for temperature T_R. In other words, setting the vapour phase mole fraction (y_{FjR}) equal to unity, and solving the

equation (50) for temperature T_R, gives the bubble point of that component, as shown in the Appendix. Critical temperatures used in the calculation of evaporation enthalpies are also shown in Figure 5-6. Moreover, the reference temperature of the air-vapour mixture is shown in Figure 5-6, which is used to calculate the majority of the properties of the vapour phase. The bubble point and critical temperature continuously increase with droplet lifetime due to fractional distillation of the components.

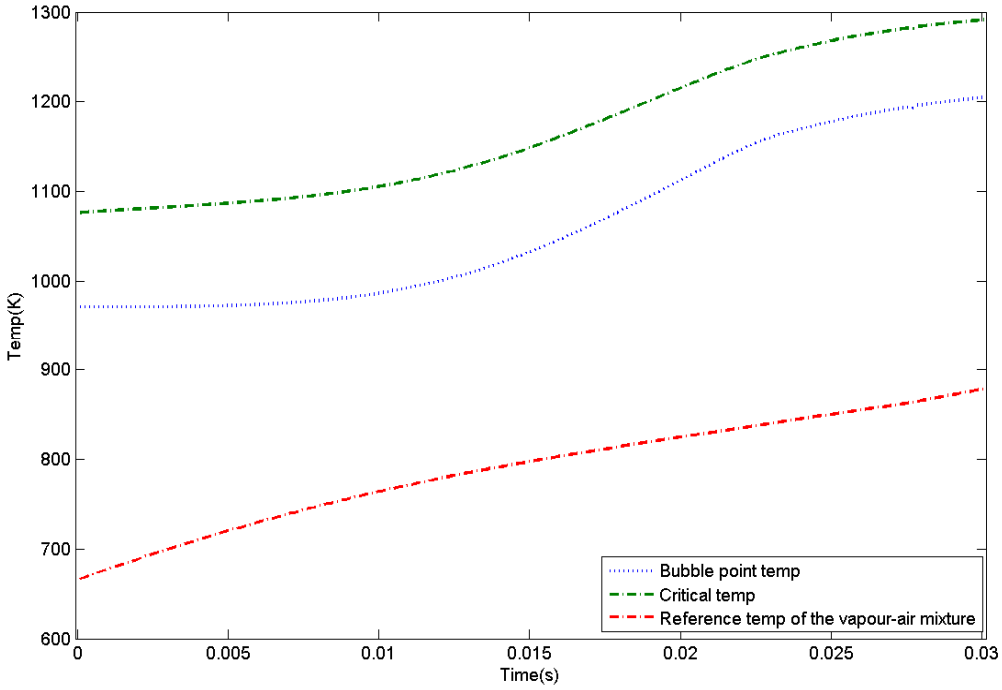

Figure 5-6: Predicted bubble point and critical temperature history of a 100-micron HFO droplet for the low-pressure evaporation and Baert's pyrolysis models (Ambient condition: T_∞ = 1200 K and P_∞ = 1 atm).

It is observed during calculations that when the same size (100-micron) droplet is exposed to a higher temperature field (1700 K), its product composition history is different. The maximum difference observed is in the pyrolysis products. As shown in Figure 5-7, the amount of polymer formation is a little higher than that found at 1200 K. In other words, the total amount polymer in the present case is 51.5% of the droplet initial mass, which is 4.3% higher than that found at 1200 K. At the same time, volatile pyrolysis gas production is reduced. As expected, as the ambient temperature increases at constant pressure, the evaporation rate and the pyrolysis rate are significantly increased and at the same time the droplet lifetime decreases (0.0427 sec compared to 0.104 sec). The reduced duration of the

liquid phase decrease with the increase in ambient temperature conforms with the experimental results obtained by Xu et al.[149], and is expected.

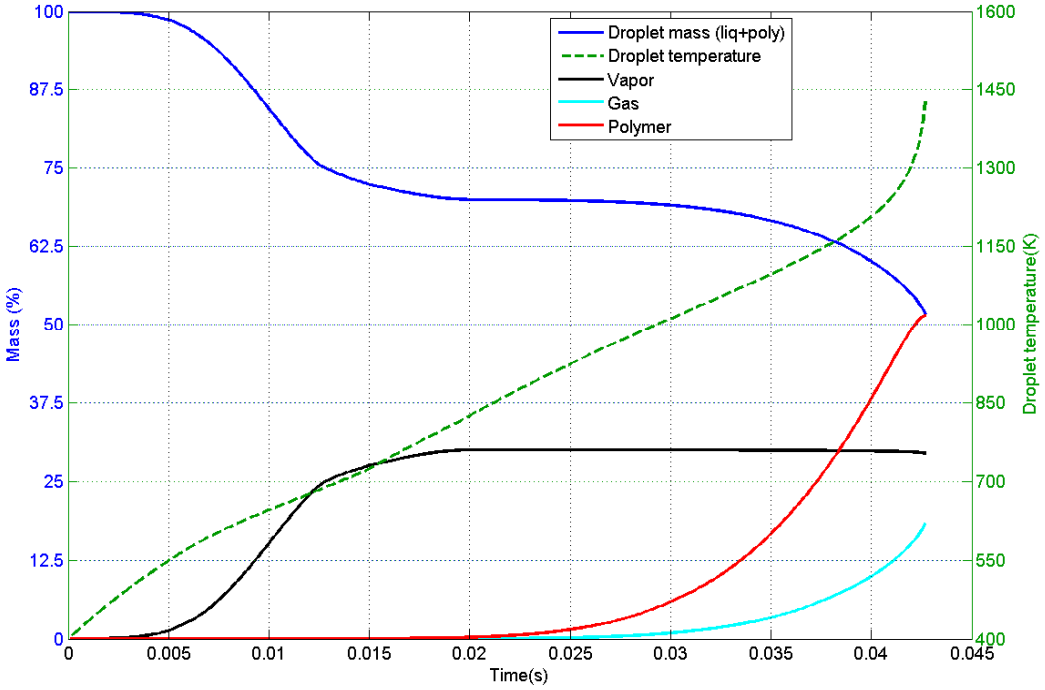

Figure 5-7: Predicted mass percentage history of a 100-micron HFO droplet along with the droplet temperature for the low-pressure evaporation and Baert's pyrolysis models (Ambient condition: T_∞ = 1700 K and P_∞ = 1 atm).

The pyrolysis model used above shows that polymer formation is a function of droplet heating rate for a 100-micron droplet. In actual engine spray combustion generally droplets are small [2] and heating rates are very high due to combustion. Therefore, Baert's pyrolysis model used in the present calculation needs to be studied in detailed for a small droplet (such as 30-micron). A smaller droplet has a smaller surface area and thus has a higher heating rate than, a bigger droplet. The sensitivity study of polymer formation for a 30-micron droplet is given in the next section.

5.2.2 30-micron droplet

To study the sensitivity of the present developed pyrolysis model using Baert's chemical kinetics, two simulations are presented; the first one is the 30-micron droplet exposed to 1200 K and the other one is the same size of droplet but exposed to a higher temperature

of 1700 K. Results of these sensitivity tests are presented in Figure 5-8 and Figure 5-9 respectively.

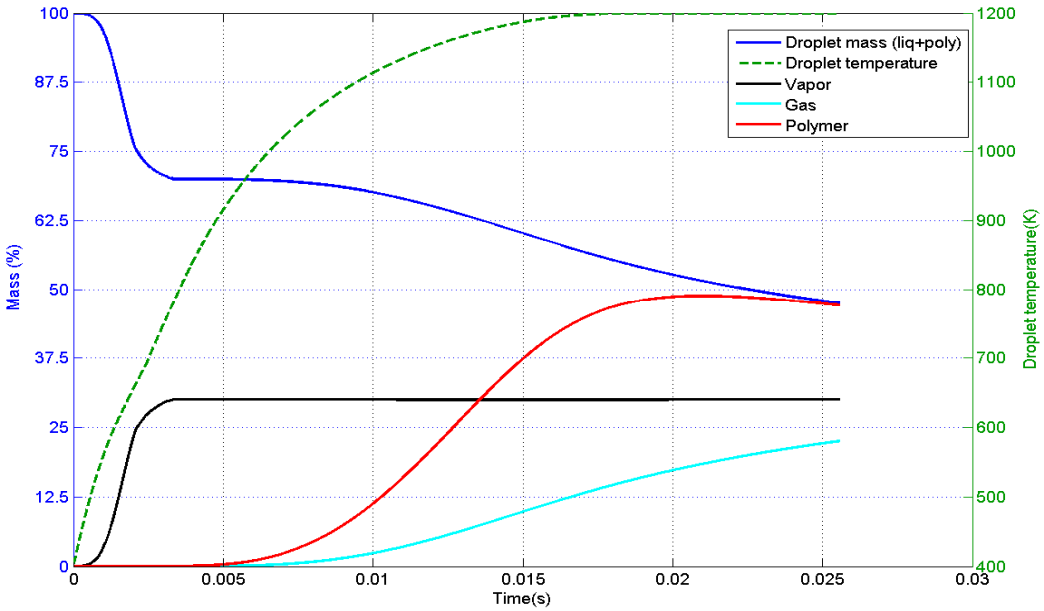

Figure 5-8: Predicted mass percentage history of a 30-micron HFO droplet along with the droplet temperature for the low-pressure evaporation and Baert's pyrolysis models (Ambient condition: T_∞ = 1200 K and P_∞ = 1 atm).

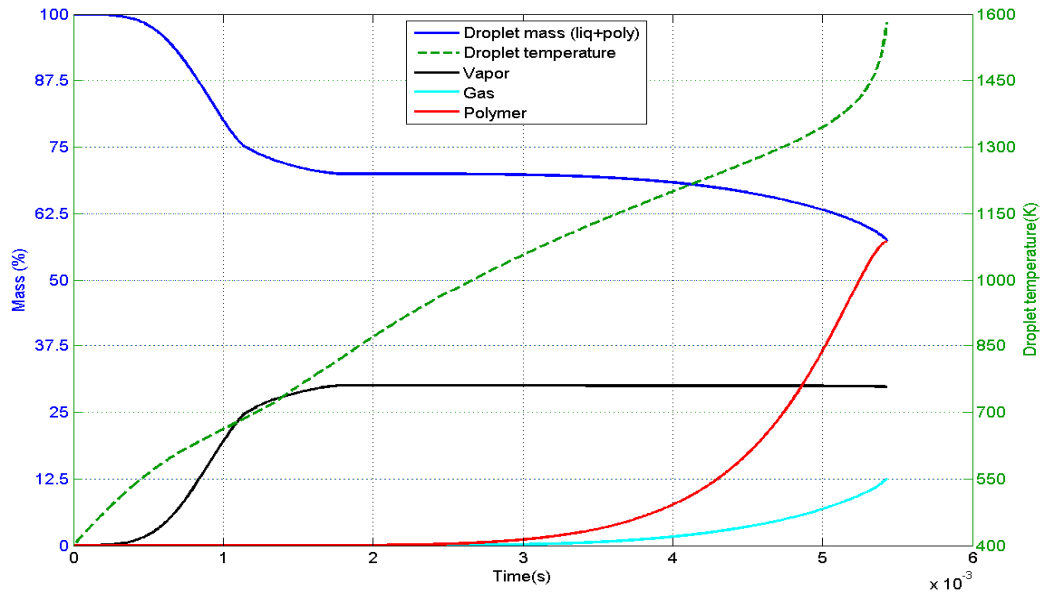

Figure 5-9: Predicted mass percentage history of a 30-micron HFO droplet along with the droplet temperature for the low-pressure evaporation and Baert's pyrolysis models (Ambient condition: T_∞ = 1700 K and P_∞ = 1 atm).

By comparing Figure 5-8 with Figure 5-1, it can be observed that when 30-micron and 100-micron droplets are exposed to 1200 K, their polymer percentages are around 47%. However, when they (30-micron and 100-micron droplets) are exposed to a higher temperature (1700 K), their polymer percentages are 57.2% and 51.5% respectively. In other words, at 1700K, the amount of polymer formation for a 30-micron droplet is 10.2% higher than at 1200 K. This means that polymer formation is sensitive to the droplet heating rate which is a function of ambient temperature and droplet surface area. This result concurs with the findings of Morrone et al.[38] that pyrolysis rate is exponentially dependent on droplet temperature and substantial changes in droplet heating rate affects the coke formation.

At a high ambient temperature or heating rate, an individual HFO droplet produces more polymers than low heating rate. The likely reason for the low amount of polymer produced at a low ambient temperature is the thermal cracking of the produced polymer. When there is a slow heating rate (high droplet lifetime), it actually allows more time for the polymer to crack into low molecular weight volatile gas. Thus, volatile gas production increases with decreasing heating rate of an HFO droplet. The formation of polymer and volatile gas is a function of heating time and droplet temperature.

Up to now only the low-pressure evaporation model is used, however, the high-pressure evaporation model may affect the droplet heating rate and ultimately the polymer formation. A one more reason to study the high-pressure model is to inspect the evaporation of heavy component. A study using the high-pressure evaporation model along with Baert's pyrolysis model for 100-micron and 30-micron droplets is given in the next section.

5.3 High-Pressure Evaporation Model along with Baert's Pyrolysis Model

5.3.1 100-micron droplet

The high-pressure vapour-liquid equilibrium model derived in section 4.5.2 is applied to a single HFO droplet along with Baert's pyrolysis model. First, normalised droplet surface

area against time obtained at 1 atmosphere pressure for both models (low and high-pressure) is shown in Figure 5-10. During this calculation, the interaction coefficients (k_{II^+} and k_{Ij}) are taken as zero. In other words, there is no interaction between air and fuel, and no interaction between individual fractions of liquid fuels either. The initial temperature of the droplet is 400 K and it is exposed to a surroundings temperature of 1200 K.

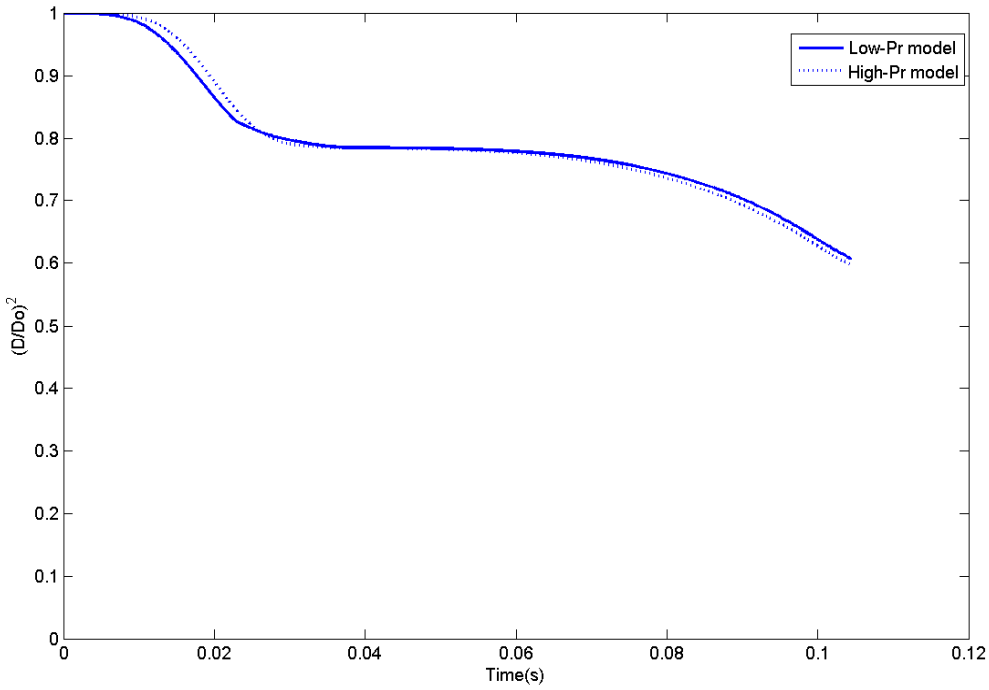

Figure 5-10: Predicted normalised droplet surface area against time of a 100-micron HFO droplet using the low and high-pressure evaporation models along with Baert's pyrolysis model at 1 atm pressure without interaction coefficients (Ambient condition: T_∞ = 1200 K and P_∞ = 1 atm).

As shown in Figure 5-10, the result for the normalised square of droplet diameter (surface area) against droplet lifetime shows low-pressure and high-pressure models differ only slightly at low ambient pressure (1 atm). Even when the comparison is made at 50 atm pressure (Figure 5-11) there is not much difference found in their evaporation rate, and similar results to 1 atm pressure are obtained. Droplet lifetime is dependent on evaporation rate plus pyrolysis rate. Since there is not much difference in the early evaporation rates, the droplet life history remains similar for the rest of its life, in both models.

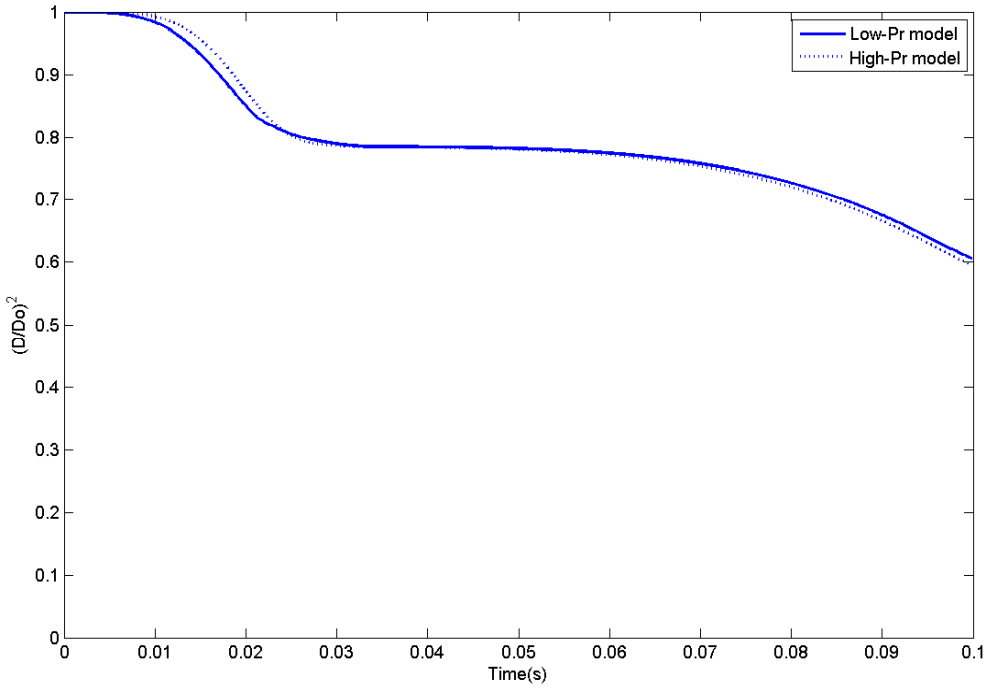

Figure 5-11: Predicted normalised droplet surface area against time of a 100-micron HFO droplet using the low and high-pressure evaporation models along with Baert's pyrolysis model at 50 atm pressure without interaction coefficients (Ambient condition: T_∞ = 1200 K and P_∞ = 50 atm).

The above results (Figure 5-10 and Figure 5-11) are obtained without any interaction parameters in equation (63), which means k_{II^+} and k_{Ij} are zero. However, Coutinho et al.[164] mentioned that at least one non-zero interaction coefficient is required to correct the phase behaviour of liquid at high pressure. These interaction coefficients provide the actual correction between EOS prediction and experimental data. Generally, interaction coefficients are derived from the experimental data. Senda et al.[165] pointed out that there are more than 200 different components existing in normal diesel or gasoline fuel and to measure their interaction coefficient is virtually impossible. The values of k_{II^+} for the interaction of individual components of HFO are not found in the literature. However, the values of k_{Ij} are found in Avlonitis et al.[166] for the interaction coefficients of nitrogen-hydrocarbon binary mixtures ranging from 0.0 to 0.3. Moreover, values of k_{II^+} for a simple polar and nonpolar mixture in Poling et al.[167] is recommended as 0.1. Therefore, in subsequent calculations these parameters are assumed as $k_{II^+} = 0.1$ and $k_{Ij} = 0.2$, and results obtained are discussed in the following section.

As noticed from Figure 5-12, when interaction between individual components of the liquid and also the interaction between liquid and gas are employed, noticeable difference in evaporation rate is observed. The evaporation rate predicted by low-pressure model is less than is predicted by high-pressure model. In other words, it is observed here that when interaction between the individual components and the interaction between components and air is applied, the overall evaporation rate found is higher than predicted by the low-pressure model. This result agrees with the observation made by Yu et al.[168] that the low-pressure model under predicts the actual evaporation rates at higher pressure. Hence, interaction coefficients for multicomponent mixture play an important role for the evaporation rate of individual volatile components.

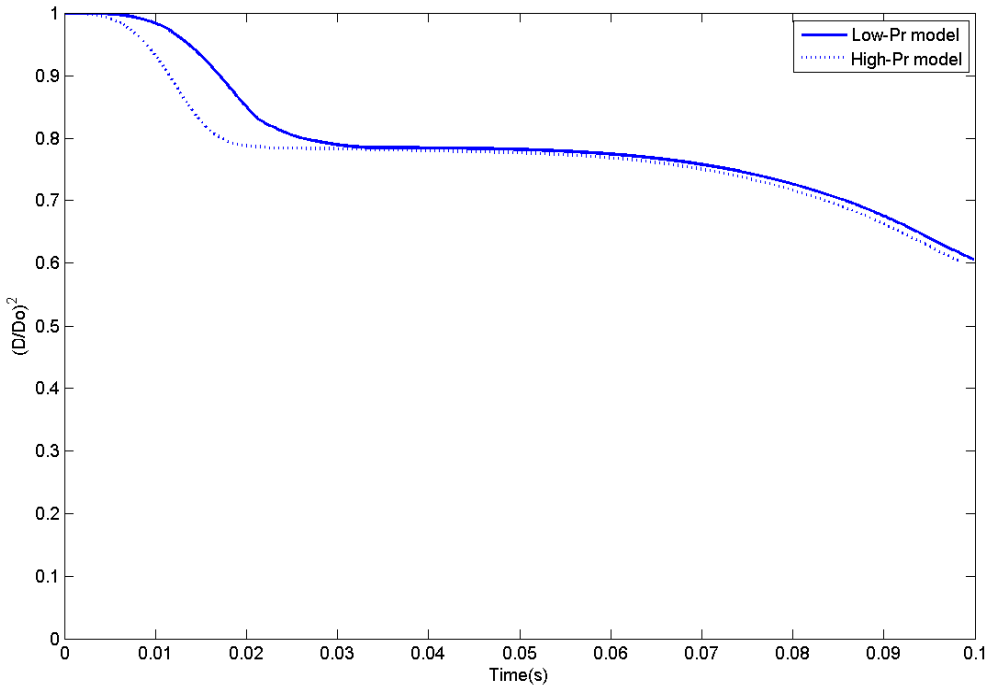

Figure 5-12: Predicted normalised droplet surface area against time of a 100-micron HFO droplet using the low and high-pressure evaporation models along with Baert's pyrolysis model at 50 atm pressure with interaction coefficients for the high-pressure model (Ambient condition: T_∞ = 1200 K and P_∞ = 50 atm).

The normalised surface area with droplet lifetime at two different ambient pressures (1 atm and 50 atm) using the high-pressure evaporation model with interaction coefficients are compared in Figure 5-13. It is clearly observed that the normalised surface area of the droplet is a function of surroundings pressure. It means that at the same ambient temperature, droplet lifetime decreases with increasing ambient pressure; hence at high

pressures droplets evaporate more quickly. Rocco [74] observed a similar result that, when ambient pressure increased while keeping temperature constant, the droplet lifetime decreases. The effect of ambient pressure on the pyrolysis model is not accounted for in the present study.

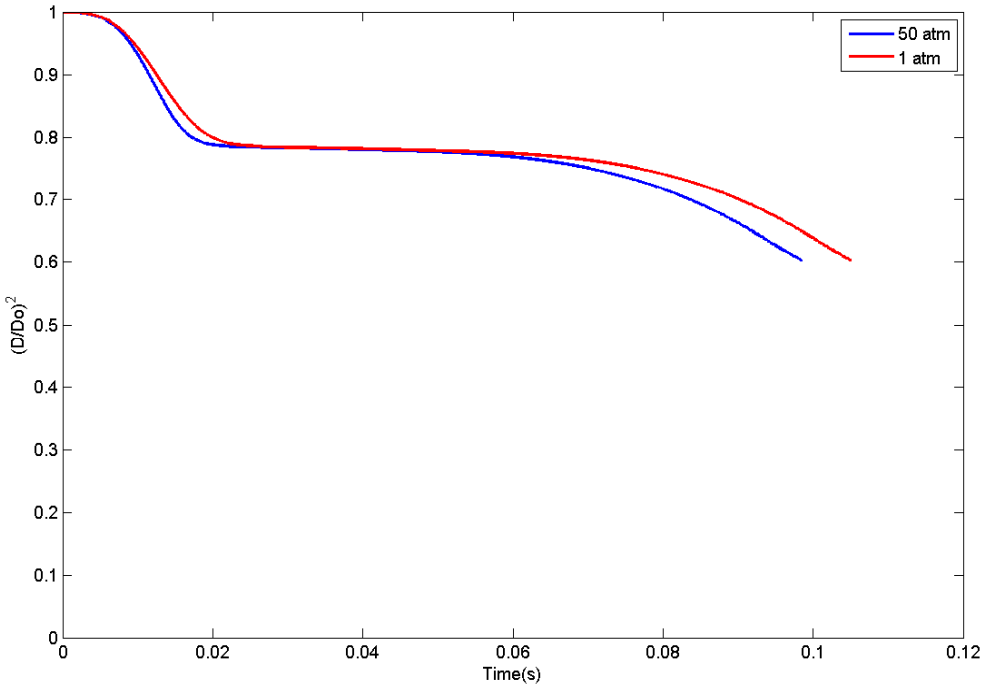

Figure 5-13: Predicted normalised droplet surface area history of a 100-micron HFO droplet at two different ambient pressures using the high-pressure and Baert's pyrolysis models with interaction coefficients (Ambient condition: T_∞ = 1200 K)

Moreover, as stated by Abraham & Magi [66], for a single component droplet it is expected that the square of the normalised droplet diameter will linearly decrease with time, while the same behaviour is not recovered for the multicomponent fuels. The present result confirms Abraham & Magi's remarks. It is also found from the comparison at different pressures that the gap between droplet surface areas is narrow at the initial stage but it becomes wider with time. The reason behind this is that the pyrolysis process in the present model is a function of droplet temperature and as the droplet depletes more mass through early evaporation, the droplet becomes smaller and heat transferred to the droplet per unit volume occurs at a faster rate. Consequently, the droplet acquires a high temperature in a shorter period of time. Therefore, pyrolysis also occurs at a quicker rate at high pressure than at low pressure.

It should be also noted here that when the heating rate is high, as shown in the previous section, an individual droplet should produce more polymer and less gas. This formed polymer remains in the droplet therefore it should lead to bigger droplet diameter and thus the droplet should have a bigger surface area. However, that is not reproduced in the present case and the reason behind this is, at 1200 K polymer formation is not very sensitive to the heating rate. Therefore, at 1200 K, a big (100-micron) or small (30-micron) droplet produce almost similar amount of polymer. Hence, the normalised droplet surface area at the end of the droplet lifetime, shown in Figure 5-13 appears similar.

Figure 5-14 presents the evaporating molar flux of the individual components of a 100-micron HFO droplet at the surface at 50 atm pressure and 1200 K for the high-pressure evaporation model using interaction coefficients. As clearly observed from the figure, the evaporation rates (molar flux) are very slow at the initial stages but with time they increase and reach to a maximum before the evaporation of components is completed. The evaporation rates of light components (n-paraffins, aromatics and naphthenes) are significantly larger than residue. Residue evaporates very little due to its high molecular weight and low volatility.

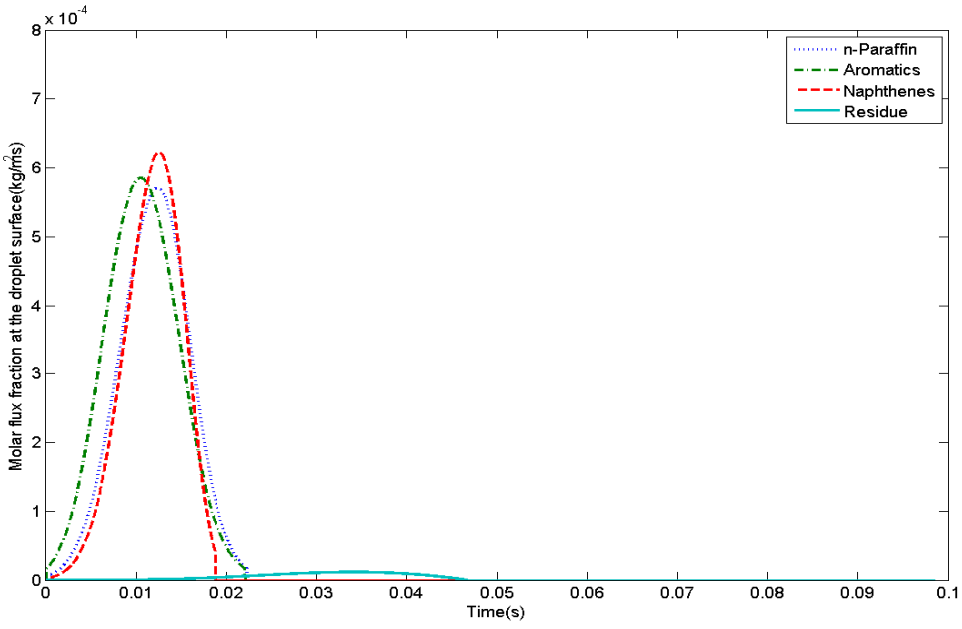

Figure 5-14: Predicted evaporating molar flux of the individual components of a 100-micron HFO droplet at the surface for the high-pressure evaporation and Baert's pyrolysis models using interaction coefficients (Ambient condition: T_∞ = 1200 K and P_∞ = 50 atm).

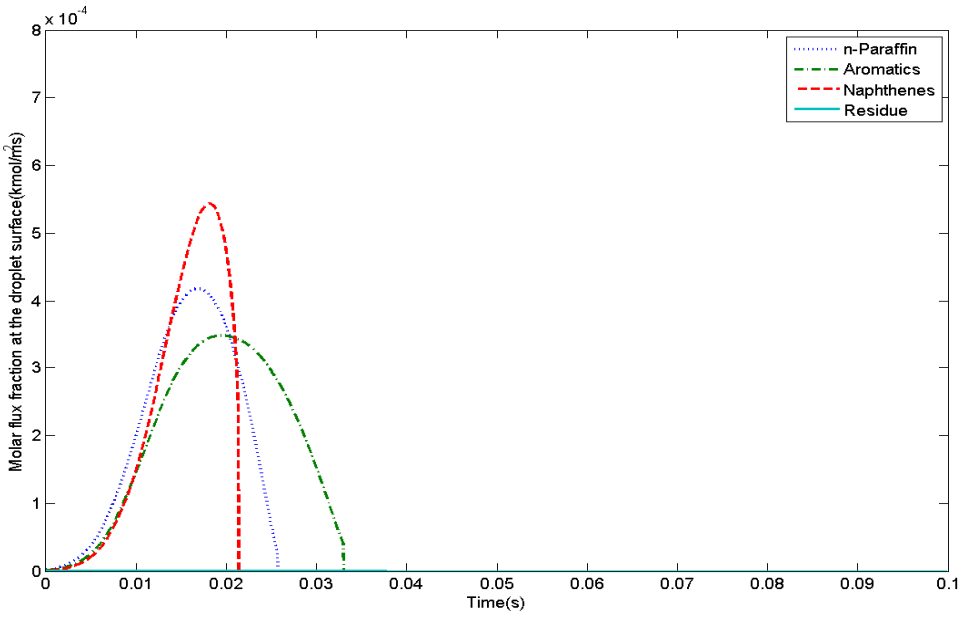

Figure 5-15: Predicted evaporating molar flux of the individual components of a 100-micron HFO droplet at the surface for the low-pressure evaporation and Baert's pyrolysis models (Ambient condition: T_{∞} = 1200 K and P_{∞} = 50 atm).

The low-pressure and the high-pressure evaporation model can also be compared by comparing Figure 5-14 and Figure 5-15. Both these figures are produced under the same ambient condition but with different VLE approaches. It is clearly seen that the predicted molar fluxes of all individual fractions using the high-pressure model (see Figure 5-14) are higher than using the low-pressure model (see Figure 5-15). Especially, the molar flux of component four (residue) observed using the low-pressure evaporation model is very low (almost negligible), while the same molar flux for the same component observed using the high-pressure evaporation model is a bit higher. This means evaporation of the residue occurs to a certain extent in the high-pressure evaporation model. The reason behind this higher molar flux of the residue could be due to interaction of high volatile components with the residue, assisting in the evaporation of the low volatile component, or otherwise it could be due to interaction of the residue with air. In the literature, the assistance effect of the individual high volatile components on the low volatile component during the evaporation is not found. However, in general terms Senda et al.[165] reported similar results for the evaporation of multicomponent fuel. They noted that the distillation temperature range of blended multicomponent fuel becomes narrow, owing to the formation of a 2-phase region between the lowest boiling temperature and highest boiling temperature. In other words, in blended multicomponent fuel, the boiling point of the least

volatile component decreases while the boiling point of the most volatile component increases.

Furthermore, in the present case the cutter stock (light hydrocarbons) is only 30% of the initial droplet mass and still the effect of interaction coefficients of cutter stock on the residue and within cutter stock components itself is noticeable. This effect could be more dominant in fuels where concentrations of light hydrocarbons are high.

Figure 5-16 shows the continuous change in the mean molecular weight of a 100-micron HFO droplet at 50 atm pressure and 1200 K ambient temperature. In Figure 5-16, the solid lines represent the liquid phase composition change, while the dotted lines denote the vapour phase. As the evaporation continues, low molecular weight and more volatile species from the individual components start depleting from the liquid phase, which leaves heavy molecular weight and less volatile species in the liquid phase. Consequently, the mean molecular weight of the liquid increases continuously with time, which can be seen from the above figure for n-paraffins, aromatics and naphthenes. A similar event also occurs in the vapour phase as molecules evaporate off from the liquid phase and transfer into vapour phase, the mean molecular weight of vapour phase increases. At one stage which is known as the critical mixing point, all properties including the mean molecular weight of the liquid phase and the vapour phase become identical. At the critical mixing point, the difference between the liquid phase and the vapour phase disappears and consequently they become one united phase.

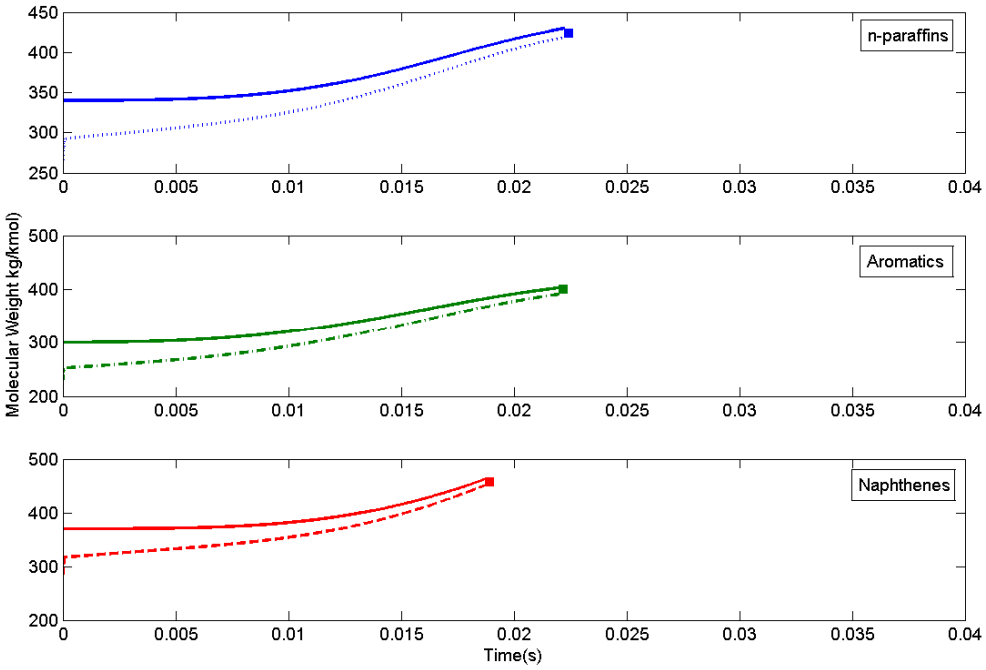

Figure 5-16: Mean molecular weight of the volatile components of a 100-micron HFO droplet in the liquid phase and vapour phase for the high-pressure evaporation model using interaction coefficients along with Baert's pyrolysis model. Where solid lines represent liquid phase, dotted lines represent vapour phase, ▪ -critical mixing point (Ambient condition: T_∞ = 1200 K and P_∞ = 50 atm).

Figure 5-17 shows the overall liquid composition and droplet temperature history of a 100-micron droplet exposed to 1200 K and 50 atm pressure. The light and more volatile components (n-paraffins, aromatics and naphthenes) simultaneously evaporate as the droplet acquires heat from the surroundings. Generally, heat flux to the droplet is divided into two parts; one part is used to increase the temperature of the droplet, while the other part is used for its evaporation enthalpy. As clearly observed from the figure, light components evaporate off before the droplet reaches 800 K. The above result aligns with the discussion by Baert [14] that pure hydrocarbons disappear from liquid phase before 800 K, whereas for pyrolysis to have an effect on droplet lifetime temperature of at least 800 K or more is essential. Figure 5-16 and Figure 5-17 evidently demonstrate that the evaporation mechanism of light components in HFO is the preferential distillation type of evaporation, where volatile components preferentially evaporate in order of their relative volatility. Especially Figure 5-16 illustrates the course of preferential evaporation in terms of the rise in the distribution mean (molecular weight) of the liquid and the vapour phase.

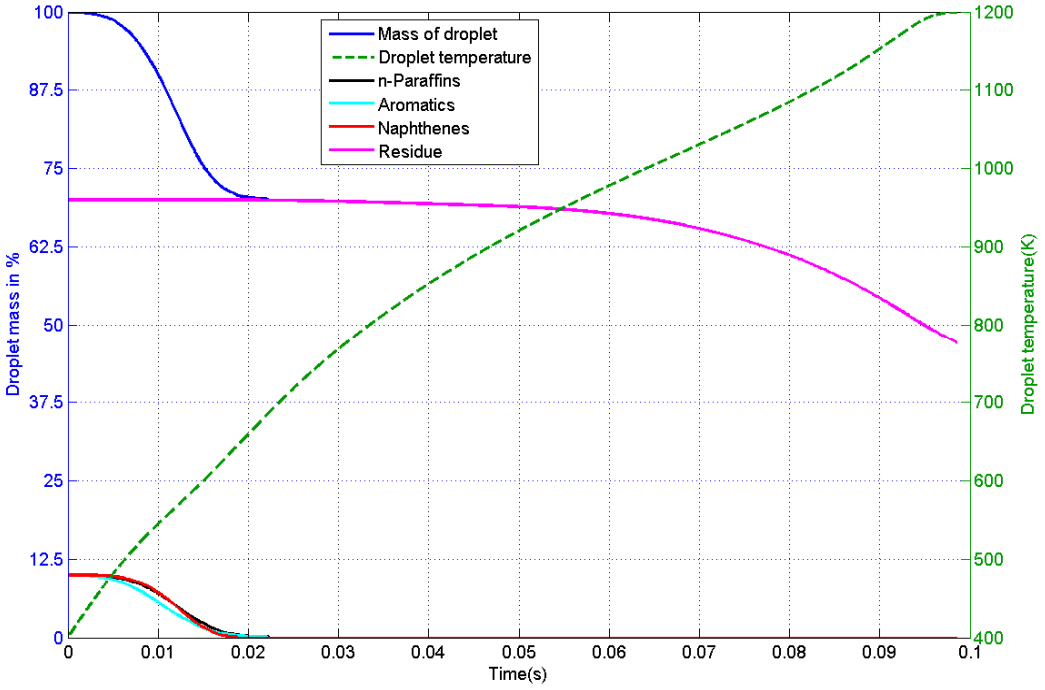

Figure 5-17: Droplet composition expressed as fraction of initial droplet mass and temperature history of a 100-micron HFO droplet for the high-pressure evaporation model using interaction coefficients along with Baert's pyrolysis model (Ambient condition: T_∞ = 1200 K and P_∞ = 50 atm).

Figure 5-18 shows the vapour phase mole fraction of the individual components at the surface of a 100-micron droplet at 50 atm pressure and 1200K, obtained through vapour-liquid equilibrium. Normal paraffins, aromatics and naphthenes evaporate in order of their volatility. As the temperature of the droplet increases, the mole fraction of the vapour phase increases sharply in the early droplet lifetime, and as a result overall evaporation rate increases. As discussed earlier, residue comprises of heavy hydrocarbons and possesses high molecular weight. However, two important outcomes are noted here with using the high-pressure model with interaction coefficients. First, residue evaporates but very late, in other words, evaporation of residue starts almost after the evaporation of paraffins, aromatics and naphthenes is finished. It seems here that evaporation of the residue is assisted by interaction with air. And second, very little amount of residue evaporates.

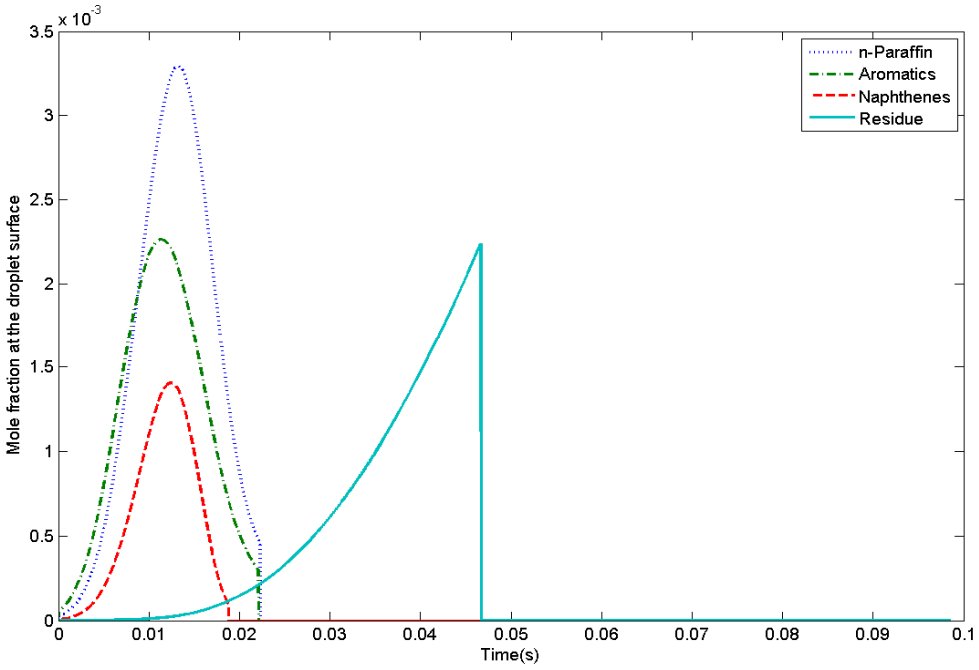

Figure 5-18: Vapour phase mole fraction at the droplet surface of a 100–micron HFO droplet for the high-pressure evaporation model using interaction coefficients along with Baert's pyrolysis model (Ambient condition: T_∞ = 1200 K and P_∞ = 50 atm).

Furthermore, the vapour phase mole fraction of residue shown in Figure 5-18 increases and abruptly it goes to zero. That is because the evaporating molar flux goes to zero and when molar flux goes to zero evaporation model is turned off in the present model. The vapour phase mole fraction of individual components at the droplet surface shown here do not necessarily represent significant of mass, they only represent the concentration of that component. Molar flux is a function the diffusivity along with the Spalding number. As discussed in the Appendix vapour phase diffusivity is given by a linear function of the component's molecular weight and temperature. Since there are no data available about the diffusion coefficient of the residue, the diffusion coefficient of the residue is set as, total diffusivity of HFO minus the sum of the diffusion coefficients of pure hydrocarbons. Given that the residual portion of heavy fuel oil evaporates a negligible amount, it is reasonable to assume its vapour phase properties. Most of the literature simply cites the vapour phase properties only of the light hydrocarbons (molecular weight < 500). Higher values for the diffusivity of the residue could lead to increased molar flux of the residue. However, no clear data are available in the literature so appropriate low values are used, based on its high molecular weight. The change in vapour phase diffusivities at the droplet surface of all HFO components along with the droplet lifetime is shown in Figure 5-19.

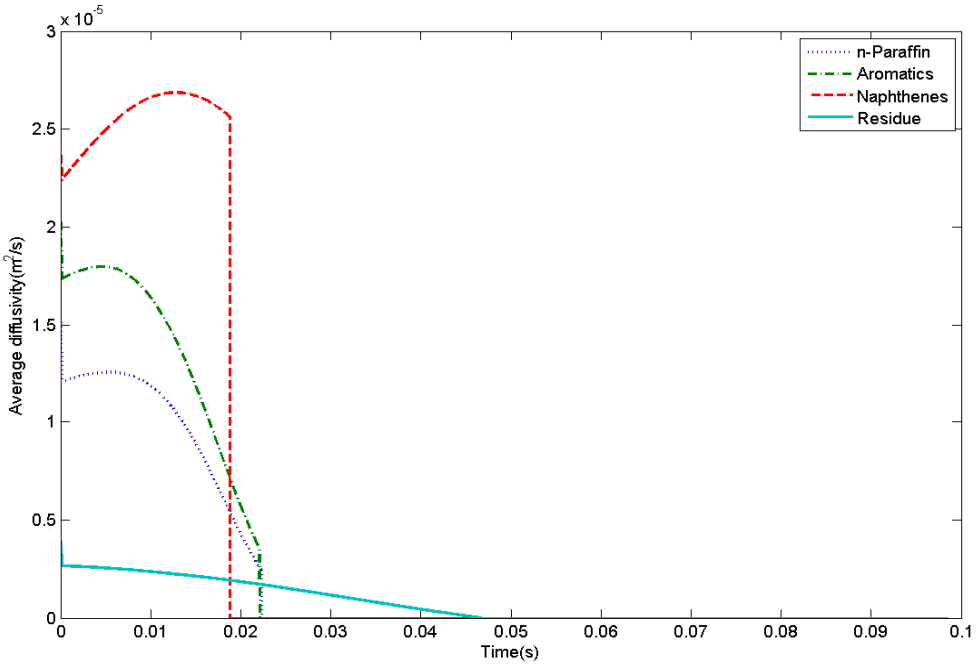

Figure 5-19: Vapour phase diffusivities of all components of a 100–micron HFO droplet (Ambient condition: T_∞ = 1200 K and P_∞ = 50 atm).

The composition history in terms of distribution functions of n-paraffins, aromatics and naphthenes is highlighted in Figure 5-20. This figure illustrates the continuous thermodynamics technique. All distribution functions are plotted at three different timings (0.0s, 0.015s and 0.02s) for n-paraffins, aromatics and naphthenes. It is clearly shown that when time t = 0, the distribution means are 340, 300, 370 for n-paraffins, aromatics and naphthenes respectively. As time increases from 0s to 0.015s and 0.015s to 0.02s, the distribution mean is shifting from left to right. The mean of the distribution for all three volatile components increases and the distribution widths narrow as evaporation proceeds. These results also indicate that evaporation occurs preferentially on the basis of volatility. The distribution function of naphthenes at t = 0.02s is not apparent in the figure because the evaporation of napthenes is finished around 0.019s.

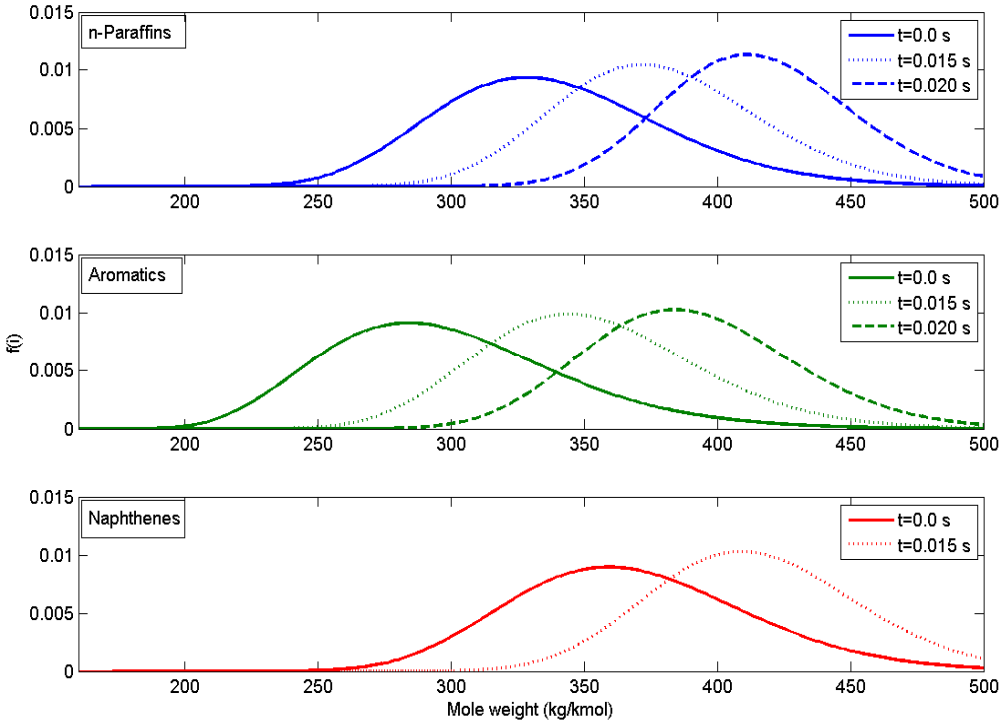

Figure 5-20: Predicted liquid phase composition distribution at various time steps for volatile components of a 100-micron HFO droplet for the high-pressure evaporation model using interaction coefficients along with Baert's pyrolysis model (Ambient condition: T_∞ = 1200 K and P_∞ = 50 atm).

Similar to Figure 5-1 for the low-pressure evaporation model, the overall mass percentage history of a 100-micron droplet at 1200 K and 50 atm ambient pressure using the high-pressure evaporation and Baert's pyrolysis models is shown in Figure 5-21. Mass loss in the early part of the droplet lifetime occurs due to the evaporation of light fractions from HFO, while it later occurs due to pyrolysis. Pyrolysis produces 22.3% gas through cracking and 46.6% polymer through polymerisation, of the original droplet mass. The total amount of vapour produced here is around 30% which is the same as the summation of mass percentage of pure hydrocarbons of HFO droplet. The above results confirm the remark made by Chen & EI-Wakil [31] that pure or light hydrocarbons in heavy fuel oil go through combustion without going through thermal decomposition because they contain more volatile components.

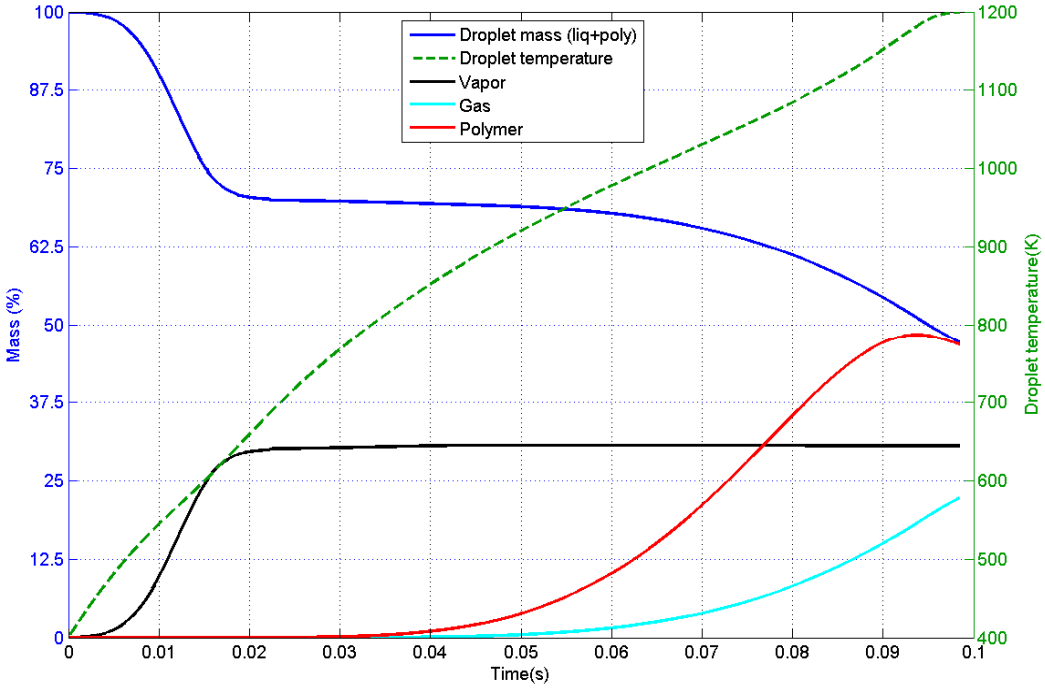

Figure 5-21: Predicted mass percentage history of a 100-micron HFO droplet along with the droplet temperature for the high-pressure evaporation model using interaction coefficients along with Baert's pyrolysis model (Ambient condition: T_∞ = 1200 K and P_∞ = 50 atm).

Once again compared to 1200 K, when the 100-micron droplet is exposed to a higher surroundings temperature (1700 K) and at the same pressure (50 atm) its product composition is found little different, as shown in Figure 5-22. The amount of polymer formation is 51% of the original droplet mass at 1700 K which is 4.4% higher than that found at 1200 K.

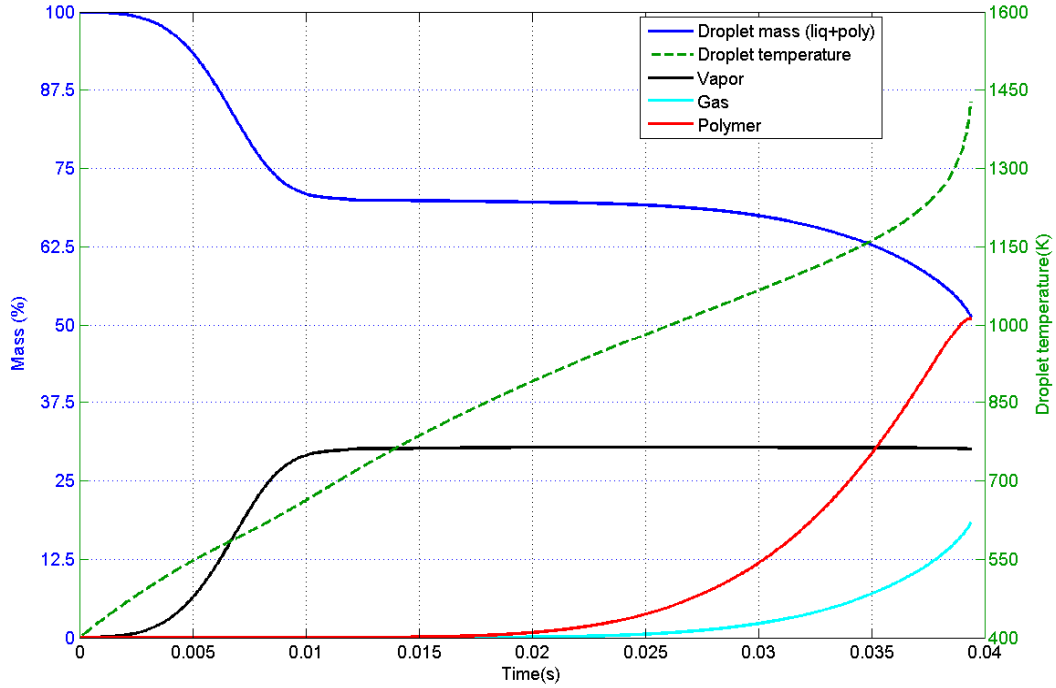

Figure 5-22: Predicted mass percentage history of a 100-micron HFO droplet along with the droplet temperature for the high-pressure evaporation model using interaction coefficients along with Baert's pyrolysis model (Ambient condition: T_∞ = 1700 K and P_∞ = 50 atm).

Hence, Baert's pyrolysis model used along with the high-pressure evaporation model shows that polymer formation is a function of droplet heating rate for 100-micron droplet. However, both models need to be studied in detail for a small droplet (such as 30-micron). The sensitivity study of polymer formation for a 30-micron droplet using the high-pressure evaporation and Baert's pyrolysis models is given in the next section.

5.3.2 30-micron droplet

Similar to the low-pressure model, to study the sensitivity of Baert's pyrolysis model along with the high-pressure evaporation model two more simulations are added; the first one is the 30-micron droplet exposed to 1200 K and the other one is the same size of droplet but exposed to a higher temperature of 1700 K. Results of these sensitivity tests are presented in Figure 5-23 and Figure 5-24 respectively.

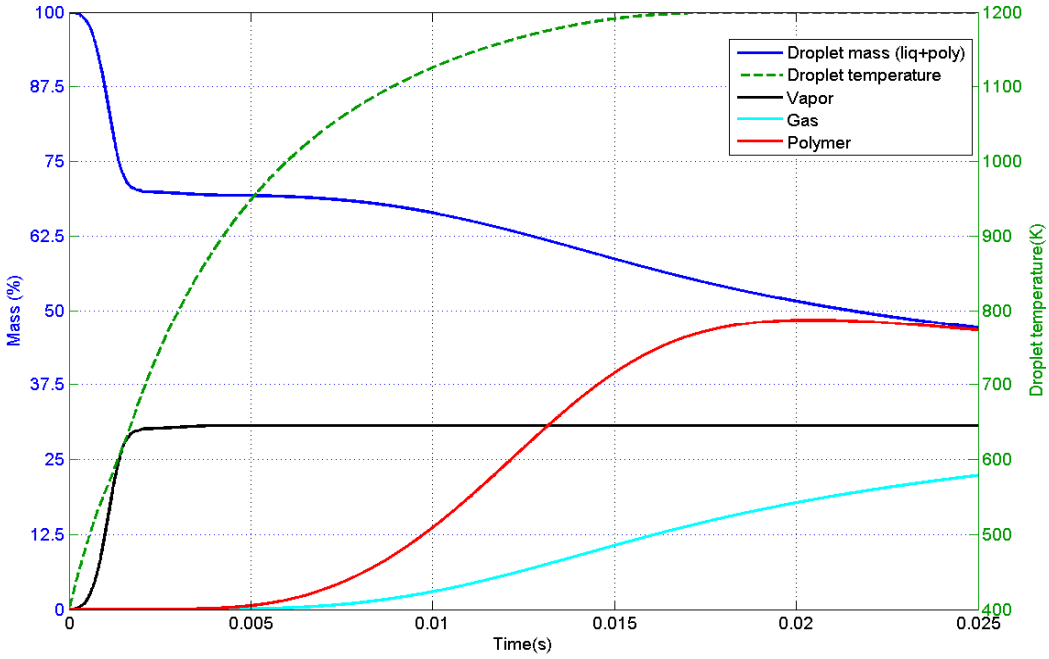

Figure 5-23: Predicted mass percentage history of a 30-micron HFO droplet along with the droplet temperature for the high-pressure evaporation model using interaction coefficients along with Baert's pyrolysis model (Ambient condition: T_∞ = 1200 K and P_∞ = 50 atm).

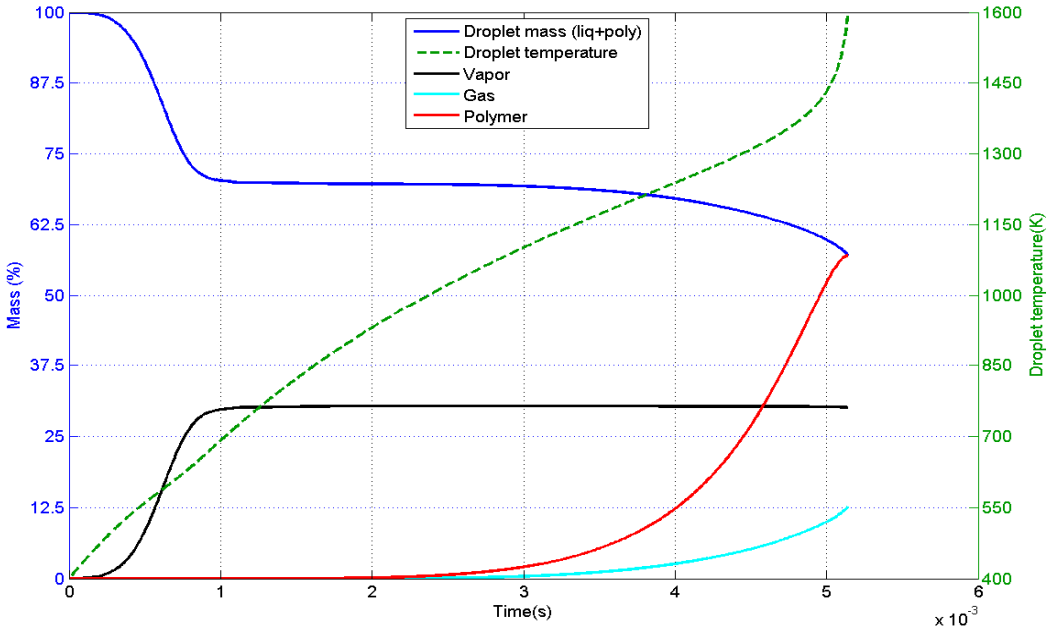

Figure 5-24: Predicted mass percentage history of a 30-micron HFO droplet along with the droplet temperature for the high-pressure evaporation model using interaction coefficients along with Baert's pyrolysis model (Ambient condition: T_∞ = 1700 K and P_∞ = 50 atm).

From Figure 5-23 and Figure 5-24, it is observed that when a 30-micron droplet is exposed to 1200 K and 1700 K, and at the same ambient pressure, the amount of polymer formation is 47% and 57% of the original droplet mass respectively. It means, at 1700 K, the amount of polymer formation is 10% higher for a 30-micron droplet than at1200 K.

The temperature profile of the droplet shows that for a 100-micron droplet (Figure 5-23), initially between 0 and 0.015 sec, droplet temperature increases slowly and later on after 0.015 sec it becomes steady, whereas in a 30-micron droplet (Figure 5-24) it increases very sharply at near the end of droplet lifetime. It means 30-micron droplet has a very high heating rate towards the end of its lifetime. To sum up, at high ambient temperature using Baert's pyrolysis model a small droplet produces more polymer than pyrolysis gas. It means that polymer formation within a small droplet is a function of droplet heating rate. A conclusion based on the low-pressure/high-pressure evaporation model along with Baert's pyrolysis model is discussed in the next section.

5.4 Modification of the Pyrolysis Model

In the above two sections, the low-pressure and high-pressure evaporation models along with Baert's pyrolysis model are discussed. It is understood that a smaller droplet is subjected to higher heating rate compared to a bigger droplet. At a high heating rate, irrespective of the low-pressure or high-pressure evaporation model, an individual (big or small) HFO droplet produces more polymer than at a low heating rate. The reason for the lower amount of polymer produced at a lower ambient temperature is the thermal cracking of the produced polymer. When there is a slow heating rate (high droplet lifetime), it actually allows more time for polymer to crack into low molecular weight volatile gas. Thus, volatile gas production increases with decreasing heating rate of an HFO droplet.

The formation of polymer and volatile gas is a function of heating time and droplet temperature. Polymer formation also depends on initial fuel composition and droplet size [38, 146]. Thus, heating rate and droplet initial size must be considered as a major factor for the pyrolysis studies of the HFO droplets. Baert's pyrolysis model shows polymer formation dependency on droplet heating rate, a small droplet produces more polymer compared to a big droplet at the same ambient condition. Generally, in an actual engine

spray combustion droplets are small [2] and heating rates are high due to combustion. Therefore, the pyrolysis model needs to be studied in detail to understand the polymer and gas formation from a single HFO droplet.

For the present modelling, reference has been made to several studies, to model the process of thermal cracking and polymerisation of HFO. Mainly there are two kind of studies reported in the literature, one deals with gas formation from heavy hydrocarbons and the other shows emission particle formation. An overview of thermal cracking and polymerisation mechanisms studied is described in the following paragraphs.

As stated by Singh et al.[150], during 1931-1934 Rice et al. studied the cracking mechanisms of organic matter and proved that mechanism involving free radicals govern the cracking of organic matter. Their first order kinetics mechanism was the base for several studies. Krishna et al.[169] studied the chemical kinetics mechanism of cracking for long residue. Their findings showed that cracking is a first order reaction. On the other hand, Martinez et al.[170] proposed the second order data fit for the asphaltenes conversion as well as for the oil+gas and coke formation. The coal flash pyrolysis studies by Doolan et al.[156] at very high temperature range (870-2000 K) showed that the tar is the main source of light hydrocarbons observed during coal pyrolysis. Al-Soufi et al. [171] studied the thermal conversion of heavy Iraqi residue between 435-480 ^{o}C. Yasar et al. [137] studied the kinetics parameters of saturates and the effect of asphaltenes on the kinetics parameters of saturates. Their results showed that addition of asphaltenes to the saturates produces an intermediate reaction rate, which suppresses the coke formation at a higher temperature. The combined mixture of saturates and asphaltenes has lower activation energy compared to saturates only. Geng & Liao [172] also studied the pyrolysis kinetics for various asphaltenes samples. Their results showed a wide range in kinetics energies for the various asphaltenes samples.

Moszkowicz et al. [151] studied experimentally and modelled the cenosphere formation for very fast pyrolysis of a heavy fuel oil droplet. Similarly Wilk [173] did experimental studies and developed a thermal decomposition model of heavy fuel oil. The result of his studies showed that the temperature inside the droplet increases uniformly, i.e. no gradients. The kinetics model developed for oil cracking by Ungerer et al.[174] describes the changes of oil composition with cracking gas and coke formation. Ranjbar & Pusch

[175] studied the pyrolysis and combustion kinetics of crude oil and discovered that composition plus heat transfer characteristics of the pyrolysis medium affects fuel formation. Urban et al.[176] explored the coke formation tendency of residual oil. They developed a relationship for a range of fuels, which predicts the coke particle diameter from the initial droplet diameter. They also established a coke formation index (CFI), which provides the potential of residual fuel oil to generate coke. The CFI is simply the mass fraction of fuel that converts to coke. Del Bianco et al.[177] provided insight on thermal cracking of petroleum residues. They also studied the change in the structure of asphaltenes and the variations in the molecular parameter were correlated. Yue. et al.[178] studied the incipient coke formation from heavy hydrocarbons. Ambalae et al.[152] studied the pyrolysis and combustion behaviour of heavy oil and asphaltenes using the thermogravimetric analyser. Their results showed that among the saturates, aromatics, resins and asphaltenes, asphaltenes contribute most to the formation of coke. They also calculated the activation energies of whole oil and asphaltenes using the *Arrhenius law*. Recently (in 2007), Ebrahimi et al.[179] studied incipient coke formation from the petroleum residue and proved that the density of pyrolysis residue is independent of the experimental condition and shows linear relation with toluene content.

As discussed in the above paragraphs, a significant amount of literature is found on the pyrolysis of heavy petroleum residue, petroleum fractions, coal and heavy fuel oil. Different researchers have different opinions about the pyrolysis process. For the pyrolysis model of a single droplet in previous section, Baert's [14] chemical kinetics model is incorporated. The mass percentage history obtained for a single droplet at 1200 K and 1 atm pressure along with the low-pressure evaporation model is shown in Figure 5-25.

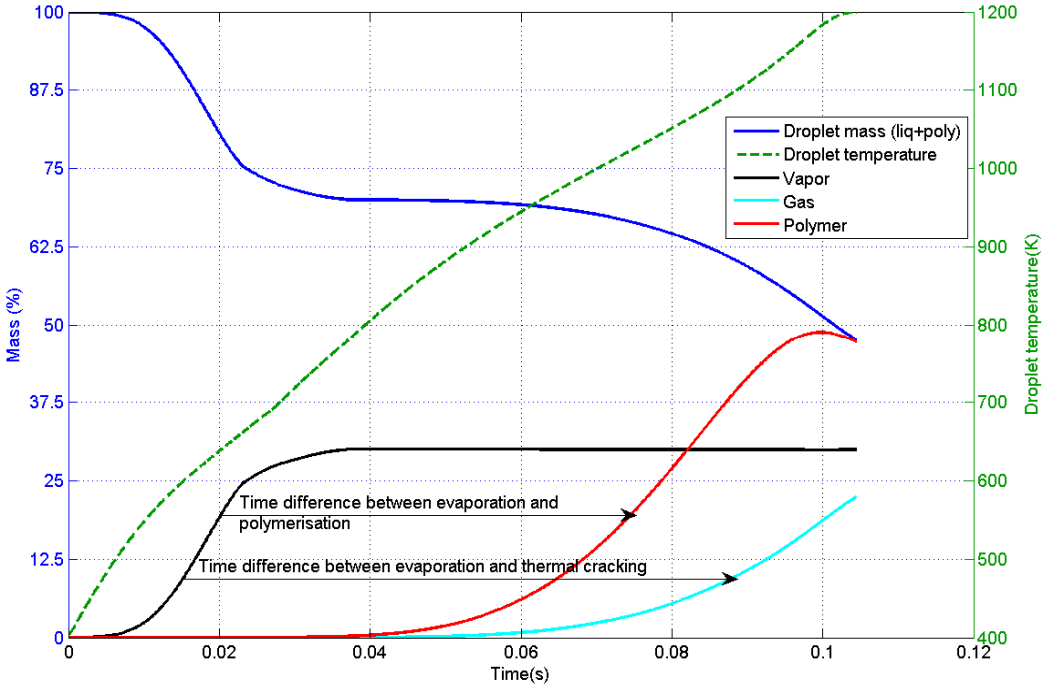

Figure 5-25: Predicted mass percentage history of a 100-micron HFO droplet along with the droplet temperature for the low-pressure evaporation and Baert's pyrolysis models (Ambient condition: T_∞ = 1200 K and P_∞ = 1 atm).

As shown in Figure 5-25, a big time gap is found between the evaporation and polymerisation and the evaporation and thermal decomposition for a 100-micron HFO using Baert's pyrolysis model. The reason behind this gap is that Baert's kinetics model contains high activation energy and small pre-exponential factors which means a large amount of energy is required to deplete the heavy molecules. On the other hand, many different chemical kinetics schemes/models are found in the literature which contains different activation energy and pre-exponential factors.

It is observed in Baert's pyrolysis model results (see Figure 5-25 or any other figure of mass percentage history in section 5.2 and 5.3) that the process of polymerisation starts prior to the thermal cracking. The reason for this is that Baert's low-temperature (LT) polymerisation constants (E_2=100*10^3 kJ/kmol and k_2= 8*10^6 1/s) yields a higher rate than the thermal cracking constants (E_1=125*10^3 kJ/kmol and k_1= 2*10^{7}1/s). This order of thermal cracking and polymerisation is contradictory to the discussion of Goldsworthy [2] and experimental results of Ikegami et al.[23]. They noted that the thermal cracking (decomposition) begins around 740 K and the polymerisation begins around 850 K. In

addition, the results of Uehara et al.[13] for TG-DTA analysis of residual fuel oil shown in 2.7.4 also shows that combustion of cutter stock and decomposition products occurs earlier than the combustion of polymer. Moreover, when Baert's pyrolysis model was incorporated to study spray combustion modelling of HFO in StarCD similar to described in next two chapters, it did not give sufficiently high rates of production of pyrolysis gas for the modelled combustion process to match the experimental data.

Hence, in order to study these issues of; (1) gap between the evaporation and polymerisation and the evaporation and thermal decomposition, and (2) order of thermal cracking of polymerisation, literature schemes/models are studied carefully and the best model which can be validated with experimental data is to be found. In the following paragraphs the schemes/models found in the literature are discussed.

After studying the literature [42, 124, 150, 152, 156, 169, 172, 174-181] it is clear that pyrolysis is a first order reaction which can be explained by a first order linear *Arrhenius law* of reaction mechanism. Therefore, *Arrhenius law* parameters collected for the various hydrocarbons from the various sources are calculated at two representative temperatures 700 K and 900 K (grey colour columns) and are summarised in the tables below (Table 5-1 & Table 5-2). Table 5-1 summarises the rate constants and *Arrhenius law* parameters for various hydrocarbons thermal cracking processes, whereas Table 5-2 summarises the same for various hydrocarbons coke formation processes.

Table 5-1: Summary of rate constants and *Arrhenius law* parameters for various hydrocarbons thermal decomposition process.

Researchers	**Feedstocks**	**Process and Temp. Range**	**Product formed**	**Order of reaction and rate equation**	**Activation Energy**	**Pre-exponential factor**	**Calculated Rate at 700 K and 900 K respectively.**
Baert [14]	Non aromatic part of the heavy fuel oil MW > 500	Th. Cracking 400-1400 K	Gases	First $\frac{dm_g}{dt} = (m_f + m_p) * k_1 e^{(-E_1/RT)} * (1 - AR)$ Where AR =Aromaticity, m_f = mass of fuel and m_p = mass of polymer	125 kJ/mol	2E+7 1/s	$\frac{dm_g}{dt} = 0.0094 * (m_f + m_p) * (1 - AR)$
							$\frac{dm_g}{dt} = 1.1162 * (m_f + m_p) * (1 - AR)$
Krishna et al. [169]	Long residue	Visbreaking 700-873 K	Distillates fractions	First $\frac{dx}{dt} = k_0 e^{(-E/RT)}(1 - x)$ Where x = weight fraction of product	224.8 kJ/mol	2.17E+12 1/s	$\frac{dx}{dt} = 3.6398\text{E-}5 * (1 - x)$
							$\frac{dx}{dt} = 0.1945 * (1 - x)$
Geng & Liao [172]	20 different samples of asphaltenes	Pyrolysis 473-873 K	Pyrolysate (products of pyrolysis)	First $\frac{dx_i}{dt} = A_i e^{(-E_i/RT)}(1 - x_i)$ Where x_i = fraction of transformed asphaltene.	173 kJ/mol (lowest)	4.38E+12 1/s	$\frac{dx_i}{dt} = 0.4698 * (1 - x_i)$
							$\frac{dx_i}{dt} = 358.11 * (1 - x_i)$
					379 kJ/mol (highest)	8.12E+24 1/s	$\frac{dx_i}{dt} = 4.2385\text{E-}4 * (1 - x_i)$
							$\frac{dx_i}{dt} = 816.9101 * (1 - x_i)$

Al-Soufi et al.[171]	Heavy Iraqi residue	Thermal conversion (visbreaking) 708-753 K	Light, middle and heavy cuts	First	99 kJ/mol (23.7 kcal/mol).	Not available	
Doolan et al. [156]	Coal	Flash pyrolysis 870-2000 K	CH_4	First $\frac{dY}{dt} = A\exp^{(-E/RT)}(Y^* - Y)$ Where A = pre-exponential factor, Y = yield of species at time t and Y^* is the yield at infinite time. $E_2 = 100$	110 kJ/mol	7E+6 1/s	$\frac{dY}{dt} = 0.0433 * (Y^* - Y)$
							$\frac{dY}{dt} = 2.8882 * (Y^* - Y)$
			C_2H_2		220 kJ/mol	5E+9 1/s	$\frac{dY}{dt} = 1.9133\text{E-}7 * (Y^* - Y)$
							$\frac{dY}{dt} = 8.5122\text{E-}4 * (Y^* - Y)$
			C_2H_4		230 kJ/mol	2E+12 1/s	$\frac{dY}{dt} = 1.3728\text{E-}5 * (Y^* - Y)$
							$\frac{dY}{dt} = 0.0895 * (Y^* - Y)$
			C_3H_6		260 kJ/mol	5E+13 1/s	$\frac{dY}{dt} = 1.9808\text{E-}6 * (Y^* - Y)$
							$\frac{dY}{dt} = 0.0406 * (Y^* - Y)$
			C_6H_6		110 kJ/mol	7E+6 1/s	$\frac{dY}{dt} = 0.0433 * (Y^* - Y)$

							$\frac{dY}{dt} = 2.8882 * (Y^* - Y)$
			CO		140 kJ/mol	2E+8 1/s	$\frac{dY}{dt} = 0.0071 * (Y^* - Y)$
							$\frac{dY}{dt} = 1.4974 * (Y^* - Y)$
Martinez et al. [170]	asphaltenes	Thermal cracking	Oil+gas and coke formation	Second $-\frac{dC_A}{dt} = k_1 C_A^{n_1} + k_2 C_A^{n_2}$ Where, C_A = asphaltene conc., k_1 = kinetics constant for oil+gas formation, $n_1 = 2,$ is the kinetics order for oil+gas formation, k_2 = constant for coke formation and $n_2 = 2$, is the order of reaction for coke formation.	63.94 kJ/mol		$-\frac{dC_{oil+gas}}{dt} = 4.58\text{E-}10 C_A^2 \left(\frac{1}{(ppm * \text{s})}\right)$
					79.22 kJ/mol		$-\frac{dC_{coke}}{dt} = 1.724\text{E-}10 C_A^2 \left(\frac{1}{(ppm * \text{s})}\right)$
Singh et al. [150]	4 different samples of residual feedstocks	Thermal cracking 673-703	Gases	First $\ln(F / F_0) = A_0 \, e^{(-E/RT)} \, t$ Where, F and F_0 are the feedstocks weight at time $t = 0$ and t	103 to	2.7E+4 to	$\ln(F / F_0) = 5.5607\text{E-}4 * t$
							$\ln(F / F_0) = 0.0284 * t$
					206 kJ/mol,	1.64E+12 1/s	$\ln(F / F_0) = 6.9563\text{E-}4 * t$
							$\ln(F / F_0) = 1.8134 * t$

Table 5-2: Summary of rate constants and *Arrhenius law* parameters for various hydrocarbons coke formation process.

Baert [14]	aromatic part of the heavy fuel oil MW > 500	Polymerisation	Coke formation	First $\frac{dm_P}{dt} = -m_P(1-AR)k_1e^{(-E_1/RT)} + m_f AR\left(k_2e^{(-E_2/RT)} + k_3e^{(-E_3/RT)}\right)$ Where AR =Aromaticity , m_f = mass of fuel and m_p = mass of polymer	kJ/mol and $E_3 = 270$ kJ/mol	$k_2 = 8E+6$ and $k_3 = 1E+13$ respectively	$\frac{dm_P}{dt} = -m_P * 0.0094 * (1-AR) + m_f * (0.2759) * AR$
							$\frac{dm_P}{dt} = -m_P * 1.116 * (1-AR) + m_f * (12.5633) * AR$
Ebrahimi et al. [179]	Petroleum residue	Thermal cracking 593-660 K	Incipient coke formation	First $\frac{dX}{dt} = k_0e^{(-E/RT)}(1-X)$ Where X = mesophase content	50.4 and	9.06E+5and	$\frac{dX}{dt} = 157.0718 * (1-X)$
							$\frac{dX}{dt} = 1076 * (1-X)$
					73.12 kJ/mol	5.5E+7 /s	$\frac{dX}{dt} = 192.2580 * (1-X)$
							$\frac{dX}{dt} = 3136 * (1-X)$
Ambalae et al. [152]	asphaltenes	Pyrolysis and combustion 648-773 K	Coke formation	First order was assumed $\frac{dC_A}{dt} = -Ae^{(-E/RT)} * C_A$ Where C_A = concentration of asphaltenes	117.7 kJ/mol	7.34E+5 /s	$\frac{dC_A}{dt} = -0.0012 * C_A$
							$\frac{dC_A}{dt} = -0.1082 * C_A$

	Heavy fuel oil	Pyrolysis and combustion 648-773 K	Coke formation	First order was assumed $\frac{dC_A}{dt} = -Ae^{(-E/RT)} * C_A$ Where C_A = concentration of heavy fuel oil	129.5 kJ/mol	44.84E+5 /s	$\frac{dC_A}{dt} = -9.7254\text{E-}4 * C_A$
							$\frac{dC_A}{dt} = -0.1366 * C_A$
Moszkowicz et al. [151]	Heavy fuel oil	Very fast pyrolysis 473-1273 K	Coke formation	First $\dot{m}_c = m_L e^{(-E/RT)}$ Where $\dot{m}_c$ = rate of coke formation and m_L = mass of liquid in the droplet	185 kJ/mol	1.45E+8 /s	$\dot{m}_c = 2.2699\text{E-}6 * m_L$
							$\dot{m}_c = 0.0027 * m_L$
Del Bianco [177]	Petroleum residue	Thermal cracking 683-743 K	Coke formation	First	267.75 kJ/mol (63.9 kcal/mol)		
Yue et al.[178]	Heavy hydrocarbons	Heating 633-693 K	Coke formation	First $\frac{dX}{dt} = k_0 e^{(-E/RT)}(1-X)$	197.5 kJ/mol	2.05E+11 /s	$\frac{dX}{dt} = 3.7462\text{E-}4*(1-X)$
							$\frac{dX}{dt} = 0.7059*(1-X)$

As shown in Table 5-1, Krishna et al.[169] proposed the activation energy *(E)* as 225 kJ/mol and pre-exponential factor as 2.17E12 1/s for the cracking of long residue. Geng & Liao [172] studied almost 20 different samples of asphaltenes from different locations. Their observations showed a big range of activation energy and pre-exponential factors. Activation energy was found between 173 to 379 kJ/mol, while the pre-exponential factor was found in the range of 4.38E+12 to 8.12E+24. Indeed their results showed a huge variation in the *Arrhenius law* parameters. The activation energy reported for the heavy Iraqi atmospheric residue cracking by Al-Soufi et al.[171] was only 99 kJ/mol (23.7 kcal/mol). Furthermore, Martinez et al.[170] proposed a second order reaction and provided activation energy of conversion of asphaltenes into oil+gas as 63.94 kJ/mol. Doolan et al.[156] conducted a study of coal flash pyrolysis in the temperature range of 870-2000 K. The kinetics parameters obtained by them for the various species formed from the cracking of tar are given in Table 5-1. Their activation energies range from 110 to 220 kJ/mol and pre-exponential factors are 7E+6 to 5E+13 1/s.

Recently, Singh et al.[150] conducted more studies on cracking of four different residual feedstocks. Their results showed that activation energy of feedstocks varies from 102 to 206 kJ/mol along with the pre-exponential factors from 2.7E+4 to 1.64E+12 1/s. It was also shown that these values were highly dependent on the crackable content of the feedstocks. Activation energy decreases with an increase in saturates and increases with an increase in asphaltenes content.

Similar to gas formation by cracking, coke formation through cracking (see Table 5-2) is also studied in great detail because it facilitates understanding of pollutant formation from liquid fuels. The activation energy reported for coke formation rate by Martinez et al.[170] is 79.22 kJ/mol. Similarly, Ebrahimi et al.[179] noted activation energy for coke formation from two different residue samples as 50.4 kJ/mol and 73.12 kJ/mol. The thermogravimetric studies of heavy fuel oil and asphaltenes by Ambalae et al.[152] showed that the activation energy for coke formation from asphaltenes was 117.7 kJ/mol and 129.5 kJ/mol for whole oil, whereas their pre-exponential factors were 7.34E5 /s and 44.84E5 /s respectively. Moszkowicz et al.[151] developed a fast pyrolysis model for heavy fuel and derived the activation energy and pre-exponential factor as 185 kJ/mol and 1.45E+8 /s respectively. The activation energy reported by Del Bianco [177] for the coke formation was found to be 267.75 kJ/mol (63.9 kcal/mol). Yue et al.'s [178] results

showed that activation energy and pre-exponential factor for coke formation were found as 197.5 kJ/mol and 2.05E+11 /s respectively.

The rate constant found for thermal cracking of heavy hydrocarbons in Table 5-1 at 700 K range from 1.1933E-7 to 0.4698 1/s, and at 900 K range from 8.5122E-4 to 816.91 1/s. Similarly, the rate constant for coke formation from the heavy hydrocarbons in Table 5-2 at 700 K range from 2.2699E-6 to 192.25 1/s, and at 900K range from 2.7E-3 to 3136 1/s. Hence, despite studying many papers in the literature no concrete conclusion is drawn about the kinetics parameters and rate constants for HFO pyrolysis. Large discrepancies are found in the literature results, because kinetics parameters vary according to sample composition and also with the origin of samples. Therefore, a pyrolysis model similar to Baert's pyrolysis model is postulated but with modified activation energies and pre-exponential factors. The rates of thermal cracking and polymerisation are given in equation (37) and (38) respectively. However, their constants are modified as shown in Table 5-3 to correct the overall combustion results of HFO. Table 5-3 also summarises the lowest and highest activation energies and corresponding pre-exponential factors obtained from Table 5-1and Table 5-2 for the pyrolysis model.

Table 5-3: Baert's, literature and modified *Arrhenius law* constants for the pyrolysis model.

Processes	**Baert's pyrolysis model**		**Literature values**		**Modified pyrolysis model**	
	Activation Energy (E) in kJ/kmol	**Reaction rate pre-exponential factor (k) in /s**	**Activation Energy (E) in kJ/kmol**	**Reaction rate pre-exponential factor (k) in /s**	**Activation Energy (E) in kJ/kmol**	**Reaction rate pre-exponential factor (k) in 1/s**
Thermal cracking	$E_1 = 125 * 10^3$	$k_1 = 2 * 10^7$	$103 * 10^3$ to $379 * 10^3$	$2.7 * 10^4$ to $8.12 * 10^{24}$	$E_1 = 85 * 10^3$	$k_1 = 8 * 10^7$
Low-temperature polymerisation	$E_2 = 100 * 10^3$	$k_2 = 8 * 10^6$	$50.4 * 10^3$ to $270 * 10^3$	$9.06 * 10^5$ to $1 * 10^{13}$	$E_2 = 90 * 10^3$	$k_2 = 5 * 10^7$
High-temperature polymerisation	$E_3 = 270 * 10^3$.	$k_3 = 1 * 10^{13}$			$E_3 = 270 * 10^3$	$k_3 = 10^{13}$

As shown in Table 5-3 the modified activation energy for thermal cracking model is lower than the values found in the literature for asphaltenes and other heavy molecules, and also lower than Baert's pyrolysis model. As stated by Doolan et al.[156] and shown by Anthony & Howard [181] the mixture may have lower activation energy than its individual members. In other words, HFO may possess lower activation energy than its individual components (asphaltenes, resins, aromatics etc.). The modified activation energy for LT polymerisation model is intermediate between the values found in the literature, and lower than Baert's pyrolysis model. Similarly, the modified pre-exponential factors for both thermal cracking and LT polymerisation are intermediate between the values found in the literature.

The activation energy and pre-exponential factor for HT polymerisation are kept the same as Baert's model. The pre-exponential factors in the present model are tuned to correct the overall combustion results of HFO to other researcher's explanations about pyrolysis. In other words, due to a large range in the literature values for pyrolysis constants, the choices of modified pyrolysis constants are approximate within the range of published values. The modified *Arrhenius law* parameters for pyrolysis model are examined in the next section where results for the low-pressure evaporation models along with modified pyrolysis model are provided and also in Chapter 7 where simulation results for spray combustion of HFO are qualitatively compared with the experimental results.

5.5 Low-Pressure Evaporation Model along with the Modified Pyrolysis Model

5.5.1 100-micron droplet

In previous sections 5.2 and 5.3 (using Baert's pyrolysis model) the dependency of polymer formation on droplet heating rate is observed. In both models (low or high-pressure evaporation), when the droplet is exposed to two different ambient temperatures (1200 K and 1700 K) its product compositions are different. At 1700 K, irrespective of the low/high-pressure evaporation models and ambient pressures, polymer formation within a single droplet is higher compared to 1200 K. Hence, in subsequent calculations either of these low or high-pressure models and ambient pressure can be used to study the polymer

formation tendency based on heating rate. Therefore, in the present section, the low-pressure evaporation model along with the modified pyrolysis model is used. Four simulations are presented here; the first and second one are of a 100-micron droplet exposed to 1200 K and 1700 K respectively, and the third and fourth one are of a 30-micron droplet exposed to 1200 K and 1700 K respectively. Results of the first and second simulations are presented in Figure 5-26 and Figure 5-27 respectively.

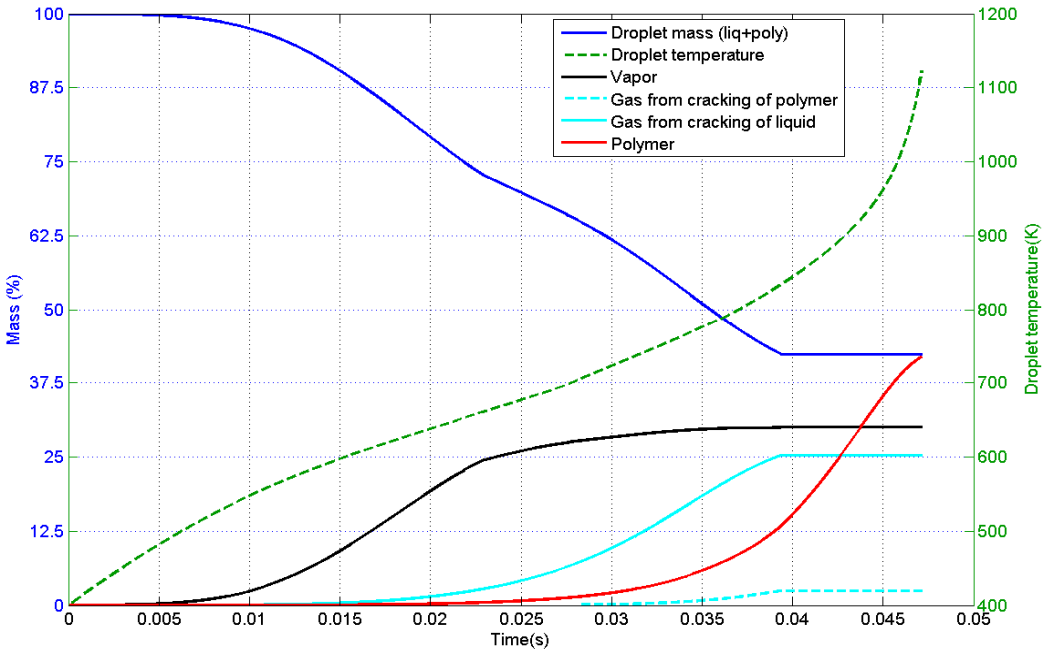

Figure 5-26: Predicted mass percentage history of a 100-micron HFO droplet along with the droplet temperature for the low-pressure and modified pyrolysis models (Ambient condition: T_∞ = 1200 K and P_∞ = 1 atm).

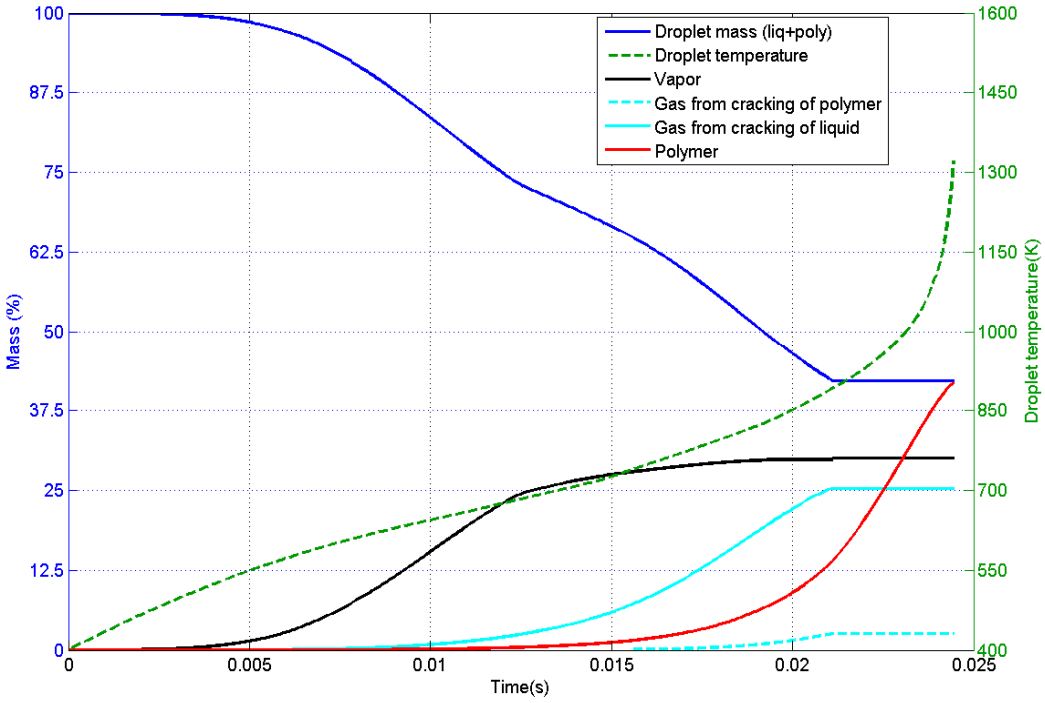

Figure 5-27: Predicted mass percentage history of a 100-micron HFO droplet along with the droplet temperature for the low-pressure and modified pyrolysis models (Ambient condition: T_∞ = 1700 K and P_∞ = 1 atm).

It can be observed from Figure 5-26 and Figure 5-27 for the low-pressure and modified pyrolysis models that when a 100-micron droplet is exposed to 1200 K, its product compositions; including polymer and gas, are almost the same as of a 100-micron droplet exposed to a 1700 K. Polymer formation in both figures is around 42% of the original droplet mass, though both droplets have different heating rates. The polymer formation dependence on heating rate using Baert's pyrolysis model (see Figure 5-1 and Figure 5-7) is not observed in the modified pyrolysis model study. However, this needs to be confirmed for a small droplet. Therefore, an additional study (the third and fourth simulations) of a small droplet (30-micron) using the low-pressure model along with the modified pyrolysis model is given in the next section.

5.5.2 30-micron droplet

Results of a 30-micron droplet exposed to 1200 K and 1700 K at 1 atm ambient pressure are presented in Figure 5-28 and Figure 5-29 respectively.

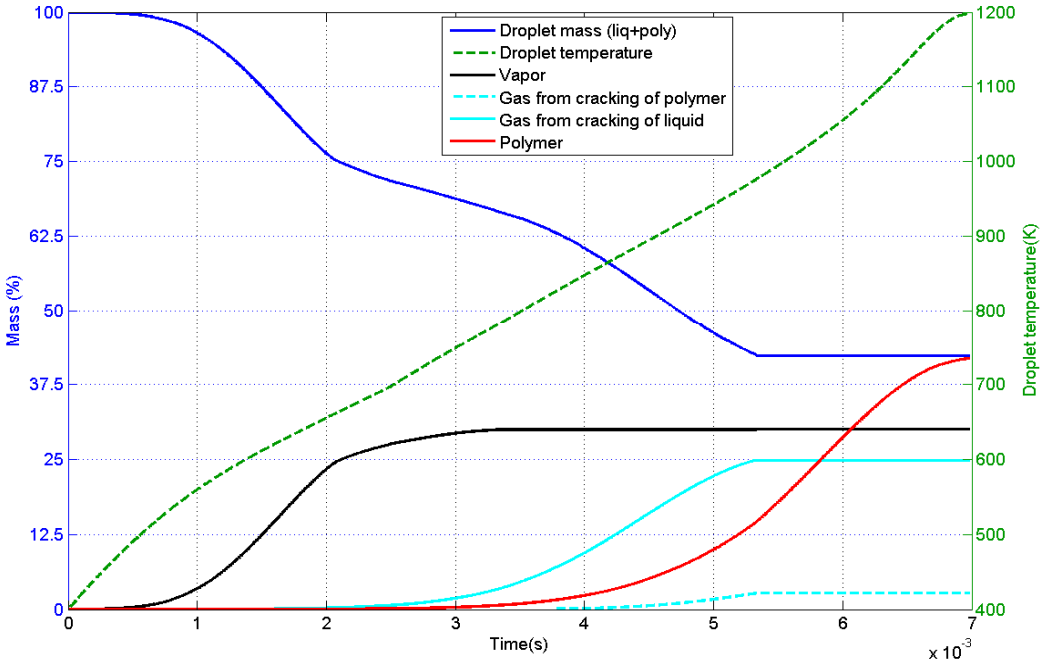

Figure 5-28: Predicted mass percentage history of a 30-micron HFO droplet along with the droplet temperature for the low-pressure and modified pyrolysis models (Ambient condition: T_∞ = 1200 K and P_∞ = 1 atm).

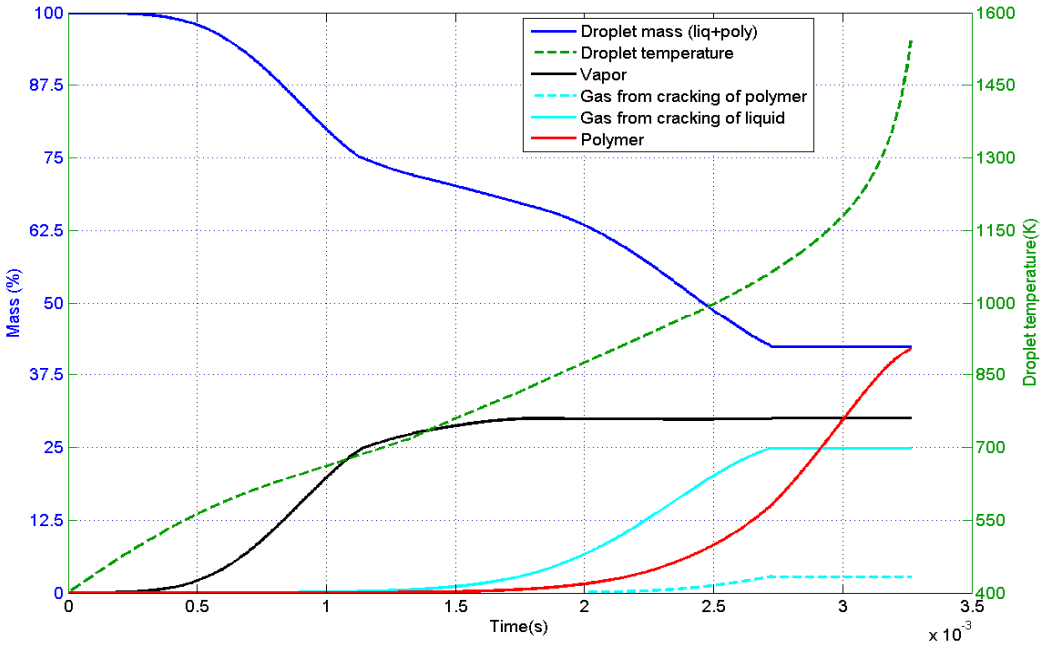

Figure 5-29: Predicted mass percentage history of a 30-micron HFO droplet along with the droplet temperature for the low-pressure and modified pyrolysis models (Ambient condition: T_∞ = 1700 K and P_∞ = 1 atm).

By comparing Figure 5-28 with Figure 5-29, it is observed that when a small (30-micron) droplet is exposed to 1200 K and 1700 K, at same ambient pressure, the amount of polymer formation is 42% in both cases. In other words, at a high or low ambient temperature a small droplet produces the same amount of polymer and pyrolysis gas. Further, by comparing Figure 5-29 with Figure 5-27 (a small droplet with a big droplet at the same ambient condition), it is clearly evident that droplet product compositions are almost same in both cases. In other words, the droplet produces the same products irrespective of the heating rate. In brief, the polymer formation which was dependent on droplet heating rate using Baert's pyrolysis model is not observed in the modified pyrolysis model.

Furthermore, Figure 5-26 to Figure 5-29 with the modified pyrolysis model shows that thermal cracking always occurs earlier than the polymerisation which agrees with the discussion of Goldsworthy [2], experimental results of Ikegami et al.[23] and the TG-DTA results of Uehara et al.[13]. Hence, the modification made to pyrolysis constants is partially justified. Heating rates over the droplet lifetime for a 30-micron droplet using the low-pressure evaporation and modified pyrolysis models observed in Figure 5-28 and Figure 5-29 are $1.14*10^5$ K/s and $3.33*10^5$ K/s respectively.

As demonstrated in the above section (section 5.5) the modified pyrolysis model does not show dependency of polymer formation on droplet heating rate. In the modified pyrolysis model, polymer formation is only a function of droplet composition. Modification of the pyrolysis model also supports the experimental results obtained by other researchers (Goldsworthy [2], Ikegami et al.[23] and Uehara et al.[13]) in terms of the order of the thermal cracking and polymerisation. Hence, this modified pyrolysis model could be used in the spray combustion calculation where droplets are generally small and heating rate is high. Spray combustion results using this modified pyrolysis model along with the low-pressure evaporation model for two representative sample of HFO are given in Chapter 7.

5.6 A Comparison of the Low-Pressure Model with the High-Pressure Model along with the Modified Pyrolysis Model for a Small Droplet at a High pressure

Due to the increased computation cost of the high-pressure EOS-VLE calculations in addition to the original cost to calculate the changes in composition of droplets in the evaporation subroutine, it is decided not to use the high-pressure EOS-VLE approach for spray combustion calculation in StarCD. As partial justification of the present choice, the comparisons of spray simulation results using the low-pressure evaporation model along with the modified pyrolysis model for HFO with the experiment results are shown in section 7.3. The low-pressure evaporation model is tested for two representative fuel samples, one with the good combustion quality and the other with poor and for two sets of experimental results. Good qualitative agreement is shown between the computer simulations and the measured experimental data, without the use of the high-pressure EOS-VLE model.

The only aspect that has not been explored in the present study is the difference in the HFO fuel spray prediction calculation using the low-pressure model (*Raoult's law)* and the high-pressure EOS-VLE model. A literature study by Siebers [131] has noted that the use of EOS-VLE calculation in the spray only has a second-order effect. Siebers [131] mentioned that more realistic VLE analysis have very little impact on the spray calculations. Moreover, Kim & Sung [73] investigated the effect of low-pressure and high-pressure models on evaporating spray. Their results showed that the fraction of evaporated fuel predicted by the low-pressure model is only about 5% less than the high-pressure model. However, in the present section efforts are made to compare the low and high-pressure VLE (with interaction coefficients) models along with modified pyrolysis model of a 30-micron single droplet (which is representative size for a droplet in developed spray) at a very high pressure.

In the present case, simulation is carried out for a 30-micron initial diameter droplet which is exposed to the 1200 K surroundings temperature and 100 atm pressure. The overall results of the simulation are the same as what is observed in previous sections. However, as expected, the effect of high pressure on a small droplet is reflected. Some distinctive

results obtained using the low-pressure model and high-pressure model are given in Figure 5-30 and Figure 5-31. In both figures, sub-figure (a) shows composition history of the pure hydrocarbons along with the droplet temperature, (b) shows liquid mole fractions of components along with normalised droplet size history, (c) shows compositions expressed as percentage of initial droplet mass, (d) shows vapour phase mole fraction at the droplet surface, (e) shows evaporating molar flux and (f) shows the overall mass balance of a droplet along with the droplet temperature.

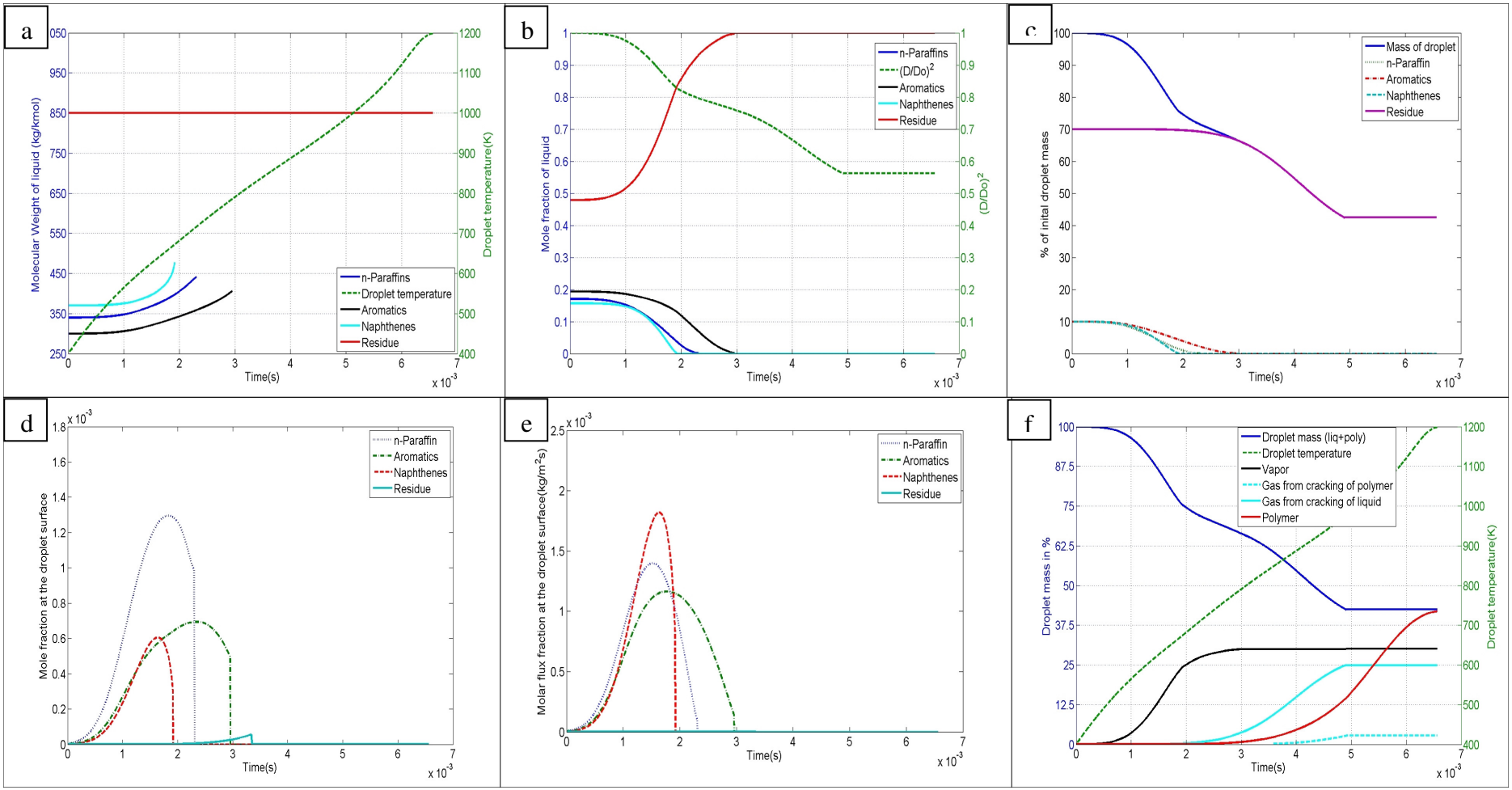

Figure 5-30: Predicted results of a 30-micron HFO droplet using the low-pressure evaporation model and modified pyrolysis model. (Ambient condition: T_∞ = 1200 K and P_∞ = 100 atm). Sub-figure (a) shows composition history of the pure hydrocarbons along with the droplet temperature, (b) shows liquid mole fractions of components along with normalised droplet size history, (c) shows compositions expressed as percentage of initial droplet mass, (d) shows vapour phase mole fraction at the droplet surface, (e) shows evaporating molar flux and (f) shows the overall mass balance of a droplet along with the droplet temperature.

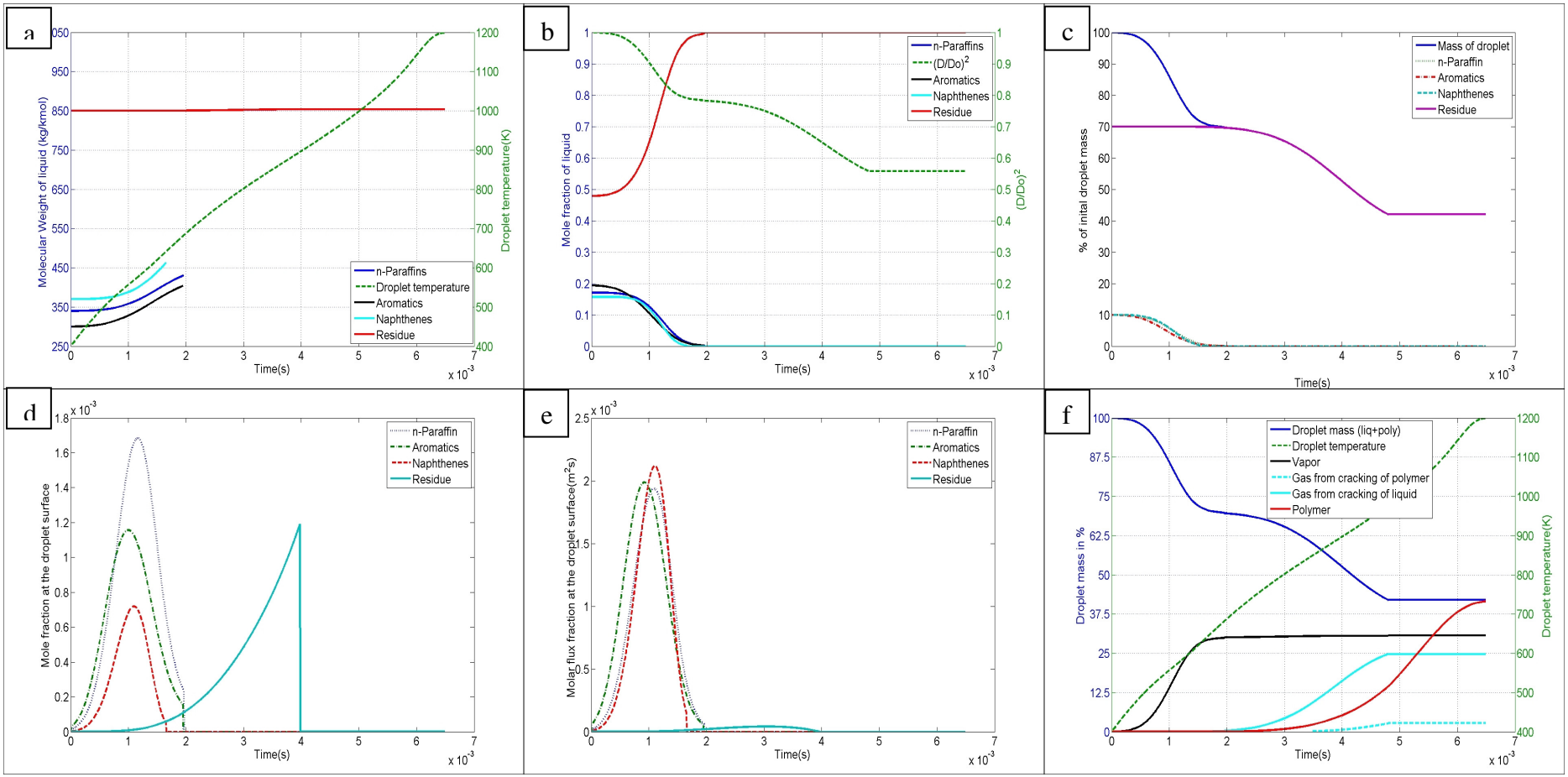

Figure 5-31: Predicted results of a 30-micron HFO droplet using the high-pressure evaporation model with interaction coefficients and modified pyrolysis model. (Ambient condition: T_∞ = 1200 K and P_∞ = 100 atm). Sub-figure (a) shows composition history of the pure hydrocarbons along with the droplet temperature, figure (b) shows liquid mole fractions of components along with normalised droplet size history, figure (c) shows compositions expressed as percentage of initial droplet mass, figure (d) shows vapour phase mole fraction at the droplet surface, figure (e) shows evaporating molar flux and figure (f) shows the overall mass balance of a droplet along with the droplet temperature.

As shown in Figure 5-30 and Figure 5-31, the droplet temperature for a small droplet (30-micron) at 100 atm pressure, increases at a faster rate than is observed for a big droplet (see Figure 5-17 of a 100 micron droplet which is exposed to 1200 K and 50 atm pressure). The reason behind this sharp increase in the droplet temperature is its smaller surface area to volume ratio. Baert [14] demonstrated that the heating rate of a single droplet is almost inversely proportional to its size. Noticeably, a high heating rate to the droplet helps in the evaporation of the light components from the surface quickly.

The mole fractions and molar fluxes obtained at the droplet surface showed that evaporation of a 30-micron droplet is a very rapid process compared to the pyrolysis. The pyrolysis of the droplet continues here at a slow rate until the end of droplet lifetime. In the present case, the droplet temperature only increases up to the initial chamber temperature. However, in reality, where the combustion of fuel occurs, the droplet temperature would increase more than the initial chamber temperature which would help to pyrolise the heavy molecules at a faster rate.

By comparison of Figure 5-30 with Figure 5-31, it is clear that overall results obtained from both models including the droplet lifetime, pyrolysis products (polymer and gas) are essentially same, except the evaporation of light components occurs at a faster rate in the high-pressure model compared to low-pressure model. The evaporation of the light components for the high-pressure model finishes in 2 ms, whereas the evaporation of the light components in the low-pressure model requires 3 ms. This faster evaporation rate does not affect the already high heating rate. Therefore, at the end, overall droplet lifetime remains the same. The choice made to avoid the complex high-pressure model implementation for spray combustion in StarCD is reasonable because the low-pressure model and high-pressure model give similar results, except the vapour concentration, at a high pressure and temperature for a small single droplet. However, where cutter stock proportion is higher than the present model, early evaporation rate for the high-pressure model could influence the early vapour concentration and composition which will affect the ignition reactions and ultimately the ignition delay.

5.7 Summary

In summary, Baert's pyrolysis model based on chemical kinetics for thermal cracking and polymerisation rate is developed. Results of this pyrolysis model show that polymer formation within a droplet is dependent on droplet heating rate and composition. Moreover, it is observed in Baert's pyrolysis model results that the process of polymerisation starts prior to the thermal cracking. This order of thermal cracking and polymerisation is contradictory to the experimental evidence. Subsequently, Baert's pyrolysis model parameters are modified. Results of the modified pyrolysis model did not show any significant dependency of polymer formation on droplet heating rate and in addition it showed thermal cracking beginning earlier than the polymerisation.

A comparison of the low-pressure model with the high-pressure model for a 30 micron droplet at high pressure show that evaporation of the volatile hydrocarbons (n-paraffins, aromatics, naphthenes) from HFO occurs at a faster rate for the high-pressure model. However, this faster evaporation does not significantly affect the droplet lifetime because modelled HFO contains only 30% volatile hydrocarbons (cutter stock) by mass. Therefore, droplet lifetime is found to be similar for both models. Thus in sprays where droplets are generally small, the VLE calculation can be obtained with sufficient accuracy by the low-pressure model avoiding the use of the complex high-pressure EOS model. However, where cutter stock proportion is higher than the present model, early evaporation rate for the high-pressure model could influence the early vapour concentration and composition which is important for ignition. An additional reason to study the high-pressure model is to inspect the effect of interaction coefficients on the evaporation rate of heavy component, the analysis showed that interaction coefficients does not significantly affect the evaporation of heavy component.

Chapter 6. Spray Combustion Modelling of Heavy Fuel Oil in StarCD

6.1 Introduction

In previous chapters, studies of characterisation techniques of heavy fuel oil, and evaporation and pyrolysis models of a single droplet are presented. The present chapter describes the application of the previously developed models using computational fluid dynamics (CFD). In CFD, a computer or a cluster of computers are used to simulate the interaction between the gas phase and the liquid phase with complex geometry. There are many commercially used CFD software packages available. In the present study StarCD v3.24 is used to carry out the spray combustion simulations of two main available experimental results, namely CVCC and FIA as described in section 2.7. The validation of models described in the present chapter with the available experimental results of CVCC and FIA is given in the next chapter.

The success of any engine CFD simulation is dependent on many factors, such as (1) accuracy of the underlying mathematical formulation of the problem, (2) accuracy of sub models used for the phase relationships, (3) numerical accuracy of the equation solution procedure and (4) availability of experimental data for comparison and validation. The present chapter describes many individual CFD models which are necessary to represent the combustion behaviour of heavy fuel oil including spray model, evaporation model, ignition model, combustion model and soot burnout models.

As stated by Goldsworthy [2], spray combustion involves many complex processes such as;

- Injection nozzle turbulence
- Fuel chemistry
- Spray-induced turbulence
- Droplet breakup
- Droplet turbulent dispersion
- Droplet heat and mass transfer

- Droplet coalescence
- Changes in properties of liquid and gas phase with time
- Ignition and combustion kinetics etc.

The overall conceptual model of a burning spray is very well explained by Dec [182]. The outline of that model is shown in Figure 6-1. As shown in the figure, after the injection, first of all liquid fuel vaporises. Then after the vaporised fuel mixes with the hot air, subsequently ignition occurs when fuel/air mixture reaches to its ignition temperature. Afterwards, burning continues and produces energy. Meanwhile pollutants are produced as undesirable products.

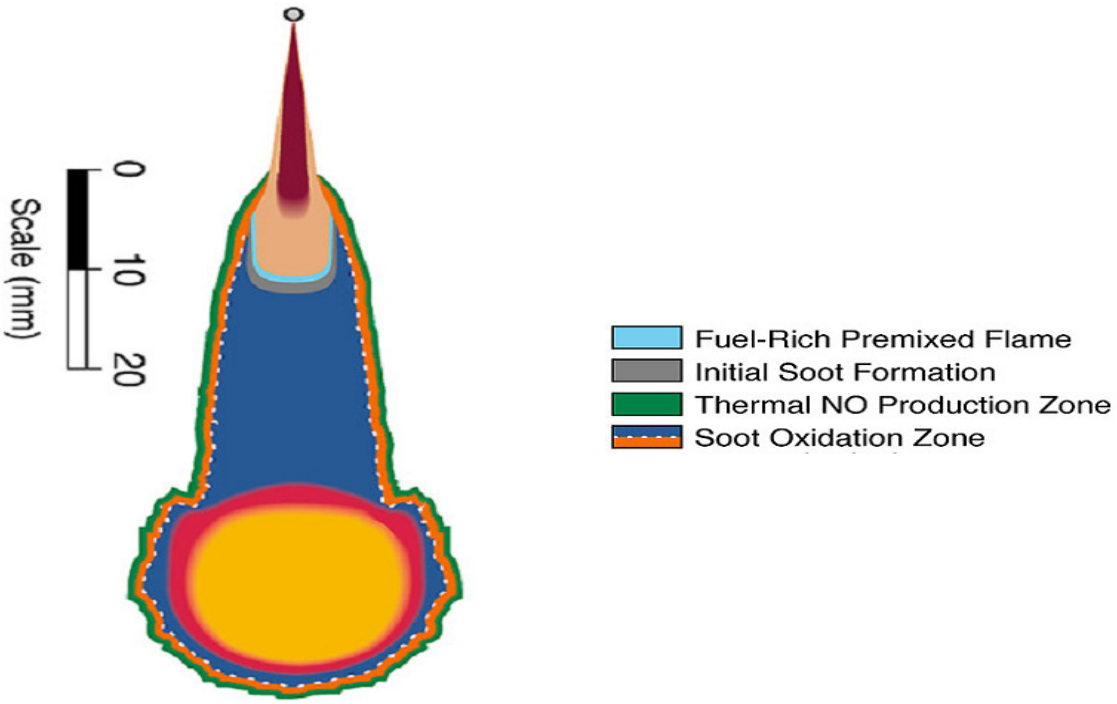

Figure 6-1: Conceptual model for ignition and combustion of diesel spray (from Dec [182]).

Dec [182] identified four main regions of spray as shown in Figure 6-1. First is fuel-rich premixed flame region. In this region, fuel mixes with oxygen before it reaches the flame front and air entrained into the spray is consumed. Second is soot formation region. Downstream of the fuel-rich region is the soot production region. Soot formation and its growth continue as very little oxygen is able to penetrate in this region because most of the surrounding air is pushed away by the flame head [128]. Third is the NO production region where NO related pollutants are produced by the thermal mechanism. NO

production is expected only around the jet periphery on the lean side of the diffusion flame indicated by the green line. Fourth is the soot oxidation region in which formed soot oxidises with the oxygen as it moves to the flame front where oxygen is readily available. Won et al.[128] also described a similar spray structure and pollutant formation process.

In a diesel engine, a point ignition source is not available. Therefore, the ignition process in this kind of engine is very important because it is dependent on the early evaporation of liquid. The pollutant formation from the fuel source is dependent on initial fuel composition, spray behaviour, droplet size and chemical reactions which occur during the entire combustion process. Reducing pollutant formation is one of the biggest challenges for the engine industry. The present chapter provides an overview of the essential models of CFD studies in the context of spray combustion. StarCD has its own ability to represent the combustion process of liquid fuel; however some models in the present study are modified to represent the complex combustion process of HFO, whose detailed description is given in the following sections.

6.2 Spray Model

6.2.1 Spray Breakup

The spray model is one of the most crucial models in engine simulation [5]. Spray dynamics involves complex physical phenomenon. The state of the air in which spray is injected has a profound effect on spray dynamics [5]. The density and turbulent nature of air are the most important properties of air that determine spray dynamics. Droplet breakup is controlled by the viscosity of liquid as well as by inertial and surface forces.

Typically heavy fuel oil possesses higher viscosity than ordinary distillate fuels [2], and StarCD's standard spray breakup models are designed for ordinary distillate fuels. Therefore in the present study, the simplest model is used for spray break up. For primary droplet breakup, StarCD's inbuilt Reitz & Diwakar atomization model [183] is used. Even though this model was introduced more than 20 years ago [184], it is still widely used in modern CFD codes. The atomization model provides the droplet size, the droplet temperature and the droplet velocities at the nozzle exit. The choice made here is based on

the discussion available in Baumgarten et al.[185] that when there is no detailed information available about the flow in the nozzle, the Reitz & Diwakar atomization model is the best default choice. Moreover, the same selection is accurately justified by Goldsworthy [186] for CFD modelling of HFO combustion for large marine engines.

The Reitz & Diwakar atomization model [184] is also known as 'blob atomization model' for primary breakup because in this model, the injected parcels of liquid in the form of 'blobs' have same characteristic size equal to the nozzle hole diameter [185]. In other words, droplets at the nozzle exit are assumed to have same diameter as the nozzle diameter. Secondary breakup models are used to break the blob into realistic droplet sizes. Moreover, for the secondary breakup of this model [183, 184] two droplet breakup regimes are identified: (1) Bag breakup and (2) Stripping breakup.

(1) Bag breakup: - non uniform pressure around the droplet causes the droplet to expand in the low pressure region and ultimately disintegrate when surface tension forces are overcome. This regime is analogous to the Rayleigh-Taylor instability, which occurs due to the development of normal forces. This instability is determined by Weber number (We);

$$We \equiv \frac{\rho |u - u_d|^2 D_d}{2\sigma_d} \geq C_{b1} \tag{80}$$

Where σ_d is the surface tension coefficient and D_d is the instantaneous diameter.

(2) Stripping breakup: - is a simple process where liquid is simply sheared/stripped off from the droplet surface. This regime is analogous to the Kelvin-Helmholtz instability [5], which occurs due to the development of tangential forces. This instability is determined as

$$Z = \frac{We}{\sqrt{\mathrm{Re}}} \geq C_{s1} \tag{81}$$

Where Re is the Reynolds number of the droplet. $\mathrm{Re} \equiv \frac{\rho |u - u_d| D_d}{\mu}$

The lifetimes for stable droplets are estimated from following equations;

$$\text{Bag breakup:} \qquad \tau_b = C_{b2} D_d^{3/2} \sqrt{\frac{\rho_d}{4\sigma_d}}$$
$$\text{Stripping breakup:} \qquad \tau_s = \frac{C_{s2}}{2} \sqrt{\frac{\rho_d}{\rho}} \frac{D_d}{|u - u_d|} \tag{82}$$

The diameter of the unstable droplet is allowed to change continuously with time as;

$$\frac{dD_d}{dt} = -\frac{(D_d - D_{d,stable})}{\tau_b} \tag{83}$$

Where $D_{d,stable}$ is the stable diameter determine at $We = 6$ and $Z = 0.5$.

Various constants used for the Reitz & Diwakar atomization model are modified and are listed in Table 6-1. The Reitz & Diwakar atomization model requires the spray angle as input. The initial cone half-angle is set to 10^o to match the visual CVCC experimental results. The constants used for the breakup model are also modified to match the visual CVCC experimental results. Furthermore, the same breakup model setup is used for FIA simulation because visual images of FIA results are not available.

Table 6-1: Constants for Reitz & Diwakar spray breakup model in StarCD.

We (bag)	$C_{b1} = 8.4$
We (stripping)	$C_{b2} = 0.5$
Te (bag)	$C_{s1} = 4.0$
Te (stripping)	$C_{s2} = 26$

6.2.2 Spray Collision and Coalescence

Spray collision and coalescence are also important phenomena after the droplet break up. However, in the present modelling, the collision model was turned off because it was

difficult to globalise the average droplet properties after collision. Some droplet properties (mean molecular weights and variances) are supplied initially when the droplet forms and traced throughout the droplet lifetime. These droplet properties need to be averaged when collision occurs. Mathematically it is quite difficult to average and tracked these properties throughout the droplet lifetime because in parallel to the collision model many other problems of modelling in StarCD (described in section 6.10) are also faced. Moreover, Goldsworthy [2] noted that large droplets formed by collision and coalescence may undergo disruptive boiling behaviour and reverse the effect of coalescence. Hence, in order to avoid the complexity during the model development and considering the effect of disruptive boiling the collision and coalescence model was turned off.

6.3 Turbulence Model

The choice of turbulence model in spray combustion modelling of engines is very important because spray behaviour very much affects the surrounding gas-motion, gas-turbulence and mixing within the gas phase [12]. In engines, combustion depends on turbulent mixing of air with fuel vapour. Hence, to get the right turbulence mixing controlled combustion, turbulence kinetic energy and turbulence dissipation rate are important. In real flow, turbulent eddies break-up into smaller ones and this continues down to the Kolmogorov scale, where intimate mixing of fuel and air occurs [12].

The RNG (residual normalization group) $k-\varepsilon$ model developed by Yakhot & Orszag [187] is widely used for engineering modelling [2, 188]. However, it is pointed out by Goldsworthy [2] that RNG and non linear cubic model in StarCD gives excessive spray penetration and mixing rate in the present context. In addition, the non linear quadratic model found to gives lower early mixing rate than the linear model [2]. The non linear quadratic model also gives penetration in between the RNG and the linear model. Therefore, in the present work $k-\varepsilon$/High Reynolds Number model is used. The turbulent kinetic energy (k) and of turbulence dissipation rate (ε) in this model are described as follows [183];

Turbulent kinetic energy (k)

$$\frac{\partial}{\partial t}(\rho k)+\frac{\partial}{\partial x_j}\left[\rho u_j k-\left(\mu+\frac{\mu_t}{\sigma_k}\right)\frac{\partial k}{\partial x_j}\right]=\mu_t(P+P_B)-\rho\varepsilon-\frac{2}{3}\left(\mu_t\frac{\partial u_i}{\partial x_i}+\rho k\right)\frac{\partial u_i}{\partial x_i} \qquad (84)$$

Where, $P\equiv S_{ij}\dfrac{\partial u_i}{\partial x_j}$, $P_B\equiv-\dfrac{g_i}{\sigma_{h,t}}\dfrac{1}{\rho}\dfrac{\partial\rho}{\partial x_i}$, σ_k = turbulent Prandlt number

Turbulent dissipation rate (ε)

$$\frac{\partial}{\partial t}(\rho\varepsilon)+\frac{\partial}{\partial x_j}\left[\rho u_j\varepsilon-\left(\mu+\frac{\mu_t}{\sigma_\varepsilon}\right)\frac{\partial\varepsilon}{\partial x_j}\right]=C_{\varepsilon1}\frac{\varepsilon}{k}\left[\mu_t P-\frac{2}{3}\left(\mu_t\frac{\partial u_i}{\partial x_i}+\rho k\right)\frac{\partial u_i}{\partial x_i}\right]$$
$$+C_{\varepsilon3}\frac{\varepsilon}{k}\mu_t P_B-C_{\varepsilon2}\rho\frac{\varepsilon^2}{k}+C_{\varepsilon4}\rho\varepsilon\frac{\partial u_i}{\partial x_i} \qquad (85)$$

Where, μ_t is the turbulent viscosity.

Coefficients used for the turbulence model are listed in the following table. More details about all other relevant coefficients are given in the StarCD Methodology Manual [183].

Table 6-2: Coefficients used for $k-\varepsilon$ /High Reynolds Number turbulence model in StarCD.

C-mu	C-Eps1	C-Eps2	C-Eps3	C-Eps4	CAPPA	Prandlt (K.E)	Prandlt (Eps)	Prandlt (Enth)
C_μ	$C_{\varepsilon1}$	$C_{\varepsilon2}$	$C_{\varepsilon3}$	$C_{\varepsilon4}$	κ	σ_k	σ_ε	σ_h
0.09	1.44	1.92	1.44	-0.33	0.419	1.00	1.219	0.90

6.4 Mass Transfer Models

When liquid fuel is injected into the combustion chamber of an engine through an injector at high velocity, it disintegrates into droplets. Meanwhile, mass transfer from and heat

transfer to the droplets occurs. In CFD modelling these mass transfer and heat transfer processes are very important because they controls the overall performance of the combustion system. As mentioned in the earlier chapters, liquid fuel becomes vapour and pyrolysis gas through evaporation and pyrolysis respectively and mixes with air before it actually burns and produces energy.

In Chapter 4 and Chapter 5, the mass transfer processes (evaporation and pyrolysis models) and their results for a single droplet are described. In the present section, the mass transfer processes for a burning spray are described including evaporation, pyrolysis and heterogeneous surface oxidation. The processes of mass transfer from the liquid phase used in the present simulation are summarised in Figure 4-3. The mass transfer processes are represented with grey colour in background whereas their products and fuel are represented with white background colour. All these mass transfer processes are implemented in the *drmast* subroutine of StarCD using FORTRAN code.

The low-pressure evaporation model [22] and modified pyrolysis model discussed in previous chapters are applied to spray combustion modelling with some changes. The main objective of the present study is to apply the detailed chemistry of the HFO using continuous thermodynamics and develop a mass transfer subroutine of the droplets in a hot and pressurised environment. The basic mass and momentum transfer equations for general incompressible and compressible fluids used in StarCD are described below [183];

$$\frac{\partial \rho}{\partial t} + \frac{\partial}{\partial t}\left(\rho u_j\right) = s_m \tag{86}$$

$$\frac{\partial \rho u_i}{\partial t} + \frac{\partial}{\partial x_j}\left(\rho u_j u_i - \tau_{ij}\right) = -\frac{\partial p}{\partial x_j} + s_i \tag{87}$$

Where,

$t - time$

$x_i - Cartesian\ coordinate$

$u_i - absolute\ fluid\ velocisty\ in\ x_i\ direction$

$p - piezometric\ pressure$

$\rho - density$

$\tau_{ij} - stress\ tesnsor\ components$

$s_m - mass\ source\ and$

$s_i - momentum\ source\ components$

Similarly, the energy conservation equation used in StarCD is;

$$\frac{\partial \rho h}{\partial t} + \frac{\partial}{\partial x_j}\left(\rho h u_j + F_{h,j}\right) = \frac{\partial p}{\partial t} + u_j \frac{\partial p}{\partial x_j} + \tau_{ij} \frac{\partial u_i}{\partial x_j} + s_h \tag{88}$$

Where is $h = static\ enthalpy = \overline{c}_p T - c_p^0 T_0 + \sum Y_m H_m = h_t + \sum Y_m H_m$ and

$T - temperature$

$Y_m - mass\ fraction\ of\ mixture\ constituents\ m$

$H_m - heat\ of\ formation\ of\ constituents\ m$

$\overline{c}_p - mean\ cons.\ presure\ specific\ heat\ at\ temperatre\ T$

$c_p^0 - reference\ specific\ heat\ at\ temp\ T_0$

$F_{h,j} - diffusional\ energy\ flux\ in\ x_j\ direction$

$s_j - energy\ source\ and$

$h_t - thermal\ enthalpy$

6.5 Ignition Model

The ignition process in diesel engines includes many individual processes such as phase change of fuel and its dispersion, the mixing of vapour with oxidizing media and the chemistry of combustion initiating reactions. Ignition is defined as the start of the extremely fast oxidation in an ignitable mixture [8]. In other words, after the evaporation of liquid into vapour, the vapour mixes with the surrounding gas and starts reacting with the available oxygen molecules. Initially this reaction rate is very slow, but after a while it increases sharply followed by formation of visible flame. This whole phenomenon is called ignition [44] .

Generally, ignition delay is the main characterising variable that measures the ignition quality of the fuels. Ignition delay is defined as the time from the start of injection to the first ignition. In heavy fuel oil, the chemical properties of cutter stock determine the ignition delay. As stated by Goldsworthy[2], cutter stock in HFO may contain aromatic and non aromatic hydrocarbons. Cutter stock containing non-aromatic hydrocarbons will have shorter ignition delay than the cutter stock with aromatic hydrocarbons. During the ignition delay time, flammable mixture of evaporated vapour and surrounding gas forms and combustion initiating reaction occurs. After ignition this mixture burns very quickly and gives a sharp rise in pressure [8].

The ignition model developed by Weisser [189] and used by Goldsworthy [2] is selected here for the ignition process of HFO. This model uses three one-step reactions to represent the low, medium and high temperature timescales, which are given as [2];

$$\tau_{low} = 2.39\times10^{-11}\left(\frac{p}{p_{ref}}\right)^{-0.1}\exp\left(\frac{14000}{T}\right) \tag{89}$$

$$\tau_{med} = 1.33\times10^{5}\left(\frac{p}{p_{ref}}\right)^{-2.125}\exp\left(-\frac{10000}{T}\right) \tag{90}$$

$$\tau_{high} = 2.50\times10^{-8}\left(\frac{p}{p_{ref}}\right)^{-1}\exp\left(\frac{TACT_{high}}{T}\right) \tag{91}$$

As seen in the above equations, the low and high temperature timescales decrease with an increase in temperature, whereas the medium temperature timescale increases with an increase in temperature. The negative temperature dependence used in the medium temperature timescale allows two-stage ignition for poor fuel oil which is demonstrated in the next chapter. Further, $TACT_{high}$ for good fuel and poor fuel is given in Table 6-3.

The overall (characteristic) timescale can be given as [2];

$$\frac{1}{\tau_{ign}} = \frac{1}{\tau_{low} + \tau_{med}} + \frac{1}{\tau_{high}} \tag{92}$$

In the present model, ignition reactions are not allowed until the ignition equivalence ratio reaches 0.3. In each cell, the ignition kinetics determines the reaction timescale till the temperature of the cell reaches the temperature at which the combined combustion kinetics and turbulence timescales take over (discussed in the next section).

6.6 Combustion Model

The combustion model provides the reaction rate once ignition has occurred. The reaction rate appears in the source terms of the enthalpy and the species transport equations. Generally, the reaction rate is determined from an empirical expression. In the present model a combustion model developed by Goldsworthy [2, 186, 190] is employed. It is assumed in the present study that fuel vapour and air are fully mixed in each computational cell.

The species developing from the evaporation of each droplet are represented by n-dodecane ($C_{12}H_{26}$). The molecular weight of the n-dodecane is similar to the lightest fraction of heavy fuel oil. Baert [14] suggested that thermal cracking yields volatile products and the majority of them are paraffinic or olefinic molecules containing < 10 carbons along with small amounts of H_2, H_2O and CO_2 molecules. In the combustion modelling, a precise form of molecule to represent the combustion is not extremely important [2]. The main important parameters are the carbon to hydrogen ratio and the lower heating value (LHV) of the fuel. In addition, the combustion rate is primarily controlled by the mixture strength and the turbulent mixing rate. In the present work, the lower heating value (LHV) of HFO is set as 40 MJ/kg and is typical of HFO found in a handbook by Petchers [191] and also in experimental measurement made by Takasaki et al. [1].

The ‘combined time’ model is implemented here to represent combustion. The combined time model uses the summation of turbulence and kinetics time scales. Therefore, the rate of combustion can be controlled either by turbulence or by kinetics or by the combination

of both. The rate of combustion is determined by local concentration of fuel, oxidant and the combined timescale. Here combustion products are assumed as CO_2 and H_2O only. The stoichiometric reaction of n-dodecane combustion with oxygen is given as follows;

$$C_{12}H_{26} + 18.5\,O_2 \rightarrow 12CO_2 + 13H_2O \tag{93}$$

The kinetic time scaled rate in the present model is derived from a one-step reaction as [2, 183];

$$Rate = A[fuel]\exp\left(-\frac{E_{ACT}}{\mathcal{R}T}\right) \tag{94}$$

Hence,

$$\tau_{kinetic} = A^{-1}\exp\left(-\frac{E_{ACT}}{\mathcal{R}T}\right) \tag{95}$$

The values of constant A and E_{ACT} in the above equations are adjusted for different qualities of heavy fuel oil to match the experimental reaction rates.

Changing the species for combustion may change the ignition and combustion behaviour. However, similar results can be achieved by changing the activation energy and the rate constant in the above equations. These rate parameters are set according to the fuel quality. Primarily the chemical nature of cutter stock and the volatile products of cracking influence the combustion rate in the context of heavy fuel oil. The details of these rate parameters are given in Table 6-3.

The turbulent mixing time scale is given as [2, 183];

$$\tau_{turbulent} = B\left(\frac{k}{\varepsilon}\right) \tag{96}$$

The combined timescale is given as [2, 183];

$$\tau = \tau_{kinetic} + \tau_{turbulent} \tag{97}$$

The overall combustion rate in kg/m^{3}s is given as [2, 183];

$$Rate = \frac{\rho}{\tau} \min\left(fuel\ mass\ fraction, \quad \frac{O_2\ mass\ fraction}{r} \right) \tag{98}$$

Where r is the stoichiometric oxygen to fuel ratio mass. The above equation (98) controls the combustion reaction rate in fuel rich regions as well as in fuel lean regions.

The parameters for reference model setting in StarCD (similar to those used by Goldsworthy [2]) are summarised in the Table 6-3 with their primary influences on models performance.

Table 6-3: Reference HFO model settings

Model parameter	**Value**	**Primary influence**
Kinetic timescale factor A	2×10^9	Combustion rate
Turbulence timescale factor B	0.06	Combustion rate
Combustion activation energy (E_{ACT})	1.2×10^5 kJ/kmol (good fuel)	Early pressure rise rate, Ignition delay
	1.35×10^5 kJ/kmol (poor fuel)	
Activation temperature for high temperature ignition timescale $(TACT_{high})$	14000 K (good fuel)	Early pressure rise rate, Ignition delay
	16000 K (poor fuel)	
Ignition timescale factor (FIGN)	4 (good fuel)	Early pressure rise rate, Ignition delay
	3 (poor fuel)	

6.7 Soot Models

According to Williams [11] and Ciajolo & Barbella [146], there are two types of soot formed during combustion. The first one is formation of soot in the liquid phase and the other one is the formation of soot in the gas phase. Incomplete combustion of liquid

produces the soot particles known as cenospheres. The gas phase soot is a consequence of many undesirable chemical reactions of fuel vapour and pyrolysis gas in the fuel rich core of the spray [146].

6.7.1 Liquid Phase Soot Burnout Model

At high temperature after most of the volatile products of evaporation and thermal decomposition have left the droplet, the polymer formed in liquid phase through pyrolysis starts oxidising with the surrounding oxygen. This process of polymer heterogeneous surface oxidation is known as the polymer burnout phase. However, sometimes due to the lack of oxygen or due to the formation of non-volatile components within the liquid phase, the liquid (which includes original liquid and formed polymer) cannot oxidise. This un-oxidised liquid is called cenospheres [192]. In general, cenospheres are carbonaceous residues of the spray droplets, full of voids [41].

In the present model, the heterogeneous surface oxidation (burnout) of the polymer is allowed only when the aromaticity of liquid reaches 0.9 or more, and 95% of the original droplet mass has been converted to polymer. A simplified and similar approach to StarCD's char burnout model for coal combustion is employed in the present work. The stoichiometric reaction of carbon (polymer) surface burnout/oxidation with oxygen is given as follows;

$$C + O_2 \rightarrow CO_2 \tag{99}$$

Analogous to the n-dodecane combustion model, the combined rate coefficient model is implemented here to represent the burnout of polymer. The polymer burnout rate can be controlled by either the diffusion rate or the chemical reaction rate.

The diffusion rate coefficient can be given as [183];

$$K_d = 5.06 \times 10^{-12} \frac{T_{Ref}^{0.75}}{d} \tag{100}$$

Where, T_{ref} is the reference temperature as explained in the Appendix.

The chemical rate coefficient can be given as [183];

$$K_c = A_{poly} \exp\left(-\frac{E_{poly}}{\mathcal{R} T_{droplet}}\right) \tag{101}$$

Where, A_{poly} is the pre-exponential factor for polymer given as 1.3 $kgm^{-2}s^{-1}(Nm^{-2})^{-n}$,

n = reaction order.

$\mathcal{R}$ = universal gas constant (8314.3 J/kmolK)

E_{poly} is the activation energy for polymer as $9.27*10^7$ in J/kmol, and

$T_{droplet}$ is the droplet temperature in K.

Hence, the overall rate coefficient can be given as [183];

$$q = \left(\frac{K_c K_d}{K_c + K_d}\right) P_g \tag{102}$$

Where, P_g is the partial pressure of oxygen in the gas phase in Pascals.

Thus, the polymer burning rate based on surface area can be obtained as [183];

$$\frac{dPoly}{dt} = -q\pi d^2 \tag{103}$$

The above equation provides the burnout rate of the polymer in the oxidising environment. According to Borman [44], the burnout rate of polymer also depends on the porosity of the formed polymer. The pyrolysis reactions establish the porosity, and depending upon the porosity, the oxygen and other gases diffuses into the pores and react. During combustion the porosity and the surface area of the droplet may change due to high temperature. Thus,

considering all chemical and physical aspects of polymer reactivity, modelling the polymer burnout from first principles is very difficult [44].

6.7.2 Gas Phase Soot Model

The soot burnout in the gas phase helps in determining the visual flame extent. In the present modelling, the basic model developed by Nishida & Hiroyasu [193] and used by Goldsworthy [2] for gas phase soot formation and burnout in the HFO combustion model is used. This model supports the experimental findings of Barbella et al.[194] that soot emission from any combustion system is a result of competition between the actual soot formation and its oxidation (consumption) processes. The present model accounts for formation and oxidation processes by empirical *Arrhenius* type equations. The production of soot in the computational cell is determined by the difference in soot formation rate and the soot consumption rate.

$$\frac{dM_S}{dt} = \dot{M}_{SF} - \dot{M}_{SC} \tag{104}$$

The soot formation rate is given by a simple one-step global reaction as;

$$\dot{M}_{SF} = A_{SF} P^{0.5} \exp\left(-\frac{E_{SF}}{\mathcal{R}T}\right) M_{FV} \tag{105}$$

Where, M_{FV} is the fuel vapour mass concentration and P is the pressure in bar.

The soot consumption rate is given as;

$$\dot{M}_{SC} = A_{SC} \frac{P_{O_2}}{P} P^{1.8} \exp\left(-\frac{E_{SC}}{\mathcal{R}T}\right) M_S \tag{106}$$

Where, M_S is the mass of soot. The parameters for the one step global reaction for soot formation and soot consumption are obtained from Li et al.[195] and are summarised in the following table .

Table 6-4: The parameters for vapour phase soot burnout rate

Soot formation rate	Soot consumption rate
$A_{SF} = 7.0*10^3$ 1/s	$A_{SC} = 2.2*10^3$ 1/s
$E_{SF} = 50.13*10^6$ J/kmol	$E_{SC} = 58.77*10^6$ J/kmol

6.8 Physical Properties of Liquid Fuel and Vapour

The physical properties of liquid fuel and the composition of liquid fuel can affect the performance of engines and pollutant emissions [196]. The following section describes the details of all properties used in the present modelling.

The density of HFO is simulated using equation (113) as shown in the Appendix. As shown in that equation, the total density of HFO is given as a function of composition. The density of individual components is assumed constant because it increases with the increase in the molecular weight but at the same time it decreases with the increase in droplet temperature. However, the total density of HFO varies as the evaporation of light components (component 1, 2 and 3) progress. The droplet viscosity is held constant as 15 mm^2/s, which is the representative viscosity at the point of injection for HFO [2]. The viscosity increases with molecular weight but it decreases with increasing temperature. Similarly, the surface tension coefficient is also taken constant as 0.04 N/m.

The heat of vaporisation or evaporation enthalpy is the amount of energy required to convert the liquid into a gas. The evaporation enthalpy can be taken as constant but it varies with temperature and it completely vanishes when the temperature of a component reaches its critical temperature [197]. The evaporation enthalpy for the light components (n-paraffins, naphthenes and aromatics) of HFO is simulated using the critical temperature relationship as shown in the Appendix. The evaporation enthalpy of residue (fraction four) is not known experimentally hence a constant value of 232 kJ/kg, as used by Goldsworthy [2], is assumed. As stated in the previous chapter, residue decomposes (cracks) at high temperature. Therefore, the decomposition enthalpy must be added to the evaporation enthalpy. Baert [14] used 1000 kJ/kg as the combined enthalpy (decomposition enthalpy and evaporation energy) of heavy fuel oil. Moreover, as stated by Goldsworthy [2], a combined higher enthalpy is needed to represent the high aromatics content of HFO.

Hence, a similar approach as Goldsworthy [2] is simulated for the evaporation enthalpy for the heavier fraction of heavy fuel oil which is given as [2, 31],

$$h_{combined} = 232 + LHV \times \exp\left(-2.7\frac{T_{cri}}{T_{drop}}\right) \quad \text{kJ/kg} \tag{107}$$

Where, T_{cri} is the critical temperature (1000 K constant) and T_{drop} is the droplet temperature. Only in this expression, the droplet temperature is limited to 850 K for the heaviest fraction of heavy fuel oil. Beyond this temperature, exothermic polymerisation rate may be comparable to the endothermic thermal cracking rate, therefore decomposition enthalpy is held constant. The decomposition enthalpy at 850 K is 1710 kJ/kmol which is higher than the value used by Baert [14].

The mean specific heat capacities of the droplet components are simulated as shown in the Appendix. It is given as the second order polynomial function of temperature for all four components. Similarly, the critical temperatures of the droplet components in the model are calculated as shown in the Appendix. The critical temperature of the entire droplet needed as an input in StarCD is assumed as 2000 K. At this temperature, StarCD causes the droplet to instantly evaporate. This value is unlikely very high compared to used by Goldsworthy [2] as 1200 K. However, it allows droplet to remain in the computation and go through surface oxidation.

All properties of vapour phase reactants ($C_{12}H_{26}$, O_2 and C) and products molecules (CO_2 and H_2O) are adopted from the standard StarCD database excluding the lower heating value (LHV) of $C_{12}H_{26}$ which is set as the similar to the LHV of HFO by modifying the formation enthalpy of the fuel scalar. All numerical relationships for the properties are developed in the *dropro* subroutine within StarCD.

6.9 Computational Grids Development for CFD

The computational grid is the one of the most fundamental aspects of CFD modelling. The process of discretisation of the spatial domain of complex geometry into the small

volumes (cells) is known as grid development. In the present modelling, the grids developed by Goldsworthy [2] have been used. These computational grids are three dimensional. A square grid is used in the centre and gradually smooth grid is used on the edge. Figure 6-2 and Figure 6-3 show the reference grid for the CVCC (180,000 cells) and the FIA (110,000 cells) respectively.

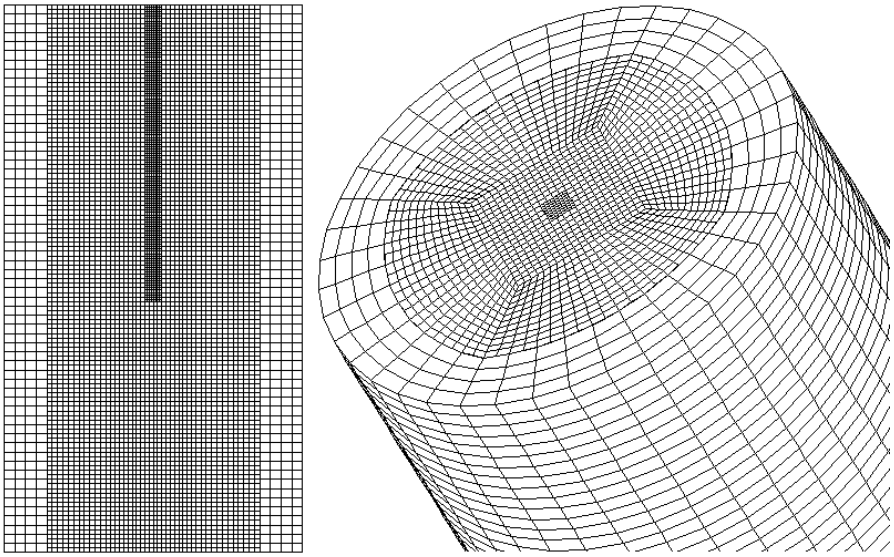

Figure 6-2: Computational grid for the CVCC, sectional view through central axis and enlarged isometric view (courtesy of Goldsworthy [2]).

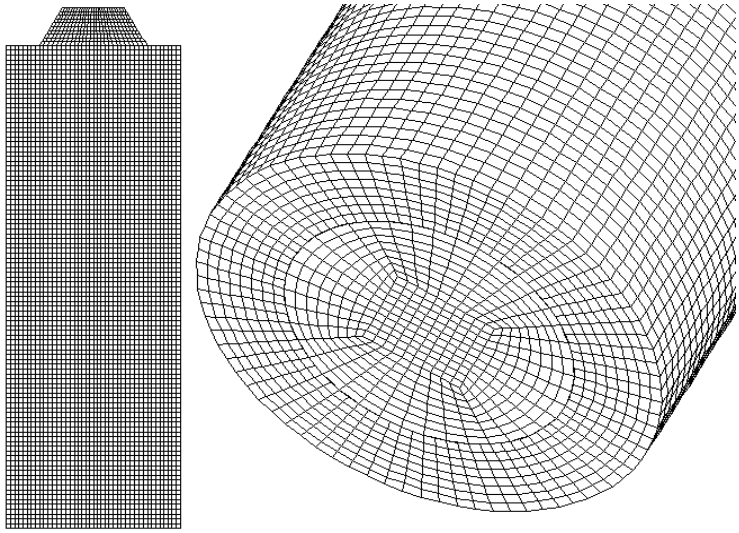

Figure 6-3: Computational grid for the FIA, sectional view through central axis and enlarged isometric view (courtesy of Goldsworthy [2]).

As shown in the above figures (Figure 6-2 and Figure 6-3), cells in the core of the spray are very fine and their dimension is in between 1-1.5 mm. The cell size in the main combustion region is in between 1.5-2 mm. In the FIA grid, the cell size at the outer

extreme increases up to 2.5 mm circumferentially, however it remains less than 2 mm axially and racially. The CVCC chamber was designed in such a way that the influence from the wall on the spray can be minimised. Therefore, cells are contracted in the visible combustion region. As noted by Goldsworthy [2], the size of the cells between the wall and the outer edge of the visible flame has an influence on the flame penetration. The cell size around the core of CVCC spray is 1 mm.

At the central square grid of the spray, an even number of cells are used so that the injector axis is aligned with the intersection of four cells. This even number arrangement gives less discretisation error compared to an odd number of cells. The sensitivity study by Goldsworthy [2] for the effect of grid size on various combustion and spray parameters (maximum rate of pressure rise, ignition delay, spray penetration at 8ms, time to maximum pressure rise rate, and maximum temperature at 8 ms) for the modelled good fuel in the FIA is shown Figure 6-4. The various parameters shown in this figure are plotted against the percentage deviation of the same parameters for finest grid, alongside cell size in the central square grid. It is clearly observed from this figure that out of all above mentioned parameters, spray penetration is greatly influenced by grid size, followed by maximum temperature. Moreover, it is observed that at the reference grid size (1.4 mm central grid size), all parameters are within 5% of the values obtained at the finest grid (0.7 mm). In other words, at the reference grid size, the maximum discretisation error has reduced to acceptable value.

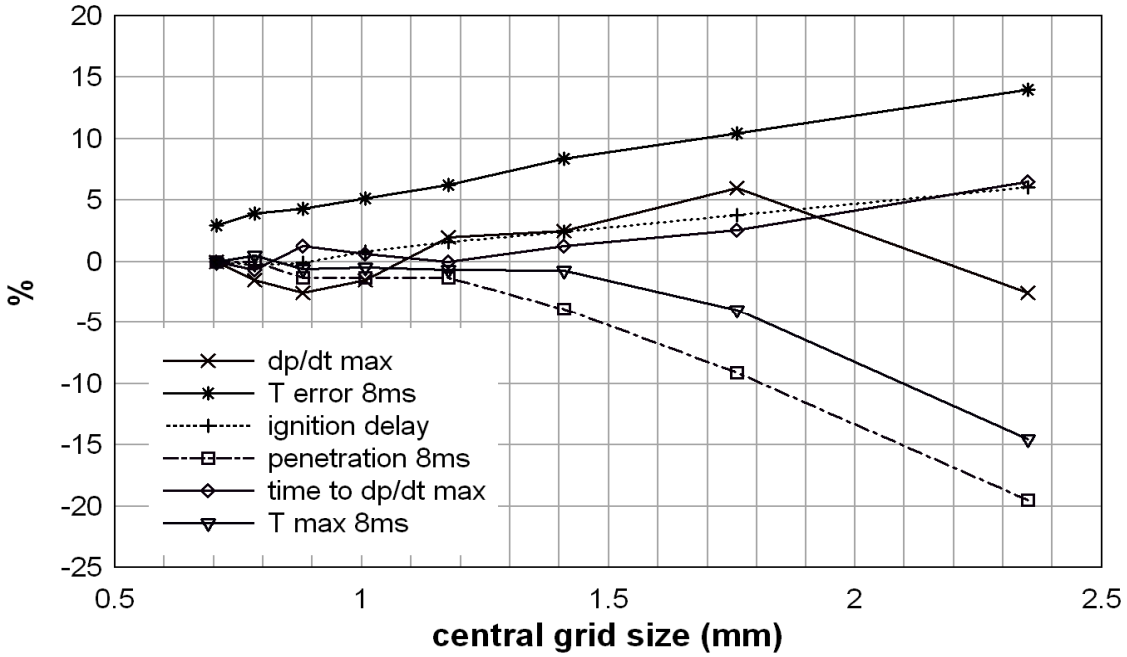

Figure 6-4: Effect of grid size on various parameters (maximum rate of pressure rise, ignition delay, spray penetration at 8ms, time to maximum pressure rise rate, and maximum temperature at 8 ms) for the modelled good fuel in the FIA (courtesy of Goldsworthy [2]).

6.10 Solution Methods

6.10.1 Solution Method

Numerical calculation plays an important role during the spray modelling. The developed model should be fast, accurate and realistic to represent the process of combustion. StarCD contains many algorithms (SIMPLE, PISO and SIMPSO) to solve the finite volume equations resulting from the discretisation of the geometry [183]. The SIMPLE algorithm generally applies to the steady-state calculation with only one corrector stage. The PISO algorithm mainly applies to transient problems with efficient iterative methods. And as the name applies the SIMPSO is a combination of SIMPLE and PISO algorithms. All these algorithms can be applied for Lagrangian multi-phase flow calculations. Lagrangian multi-phase flow consists of two phases, one the continuous phase (gas phase) and the other dispersed phase (liquid droplets). The motion of the dispersed phase is generally affected by the continuous phase and vice versa. Generally, PISO algorithm is mandatory for unsteady calculation. In the present modelling context the PISO algorithm

with “Coupled flow” type of two-phase Lagrangian calculation is employed. This allows the coupling between the continuous phase and the dispersed phase. The continuous phase properties and the dispersed phase properties significantly influence each other.

The droplet Courant number controls the number of time steps needed to trace the droplet within the cell and it determines the accuracy of trajectory calculations. For the numerical stability of the droplet, the Courant number must lie in between 0 and 1. In general, the Courant number equals 0.35 requiring about three time steps. In the present calculation the courant number is taken as 0.3 for accuracy.

The proper selection of solution procedure for numerical calculation of coupled type flow in StarCD is very important. There are two types of procedures available in StarCD for coupled type flow (1) Standard and (2) Predictor Only. The improper selection of solution procedure caused many problems during the subroutine development and subsequently it affected the progress of the present project. Hence, these procedures are described in detail; the definitions of these two procedures are given in [183] as;

1) Standard:- In this procedure, source terms associated with droplets are calculated during the predictor and each corrector stage of PISO algorithm and then under-relaxed using the factor specified in the Under-Relaxation of Lagrangian sources box.

   In other words, during the predictor stage, the positions, velocities, temperatures and sizes of the computational droplets are obtained by simultaneous solution of the dispersed and continuous phase equations, using the sub-cycling time step for the former to cover the overall time step employed for the latter. The two sets of equations are implicitly treated. This is accomplished by means of the dispersed-phase-related source terms in the carrier fluid equations. An under-relaxation factor may be applied to these terms to improve convergence.

   A similar procedure is repeated in the corrector stages, at the end of which the dispersed elements (droplets) are assigned their final positions, velocities, etc. for the interval. The next time step is then commenced.

2) Predictor Only:- Source terms are calculated only once and are kept constant during the corrector stage.

   That means the corrector stage is bypassed completely in this procedure, which reduces the computation power requirement and gives a faster but less accurate solution.

During the earlier part of this project, subroutines for droplet mass transfer *(drmast)* and droplet properties *(dropro)* were developed to be compatible with the Standard solution procedure approach. Using this approach, it is found that StarCD goes through many sub time steps within one time step during the predictor stage and it repeats the same procedure during the corrector stage. Sometimes it is found that StarCD goes through predictor-corrector stages of a complete time step once, and soon it repeats the predictor-corrector stages completely. Moreover, sometime StarCD starts the repetition of the predictor-corrector in the middle of a time step. This procedure caused many problems for the integration of the equations for polymerisation rate (37) and thermal cracking rate (38), because integration needs to be restarted when the predictor-corrector restarts. For new every sub-time step, the total amount of polymer formed at the previous time is required. Attempts are made to store this value using the *postdat* subroutine, but *posdat* subroutine is only called either at the beginning of the time step or at the end of the time step. Thus, it is not possible to store and recover these values in the middle of a time step. Moreover, there is not only a single variable available for the user within StarCD, which identifies when and why the predictor-corrector restarts. Hence, it is found very difficult to use the Standard solution procedure to develop the droplet mass transfer subroutine *(drmast)* because the equations (37) and (38) in this subroutine require the total amount of polymer formed. It is not a big issue to develop the model for when StarCD repeats the complete time step but it became more difficult when StarCD starts the repetition of the predictor-corrector in the middle of a time step. Therefore in the present modelling study Predictor Only (second approach) is used. In this procedure StarCD goes forward only but by using a small time step value (5×10^{-6} s), the loss of accuracy of the computation is been minimised.

6.10.2 Parallel Running StarCD on Multiple CPU

After the selection of a solution procedure, another problem was identified. The second problem was running StarCD on multiple CPUs. When a droplet leaves one CPU to transfer to another during the iteration the information stored in user arrays is lost. In the present model, some properties of the liquid such as; the mean molecular weight, the width of the distribution function, the total mass of polymer and the total mass of gas are traced for each parcel in the spray. Some of these properties are essential throughout the droplet life time for the purpose of mass balance. It means that these properties of the droplets, which are stored with the droplets and are required for further processes; go missing during the change of CPUs. To solve this problem, some message passing interfaces (subroutines) were tried. However, these message passing routings only can be applied in the *posdat* subroutine and the *posdat* subroutine is only called either at the beginning of the time step or at the end of the time step. Hence, still this problem remains unsolved because droplets can move to a new processor (CPU) within an integration time step. Therefore, all processing is been done on a single CPU, which does not affect solution accuracy but only computation time

6.11 Summary

The present chapter summarises the development of an integrated computer simulation model for heavy fuel oil. It provides an extension of the previously developed models for a single droplet, as well as some additional subroutines for the spray combustion of heavy fuel oil. The improved subroutines include modified models for; mass transfer, droplet properties, ignition, combustion and soot formation. The validation of CFD models developed in the present chapter with the available experimental results from the literature is given in the next chapter.

Chapter 7. Qualitative Comparison of Spray Combustion Modelling Results with Published Experiential Data

7.1 Introduction

In previous chapters, models for evaporation and pyrolysis of a single droplet and also for a burning spray are described. These models employ the available experimental information to predict the combustion behaviour of heavy fuel oil. Those developed models are not convincing unless they are validated against the real conditions of a burning spray. Therefore, the present chapter outlines the comparison of the theoretical predictions against the limited available experimental data in the literature. As discussed in the literature survey (Chapter 2), experimental data from two constant volume combustion chambers are available for the combustion of heavy fuel oil spray and are used for the validation of the present models. In other words, the present chapter explores the theoretical spray model validation against the experimental results from the Visual Constant Volume Combustion Chamber (CVCC) and Fuel Ignition Analyser (FIA). These two sets of experimental data provide validation of the generality of the present models. Furthermore, the present models are also validated against the simplified models developed by Goldsworthy [2] for the combustion of heavy fuel oil in a high pressure environment.

The data from the CVCC from Kyushu University provides flame and spray observations, whereas the data from Fuel Ignition Analyser (FIA) developed by FUELTECH Norway provides chamber pressure data [2]. Injection for the CVCC proceeds beyond ignition, for a total of 25 ms, whereas injection for the FIA finishes before combustion starts. Therefore, turbulent mixing rates are decreasing throughout combustion in the FIA; on the contrary, fuel is burnt during injection in the CVCC. The experimental results of CVCC and FIA are summarised in section 7.2.1 and 7.2.2 respectively.

7.2 Literature Experimental Results

7.2.1 Constant Volume Combustion Chamber (CVCC) Results

The experiment set up for the combustion of bunker fuel oil (heavy fuel oil) using the CVCC is shown in Figure 2-11. As shown in that figure, a high speed video camera is used to capture the visual extent of the burning spray at 1 ms intervals. Measurement of heavy fuel oil combustion using the CVCC is described in detail by Takasaki et al.[1]. A back-diffused laser technique (BDL) is employed to identify the unevaporated fuel and soot inside the burning spray.

The available data from Takasaki et al.[1] helped in the present study to set up the model parameters for spray angle, ignition delay, spray penetration and the spatial extent of combustion. Takasaki et al.[1] measured the combustion characteristics of two different heavy fuel oils; one with good combustion characteristics (BFO-S) and the other with poor characteristics (BFO-A). The data from the back-diffused laser experiment demonstrate that the spray has penetrated about 160 mm by 7 ms after the start of injection. Once combustion has started, soot will form in the vapour phase but the present visualisation technique does not differentiate between the unburnt fuel and formed soot.

7.2.1.1 Test Fuels for CVCC

The detailed chemical characteristics of the fuels used by Takasaki et al.[1]. are summarised in this section. According to Takasaki et al.[1], marine diesel engines which used BFO-A suffered heavy wear of cylinders, whereas the same engines have not faced any problems when BFO-S was used as a fuel. Therefore, BFO-S is considered as a good fuel and BFO-A as a poor quality fuel oil. Table 7-1 summarises the compositions by silica-gel chromatography obtained by Takasaki et al.[1] and the basic properties of both these fuels.

Table 7-1: Compositions and properties of heavy fuel oil (from Takasaki et al.[1]).

Compositions		BFO-S	BFO-A
Saturated hydrocarbons (% by weight)	Paraffins	20.3	5.2
	Naphthenes	10.4	19.0
Aromatic hydrocarbons (% by weight)	1 Ring	23.6	30.4
	2 Ring	15.7	28.1
	3 Ring	3.9	6.9
	> 4 Ring	4.6	2.4
Sulfied aromatic hydrocarbon (% by weight)		8.9	2.4
Asphaltene (% by weight)		9.5	4.6
Unknown(% by weight)		3.2	1.0
Total(% by weight)		100	100
Physical Properties			
Density at 15 ^{0}C kg/mm^3		990	986
Kinematic viscosity at 50 ^{0}C mm^2/s		357	320

As shown in the above table, results of composition analysis of both the fuels showed that BFO-A (poor fuel) contains 24% saturated hydrocarbon, which is lower than good fuel BFO-S (31%). The percentage of aromatic hydrocarbons is very high (67%) in BFO-A compared to BFO-S (47%). Both these fuels contain residue of more than 50% by volume and the properties of the residue have not been verified except for the overall properties given in the Table 7-1. The distillation temperature profiles obtained by Takasaki et al.[1] of these two fuels are shown in Figure 7-1.

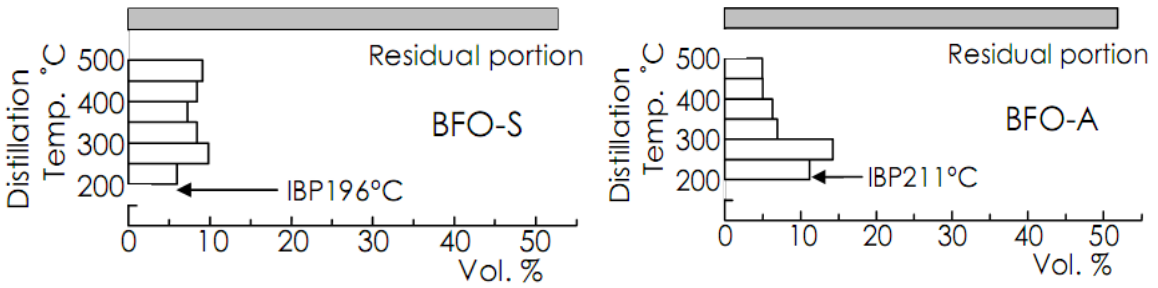

Figure 7-1: Distillation temperatures of BFO-S and BFO-A (courtesy of Takasaki et al.[1]).

It is clear that BFO-S (good fuel oil) contains a greater amount of high-boiling point distillate than the BFO-A (poor fuel oil). In other words, BFO-A contains more low-boiling point distillate in the range of 200-300 ^{o}C compared to BFO-S. The distillation of these fuels only gives the idea about the boiling point of the cutter stock but it does not give any idea about the chemical nature (composition/structure of the molecules) of the cutter stock. Hence, gas chromatography was employed to understand the chemical nature of the cutter stock. The gas chromatographs of both these fuels obtained by Takasaki et al.[1] are shown in Figure 7-2.

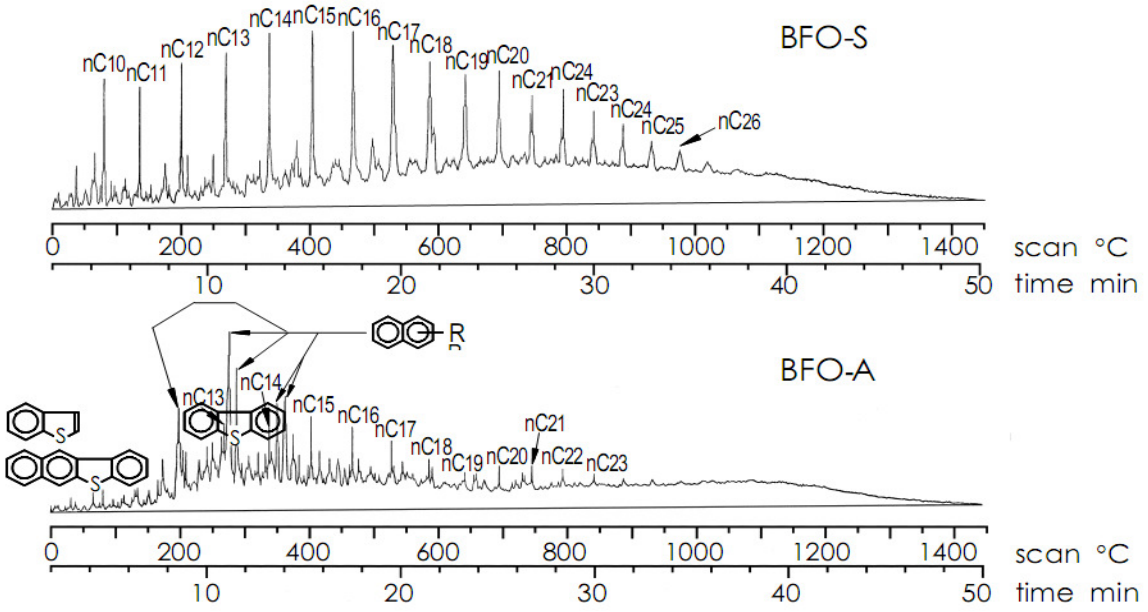

Figure 7-2: Gas chromatography analysis of BFO-S and BFO-A (courtesy of Takasaki et al.[1]).

Chromatographic analysis of the cutter stock shows that in trouble free BFO (BFO-S) sharp peaks of paraffins are observed while in troublesome BFO (BFO-A) naphthalene (aromatics) peaks are found.

The above mentioned information is worthwhile to note here because it actually helped in setting up the composition of the good fuel oil and the poor fuel oil for the simulation. The higher percentage of paraffins as mentioned in Table 7-1 and the chromatogram of the cutter stock of BFO-S reveals that the cutter stock of BFO-S is mainly paraffinic in nature. On the other hand, the higher percentage of aromatics (refer Table 7-1) and the chromatogram of the cutter stock of BFO-A reveals that the cutter stock of BFO-A is more aromatic in nature. This composition information is vital because to apply the continuous

thermodynamics model developed in Chapter 4, the detailed composition of cutter stock (see Table 4-1) is necessary. Both the fuels are assumed to contain 30% cutter stock and 70% residue. The compositions of cutter stocks of the good fuel and the poor fuel used in the simulation are given in Table 7-2. The simulated good fuel oil contains 15% n-paraffins by mass in the HFO, this means 50% of the cutter stock is n-paraffins. On the other hand, the cutter stock of poor fuel oil is set to contain 15% aromatics by mass in the HFO. This means 50% of the cutter stock is aromatics. Thus, by changing the detailed composition of the cutter stock, the nature of cutter stock is established to coincide with the experimental findings.

Table 7-2: Composition of the good fuel and the poor fuel used in the simulation.

Components	**Mass Fraction (%)**		**Distribution Origin (γ)**	**Distribution mean (θ) (Mean Molecular weight)**	**Standard Deviation (σ)**
	Good fuel	**Poor fuel**			
n-Paraffins	0.15	0.05	160	340.00	43.69
Aromatics	0.05	0.15	160	300.00	45.75
Naphthenes	0.10	0.10	160	370.00	45.47
Total	**0.3**	**0.3**			
Residue	**0.7**	**0.7**	500	850.00	320.15

The experimental visual flame images for combustion of the good fuel and the poor fuel in the CVCC are presented in Figure 7-3 and Figure 7-5 respectively. It is clearly observed from these figures that good fuel (BFO-S) ignites 3 ms after the start of injection whereas the poor fuel (BFO-A) ignites almost 7 ms after the injection. The chamber is initially at 2.5 MPa pressure and 873 K. During the simulation, fuel with 50 MPa pressure is injected through a nozzle which is 0.16 mm in diameter, for a 25 ms period. The total injected fuel mass is 0.124 g.

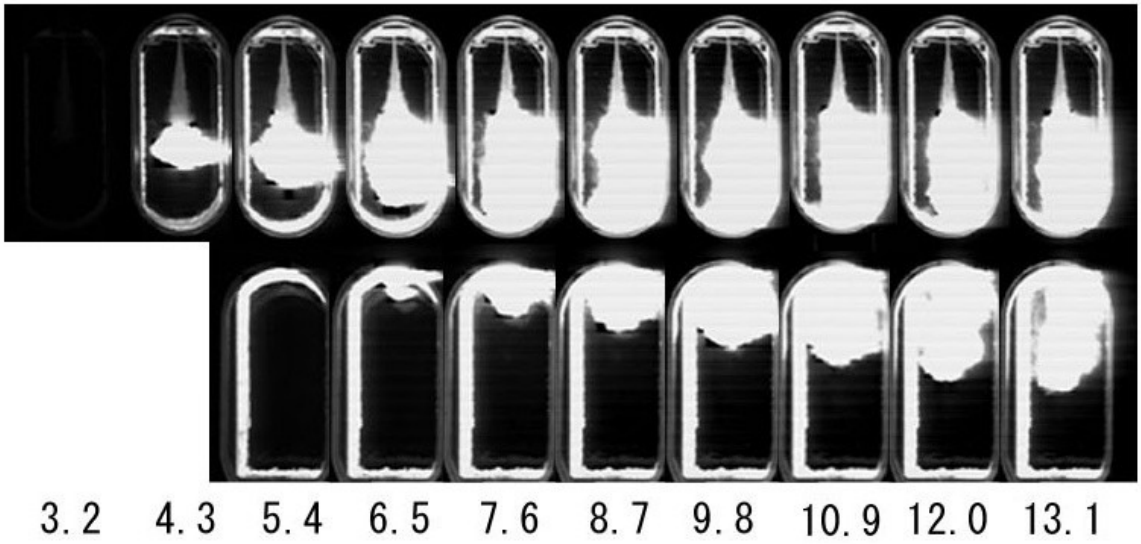

Figure 7-3: Visual flame images for the CVCC good fuel (BFO-S) in the upper and lower windows of the CVCC, against time (ms) from start of injection (courtesy of Takasaki et al.[1]).

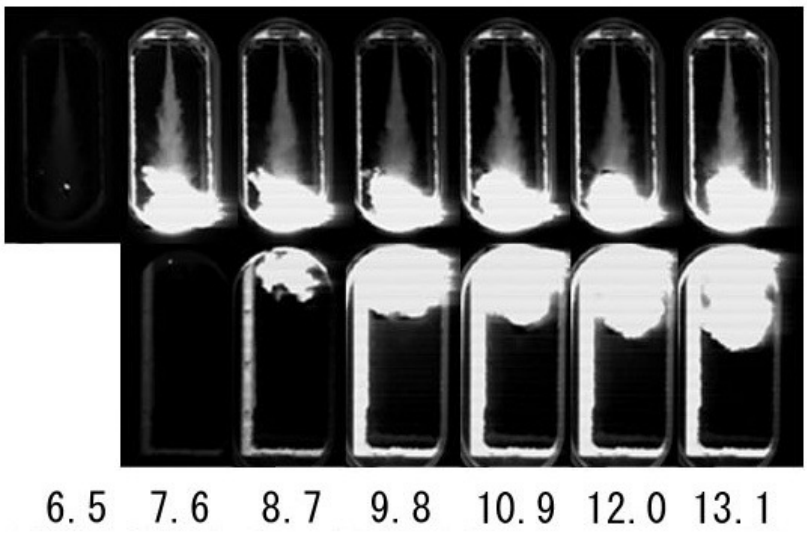

Figure 7-4: Visual flame images for the CVCC poor fuel (BFO-A) in the upper and lower windows of the CVCC, against time (ms) from start of injection (courtesy of Takasaki et al.[1]).

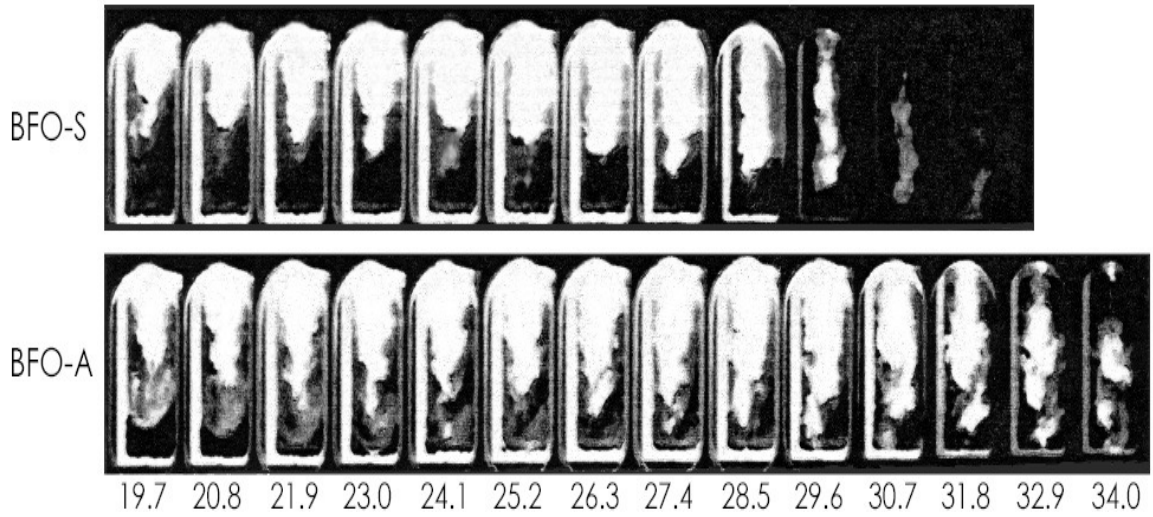

Figure 7-5: Visual flame images for the CVCC good fuel (BFO-S) and poor fuel (BFO-A) in the lower window of the CVCC, against time (ms) from start of injection (courtesy of Takasaki et al.[1]).

Figure 7-5 shows the visual flame images of the good fuel and the poor fuel beyond 19.7 ms and till 34 ms from the start of the injection. It is clearly observed that as the combustion precedes the flame extent moves toward the bottom wall of the chamber in an irregular pattern.

7.2.2 Fuel Ignition Analyser (FIA) Results

As mentioned in the literature survey, the Fuel Ignition Analyser (FIA) is a commercial version of the CVCC and it is a useful tool to measure the combustion characteristics of heavy fuel oil. The FIA chamber is initially at 4.5 MPa pressure and 773 K. During the simulation, fuel with 40 MPa pressure is injected through a nozzle which is 0.32 mm in diameter for a 3.6 ms period. The total injection fuel mass is 0.06 g. The data obtained from the tests are described in Figure 7-6 for good fuel, poor fuel and very poor fuel. The pressure change vs. time results shown for good, poor and very poor fuels are obtained from the mean of the data obtained from 10 or more tests. Here, the test fuels are not the same as the test fuels used in the CVCC. The result shows that ignition of the poor fuel and the very poor fuel occurred in two-stages as apparent from the two local maxima in the pressure change. Goldsworthy [2] noted that by reducing the ignition timescale factor, the ignition delay of the fuel can be reduced and subsequently the tendency of two-stage ignition can be diminished.

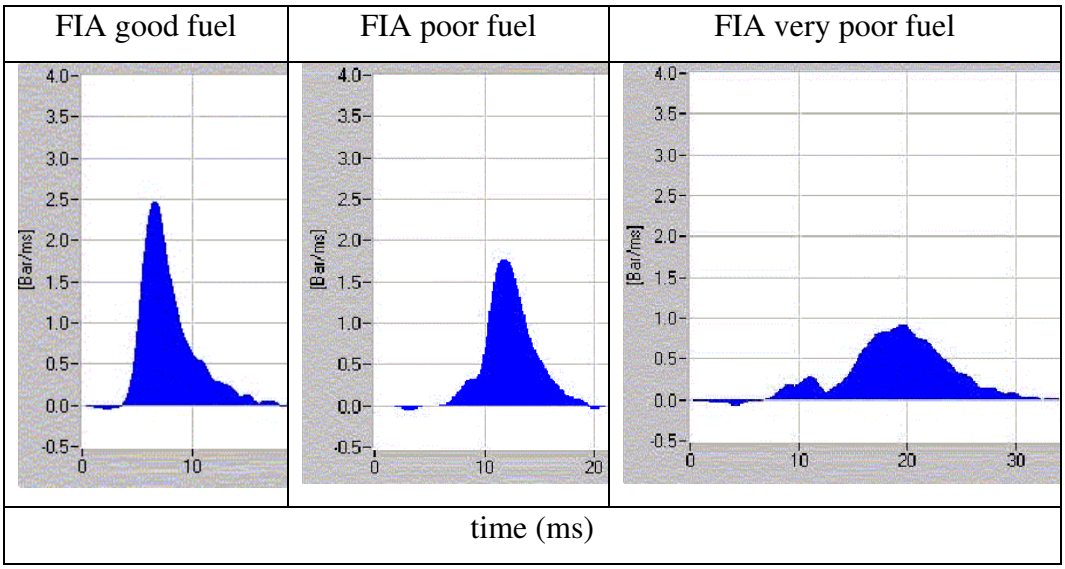

Figure 7-6: Measured pressure rise rate (bar/ms) in the FIA for a good, poor and very poor heavy fuel oil (courtesy of Goldsworthy [2] and Fueltech AS, Norway).

7.3 Simulations Results and Discussions

The comparison of CFD simulations of good and poor fuel oils with the CVCC and FIA experimental data are given in this section. To explore the impact of lighter and heavier cutter stock, the modelled mean molecular weights of the components and the compositions of pure hydrocarbons (n-paraffins, aromatics and naphthenes) in cutter stock can be altered. In the present study, the variable influence for the cutter stock is taken as its ignition quality parameters such as the combustion activation energy, activation temperature for high temperature ignition timescale and ignition factor along with its original composition. Predicted spray angle, flame location, pressure rise rate are optimally matched to the measurement using the reference model settings given in Table 6-3.

As noted by Goldsworthy [2], further tuning of HFO model constants could help to match the experimental data closely. However, consistent data are used here in order to maintain the generality of the models. Therefore, apart from the compositions and the ignition model settings, only the activation energies for the combustion kinetics of the good and poor fuel oil (given in Table 6-3) are changed to match the experimental results. These model setting parameters given in Table 6-3 are indicative only, however they facilitate to adjust the ignition delay, distance from the nozzle to the start of flame in the CVCC and

early pressure rise rate in the FIA. A higher value of activation energy gives a longer ignition delay, a longer distance from the nozzle to the start of flame in the CVCC and smaller pressure rise rate. The combustion behaviour may also depend on the models chosen for turbulence and spray dynamics.

7.3.1 CVCC

7.3.1.1 Good Quality Fuel

The relative composition of the cutter stock and residue used to simulate good quality and poor quality HFO is given in Table 7-2. Both (good and poor) fuel oils in these simulations are made up of 30% cutter stock and the rest is residue. The composition in terms of the mean molecular weights and the width of the distribution functions used for all four fractions are the same as those used for a single droplet (refer to Table 4-1). The reference ignition model settings parameters given in Table 6-3 are chosen to match the modelled and measured delay times. The ignition delay time observed from the experimental results of CVCC and modelling results of Goldsworthy [2] for the good fuel oil is 3 ms after the start of injection.

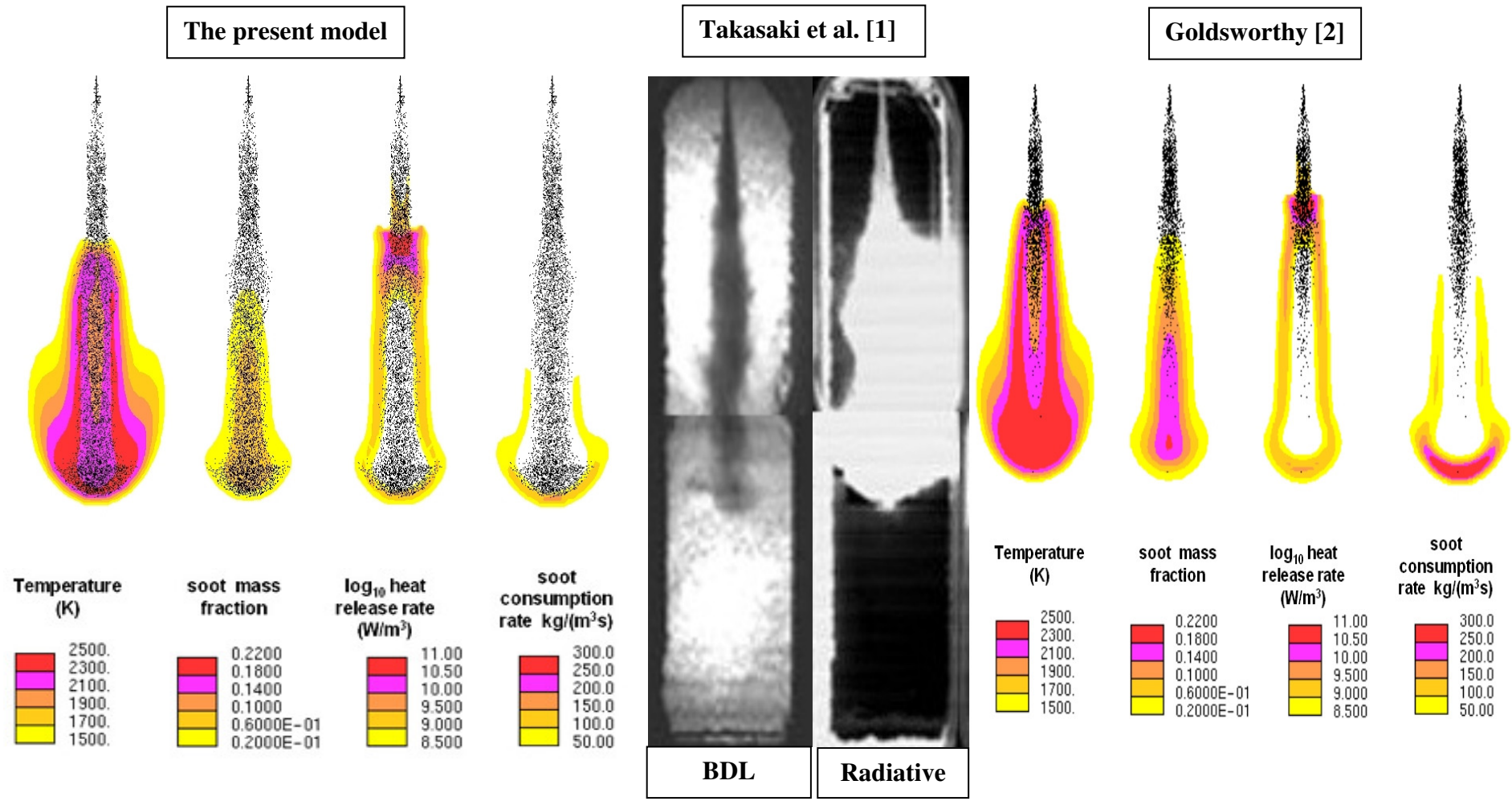

Figure 7-7: Comparison of the present modelled spray results (chamber temperature, soot extent, heat release rate and soot consumption rate) with Goldsworthy's modelled spray results and Takasaki et al.'s measured spray results for soot/spray and visual flame extent of good fuel using the CVCC.

As shown in Figure 7-7, the CVCC simulation results of the present model are compared with Goldsworthy's [2] modelled chamber temperature, gas phase soot extent, heat release rate and gas phase soot consumption rate results and Takasaki et al.'s [1] measured spray results for soot/spray and visual flame extent of good fuel oil; at a consistent spatial scale. The present model results show good agreement with both the modelled and the experimental results at 6 ms after the start of combustion which is 9 ms after the start of injection. The ignition delay in the modelled fuel oil is determined as the time from the start of injection to the appearance of ambient temperature of 1500 K or more. An ignition delay of 3 ms is observed in the present results. This ignition delay observed from the present result of modelled good fuel oil is same as observed by Goldsworthy [2] and Takasaki et al.[1]. This value are set in the present model by setting the ignition factor (FIGN) equal to 4, as shown in Table 6-3. The ignition delay in CVCC experiments is determined as the time from the start of injection to the appearance of a bright flame.

The gas/vapour phase soot mass fraction and its consumption rate observed in the present simulation results are lower than obtained by Goldsworthy [2]. There are two reasons behind this, the first reason is that the soot formation in the present case is divided into two different mechanisms (liquid phase soot and gas phase soot) and what is shown in the figure is only the gas phase soot mass fraction and its consumption rate. The second reason is the lower concentration and combustion rate of the fuel vapour in the gas phase. Since droplets have lower evaporation and pyrolysis rate in the present model they did not produce the same amount of vapour and pyrolysis gas as found in Goldsworthy [2]. The gas phase soot formation is a function of fuel vapour and temperature. Therefore, the gas phase soot mass fraction and its consumption rate observed in the present simulation results are low.

In the centre and towards the bottom of the spray, a temperature contour has lower temperature than that obtained by Goldsworthy [2]. It looks like that the droplets in that region are still pyrolysing therefore absorbing the energy from the surroundings leading to a lower temperature compared to that obtained by Goldsworthy [2]. Moreover, the $\log_{10}$ heat release rate shown in Figure 7-7 coincides with the high temperature region (2300-2500 K). It means that the temperature in the ambient is increased where most heat release through combustion is taking place.

Furthermore, there are more unburnt/unevaporated droplets apparent in spray than for the modelled spray results of Goldsworthy [2]. There are three possibilities behind this; (1) either these droplet are yet pyrolysing; producing polymer and pyrolysis gas, or (2) these droplets are full of polymer and burning through surface oxidation, or (3) these droplets are liquid phase cenospheres remaining at the end of surface oxidation. Polymer formed in the droplet burns through surface oxidation. However, if there is a lack of oxygen in the region the polymer cannot oxidise and remains as liquid phase cenospheres. More detail about cenosphere formation is given in the next paragraph. Further, Goldsworthy [2] used 1200 K as the critical temperature of the liquid droplet which enforced droplets to instantly evaporate at that temperature. Therefore, when the droplet reaches to 1200 K, it instantly evaporates and disappears from the spray. In the present model the critical temperature of droplet is set as 2000 K to allow droplets to remain in liquid phase and go through surface oxidation mechanism after polymerisation is finished. The droplets (parcels) shown in the above figure are representative droplets only, it is not the actual size of the droplets. Each dot is a parcel comprised of many droplets, actual size of the droplet is not represented here. The droplets in the outer regions of the spray are very small and may not be obvious in the experimental data.

As illustrated in Figure 4-3, as soon as modelled fuel enters into the chamber it follows number of mass transfer processes. The heterogeneous surface oxidation of the polymer is the last process. This heterogeneous surface oxidation (discussed in section 6.7.1) requires high temperature and oxygen to oxidise the formed polymer. However, some droplets which are full of polymer may remain in the liquid phase due to unavailability of either high temperature or oxygen. In order to show the reason behind the unburnt droplets in the core of the spray, temperature of droplets along with the oxygen concentration, carbon dioxide concentrations, polymer burnout rate, mixture fraction 1 and fuel vapour concentration of good fuel using CVCC 6 ms after the start of combustion is shown in Figure 7-8.

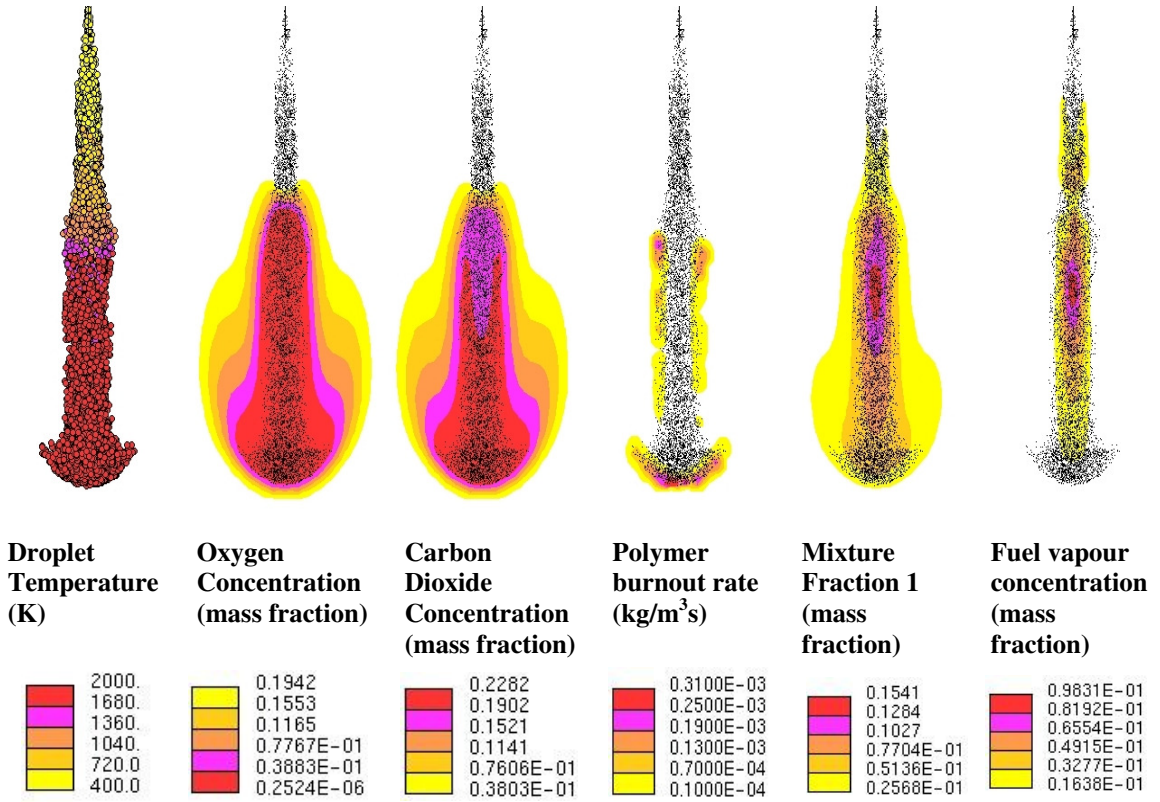

Figure 7-8: Temperature of droplets along with the oxygen concentration, carbon dioxide concentrations, polymer burnout rate, mixture fraction 1 and fuel vapour concentration of good fuel using the CVCC 6 ms after the start of combustion.

As droplets travel through the pressurised hot CVCC and more towards the combustion region they gain heat and thus their temperature increases. The temperature variation of droplets shows the effect of combustion on the spray. As shown in the above figure, the concentration of the oxygen is very low in the centre of the spray therefore the polymer from the droplets cannot oxidise with the oxygen. Hence, this formed polymer remains in the liquid droplet as unburnt liquid which is known as cenospheres [41]. This result concurred with the remark of Versaevel et al.[5] that as combustion progresses, the available oxygen disappears from the leading part of the spray jet. Simultaneously, the high carbon dioxide concentration in the core of the spray confirms that the oxygen from that region is used by earlier oxidation reactions (combustion of vapour and pyrolysis gas). Carbon dioxide is a product of combustion in both the reactions (see eq. (93) and (99)).

Moreover, the polymer burnout rate (surface oxidation) is shown in Figure 7-8 which confirms that when polymer reaches the favourable combustion region it starts burning. Most of the polymer is burning at the bottom and at the surface of the spray where

appropriate amount of oxygen to oxidise and temperature are available. Six (6) ms after the start of combustion the maximum polymer burnout rate is $0.31*10^{-3}$ kg/m^{3}s.

Further, mixture fraction of leading reactant n-dodecane (reactant 1) and concentration of fuel vapour in the chamber are shown in Figure 7-8. The mixture fraction 1 shows the total mass of burned and unburnt fuel vapour whereas concentration of fuel vapour (unburned vapour) only shows the vapour present at that time.

By comparing the fuel mixture fraction 1 from Figure 7-8 with the vapour phase soot mass fraction in Figure 7-7, it is observed that gas/vapour phase soot mass fraction is higher than the total amount of vapour produced and burned so far. In other words, the maximum gas phase soot mass fraction observed in the bottom-centre region of the spray is 0.1, whereas the fuel mixture fraction, which represents the total mass of burned and unburnt fuel vapour, in that region is 0.077. It means vapour phase soot concentration in that region is higher than the mixture fraction 1, which is contradictory and not feasible. Hence, to get the same practical spatial patterns of gas phase soot while reducing soot concentration to realistic levels, both soot formation and consumption rates need to be substantially reduced, that can be achieved by reducing the rate constants. No quantitative data are available to reset the rate constants thus they are left unchanged. The vapour phase soot modelling process is decoupled from the combustion energy and material balance, so excessive soot levels has no effect on energy and material balance.

Furthermore, the present model showed good resemblance when compared with Takasaki et al.'s experimental results. In the results of Takasaki et al. (see BDL image of Figure 7-7) unburnt liquid or soot particles in the core of the spray are clearly observed and the same observations are made for the present model. The dark colour in the BDL image shows that there may be unburnt liquid or soot particles (liquid phase and vapour phase) in the core of the spray after 6 ms from the start of combustion. The modelled flame penetration in the present work is taken as the extent of soot consumption rate indicating the extent of luminous flame. The flame penetration as indicated by the soot consumption rate is similar to the observed modelled results of Goldsworthy[2] and measured spray results of Takasaki et al.[1]. In the next section, a study of a single parcel from the above discussed spray is presented.

7.3.1.1.1 Study of a Single Parcel within the Good Quality Fuel Spray

In the above sections, a comparative study of the burning spray for a good quality fuel is outlined. This study provides the overall picture of the combustion chamber, but it is very important to gain insight into the spray and study the individual processes of combustion in individual droplets. In the present section, a study of a single parcel within the spray is given. In StarCD simulation, the parcel represents a group of droplets having the same properties such as velocity, size, temperature, density, etc. The details of the parcel size, number of droplets in the parcel, temperature, composition, evaporation rates, and mass balance of the parcel are discussed in the following paragraphs. The calculation is shown for only a selected parcel (parcel no. 50) from numerous parcels in the spray. This parcel is injected at $35*10^{-6}$ sec after the start of injection. The choice of the parcel is arbitrary but it allowed to demonstrate the significance of all individual developed subroutines. This parcel is fully burnt in the spray so that no residue is left after the completion of combustion.

Figure 7-9 and Figure 7-10 show the mass balance of the entire parcel, where mass of the liquid parcel as well as its combustion products are shown with the lifetime of parcel and the droplet temperature respectively. Furthermore, the modelled aromaticity of the droplet is also shown in both the figures to demonstrate the change of aromatic content of the droplet with time and temperature. As shown in Figure 7-9, the light components in the HFO mixture evaporate rapidly from the liquid and convert into vapour (shown with black line in the figure). After that, this vapour mixes with the surrounding air and reacts with the oxygen and the combustion starts at a suitable combustion temperature in the vapour phase.

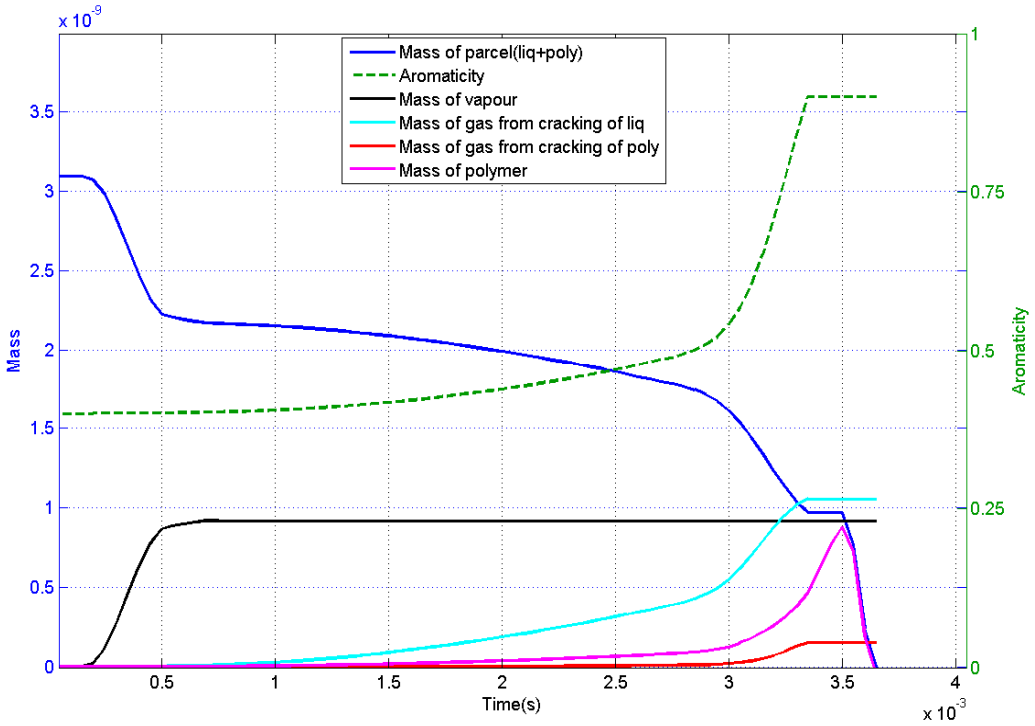

Figure 7-9: Mass balance of the parcel (original liquid components + products) with respect to lifetime of the parcel of modelled good fuel oil in the CVCC (The chamber is initially at 2.5 MPa pressure and 873 K).

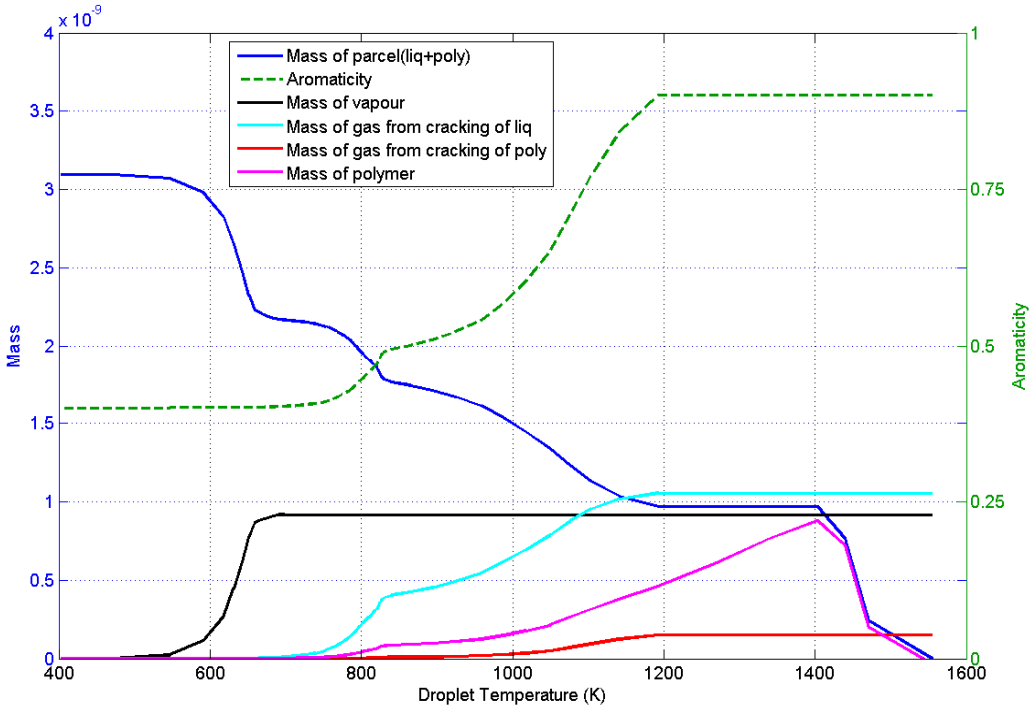

Figure 7-10: Mass balance of the parcel vs. droplet temperature of the modelled good fuel oil in the CVCC (The chamber is initially at 2.5 MPa pressure and 873 K).

After the evaporation, as the droplet temperature increases the thermal cracking of the liquid starts. The thermal cracking is an endothermic process; therefore, it requires a lot of energy. This thermal cracking produces the light hydrocarbon gases from the liquid phase. As shown in Figure 7-9 thermal cracking produces gases from the non-aromatic part of the original liquid plus formed polymer (see section 4.4.2 for details about the pyrolysis model). Thus, the thermal cracking leaves the heavy aromatics and more carbon laden content in the liquid phase. As a result, the liquid phase becomes more carbon rich as the thermal cracking proceeds.

In order to include the adequate effect of the thermal cracking on the liquid phase, the aromaticity of component 4 (residue) was modelled in the present simulations. As noted in section 4.4.2, thermal cracking reduces only the heavy non-aromatic molecules from the liquid (original liquid + formed polymer). Therefore, as thermal cracking progresses, the concentration of aromatic molecules in the droplet increases and this increases the modelled aromaticity from 0.4 to 0.9. Thermal cracking ceases, when the non-aromatic fuel molecules from the liquid have broken-down through thermal cracking and left the droplet. In the present case, thermal cracking is set to finish when the aromaticity of the liquid reaches 0.9. Because of this, as shown in Figure 7-9 and Figure 7-10 thermal cracking of the liquid phase is completed at 1200 K or 3.3 ms (when 90% of the non-aromatic molecules have left the droplet). The remaining 10% non-aromatic molecules in the liquid phase at the end of thermal cracking are the heaviest non-aromatic molecules therefore they polymerise. The polymer formed through polymerisation is burnt later through surface oxidation or remains in the droplet as residue. Once the thermal cracking finishes the aromaticity of the liquid phase remains constant. Meanwhile, thermal cracking also reduces the non-aromatic molecules of the formed polymer producing gas which is shown with a red line in both figures.

Simultaneously with the thermal cracking, the process of polymerisation in the liquid phase is shown in Figure 7-9 and Figure 7-10. The heavy aromatic molecules in the liquid phase (residue) are recombined at high temperature through polymerisation. The processes of polymerisation and thermal cracking continue until all non-aromatic molecules are converted into gas and all aromatic molecules are converted into polymer.

After the completion of thermal cracking and polymerisation the surface oxidation of formed polymer and heavy non-aromatics molecules starts. The heterogeneous surface oxidation or polymer soot burnout phase is the last process for the droplet to follow. The constraint to begin the surface oxidation is discussed in section 6.7.1. The heterogeneous surface oxidation (burnout) of the polymer is allowed only when the aromaticity of liquid reaches 0.9 or more, and 95% of the droplet mass has been converted to the polymer. As shown in Figure 7-9 and Figure 7-10 the surface oxidation starts at 3.5 ms or1400 K respectively. In this surface oxidation, the formed polymer oxidises with the available oxygen in the surroundings. Depending on the oxygen concentration and the temperature of the droplet, the surface oxidation progresses. In the present case, the present parcel is fully burnt and disappears at the end. Therefore, the droplet mass reduces to almost zero at the end of its lifetime.

Figure 7-11 shows the density, diameter, temperature and the number of droplets in the parcel with respect to time. In this figure, there are four y-axes; the colour of the line represents the colour of the axis and vice versa. As shown in Figure 7-11 the parcel diameter and the number of droplets are almost inversely proportional. This is because as the parcel enters into the chamber it breaks up into many droplets therefore its diameter decreases and the number of droplets in the parcel increases. Initial breakup of the present parcel completes approximately within 0.2 ms after the start of the injection. Hence, after 0.2 ms after the start of injection, the number of droplets within the parcel remains constant throughout its lifetime however droplet diameter slowly decreases due to mass transfer. The density of the parcel continuously increases due to evaporation of light constituents. The plateau in droplet density (abrupt change of slope) approximately 0.7 ms after the start of injection shows that all light components are evaporated off and the heavy residue which has density around 1002 kg/m^3 is the dominant component in the droplet. Modelled droplet density is only a function of droplet composition and not temperature.

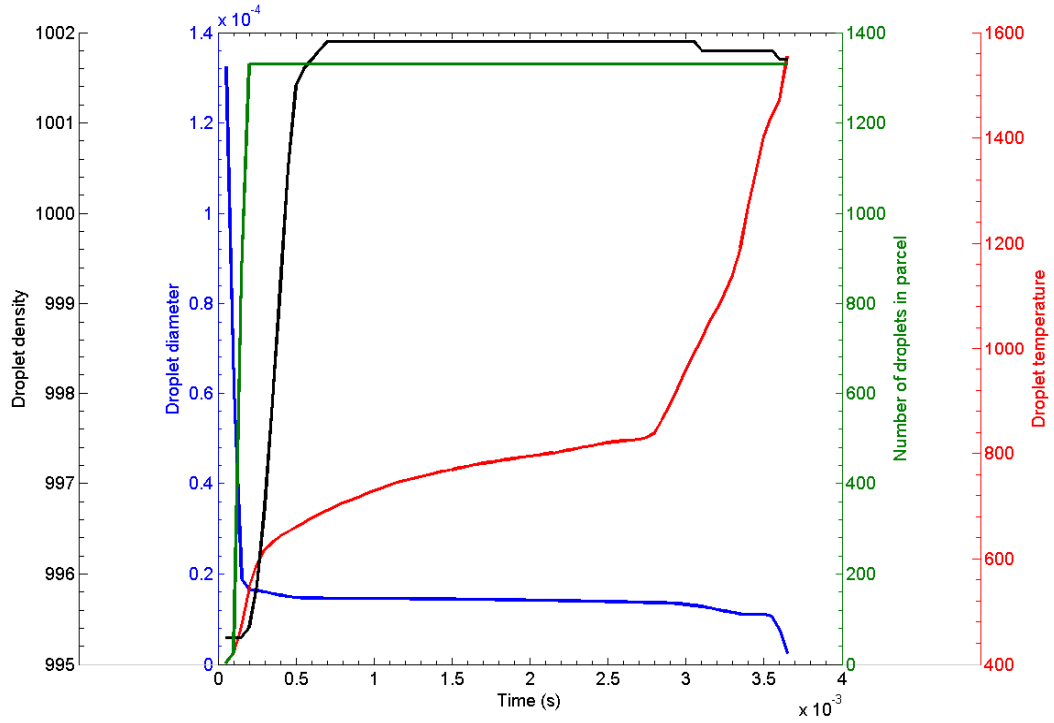

Figure 7-11: Density, diameter, temperature and number of droplets in the parcel with respect to the lifetime of parcel of the modelled good fuel oil in the CVCC (The chamber is initially at 2.5 MPa pressure and 873 K).

Furthermore, the droplet temperature shown with red line increases rapidly during the 0.2 ms after the start of injection while in the single droplet case in Chapter 5 it was increasing linearly with time. The reason for this sharp increase is the droplet breakup; as the parcel breaks into the small droplets, droplet surface area to volume ratio increase which leads to a high heating rate and thus droplet temperature increases rapidly. Later on, droplet temperature increases slowly (see between 0.2 ms and 2.8 ms) though heating continued because most of the gained energy is now utilised in the evaporation enthalpy and decomposition enthalpy. In other words, the plateau in temperature history is observed during the major part of the evaporation and pyrolysis. Ikegami et al.[23] and Goldsworthy [2] explained that thermal cracking in pyrolysis is an endothermic process and it requires lot of energy therefore the plateau in temperature history during the thermal cracking is obvious. However, again after 2.8 ms droplet temperature increases very rapidly once the droplet becomes small and it reaches the combustion zone (high temperature region) where the combustion of evaporated species occurs. This can be confirmed from Figure 7-12. As shown in Figure 7-12, after 2.8 ms droplet enters into the zone where maximum temperature is in between 1000 to 2000 K. This is leads to a high

heat transfer rate to the droplet and thus after 2.8 ms droplet temperature increases rapidly. In the present model, combustion energy of polymer (liquid phase soot) is included in the overall energy balance unlike the vapour phase soot. The decrease in the ambient temperature during 0 to 0.5 ms also shows that evaporation of the light components is absorbing energy from the surroundings. Heating rates observed in Figure 7-11 during evaporation and pyrolysis are $5.14*10^5$ K/s and $2.28*10^5$ K/s respectively.

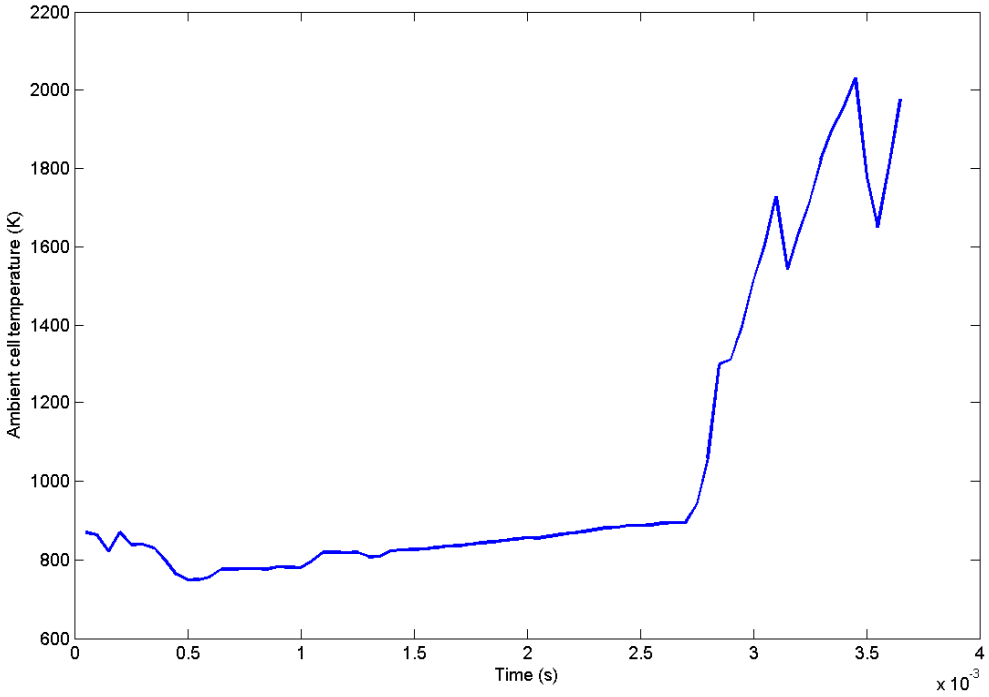

Figure 7-12: Ambient cell temperature of the parcel with respect to the lifetime of parcel of the modelled good fuel oil in the CVCC (The chamber is initially at 2.5 MPa pressure and 873 K).

Figure 7-13 shows the mean molecular weights and the bubble points of the light hydrocarbons in the cutter stock of the modelled good fuel oil. The mean molecular weights of the n-paraffins, aromatics and naphthenes increase as the evaporation progresses. It is clear that the evaporation of the light hydrocarbons of the present parcel is very rapid and finishes within 0.7 ms of the droplet lifetime. In other words, less than 0.7 ms or 700 K temperature is required to evaporate the cutter stock, which is 30% by mass of the droplet. The droplets spend most of their lifetime in the pyrolysis and the surface oxidation process. This partially justified the use of the low-pressure evaporation model rather than the high-pressure evaporation model. The bubble point temperatures shown in

Figure 7-13 of n-paraffins ranging from 536 to 609 K, aromatics ranging from 568 to 705 K and naphthenes ranging from 580 to 646 K.

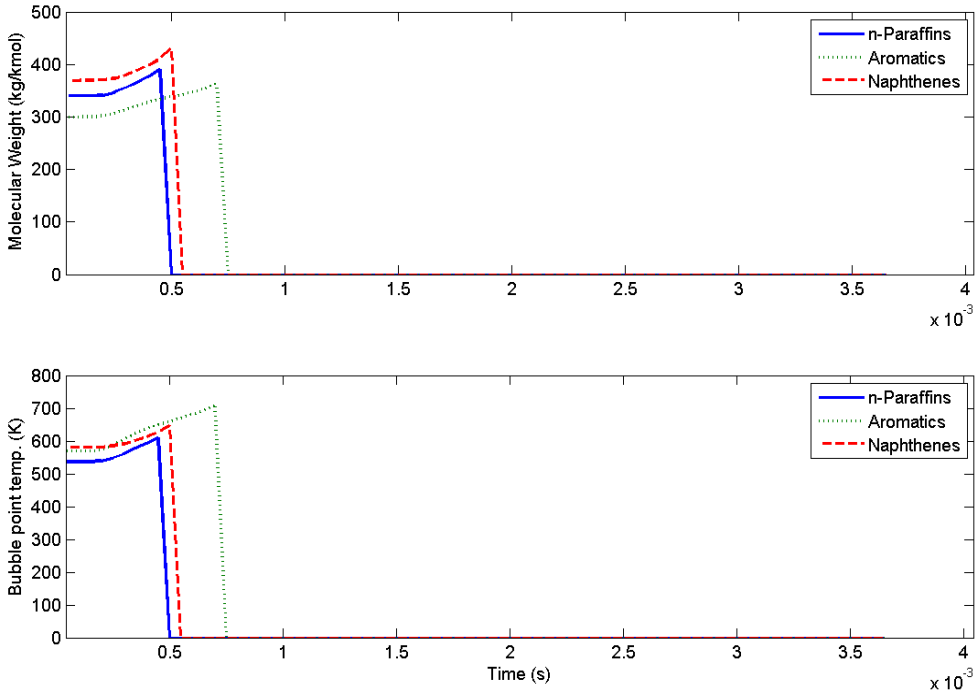

Figure 7-13: Mean molecular weights and bubble points of the light hydrocarbons in the cutter stock with respect to the lifetime of parcel of the modelled good fuel oil in the CVCC (The chamber is initially at 2.5 MPa pressure and 873 K).

The mass transfer rates of all four components with the droplet temperature are shown in Figure 7-14. Components 1, 2 and 3 are light components and go thorough evaporation only. The evaporation rates of components 1, 2 and 3 are clearly a function of the droplet temperature and also of composition. The evaporation rate of a particular component and the mean molecular weight of that component increase together but it starts decreasing at the end of its lifetime due to low concentration in the droplet though the droplet temperature is still increasing. The fourth component (residue) is the heaviest component in the HFO mixture and does not evaporate but it goes through the pyrolysis and surface oxidation (or liquid phase soot burnout). Therefore, in the mass transfer rate of component 4, two peaks are apparent; one represents the pyrolysis gas and the second represents polymer burnout rate. The polymer burnout rate shows that surface oxidation of the present parcel starts when the droplet reaches 1400 K.

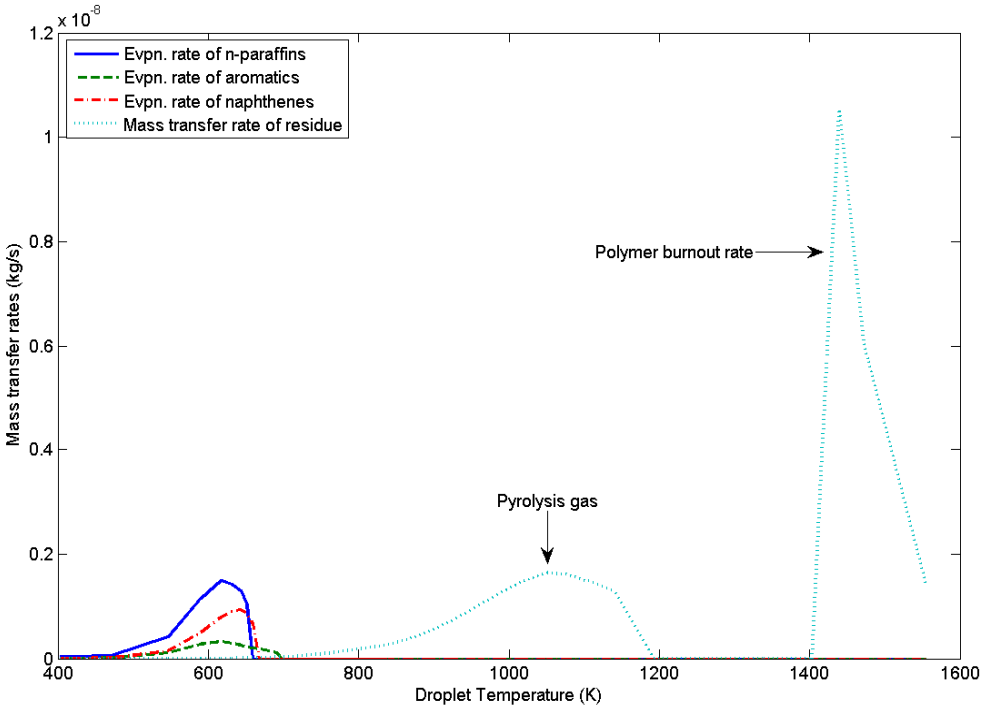

Figure 7-14: Mass transfer rates of all components with droplet temperature of the parcel of the modelled good fuel oil in the CVCC (The chamber is initially at 2.5 MPa pressure and 873 K).

In summary, as shown in Figure 7-7 the present model results show good qualitative agreement with both the modelled and the experimental results at 6 ms after the start of combustion.

7.3.1.2 Poor Quality Fuel

In the previous section the modelled good fuel oil was studied. The study in the present section is of poor fuel oil simulation results. The comparison of the present model with modelled chamber temperature, soot extent, heat release rate and soot consumption rate results of Goldsworthy [2] and measured spray results of Takasaki et al.[1] for soot/spray and visual flame extent of the poor fuel using CVCC is shown in Figure 7-15. The present model results show good agreement with both the modelled and the experimental results at 6 ms after the start of combustion which is 13 ms after the start of injection because an ignition delay of 7 ms was observed in the results for both. This ignition delay observed from the present model result of poor fuel oil is same as observed by Goldsworthy [2] and Takasaki et al.[1]. This value are set in the present model by setting the ignition factor equal (FIGN) to 3, as shown in Table 6-3.

These ignition factors for both good and poor fuel oil are almost similar, and lower than that used by Goldsworthy [2]. This is probably because the rate of production of combustible gases from the residual portion is higher in Goldsworthy's model than the present model, thus the core of unburnt vapour has a higher vapour concentration. The present model predicts the rate of production of combustible gases from the residual portion from first principles using pyrolysis kinetics whereas Goldsworthy's approach is empirical. This means ignition factor for the poor fuel oil in Goldsworthy's model was set very high to inhibit the onset of full combustion. In addition, the qualities of cutter stock in the present model are set depending on the nature (more paraffinic for the good fuel oil and more aromatic for the poor fuel oil) of cutter stock. This may help to achieve similar ignition factors in both fuels.

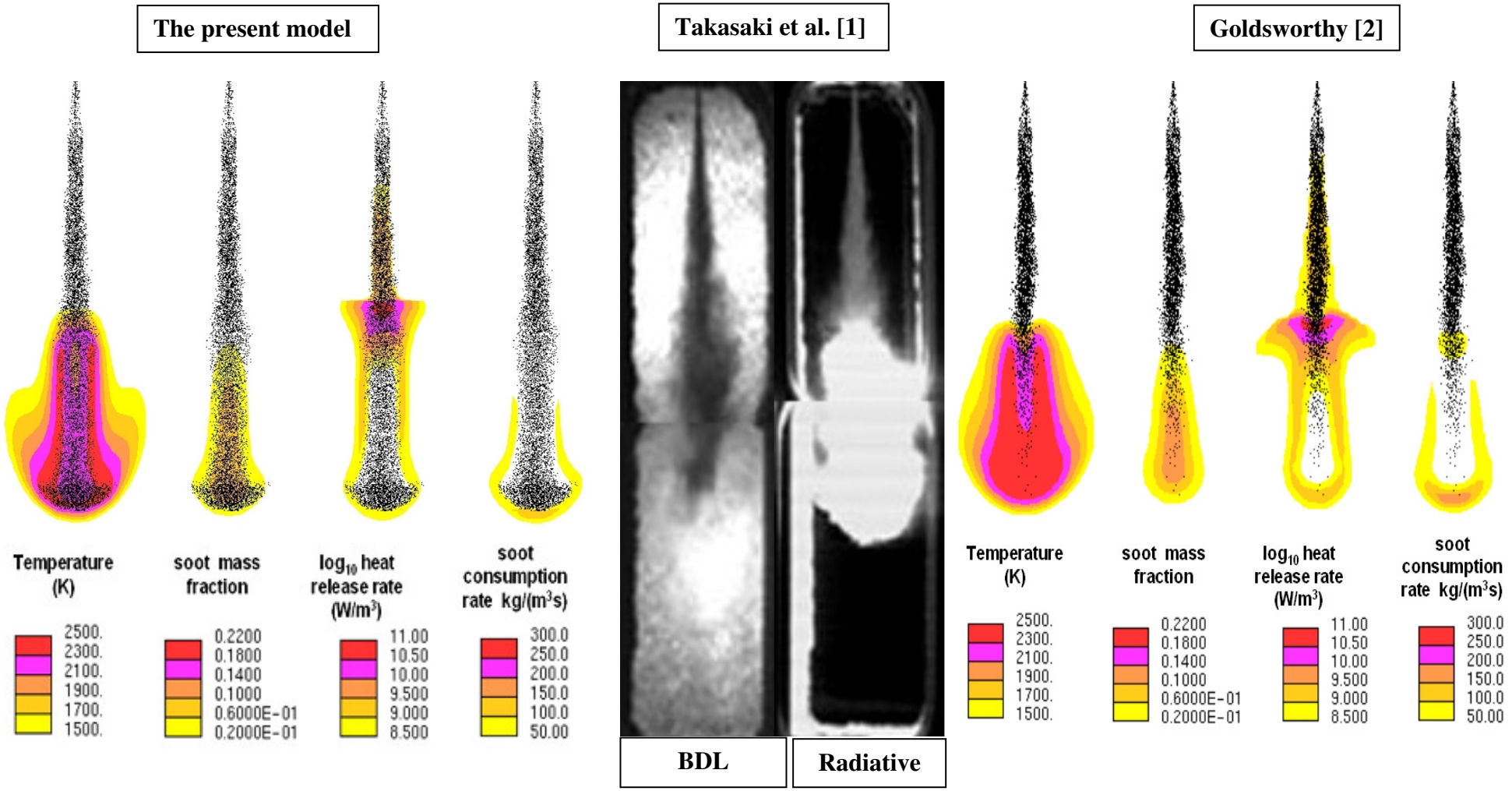

Figure 7-15: Comparison of the present modelled spray results (chamber temperature, soot extent, heat release rate and soot consumption rate) with Goldsworthy's modelled spray results and Takasaki et al.'s [1] measured spray results for soot/spray and visual flame extent of poor fuel using the CVCC.

In the results of Takasaki et al.[1] shown in Figure 7-15 unevaporated/unburnt liquid in the core of the spray is clearly observed and the same observations are made for the present model. The modelled flame penetration in the present work is taken as the extent of soot consumption rate indicating the extent of luminous flame. The flame penetration indicated by the soot consumption rate is almost similar to that observed in the results of Goldsworthy [2] and experimental results of Takasaki et al.[1]. However, there are some differences observed in gas phase soot mass fraction and gas phase soot consumption rate and high temperature region. The explanations for these differences are similar to those explained for good fuel oil.

The modelled flame lift-off distance from the nozzle is indicated by ambient temperature contour of 1500 K. At the flame lift-off point the temperatures are very close therefore the choice of lift-off point temperature is not critical. The modelled flame lift-off distance obtained from the present model result showed good agreements with the modelled results of Goldsworthy [2] and the experimental results of Takasaki et al.[1]. At the lift-off point, high heating rates are found. As noted by Goldsworthy [2], by altering the activation energy for combustion, the flame lift-off distance from the nozzle can be altered. A higher activation energy for the combustion leads to a higher ignition delay and more flame lift-off distance. This is can be observed by comparing the present model results in Figure 7-7 with Figure 7-15. The higher activation energy used for the combustion of poor fuel oil (see Table 6-3) gives more flame lift-off distance than the modelled good fuel oil.

In order to make the comparison between the poor fuel oil and the good fuel oil, the temperature of droplets along with the oxygen concentration, carbon dioxide concentrations, polymer burnout rate, mixture fraction 1 and fuel vapour concentration of poor fuel using the CVCC 6 ms after the start of combustion are shown in Figure 7-16.

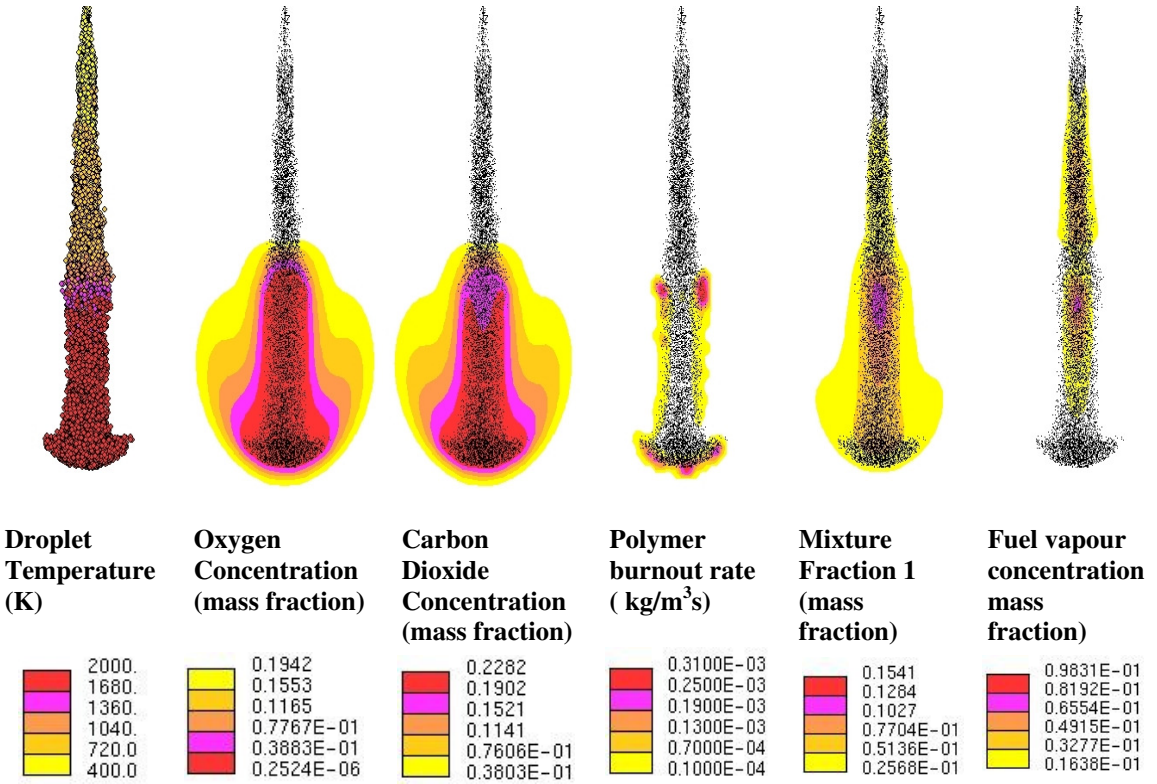

Figure 7-16: Temperature of droplets along with the oxygen concentration, carbon dioxide concentrations, polymer burnout rate, mixture fraction 1, and fuel vapour concentration of the modelled poor fuel using CVCC 6 ms after the start of combustion.

The temperature of the droplets increases from 400 K at the nozzle exit to 1040 K at the flame lift-off point. At the flame lift-off point, the droplets are first exposed to the combustion region. Then, as the droplets move further down in the core of spray they are heated to higher temperature. The temperature variation in droplets shows the effect of combustion in the gas phase on the spray. As shown in the above figure, in the centre of the spray, the concentration of the oxygen found is very low. As a result the polymer formed within the droplet by polymerisation cannot oxidise. Hence, this formed polymer remains in the liquid phase as unevaporated/unburnt liquid which is known as cenospheres.

7.3.1.2.1 Study of a Single Parcel within the Poor Quality Fuel Spray

Similar to the good fuel oil, the study of a single parcel within the spray is presented in this section. The choice of parcel (parcel no. 50) is same as the good fuel oil and it is injected at the same time ($35*10^{-6}$ sec).

Figure 7-17 and Figure 7-18 show the mass balance of a parcel within the poor fuel oil spray, where mass of the liquid droplet as well as its combustion products are shown with the parcel lifetime and the droplet temperature respectively. As expected, the droplets in the poor fuel oil simulations require a longer time to burn than the good fuel oil. The comparison between the good fuel oil parcel and the poor fuel oil parcel is discussed in the next section. The droplet density, diameter, temperature and the number of droplets in the parcel with respect to time are shown in Figure 7-19. The present parcel is injected at the same time as the one in the good fuel oil but due to variation in its composition and ignition parameters, its property history is different. The ambient cell temperature of the parcel with respect to lifetime of the parcel of modelled poor fuel oil is given in Figure 7-20. The mean molecular weights, bubble points and the mass transfer rates of components of the modelled poor fuel oil are shown in Figure 7-21 and Figure 7-22 respectively. The comparison of the modelled good and poor fuel oil results is discussed in the next section.

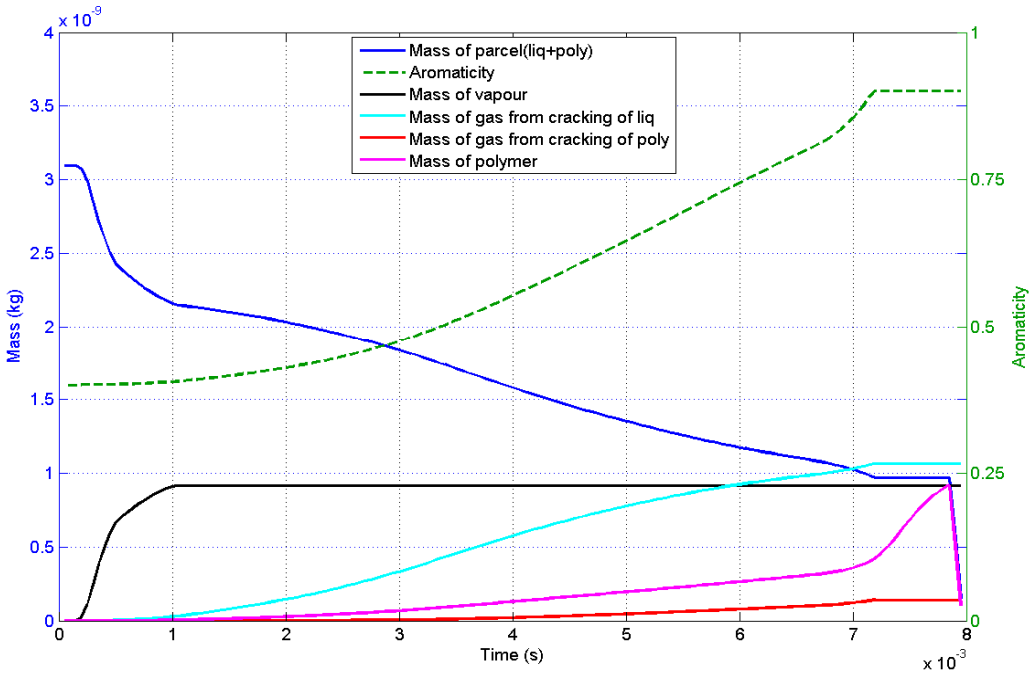

Figure 7-17: Mass balance of the parcel (original liquid components + products) with respect to the parcel lifetime of the modelled poor fuel oil in the CVCC (The chamber is initially at 2.5 MPa pressure and 873 K).

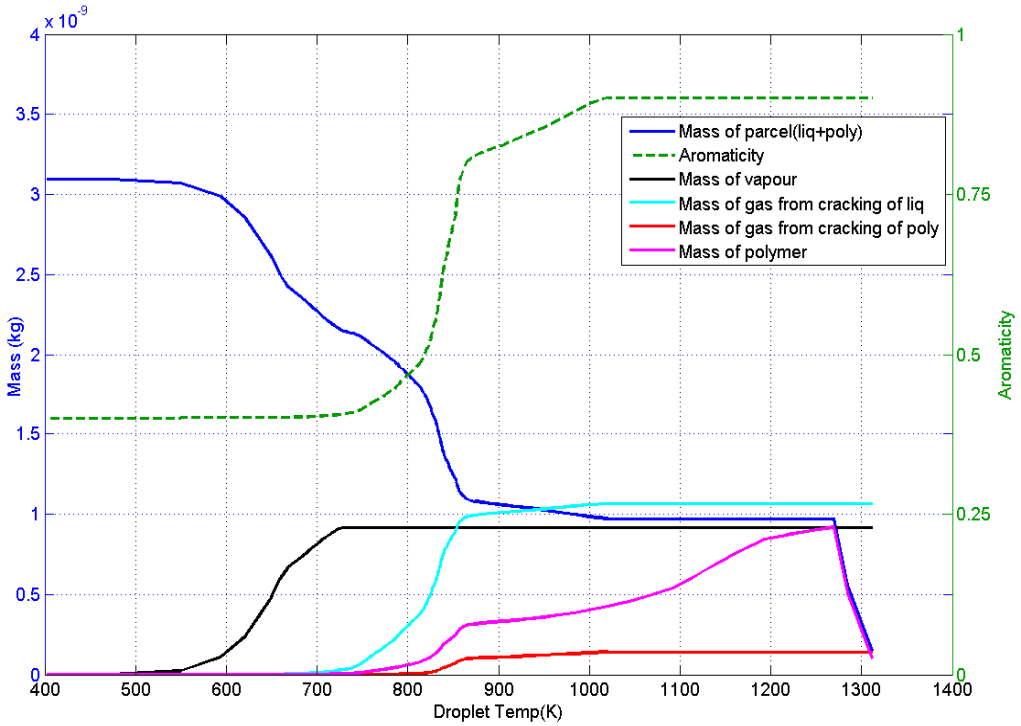

Figure 7-18: Mass balance of the parcel vs. droplet temperature of the modelled poor fuel oil in the CVCC (The chamber is initially at 2.5 MPa pressure and 873 K).

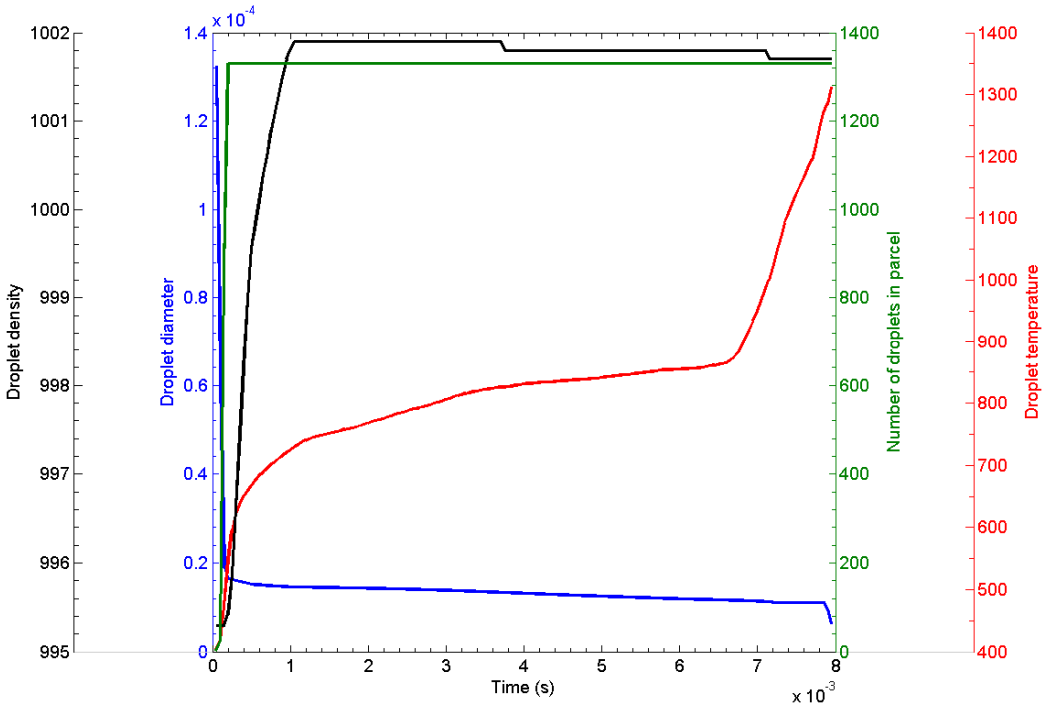

Figure 7-19: Density, diameter, temperature and number of droplets in the parcel with respect to the parcel lifetime of the modelled poor fuel oil in the CVCC (The chamber is initially at 2.5 MPa pressure and 873 K).

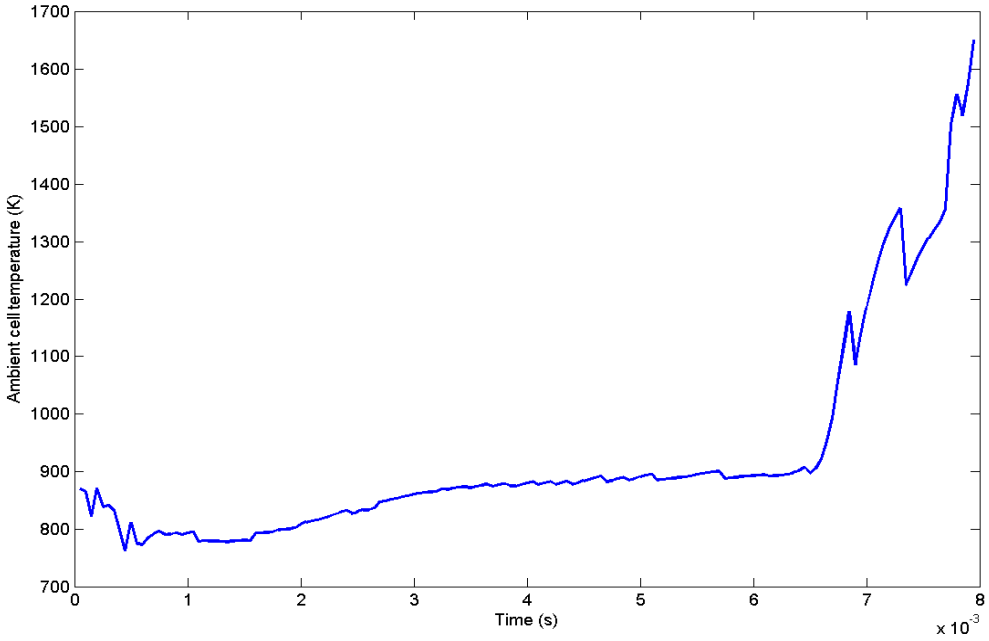

Figure 7-20: Ambient cell temperature of the parcel with respect to lifetime of parcel of the modelled poor fuel oil in the CVCC (The chamber is initially at 2.5 MPa pressure and 873 K).

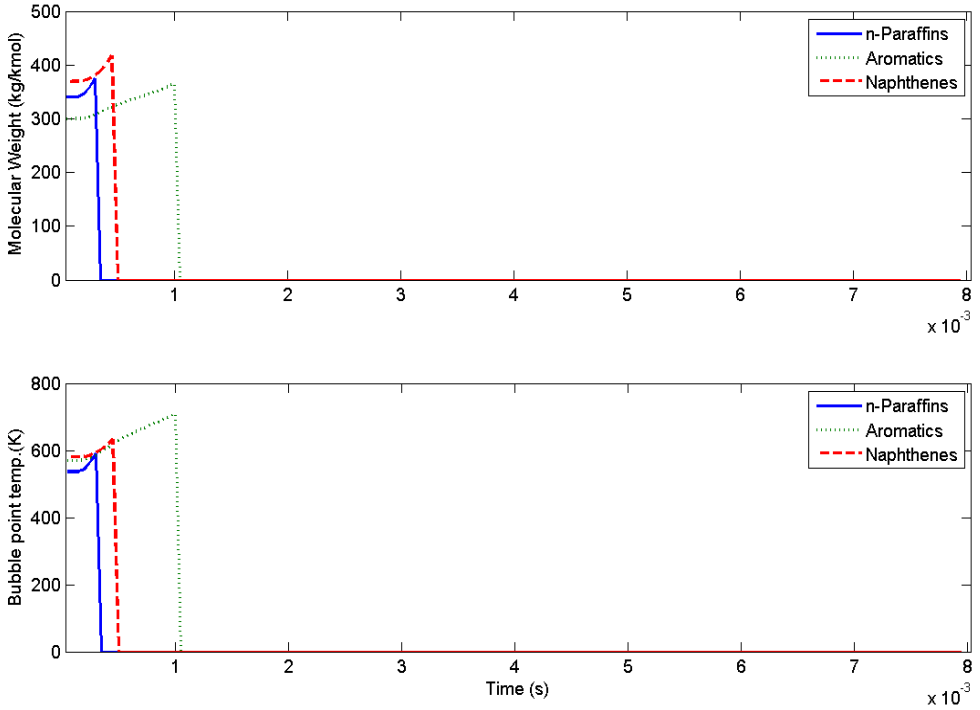

Figure 7-21: Mean molecular weights and bubble points of the light hydrocarbons in the cutter stock with respect to lifetime of parcel of the modelled poor fuel oil in the CVCC (The chamber is initially at 2.5 MPa pressure and 873 K).

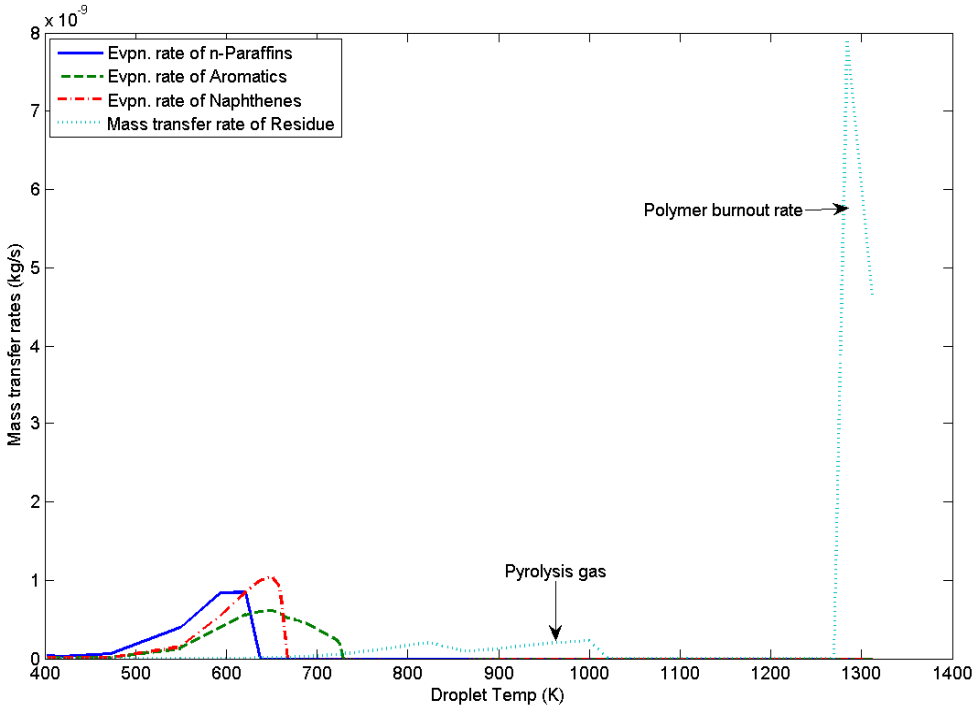

Figure 7-22: Mass transfer rates of all components with droplet temperature of the modelled poor fuel oil in the CVCC (The chamber is initially at 2.5 MPa pressure and 873 K).

7.3.1.3 Comparison of Good Fuel Oil and Poor Fuel Oil Simulation Results

The comparison of mass transfer rates of the good fuel oil and the poor fuel oil evidently show that the mass transfer rate of the poor fuel oil is slow. The reason behind this slow mass transfer rate is the heat transfer environment. The simulated poor fuel oil has poor ignition quality which explains why it ignites late and thus the evaporation and the pyrolysis, which are a function of the droplet temperature, start late. The total amount of vapour and pyrolysis gas produced from both the parcels are almost same at the end of the droplet lifetime but their production rates vary according to the ignition behaviour of the fuel. The good fuel oil parcel required 0.7 ms to evaporate its cutter stock while the poor fuel oil required 1 ms. The droplet lifetime observed for the good fuel oil is 3.7 ms which is about half the droplet lifetime observed for the poor fuel oil (8 ms).

On the other hand, the rate of combustion of polymer (liquid phase soot burnout) observed for the poor fuel oil is faster than the good fuel oil. The liquid phase soot burnout is identified by a decrease in the polymer mass at the end of the droplet lifetime. Perhaps this

faster rate found for the poor fuel oil is due to greater availability of oxygen in the surroundings. There may be less oxygen available where the combustion of polymer occurred for the good fuel oil, thus it has a slow liquid phase soot burnout rate. The maximum number of droplets in a parcel is function of spray chamber temperature, pressure and nozzle diameter. Since the choice of the parcel for good fuel oil and poor fuel oil is the same, chamber temperature, pressure and nozzle diameter is the same and they are injected at the same time, the number of droplets is also similar.

Furthermore, the flame lift-off distance observed for the poor fuel oil is higher than that observed for the good fuel oil. As explained earlier, this flame-lift off distance is a function of the ignition quality of fuel; good fuel oil has a short flame lift-off distance while poor fuel oil has a long flame lift-off distance. Consequently, the luminous area of the poor fuel oil is smaller than the good fuel oil. By comparing Figure 7-11 with Figure 7-19, it is also evident that the good fuel oil droplet has gained almost 300 K more in temperature than the poor fuel oil droplet. The proper reason behind this is the high-temperature region (2300-2500 K). The temperature contours shown in Figure 7-7 and Figure 7-15 for good and poor fuel oil respectively show that good fuel oil has bigger high-temperature region (2300-2500 K) than the poor fuel oil. Because of this, droplets in the good fuel oil gain more heat (energy) than the poor fuel oil.

In the present model, for both fuels, complete burnout of the polymer is predicted. No qualitative data in the literature are available to confirm this. Unburnt polymer could damage engines or it may be emitted as Black Carbon (BC). The Black Carbon (BC) is the second largest contributor to the rising global temperatures. The burnout rate of polymer also depends on the porosity of the formed polymer. The pyrolysis reactions establish the porosity, and depending upon the porosity, the oxygen and other gases diffuses into the pores and react. During combustion the porosity and the surface area of the droplet may change due to high temperature. Hence, further studies are essential to understand this polymer burnout mechanism.

7.3.2 Fuel Ignition Analyser (FIA)

Using the same fuel composition and reference model settings (Table 6-3) for the simulations as the CVCC, the pressure rise rates in the FIA are calculated. The pressure rise rates plotted against the time from the start of the injection for the good fuel and the poor fuel are given in Figure 7-23. First of all, the present simulation results of FIA are compared with modelled pressure rise rate results of Goldsworthy[2]. By comparing Figure 7-23 with Figure 7-24, it is observed that the modelled pressure rise rate in the present FIA result follows similar pattern as modelled pressure rise rate results of Goldsworthy [2]. The ignition delays observed in Figure 7-23 for good fuel and poor fuel oil are 6 ms and 10 ms respectively. The ignition delay in the FIA is taken as the time from the start of the injection to the significant increase (> 0.25 bar/sec) in pressure rise rate. These ignition delay results are 1 ms less than the FIA results of Goldsworthy [2] for good and poor fuel oils.

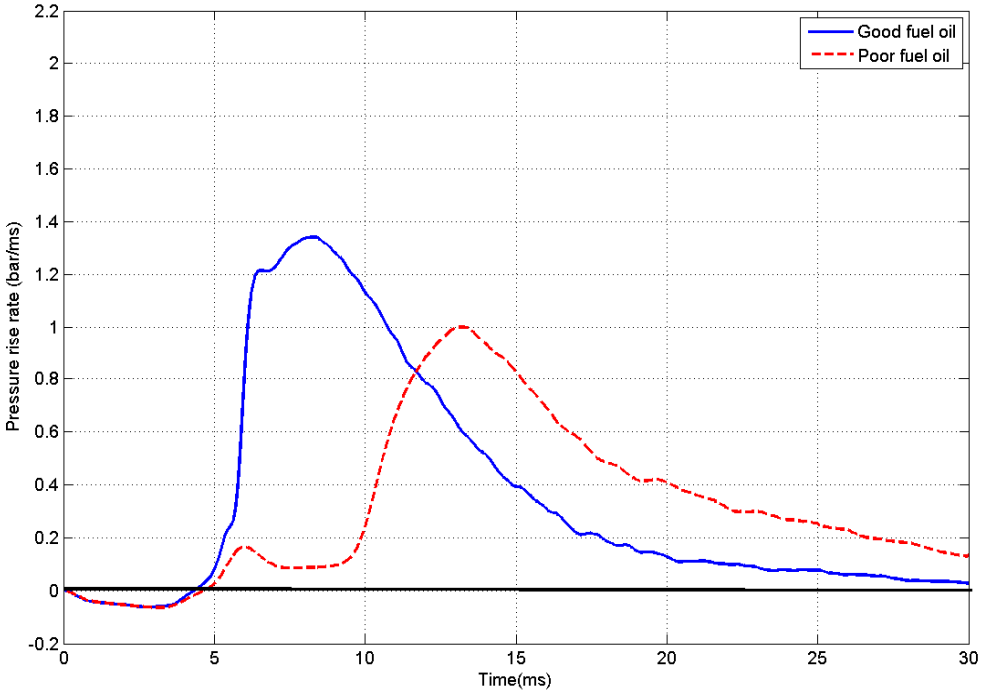

Figure 7-23: Modelled pressure rise rate against time after the start of injection for the good fuel and poor fuel oil using the present model with 30% cutter stock and reference model settings in the FIA.

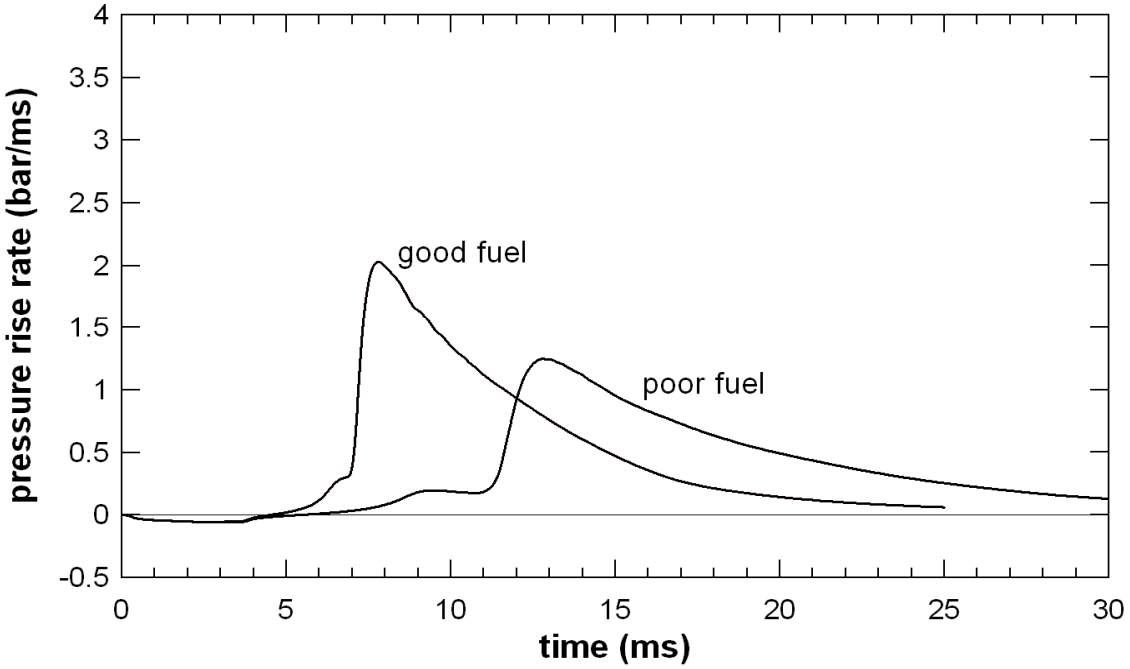

Figure 7-24: Goldsworthy's modelled pressure rise rate against time after the start of injection for the modelled good fuel and the modelled poor fuel oil in the FIA (courtesy of Goldsworthy [2]).

However, there is some difference observed in the maximum pressure rise rate, though both models contained the same proportion of cutter stock to residue. There are two key reasons behind this difference. First, Goldsworthy [2] has altered the ignition parameters and held the mid boiling point constant to set the quality of cutter stocks, which is similar to holding the mean molecular weight of the cutter stock components constant in the present model. However, to allow the fractional distillation of the light components, mean molecular weights cannot be held constant. As explained by Goldsworthy [2] the mid boiling point affects the maximum pressure rise rate. The lower mid boiling results in rapid early evaporation and which leads to the faster ignition and a higher pressure rise rate. On the other hand, in the present modelling, the quality of cutter stock has been set using different compositions for the cutter stock. The present cutter stock may possess different evaporation behaviour (different molecular weights and bubble points range) from that used by Goldsworthy [2].

Using a lower mean molecular weight for the components may help in achieving higher maximum pressure rise rates. However, in the paper of Takasaki et al.[1] the mean molecular weights of the individual compounds of the cutter stock are not found.

Therefore, the same mean molecular weight ranges as used in publication by Garaniya & Goldsworthy [22] are used in CFD simulations for FIA and CVCC. The choice of the mean molecular weights of the cutter stock is justified by Baert's [14] discussion about the composition of HFO [14]. Baert [14] suggested that the pure hydrocarbon compounds of HFO (cutter stock base) contain molecular weights between 160 and 500. Furthermore, Goldsworthy [2] has used 1200 K as the critical temperature of the droplet. It means when the droplet reaches 1200 K, it instantly evaporates. This results in faster evaporation rates and higher pressure rise rates. In the present modelling, the critical temperature of droplet is set to 2000 K to allow droplet to go through the liquid phase soot burnout process. This higher critical temperature will suppress the evaporation rate of the droplet. In addition to the critical temperature, the rate of production of combustible gases from the residual portion is higher in Goldsworthy's model than the present model. In Goldsworthy's model, the higher saturation pressure setting of the residue over the temperature range is mainly gives the higher rate of production of combustible gases. The present model predicts the rate of production of combustible gases from the residual portion from first principles using pyrolysis kinetics whereas Goldsworthy's approach is empirical.

Secondly, as shown in Figure 7-25, the initial proportion of cutter stock in HFO also significantly affects the maximum pressure rise rate. Increasing cutter stock from 30% to 40% by mass, leads to earlier ignition and a higher maximum pressure rise rate. When a 40% cutter stock for good fuel oil (20% n-paraffins, 10% aromatics and 10% naphthenes) is used, maximum pressure rise rate is found around 2 bar/sec, which is 0.7 bar/sec higher than using 30% cutter stock. Similarly, when a 40% cutter stock for poor fuel oil (10% n-paraffins, 20% aromatics and 10% naphthenes) is used maximum pressure rise rate is found > 1.4 bar/sec, which is 0.4 bar/sec higher than using 30% cutter stock. These results using 40% cutter stock shown in Figure 7-25 are closer to the original experimental FIA results (Figure 7-6), than using 30% cutter stock results (Figure 7-23). However, since the actual amount of cutter stock in the experimental FIA sample is not known, and to maintain consistency cutter stock was proportion was left as 30% (same as the CVCC and a single droplet) for subsequent analysis. Thus, because of these above mentioned reasons difference in the maximum pressure rise rate is observed.

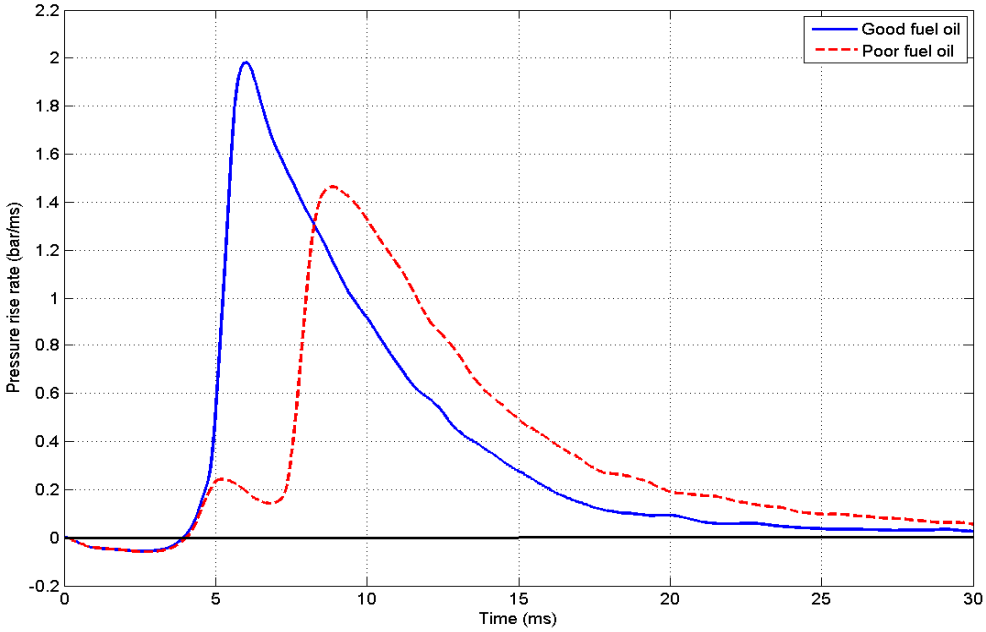

Figure 7-25: Modelled pressure rise rate against time after the start of injection for the good and poor fuel oil using 40% cutter stock and reference model settings in the FIA.

The present modelled pressure rise rates using 40% cutter stock can also be compared with FIA experimental results (Figure 7-6) for good fuel, poor fuel and very poor fuel. By comparing Figure 7-25 with Figure 7-6, it is clearly observed that the ignition delay time and maximum pressure rise rate of modelled good fuel using 40% cutter stock is intermediate between the FIA good fuel and the FIA poor fuel. The ignition delay time and the maximum pressure rise rate of the modelled poor fuel using 40% cutter stock are intermediate between the FIA poor fuel and FIA very poor fuel.

The modelled heat release rates (ROHR) against time after the start of injection for the modelled good and the poor fuel oils with 30% cutter stock and reference model settings in the FIA are shown in Figure 7-26.

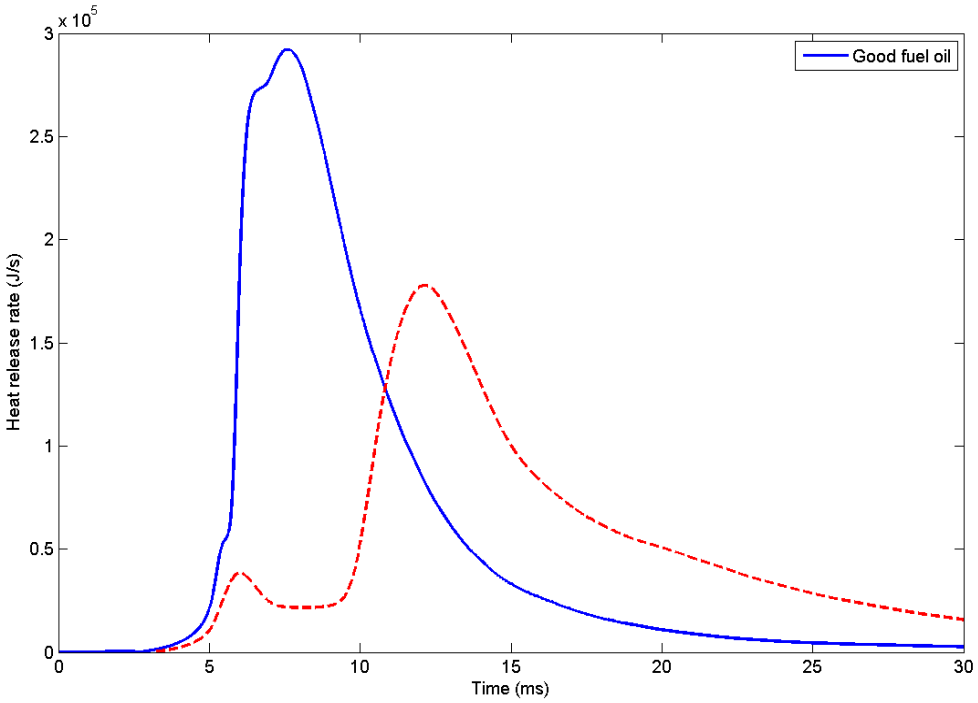

Figure 7-26: Modelled heat release rates against time after the start of injection for modelled good and poor fuel oils using the present model with 30% cutter stock and reference model settings in the FIA.

Two-stage (double hump) ignition is apparent for poor fuel oil as shown in Figure 7-23 and Figure 7-26. To understand this two-stage ignition as well as to demonstrate the procession of ignition and combustion in the FIA, the spatial distribution of droplet temperature (in K), ambient temperature (in K), equivalence ratio, fuel vapour concentration and fuel mixture fraction of the modelled poor fuel oil at a 1 ms interval from 5 to 11 ms using 30% cutter stock and reference model settings are shown in Figure 7-27 and Figure 7-28. The fuel mixture fraction shows the total amount of burned or unburnt fuel vapour while fuel vapour concentration shows only the unburnt fuel vapour. Both of these factors are plotted with the same scale for better comparison. Equivalence ratio shown in Figure 7-27 is calculated using fuel vapour, air and combustion products, it gives the same value whether the fuel vapour is burnt or unburnt. Therefore it looks similar to mixture fixture fraction 1. As noted earlier, fuel injection in the CVCC proceeds for 25 ms while in the FIA it only lasts for 3.6 ms. Thus, in the CVCC, injection proceeds beyond ignition, while in the FIA injection ceases before the start of combustion.

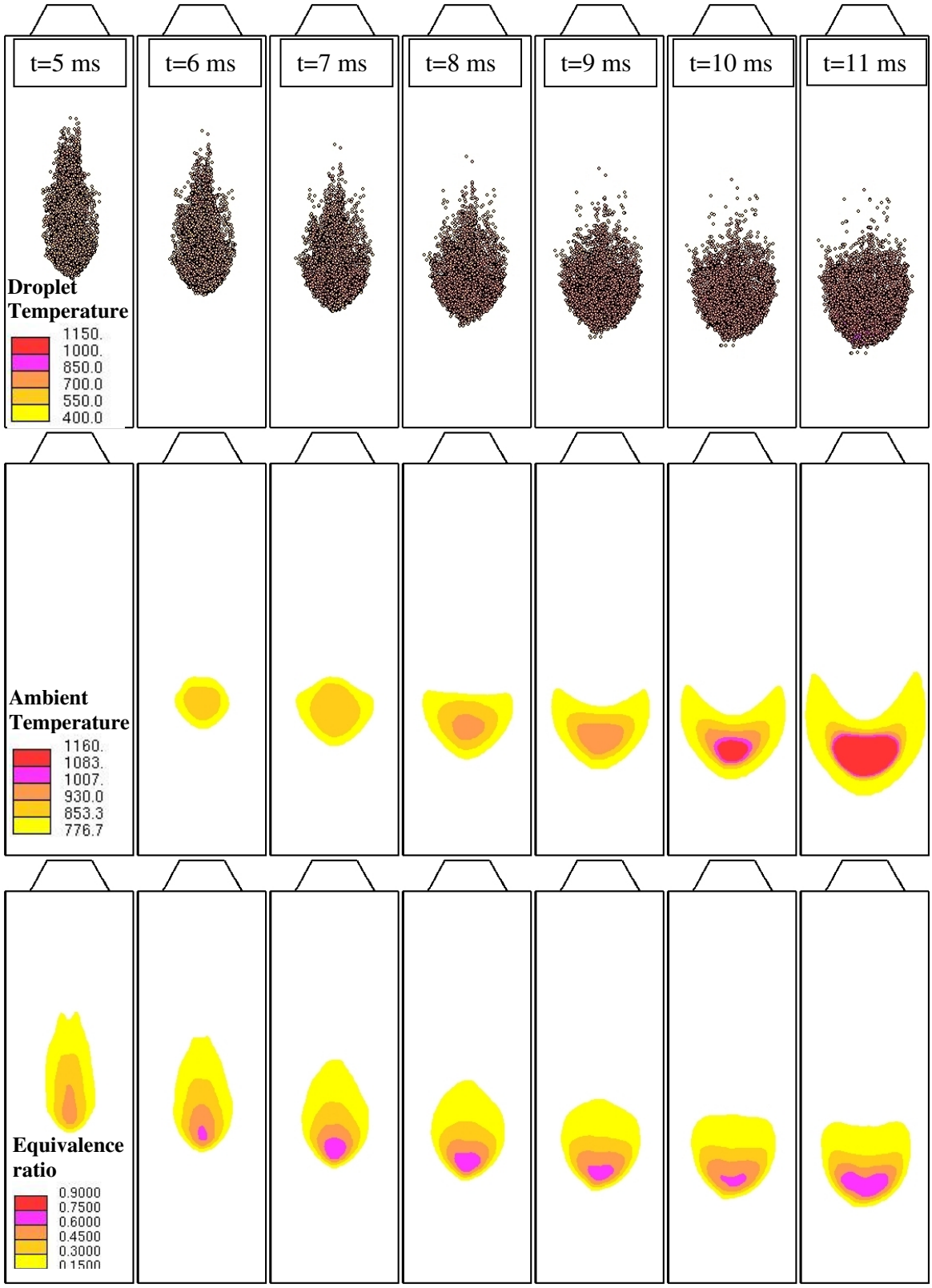

Figure 7-27: The spatial distribution of droplet temperature (in K), ambient temperature (in K) and equivalence ratio of the modelled poor fuel oil using 30% cutter stock and reference model settings in the FIA.

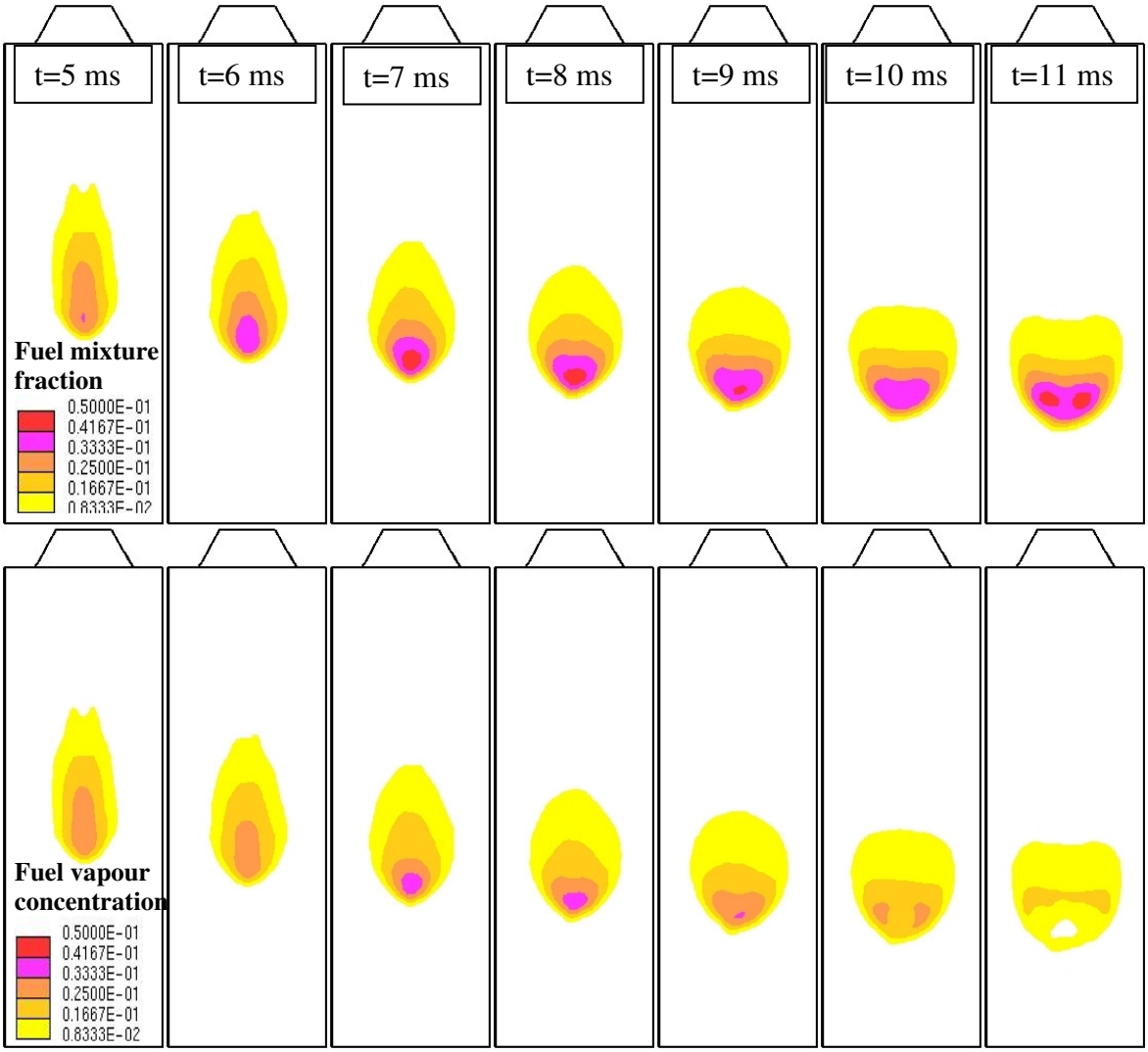

Figure 7-28: The spatial distribution of fuel vapour concentration (in mass fraction) and fuel mixture fraction (in mass fraction) of the modelled poor fuel oil using 30% cutter stock and reference model settings in the FIA.

From Figure 7-27 and Figure 7-28, it is observed that at 5 ms, fuel injection is completed and the cutter stock from the HFO has started evaporating but ignition is not started yet. This can be confirmed from the comparison of fuel mixture fraction and fuel vapour concentration. The spatial concentration of fuel mixture fraction and fuel vapour concentration at 5 ms looks almost identical, which means fuel is evaporated but it is not consumed by ignition reactions yet. Therefore, at 5 ms not much change in pressure rise rate is observed (Figure 7-23). However, at 6 ms, difference in the concentration of fuel mixture fraction and fuel vapour concentration is apparent which means ignition reactions are initialised. Certainly, the high equivalence ratio also favours the suitable ignition condition. Therefore, pressure rise rate slightly increases.

At 7 ms, ignition reactions further proceeded. Thus temperature in some cells reaches above 920 K which is the takeover temperature from ignition to combustion. According to this temperature and favourable equivalence ratio (> 0.3), combustion should start soon. However, the pressure rise rate decreases meaning combustion could not began. No doubt, at 6 ms some cells were ignited but because of the movement of droplets, surrounding fuel vapour was carried further down the chamber. This movement of vapour causes dilution in the vapour-air mixture which inhibits the combustion reactions. This small ignition phenomenon between 5 and 7 ms gives the first peak in the pressure rise rate.

Now at 8 and 9 ms, most importantly velocity of the fuel droplets relatively decreases due to the wall boundary of the chamber and consequently there is less mixing with the fresh air. Therefore, around 9 ms, ignition reactions commence once again which can be confirmed from the decrease in the fuel mixture fraction. Since movement of droplets and vapour are very little, the present favourable ignition condition helps to restart combustion. Therefore, at 10 ms, due to combustion, the temperature of chamber reaches above 1160 K and consequently the fuel mixture fraction decreases. This combustion reflects as a big peak in the pressure rise rate.

In the literature, two types of explanations are found about two-stage ignition behaviour of poor and very poor fuel oil. According to Goldsworthy [2], many hydrocarbons show a negative temperature dependence of reaction rate on temperature in the mid range of ignition temperatures. This type of negative temperature dependence leads to two-stage ignition [2]. Whereas according to Aabo [198], this double hump is due to: (1) the combustion of the cutter stock followed by (2) the combustion of the residue. The combustion of the cutter stock starts early which helps the actual combustion of the residue [1]. However, with the present model it is possible to examine this contradiction. To study the sensitivity of two-stage ignition for the modelled poor fuel oil two simulations are presented; the first one is to highlight the effect of the negative temperature dependence term in the ignition model on the pressure rise rate for the modelled poor fuel oil and the other one is to highlight the effect of ignition model parameters on the pressure rise rate for modelled poor fuel oil. Results of these sensitivity tests are presented in Figure 7-29 and Figure 7-30.

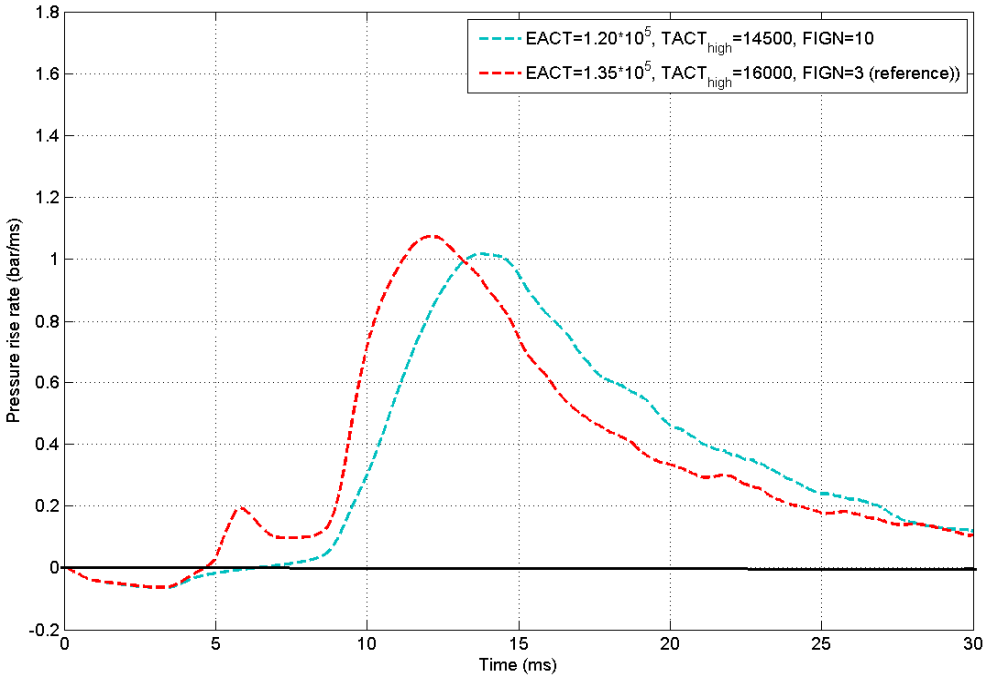

Figure 7-29: Modelled pressure rise rate against time after the start of injection for the modelled poor fuel oil with 30% cutter stock and <u>without</u> the negative temperature dependence term in the ignition model in the FIA (E_{ACT} is in kJ/kmol and $TACT_{high}$ is in K).

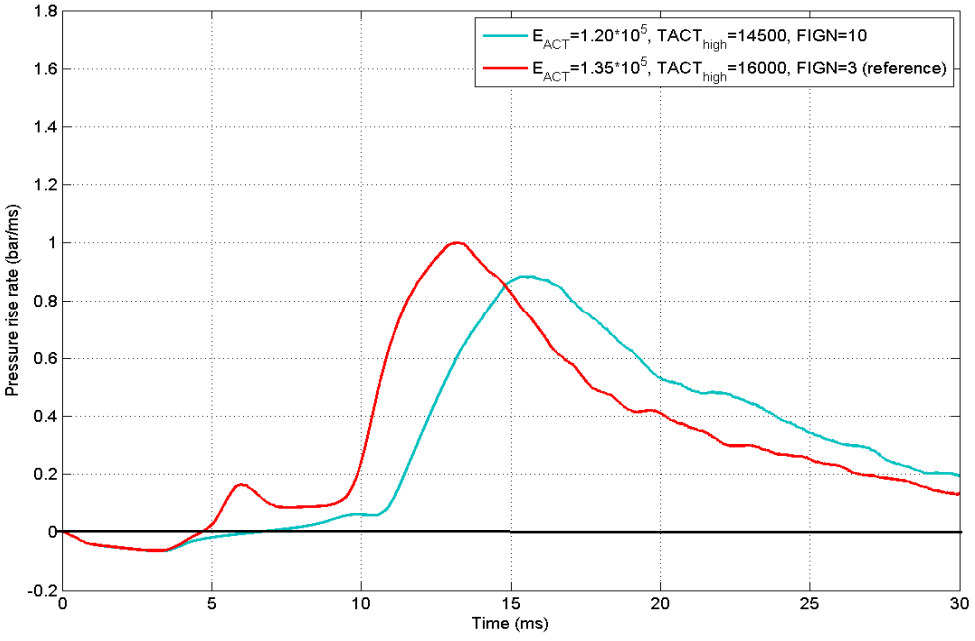

Figure 7-30: Effect of ignition model parameters on the pressure rise rate for the modelled poor fuel oil using 30% cutter stock and <u>with</u> the negative temperature dependence term in the ignition model the FIA (E_{ACT} is in kJ/kmol and $TACT_{high}$ is in K).

By removing the negative temperature dependence term in the ignition model (τ_{med} is taken as zero in equation (92)) simulations results for two different model settings; a reference model and a different model with E_{ACT}= 1.2×10^5 kJ/kmol, $TACT_{high}$ = 14500 K and FIGN = 10, are obtained for the poor fuel oil in the FIA, these are shown in Figure 7-29. The purpose of these different settings is to demonstrate the effect of negative temperature term in ignition while maintaining similar ignition delay. As shown in Figure 7-29, ignition delay of the current reference model without the negative temperature dependence term in the present case is 9 ms which is 1 ms lower than the previous case with the negative temperature dependence (10 ms) shown in Figure 7-23 or in Figure 7-30. It means ignition without the negative temperature dependence term occurs at a faster rate. Moreover, a double peak in the pressure rise rate of the current reference model without the negative temperature dependence term in the ignition model is still apparent. Similarly, the ignition of model with E_{ACT}=1.2×10^5 , $TACT_{high}$ = 14500 K and FIGN = 10 without the negative temperature dependence term in the ignition model occurs at a faster rate (compare Figure 7-29 with Figure 7-30) but a double peak in the pressure rise rate does not appear.

Further, as shown in Figure 7-30, when the activation energy for combustion E_{ACT} and the activation temperature for high temperature ignition timescale $TACT_{high}$ are decreased from 1.35×10^5 to 1.2×10^5 kJ/kmol and 16000 to 14500 K respectively, along with increasing in the ignition timescale factor FIGN from 3 to 10, the two-stage ignition becomes less apparent. In other words, with decreasing E_{ACT} and $TACT_{high}$ while setting FIGN high to maintain the same ignition delay, the size of the first peak in the pressure rise rate becomes smaller and later. Here, the ignition timescale factor (FIGN) helps to maintain a high ignition delay at a low E_{ACT} and $TACT_{high.}$. From Figure 7-30, it is clearly observed that higher values for E_{ACT} and $TACT_{high.}$ while setting FIGN low, are mainly responsible for big first peak in the two-stage ignition.

From Figure 7-29 and Figure 7-30 it is clear that the two-stage ignition is dependent on the ignition model parameters ($E_{ACT,}$ $TACT_{high}$ and FIGN) settings. If values for $E_{ACT,}$ and $TACT_{high}$ are high (1.35×10^5 kJ/kmol and 16000 K respectively) along with the low FIGN (3) in the ignition model then the two-stage ignition is clearly apparent whether the negative temperature dependence term is present or not, and if values for $E_{ACT,}$ and

$TACT_{high}$ are low (1.20×10^5 kJ/kmol and 14500 K respectively) along with the high FIGN (10) then the two-stage ignition does not appear without the negative temperature dependence term in the ignition model. It means two-stage ignition in the poor fuel oil is a consequence of ignition model parameters settings. This is also explains why a double hump does not appear in the modelled good fuel oil. The modelled good fuel oil has a smaller $E_{ACT,}$ and $TACT_{high}$ due to its lower aromatic content and thus combustion starts very quickly, without showing a two-stage ignition.

Furthermore, the changes in $E_{ACT,}$, $TACT_{high}$ and FIGN for poor fuel oil is not reflected in the CVCC results because the ignition delay observed in Figure 7-30 for the reference setting and a simulation with E_{ACT}=1.2×10^5 ,$TACT_{high}$ = 14500 K and FIGN = 10 are nearly the same. In other words, when the poor fuel oil is simulated in the CVCC with these different model settings, only a little difference is observed in the spatial characterisation of the combustion process.

The pronounced early hump (first peak) in pressure rise rate is qualitatively similar to the early hump seen for experimental results for the very poor fuel in the FIA, as shown in Figure 7-6 (The FIA experimental results represent the average of a number of shots and thus the shape of the hump will tend to be smoothed out to a certain extent.) The same pronounced early hump did not appear in Goldsworthy's simulations. This is probably because the rate of production of combustible gases from the residual portion is higher in Goldsworthy's model than the present model, so the core of unburnt vapour has a higher vapour concentration, and the dilution effect from the downward movement of the vapour core is not sufficient to suppress onset of full combustion. The present model predicts the rate of production of combustible gases from the residual portion from first principles using pyrolysis kinetics whereas Goldsworthy's approach is empirical. The behaviour of the present model with regard to the pronounced hump tends to support the theory that the mechanism is one of insufficient vapour in the early stages of combustion in the FIA itself, rather than the influence of the negative temperature regime in the ignition kinetics.

To sum up, in the above section, results of the present model are compared with the FIA results supplied by Fueltech Norway and with the modelled results of Goldsworthy [2]. Good qualitative agreement is shown between the computer simulations and the measured

experimental and literature modelled data. The present developed model has an ability to optimally match the experiments provided that detailed composition of the chemically complex HFO is available. In above section composition of the fuels used in experiments and models may not be the same thus precise prediction cannot be achieved. However, an attempt is made to optimise the result which can match with the experiments and simulation results.

7.3.3 Characterised Fuel

The present section provides the simulation results for burning spray of the characterised fuel described in Chapter 3 using StarCD and detailed study of a single parcel within the spray. The present sample was collected from a cargo ship and was delivered to the ship at the port of Sydney, New South Wales, Australia. The chemical characterisation of the present sample was carried out at the University of Tasmania chemistry lab and results are obtained which are discussed in Chapter 3. Indeed it is always hard to be conclusive about the quality of fuel oil without measured combustion data of the fuel. Though there are not measured combustion data available for this fuel oil, it will be useful to present some simulation of this fuel. Because the fuel was not known to cause combustion problems it is assumed to be a good fuel.

All previous models of HFO in the present study were developed for four specific components namely, n-paraffins, aromatics, naphthenes and residue. In those models, cutter stock was considered as a mixture of three lighter components: n-paraffins, aromatics, naphthenes. Through the characterisation experiment, the present HFO sample was divided into SARA fractions (Saturate, Aromatics, Resin and Asphaltenes). These SARA components are different from those components used in all previous models. In order to maintain consistency, the developed models require the proportions of n-paraffins, aromatics, naphthenes and residue in HFO sample.

The separated saturates of the present HFO sample contained both n-paraffins and naphthenes. Since there was not any good technique available which can easily separate the saturate into n-paraffins and naphthenes, the fractionated saturate was taken as a mixture of n-paraffins and naphthenes. However, for the sake of completeness and

comparison the developed model requires four components. Therefore, the saturate fraction (11% of the total mass) is split into 10% n-paraffins and 1% naphthenes. The chromatogram of the saturate fraction (Figure 3-2) clearly confirms that saturate mainly consists of paraffin but there may be some napthenes peaks which are not identified. As described in Chapter 3, the present characterised heavy fuel oil consists of 17% cutter stock and the rest as residue. The composition of cutter stock is more thoroughly described in Chapter 3. However, the detailed composition of cutter stock in terms of distribution parameters used for the simulation is given in Table 7-3. This composition is derived directly from the measurement described in Chapter 3. The combustion model parameters (reference model settings) used in the present simulation are the same as the modelled good fuel oil as the characterised fuel was not known to produce ignition and combustion problems in ship engines.

Table 7-3: Composition of the cutter stock of the simulated characterised fuel.

Components	**Mass Fraction (%)**	**Distribution Origin (γ)**	**Distribution mean (θ) (Mean molecular weight)**	**Standard Deviation (σ)**
n-Paraffins	0.10	146	237.00	43.69
Aromatics	0.06	120	165.00	45.75
Naphthenes	0.01	160	200.00	45.47

An ignition delay of 4.5 ms is observed for the present characterised fuel sample which is intermediate between the ignition delay observed by Takasaki et al.[1] for good fuel oil and poor fuel oil. The ignition delay is a function of fuel to air mixture ratio (equivalence ratio) as well as ignition characteristics of the fuel. In order to start the combustion the equivalence ratio has to be 0.3 or more. In the present sample, the proportion of cutter stock is only 17% therefore a lot of time is required to start the combustion of this fuel. The proportion of cutter was determined through gas chromatography analysis. A careful distillation of the present sample in laboratory may show-up a higher proportion of cutter stock which could solve the issue of long ignition delay. However, due to limited resources and time further experimentation was restricted.

First of all, the present characterised fuel sample is compared with Takasaki et al.'s measured spray results for soot/spray and visual flame extent of good fuel and poor fuel oil using CVCC at 6 ms after the start of combustion as shown in Figure 7-31.

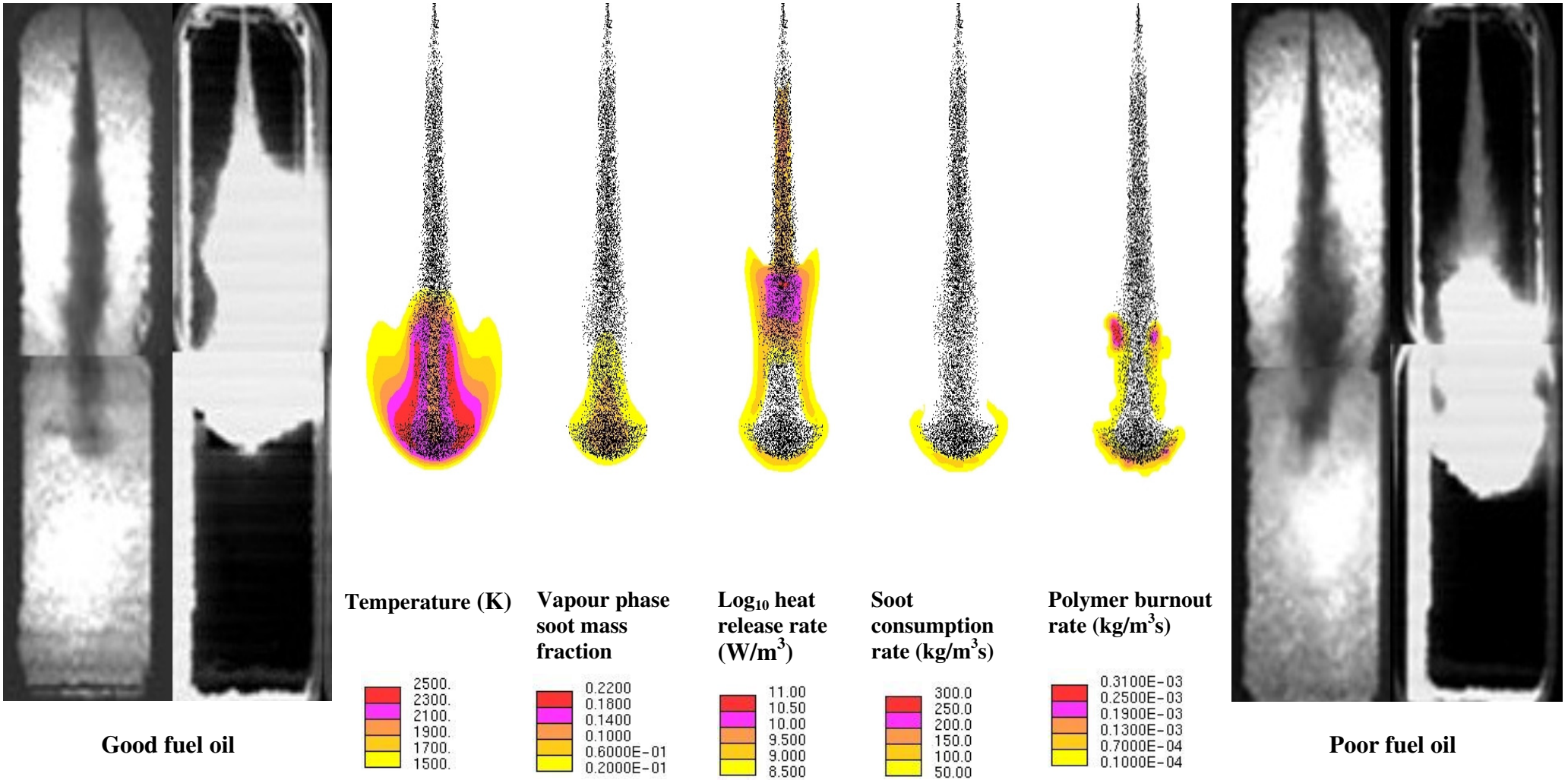

Figure 7-31: The comparison of characterised fuel with measured results of Takasaki et al. for soot/spray and visual flame extent of good and poor fuel oils 6 ms after the start of combustion in the CVCC.

As shown in Figure 7-31, the present characterised fuel simulation results 6 ms after the start of combustion are intermediate between the measured results of Takasaki et al. for good and poor fuel oils. Modelled flame lift-off distance remains much greater than the good fuel oil. Additional simulation results for the spatial distribution of droplet temperature, ambient temperature, oxygen concentration, polymer burnout rate, vapour phase soot mass fraction, soot consumption rate, equivalence ratio and log of heat release rate at 4, 7.2, 9.6, 12.8 and 16 ms after the start of injection are shown in Figure 7-32 to Figure 7-35.

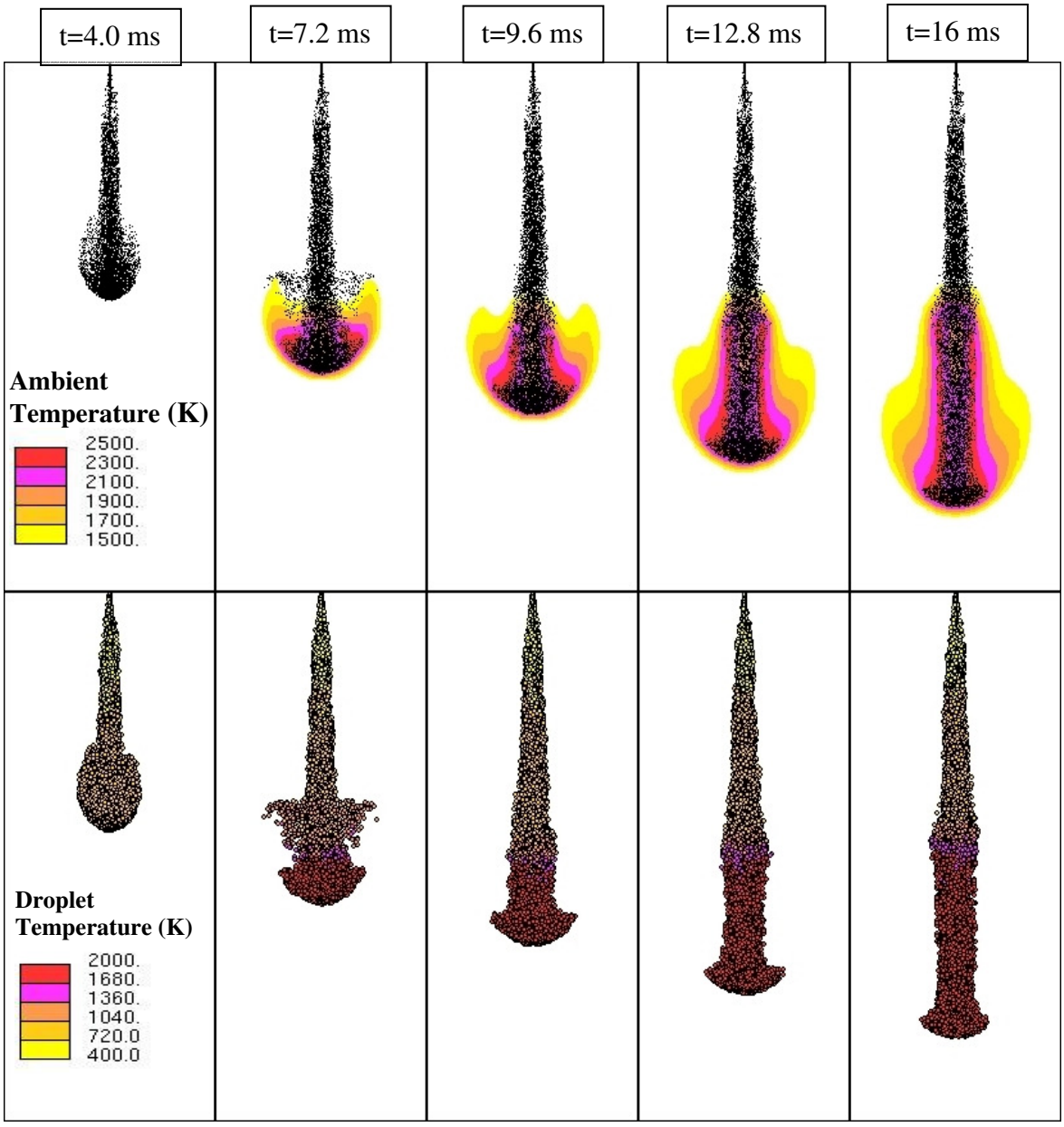

Figure 7-32: The spatial distribution of ambient and droplet temperature of the characterised fuel in the CVCC.

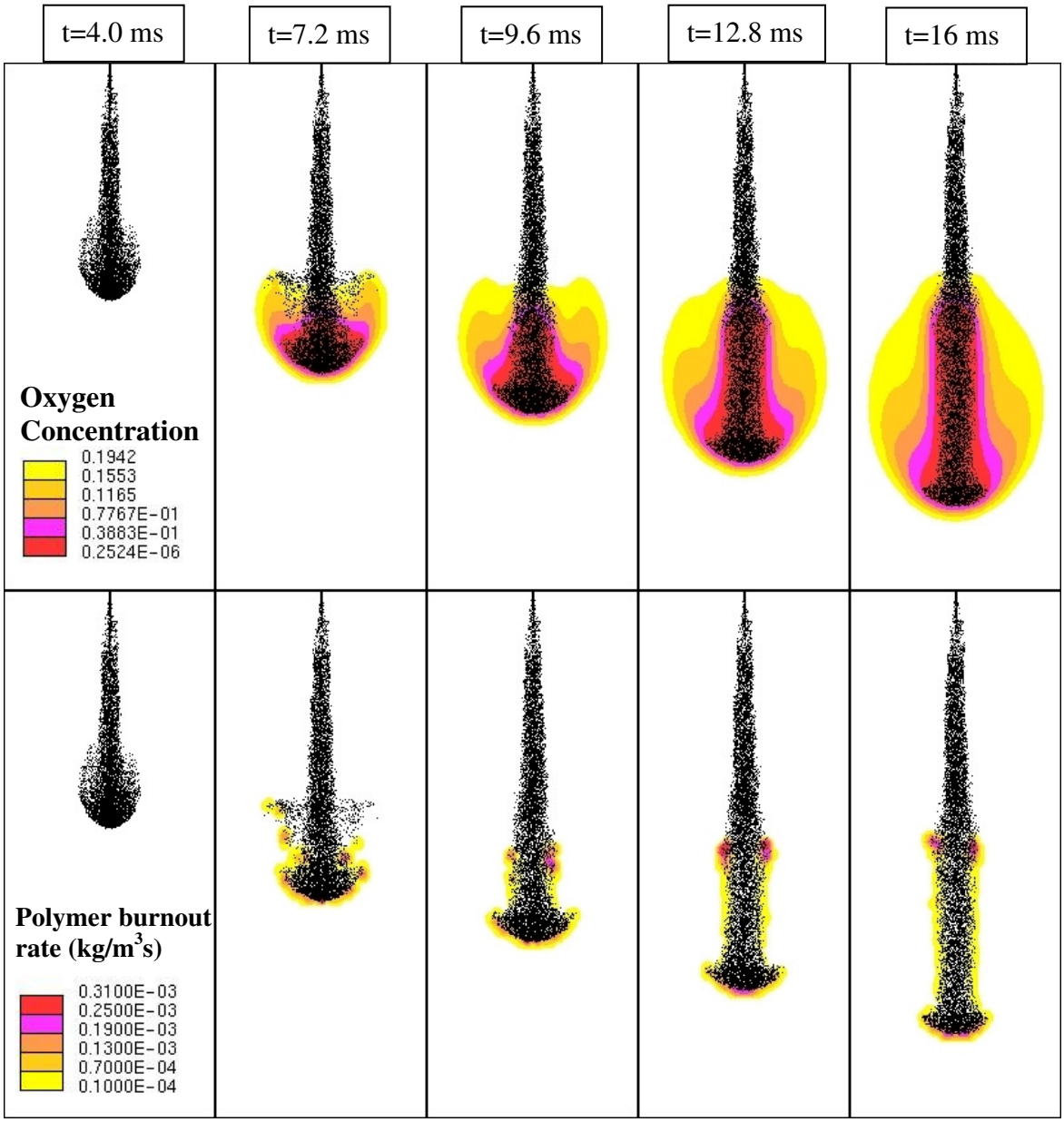

Figure 7-33: The spatial distribution of oxygen concentration and polymer burnout rate of the characterised fuel in the CVCC.

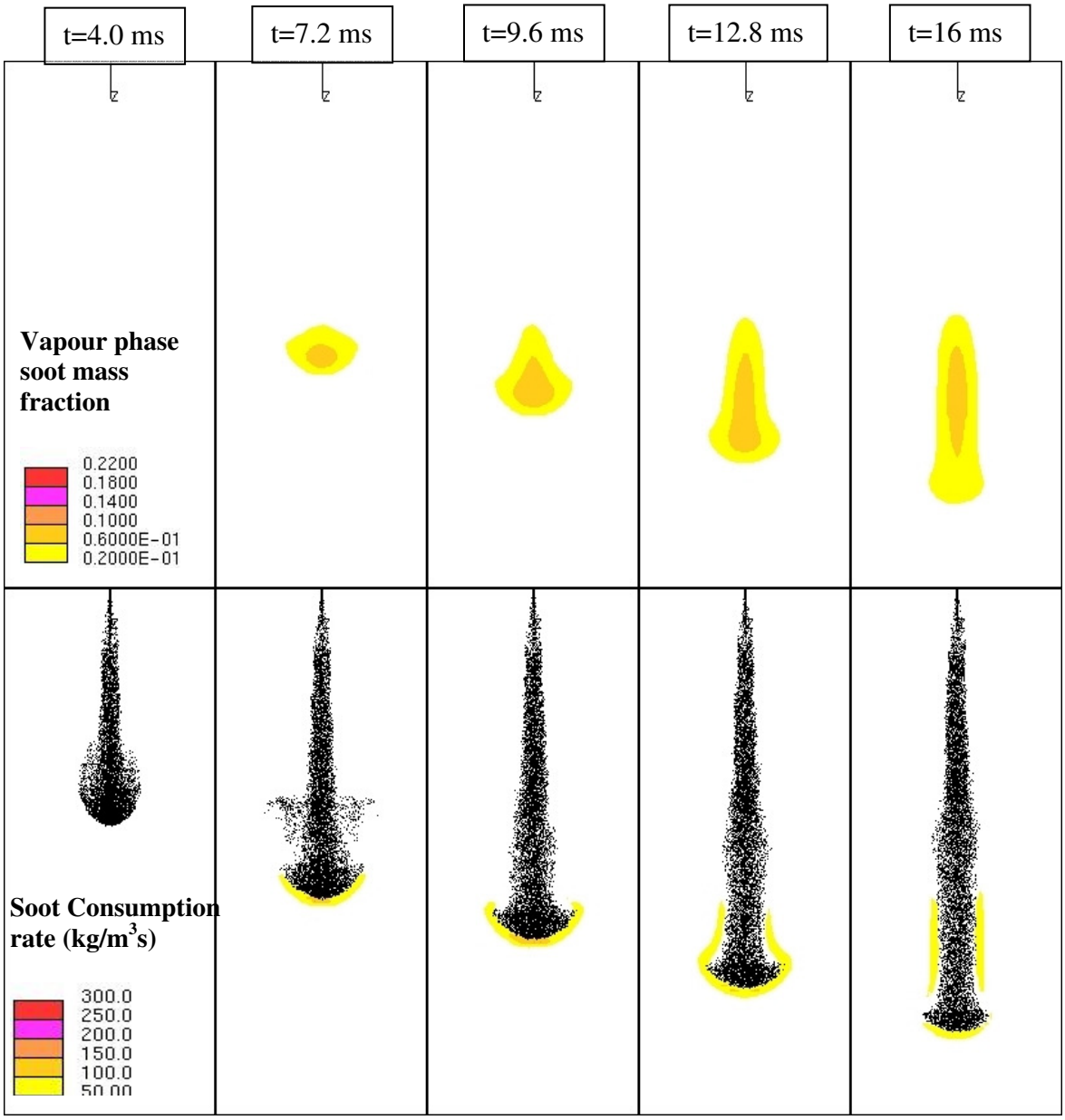

Figure 7-34: Vapour phase soot mass fraction and soot consumption rate of the characterised fuel in the CVCC.

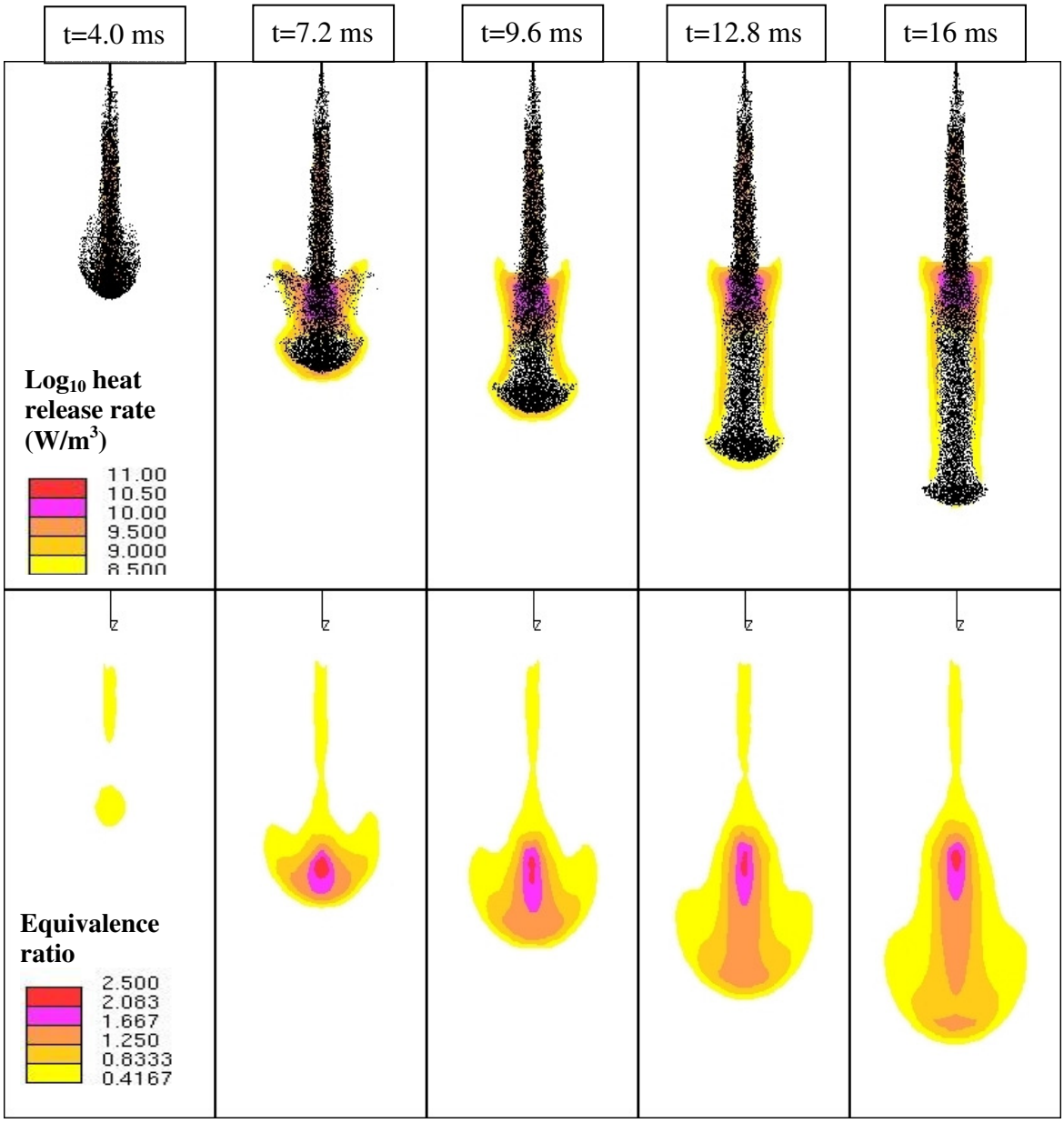

Figure 7-35: The spatial distribution of Log of heat release rate and equivalence ratio of the characterised fuel in the CVCC

The importance of evaporation, ignition and combustion is shown by various means in Figure 7-32 to Figure 7-35. Figure 7-32 shows the temperature distribution of the droplet and as well as of ambient. The effect of combustion on the spray can be observed. At around 7.2 ms after the start of injection, droplets from the spray start disappearing once combustion starts. The start of combustion is verified by equivalence ratio shown in Figure 7-35 and ambient temperature shown in Figure 7-32. As mentioned earlier, 0.3 and 900 K are set as the point of onset of full combustion. The unburnt droplets found at 16 ms in Figure 7-32, whose temperature is close to 2000 K, are either pyrolysing, or burning through surface oxidation, or they are the unburnt polymer remaining as cenospheres. The effect of temperature on vapour phase soot mass fraction and its consumption rate is shown in Figure 7-34. The cutter stock of the present sample is lighter than the cutter stock used in the previous models of the good and poor fuel oils. The effect of lighter cutter stock is discussed in the next section.

7.3.3.1 Study of a Single Parcel within the Characterised Fuel Spray

Again, the same parcel (parcel no. 50) as used in the previous models of the good and poor fuel oils is selected here to study the mass balance of the parcel and other individual droplet properties are plotted in Figure 7-36 to Figure 7-38

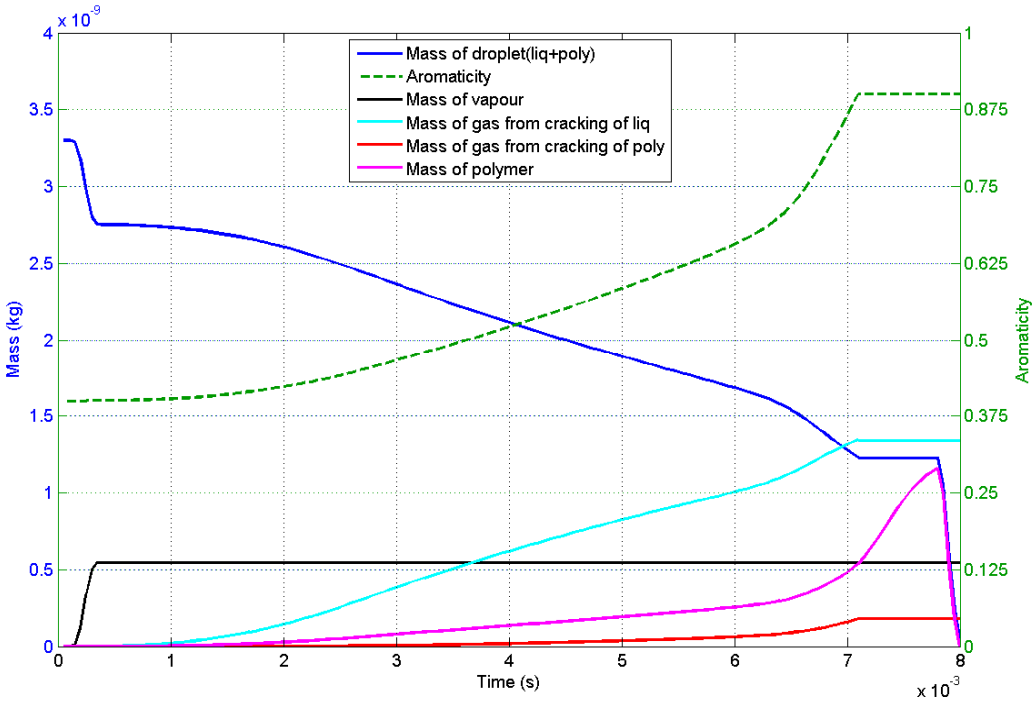

Figure 7-36: Mass balance of the parcel (original components + products) with respect to the parcel lifetime of the modelled characterised fuel in the CVCC (The chamber is initially at 2.5 MPa pressure and 873 K).

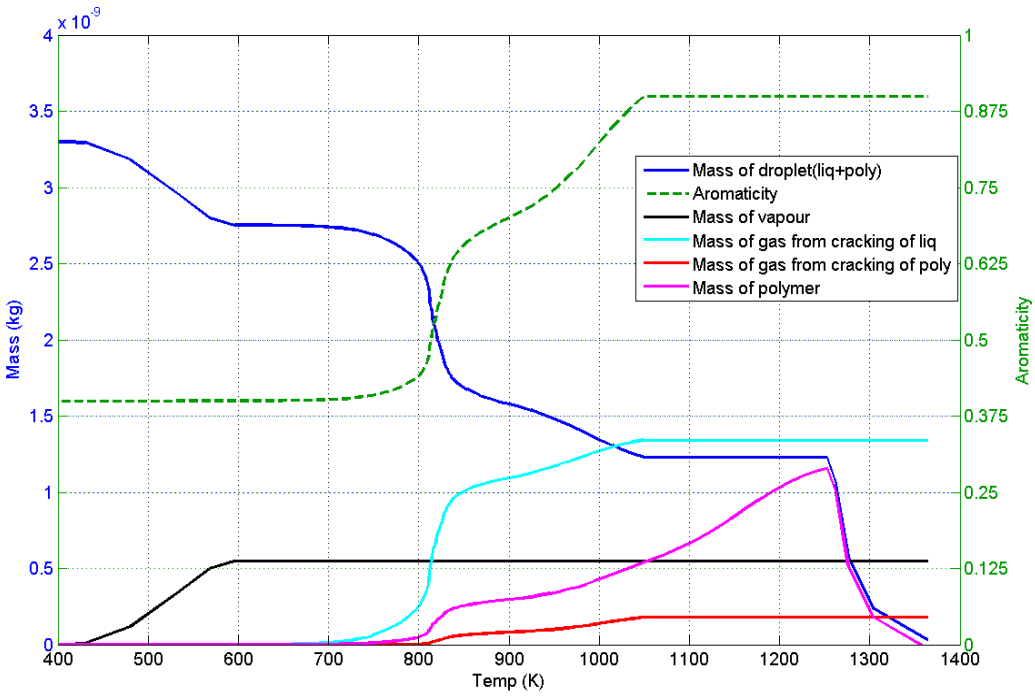

Figure 7-37: Mass balance of the parcel of the characterised fuel oil with respect to temperature of the droplet in the CVCC (The chamber is initially at 2.5 MPa pressure and 873 K).

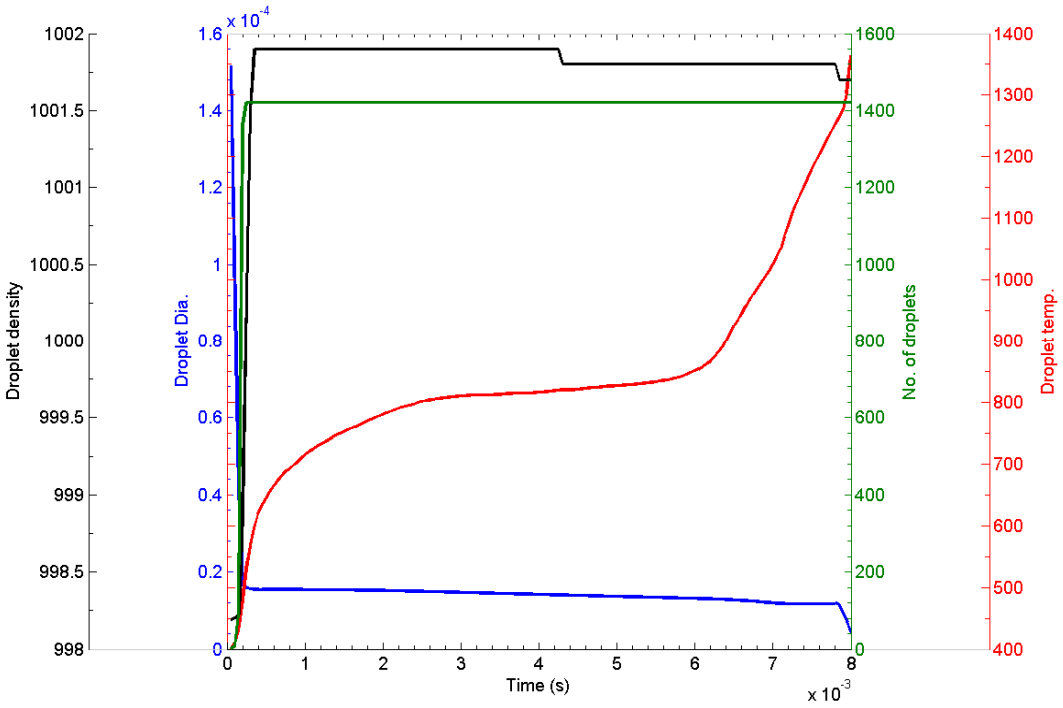

Figure 7-38: Density, diameter, temperature and number of droplets in the parcel with respect to of the modelled characterised fuel in the CVCC (The chamber is initially at 2.5 MPa pressure and 873 K).

As shown in Figure 7-36 to Figure 7-38, cutter stock of the present sample evaporates very rapidly compared to the fuels studied in the previous sections. There are two reasons behind this rapid evaporation: (1) the present sample contains only 17% cutter stock (2) the cutter stock of the present sample contains very light molecules compared to those used in the previous developed models. The cutter stock in the present simulation evaporates off before the droplet reaches 600 K. On the other hand, a large amount of polymer is apparent because the present sample contains 83% heavy residue. However, the formed polymer starts oxidising when it reaches a suitable heterogeneous combustion condition. The parcel in the present case disappeared after evaporation, pyrolysis and heterogeneous surface oxidation.

7.4 Summary

In summary, the present chapter provides the simulation results for two different constant volume spray combustion chambers which are used to examine the combustion characteristics of HFO. A CFD simulation of the characterised HFO is performed using

the developed evaporation and pyrolysis models. The developed models are tested for two representative fuel qualities; one with good combustion quality and the other with poor. The detailed study of a parcel within the spray has provided insight into the combustion process. Good qualitative agreement is shown between the computer simulations and the measured experimental data.

Overall, the developed models behave well when compared with the limited available data from the CVCC and FIA. However, many limitations are faced during the modelling. HFO is comprised of many dissimilar and complex hydrocarbons, and in addition to this many mass transfer processes are happening simultaneously during the combustion. There is not much literature available with the detailed measurement of combustion characteristics of HFO. However, efforts are made to combine the latest literature information in one model to match the experiment results. The choice of turbulence model also affects the spray combustion behaviour, a difference turbulent model with different dispersion rate and droplet persistence may change flame extent. Experimental data on the individual mass transfer processes (evaporation, thermal cracking, polymerisation and surface oxidation etc.) would be very useful to setup the models. An experiment using distillation of HFO sample could provide the proportion of cutter stock in the sample. By injecting the residue of distillation in the form of a known size droplets in high temperature and pressure inert environment could provide mass of polymer, mass of thermal cracking gases and the rate of polymerisation. Here, the mass of cracking gases can be calculated by subtracting the mass of polymer from the total mass of the distillation residue sample (droplets). Oxidising the formed polymer in oxidising media (air) could give the surface oxidation rate. Establishing heating rates similar to spray combustion would be essential.

In a separate experiment, the rate of thermal cracking of the distillation residue can also be obtained by using experimental set up similar to Singh et al.[150]. A comprehensive compositions measurement of pyrolysis gases would be useful to simulate the combustion reactions. Compositions of pyrolysis gases can be measured using a procedure similar to the coal flash pyrolysis procedure used by Doolan et al.[156]. Further, experiment set up described in Nguyen et al.[199] has potential to provide require data on the individual mass transfer processes including evaporation, thermal cracking and polymerisation.

Using their photographic technique would also allow monitoring of the droplet size during pyrolysis. More recommendations and limitations of the present model are presented in the next chapter.

Chapter 8. Conclusions and Recommendations

This chapter summarises conclusions of the present study, which includes experimental procedure for the chemical characterisation of heavy fuel oil, evaporation and pyrolysis models for a single droplet and spray combustion of HFO. It also provides some specific conclusions based on experimental validation results. Moreover, it provides recommendations for further research work.

8.1 Summary and Conclusions

8.1.1 Literature and Chemical Characterisation of HFO

An extensive literature review on heavy fuel oil, modelling of multicomponent fuels, evaporation, pyrolysis and the spray combustion of heavy fuel oil is presented in Chapter 2. An overview of continuous thermodynamics techniques and the effect of ambient pressure on fuel evaporation is also provided in that chapter.

A comprehensive review on the experimental procedures for the separation of heavy fuel oil fractions based on chemical functionality groups is given in Chapter 3. Sequential elution solvent chromatography (SESC) was used to separate heavy fuel oil into SARA fractions; Saturates, Aromatics, Resins and Asphaltenes. The present procedure provided detailed information on the amounts and chemical characteristics of the separated fractions. An extended study using gas chromatography, mass spectrometry and elemental analysis provided further characterisation of the HFO. Gas chromatography and mass spectrometry provided the mean molecular weights of the separated fractions.

It was identified that gas chromatography alone is not sufficient to determine the overall composition of HFO, since HFO contains a very large range of molecules and among them, gas chromatography is only able to analyse the light molecules. Therefore, mass spectrometry was employed to determine the mean molecular weights, molecular weight range and the representative structure of the separated fractions. The mass spectrometry and elemental analysis show a wide range of molecular weight distributions and volatility for separated HFO fractions. The results also show that the separated saturate fraction

contains a cyclic structure with attached aliphatic hydrocarbons in side chains and the separated aromatics fraction was composed of tetracyclic aromatic rings with aliphatic side chains. In brief, a detailed procedure to obtain the required information for the continuous thermodynamics modelling of heavy fuel oil is provided in Chapter 3. A CFD simulation of the present characterised HFO using the developed evaporation and pyrolysis model is presented in Chapter 7.

8.1.2 Model Development and Results for a Single Droplet

Heavy fuel oil is known to contained many dissimilar structure hydrocarbons. During combustion of an HFO droplet, fuel composition within the droplet changes due to evaporation (fractional distillation), thermal cracking, polymerisation and heterogeneous combustion of soot particles. Because of these many complex processes happening simultaneously, no model found in the literature can calculate the combustion behaviour of heavy fuel oil accurately. The mathematical model presented in Chapter 4 calculates the evaporation and pyrolysis process of a stationary single droplet. In the present model heavy fuel oil is assumed to comprise of four hydrocarbons groups such as paraffins, aromatics, napthenes and heavy residue. The light components (n-paraffins, aromatics and naphthenes) in HFO evaporate through evaporation while the heavy component (residue), which is composed of heavy and polar hydrocarbons, is subjected to pyrolysis (thermal cracking and polymerisation).

Different components of HFO have different evaporation rates because they evaporate in order of their relative volatility. This evaporation is a fractional distillation kind of process. For such a fuel, an application of multiple distribution functions using continuous thermodynamics modelling approach is necessary for the accurate representation of fuel components throughout the evaporation. In continuous thermodynamics modelling of multicomponent fuel, the composition of a group similar structure species of the component of is simply represented by two parameters instead of thousands of mole fractions, as required in the conventional discrete modelling.

The developed evaporation model includes *Raoult's low* and Clausius-Clapeyron equation to calculate the vapour-liquid equilibrium (VLE) at low pressure, and a non-linear

equation of state at elevated pressure. The formulations for high-pressure VLE were developed for the semicontinuous mixture and a generic approach to the EOS is used. Therefore, depending on the mixture compositions (continuous or semicontinuous) these formulations can be applied by using one of the EOS from three basic EOS (Peng-Robinson (PR), Soave-Redlich-Kwong (SRK) and Redlich-Kwong (RK)). The choice of EOS is dependent on the available practical data on the multicomponent mixture. Further, analytical predictions of temperature history of an individual droplet are improved by using the enthalpy of decomposition and specific heat of polymer formed in the liquid phase. Correlations for calculating the various transport properties of all four components of heavy fuel oil are formulated.

At first, the developed low/high-pressure models along with Baert's pyrolysis model are applied to study the evaporation and pyrolysis of a stationary single droplet, which is given Chapter 5. There are not significant differences observed in evaporation rates of the light molecules using either the low-pressure model or high-pressure model when they are compared without any interaction coefficients. However, significance differences are observed in the evaporation rates of light components of the HFO when interaction between the individual components and between the components of HFO and air are applied. Evaporation occurs at a faster rate when using interaction coefficients. Thus, interaction coefficients play an important role during the high-pressure EOS-VLE modelling.

Calculation results of the low/high-pressure model along with Baert's pyrolysis model showed that at a high heating rate, irrespective of low-pressure or high-pressure evaporation model, an individual HFO droplet produces more polymer than at a low heating rate. In other words, Baert's pyrolysis model showed that polymer formation is a function of droplet heating rate; a small droplet (possesses high heating rate) produces more polymer compared to a big droplet at the same ambient condition. In engine spray combustion generally droplets are small and heating rates are high. Moreover, it is observed in Baert's pyrolysis model results that the process of polymerisation starts prior to the thermal cracking. This order of thermal cracking and polymerisation is contrary to the experimental evidence. Further, for the subsequent spray combustion simulation, Baert's pyrolysis model did not give a sufficient rate of production of pyrolysis gas for the modelled combustion process to match the measured data. Thus, Baert's pyrolysis model

could be not applied in spray combustion calculations directly. Therefore, the pyrolysis model was studied in depth to understand the polymer formation and gas production from a single HFO droplet. Despite studying many papers in the literature, no concrete conclusion was drawn about the kinetics parameters and rate constants for HFO pyrolysis because kinetics parameters vary according to sample composition and also with the origin of samples. Consequently, a pyrolysis model similar to Baert's pyrolysis model is postulated with modified activation energies and pre-exponential factors informed by the study of pyrolysis kinetics. Results of the modified pyrolysis model did not show any significant dependency of polymer formation on droplet heating rate and in addition it showed thermal decomposition beginning earlier than the polymerisation.

A comparison of the low-pressure model with the high-pressure model for 100-micron and 30-micron droplets at high pressure and temperature showed that evaporation of the volatile hydrocarbons (n-paraffins, aromatics, naphthenes) from HFO occurs at a faster rate for the high-pressure model. However, this faster evaporation does not significantly affect the droplet lifetime because modelled HFO contains only 30% volatile hydrocarbons (cutter stock) by mass. Therefore, droplet lifetime is found to be similar for both models. Thus in spray combustion simulation where droplets are generally small, the VLE calculation can be obtained with sufficient accuracy by the linear VLE of the low-pressure model avoiding the use of the complex high-pressure non-linear EOS model. On the other hand, where cutter stock proportion is higher early evaporation rate for the high-pressure model could influence the early vapour concentration and composition which is important for ignition. However, ignition delay can be adjusted with the ignition factor (FIGN).

The models presented Chapter 4 and Chapter 5, give good agreement with the previous single droplet modelling results and limited available experimental results. However, many uncertainties are faced during the modelling. HFO is comprised of many dissimilar and complex hydrocarbons, and in addition to this many mass transfer processes are happening simultaneously during the combustion. There is not much literature available with the detailed measurement of individual mass transfer processes. However, efforts are made to combine the latest literature information in one model to match the experiment results. The present models demonstrate that continuous thermodynamics combined with simplified chemical kinetics has the ability to model the evaporation and pyrolysis

processes for complex multicomponent mixtures. Compositions of the fuel used in the present model are not from any particular fuel sample, rather they are representative only but they demonstrate the importance of individual mass transfer processes.

8.1.3 Spray Model Development

In the present study, an advanced model for spray combustion of heavy fuel oil is developed which practically includes all the mass transfer processes listed in the literature as occurring during combustion. Continuous thermodynamics and pyrolysis chemical kinetics are used to model the behaviour of multicomponent and chemically complex HFO in spray combustion. The low-pressure evaporation model along with the modified pyrolysis model developed for a single droplet in the previous chapters is employed for the spray combustion calculation. Chapter 6 summarises the basic conception and development of an integrated computer simulation model for spray combustion of heavy fuel oil in high–pressure environment. The present spray calculation study is built on the previously developed model for HFO spray combustion by Goldsworthy [2]. The recommendations made by Goldsworthy [2] to develop the accurate model for evaporation, thermal cracking, polymerisation and heterogeneous combustion of polymer particles of the HFO droplet are justified. The models are integrated in StarCD through user subroutines. Key user subroutines include supplementary models for; mass transfer (evaporation and pyrolysis), droplet properties, liquid phase soot formation and its heterogeneous combustion.

The models for ignition, combustion, gas phase soot formation and its combustion are accepted from Goldsworthy [2] and directly used in the present study. The ignition model parameters are set according to the ignition quality of the good fuel oil and the poor fuel oil. The difficulties faced and the problems which occurred during the development of models in the StarCD are identified and described in the last section of Chapter 6.

8.1.4 Spray Calculation Validation with Experimental Results

The developed models are tested for two representative fuels; good fuel oil and poor fuel oil and two sets of experimental results; CVCC and FIA. The data from the CVCC

provides flame and spray observations, whereas the data from the FIA provides chamber pressure rise rate. The combustion characteristics obtained in the simulations are, overall well representative of the experimentally observed behaviour. The comparison of present simulation results with simulation results of Goldsworthy [2] and experimental results of Takasaki et al.[1] for the CVCC showed good agreement. In particular the ignition delay, burn rate and the spatial distribution of spray are closely matched. The study of a single parcel within the spray showed the process of fractional distillation, thermal cracking, polymerisation and heterogeneous combustion of formed polymer.

Two-stage ignition is apparent for the FIA simulation of poor fuel oil which is qualitatively similar to the two-stage ignition seen for experimental results for the poor and very poor fuel in the FIA. It is understood that this two-stage ignition is a consequence of ignition model parameters settings. Higher values for the activation energy for combustion and the activation temperature for high temperature ignition timescale while setting the ignition timescale factor low are mainly responsible for the two-stage ignition. The same pronounced two-stage ignition did not appear in Goldsworthy's simulations. This is probably because the rate of production of combustible gases from the residual portion is higher in Goldsworthy's model than the present model, so the core of unburnt vapour has a higher vapour concentration, and the dilution effect from the downward movement of the vapour core is not sufficient to suppress onset of full combustion. The present model predicts the rate of production of combustible gases from the residual portion from first principles using pyrolysis kinetics whereas Goldsworthy's approach is empirical. The behaviour of the present model with regard to the pronounced two-stage ignition tends to support the theory that the mechanism for two-stage ignition is one of insufficient vapour in the early stages of combustion in the FIA itself, rather than the influence of the negative temperature regime in the ignition kinetics.

Further, a simulation result is provided in Chapter 7 to predict the combustion behaviour of characterised fuel sample in CFD.

Overall, the developed models performed well with the limited available data from the CVCC and FIA. However, many limitations are faced during the modelling. HFO is comprised of many dissimilar and complex hydrocarbons, and in addition to this many mass transfer processes are happening simultaneously during the combustion. There is not

much literature available on the individual mass transfer processes. Experimental data on the individual mass transfer processes such evaporation, thermal cracking, polymerisation and surface oxidation etc. would be very useful to setup the models. The choice of turbulence model also affects the spray combustion behaviour, a different turbulence model leading to different dispersion rate and droplet penetration may change flame extent. Other identified limitations of the present developed model and recommendations for further research in the present research area are given in the next section.

8.2 Recommendations/Key Aspects for Future Research

8.2.1 Experimental Investigations

It is clear that more experimental investigations are required for the HFO droplet because it consists of many components. A surrogate mixture closely representing HFO composition would help in understanding the evaporation and pyrolysis of multicomponent fuel. Experiments including chemical characterisation, evaporation and pyrolysis study of a single droplet in a high temperature field would shed more light on the combustion characteristics of such complicated commercial fuel. The present developed model is superior to the model found in literature but still it requires further experimental validation. A comprehensive study including characterisation of HFO, its combustion behaviour in the real commercial engine and studying the same fuel for spray combustion in the CVCC would provide the valuable information required for the present model.

Moreover, data may be found in the literature for the light components of HFO but a lot more investigation is required for the heavy components (residue). Especially, the evaporation characteristic of the heavy residue in HFO is not known and there may be a case where residue may evaporate by following the evaporation of the light components in the mixture due to interactions. Detailed data on the interaction coefficients between the individual liquid components and between the liquid components and air are certainly needed to use the non-linear EOS high-pressure model. A detailed experiment explained in Chapter 7 to obtain global *Arrhenius law* parameters (rate constants) for pyrolysis of the characterised fuel would help to improve the thermal cracking and polymerisation model.

A comprehensive compositions measurement of pyrolysis gases would be useful to simulate the combustion reactions. Further studies are essential to understand the polymer burnout mechanism. The current model would give better results of the multicomponent mixtures, when the physical and chemical properties are known experimentally.

8.2.2 Multicomponent Fuel Modelling Alternative Approaches

The continuous thermodynamics modelling approach enables sophisticated modelling of the commercial fuel to be used in diesel engines simulation. However, during the modelling of a single droplet and spray combustion, some weaknesses in the present modelling are identified. It is found that towards the end of a particular component's lifetime when the composition of that component and that of the ambient are significantly different, at that time the predicted width of the distribution ($\sigma^2 = \psi - \theta^2$) function (either liquid phase or vapour phase) of that component becomes negative, which is unrealistic. This affects both liquid phase and vapour phase composition. The other weakness of the present approach is its unbound distribution function. Sometimes it is found that at the tail end of the evaporation process, excessively high mean molecular weight of the composition can be predicted, though there is only a small amount of droplet mass left.

These above mentioned two weaknesses of the continuous thermodynamic modelling can occur simultaneously. The second weakness can be resolved by using a bound distribution function but still the first weakness remains. A β-distribution found in the literature is a bound type distribution function which can be given as [119] ;

$$f(u) = \frac{\Gamma(\alpha+\beta)}{\Gamma(\alpha)\Gamma(\beta)} u^{\alpha-1}(1-u)^{\beta-1} \qquad 0 < u < 1 \tag{108}$$

Where α and β are distribution variables, Γ is the gamma function, and u is the scaled distribution variable. The mean and the variance of the distribution can be given as [119] ;

$$\theta = \frac{\alpha}{\alpha+\beta}, \qquad \sigma^2 = \frac{\alpha\beta}{(\alpha+\beta)^2(\alpha+\beta+1)} \tag{109}$$

The β-distribution function has one further advantage over the Γ-distribution function being that its shape is more flexible. The peak of the distribution in the β-distribution function can be located anywhere in between the upper limit and lower limit, whereas in the Γ-distribution it is skewed at the lower end.

Each individual equation of state (EOS) has its own advantages and disadvantages. The results of phase equilibrium obtained by Zhu & Aggarwal [81] using different EOS showed a wide scatter in the mole fractions at the surface. In the present model SRK EOS is used in the calculation. However, as shown by Zhu & Aggarwal [81] it will be useful to study the capability of different EOS for predicting the best VLE during the evaporation of a droplet to match with the experimental results.

The possible effect of high pressure on thermal cracking and polymerisation rates needs to be explored perhaps by studying the pyrolysis of a single droplet at different pressures.

In the present modelling, the combustion mechanism of species in the vapour phase is represented by n-dodecane combustion only. The ignition qualities of the fuels are set by changing the ignition parameters and activation energy for the high-temperature kinetics. However, there will be a different range of species evolving from the droplet depending upon their relative parent composition. In other words, more aromatic rich fuels will have a range of species evolving as aromatics and similarly the paraffinic rich fuel will have range of species evolving as paraffinic. In addition, thermal cracking gases could be paraffinic or olefinic molecules containing up to 10 carbon atoms along with H_2, H_2O and CO_2 [14]. Therefore, further development of the combustion reactions of more individual species (other than just n-dodecane) in a CFD environment would be useful for precise spray combustion of HFO.

The presently developed model could also be used for any other multicomponent fuel which has similar evaporation and pyrolysis processes.

References

1. Takasaki, K., H. Tajima, M. Nakashima, H. Ishida, and S. Osafune. *Combustion Characteristics of Trouble Making Bunker Fuel Oil*. in *CIMAC*, 2001, at Hamburg. p. 620-629.
2. Goldsworthy, L. *Computational Fluid Dynamics Modelling of Residual Fuel Oil Combustion in the Context of Marine Diesel Engines.* International Journal of Engine Research, 2006. **7**: p. 181-199.
3. Shuo, M. *Maritime Economics*. 1999: World Maritime University (e-book).
4. Rodrigue, J.-P., B. Slack, and C. Comtois. *The Geography of Transport Systems*. 2006, New York, USA: Routledge.
5. Versaevel, P., P. Motte, and K. Wieser. *A New 3d Model for Vaporizing Diesel Sprays Based on Mixing-Limited Vaporization.* SAE International, Paper No.-2000-01-0949, 2000.
6. Strom, A., H. Tajima, S. Murakami, and S. Asaura. *Combustibility Evaluation of Heavy Fuel Oil by Modified Fuel Ignition Analyzer*. in *Proceedings of the 7th International Symposium on marine engineering*, 2005, at Tokyo. p. 1-8.
7. Wang, J. and E.J. Anthony. *A Study of Thermal-Cracking Behavior of Asphaltenes.* Chemical Engineering Science, 2003. **58**(1): p. 157-162.
8. Baert, R.S.G. *Auto Ignition of Heavy Fuel Oil Sprays at High Pressure and Temperatures.* Journal of Engineering for Gas turbines and Power, 1990. **112**: p. 324-330.
9. Steernberg, K. and S. Forget. *The Effects of a Changing Oil Industry on Marine Fuel Quality and How New and Old Analytical Techniques Can Be Used to Ensure Predictable Performance in Marine Diesel Engines*. in *CIMAC Congress*, 2007, at Vienna. Paper No.198.
10. Hamosfakidis, V. and R.D. Reitz. *Optimization of a Hydrocarbon Fuel Ignition Model for Two Single Component Surrogates of Diesel Fuel.* Combustion and Flame, 2003. **132**(3): p. 433-450.
11. Williams, A. *Fundamentals of Oil Combustion.* Progress in Energy and Combustion Science, 1976. **2**(3): p. 167-179.
12. Saario, A., A. Rebola, P.J. Coelho, M. Costa, and A. Oksanen. *Heavy Fuel Oil Combustion in a Cylindrical Laboratory Furnace: Measurements and Modeling.* Fuel, 2005. **84**(4): p. 359-369.
13. Uehara, J., K. Shimizu, T. Omata, and T. Hatashi, *Effect of Asphaltene and Carbon Residue in Marine Fuel on Combustion Performance*, in *CIMAC Congress*. 1998: Copenhagen.
14. Baert, R.S.G. *A Mathematical Model for Heavy Fuel Oil Droplet Vaporization and Pyrolysis in a Heavy Temperature Inert Gas.* Combustion Science and Technology, 1993. **90**: p. 125-147.
15. Ramanathan, V. and G. Carmichael. *Global and Regional Climate Changes Due to Black Carbon.* Nature Geosci, 2008. **1**(4): p. 221-227.
16. *Prevention of Air Pollution from Ships, Second Imo Ghg Study 2009*, in *International Maritime Organisation (IMO)*. April 2009: London, UK.
17. Rakowski, S., M. Fischer, G. Stiesch, and G.P. Merker. *Advanced Evaporation Models for Gasoline and Diesel Spray Investigations*. in *Proceedings of the 20th ILASS – Europe Meeting 2005*, 2005.

18. Tamim, J. and W.L.H. Hallett. *A Continuous Thermodynamics Model for Multicomponent Droplet Vaporization.* Chemical Engineering Science, 1995. **50**(18): p. 2933-2942.
19. Hallett, W. and C. Grimwood. *A Simple Continuous Mixture Droplet Evaporation Model with Multiple Distribution Functions*. in *Combustion Institute*, 2001, at Canadian Section. Spring Meeting. p. 31.1 - 31.6.
20. Hallett, W., N.A. Clark, and M. White. *Evaporation of Biomass Pyrolysis Oil Droplets - Ii*. in *Combustion Institute.*, 2003, at Canadian Section. Spring Meeting p. 41.1 - 41.6.
21. Hallett, W.L.H. and N.A. Clark. *A Model for the Evaporation of Biomass Pyrolysis Oil Droplets.* Fuel, 2006. **85**(4): p. 532-544.
22. Garaniya, V. and L. Goldsworthy. *Vaporization and Pyrolysis Modelling of a Single Droplet of Heavy Fuel Oil Using Continuous Thermodynamics.* ANZIAM Journal, 2007. **49** p. C116-C138.
23. Ikegami, M., G. Xu, K. Ikeda, S. Honma, H. Nagaishi, D.L. Dietrich, and Y. Takeshita. *Distinctive Combustion Stages of Single Heavy Oil Droplet under Microgravity.* Fuel, 2003. **82**(3): p. 293-304.
24. Tajima, H., *Personnel Communications* 2008.
25. Villasenor, R. and F. Garcia. *An Experimental Study of the Effects of Asphaltenes on Heavy Fuel Oil Droplet Combustion.* Fuel, 1999. **78**(8): p. 933-944.
26. Savage, P.E., M. Klein, and S. Kukes. *Asphaltene Reaction Pathways-Thermolysis.* Ind. Eng. Chem. Proc. rev. Dev, 1985. **24**: p. 1169.
27. Evdokimov, I.N., N.Y. Eliseev, and B.R. Akhmetov. *Asphaltene Dispersions in Dilute Oil Solutions.* Fuel, 2006. **85**(10-11): p. 1465-1472.
28. Andrews, A.B., R.E. Guerra, O.C. Mullins, and P.N. Sen. *Diffusivity of Asphaltene Molecules by Fluorescence Correlation Spectroscopy.* J. Phys. Chem. A, 2006. **110**(26): p. 8093-8097.
29. Demirbas, A. *Asphaltene Yields from Five Types of Fuels Via Different Methods.* Energy Conversion and Management, 2002. **43**(8): p. 1091-1097.
30. Badre, S., C. Carla Goncalves, K. Norinaga, G. Gustavson, and O.C. Mullins. *Molecular Size and Weight of Asphaltene and Asphaltene Solubility Fractions from Coals, Crude Oils and Bitumen.* Fuel, 2006. **85**(1): p. 1-11.
31. Chen, C.S. and M.M.EI-Wakil. *Experimental and Theoretical Studies of Burning Drops of Hydrocarbon Mixtures.* Proceedings for Instrumentation and Mechanical Engineers, 1969. **184 (Pt. 3J)**: p. 95-108.
32. Hottel, H.C., G.C. Williams, and H.C. Simpson. *Combustion of Droplets of Heavy Liquid Fuels*. in *Fifth Symposium (International) on Combustion*, 1955, at The Combustion Institute. p. 101.
33. Godsave, G.A.E. *Studies of the Combustion of Drops in a Fuel Spray, the Burning of Single Drops of Fuel*. in *4th Symposium (International) on Combustion*, 1953: The combustion Institute, Baltimore, MD. p. 819-831.
34. Wood, B.J., H. Wise, and S.H. Inami. *Heterogeneous Combustion of Multicomponent Fuels.* Combustion and Flame, 1960. **4**: p. 235-242.
35. Michael, M.I. and M.M. EI-Wakil. *On the Self Ignition of Hydrocarbon Mixtures*. in *11th Symposium (International) on combustion,*, 1967: The combustion Institute, Pittsburgh, PA. p. 1027-1055.
36. Shyu, R.R., C.S. Chen, G.O. Goudie, and M.M. El-Wakil. *Multi-Component Heavy Fuel Drop Histories in a High-Temperature Flow Field.* Fuel, 1972. **51**(2): p. 135-145.

37. Lightman, P. and P.J. Street. *Single Drop Behaviour of Heavy Fuel Oils and Fuel Oil Fractions.* Journal of the Institute of Energy 1983. **56**(426): p. 3-11.
38. Marrone, N.J., I.M. Kennedy, and F.L. Dryer. *Coke Formation in the Combustion of Isolated Heavy Oil Droplets.* Combustion science and technology, 1984. **36**(3-4): p. 149-170.
39. Urban, D.L. and F.L. Dryer. *New Results on Coke Formation in the Combustion of Heavy Fuel Droplets*. in *23rd Symposium (International) on combustion*, 1990: The Combustion Institute. p. 1437-1443.
40. Zhao, S., Z. Xu, C. Xu, and K.H. Chung. *Feedstock Characteristic Index and Critical Properties of Heavy Crudes and Petroleum Residua.* Journal of Petroleum Science and Engineering, 2004. **41**(1-3): p. 233-242.
41. Goldstein, H.L. and C.W. Siegmund. *Influence of Heavy Fuel Oil Composition and Boiler Combustion Conditions on Particulate Emissions.* Environ. Sci. Technol., 1976. **10**(12): p. 1109-1114.
42. Bomo, N., J. Lahaye, G. Prado, and G. Claus. *Formation of Cenospheres During Pyrolysis of Residual Fuel Oils.* Symposium (International) on Combustion, 1985. **20**(1): p. 903-911.
43. Whitehead, D.M., J.C. Finns, and P.C. Beadle. *Studies Related to Residual Fuel Oil Composition and the Formation and Burnout of Particulates During Combustion* Erdoel und Kohle, Erdgas, Petrochemie vereinigt mit Brennstoff-Chemie, 1983. **36**(12): p. 557-581.
44. Borman, G.L. and K.W. Ragland. *Combustion Engineering*. 1998: McGRAW HILL Singapore
45. Treybal, R.E. *Mass-Transfer Operations*. Second Second. 1981: McGraw-Hill Book Company-Singapore.
46. Sazhin, S. *Modelling of Heating, Evaporation and Ignition of Fuel Droplets: Combined Analytical, Asymptotic and Numerical Analysis.* Journal of Physics: Conference Series, 2005. **22**: p. 174-193.
47. Givler, S.D. and J. Abraham. *Supercritical Droplet Vaporization and Combustion Studies.* Progress in Energy and Combustion Science, 1996. **22**(1): p. 1-28.
48. Miller, R.S., K. Harstad, and J. Bellan. *Evaluation of Equilibrium and Non-Equilibrium Evaporation Models for Many-Droplet Gas-Liquid Flow Simulations.* International Journal of Multiphase Flow, 1998. **24**(6): p. 1025-1055.
49. Abramzon, B. and W.A. Sirignano. *Droplet Vaporization Model for Spray Combustion Calculations.* International Journal of Heat and Mass Transfer, 1989. **32**(9): p. 1605-1618.
50. Sirignano, W.A. *Theory of Multicomponent Fuel Droplet Vaporization.* Archive of Thermodynamics and Combustion 1979. **9**: p. 235-251.
51. Ranz, W.E. and W.R. Marshall. *Evaporation from Drops Part 1.* Chemical Engng Progress, 1952. **48**(3): p. 141-146.
52. Arcoumanis, C., M. Gavaises, and B. French. *Effect of Fuel Injection Processes on the Structure of Diesel Sprays.* SAE International, Paper No.-970799, 1997.
53. Ranz, W.E. and W.R. Marshall. *Evaporation from Drops Part 2.* Chemical Engng Progress, 1952. **48**(3): p. 173-180.
54. Sirignano, W.A. *Fuel Droplet Vaporization and Spray Combustion Theory.* Progress in Energy and Combustion Science, 1983. **9**(4): p. 291-322.
55. Law, C.K. *Multicomponent Droplet Combustion with Rapid Internal Mixing.* Combustion and Flame, 1976. **26**: p. 219-233.
56. Kneer, R., M. Schneider, B. Noll, and S. Wittig. *Diffusion Controlled Evaporation of a Multicomponent Droplet: Theoretical Studies on the Importance of Variable*

Liquid Properties. International Journal of Heat and Mass Transfer, 1993. **36**(9): p. 2403-2415.
57. Law, C.K. *Internal Boiling and Superheating in Vaporizing Multicomponent Droplets.* AIChE Journal, 1978. **24**(4): p. 626-632.
58. Law, C.K. and H.K. Law. *A D^2 Square Law for Multicomponent Droplet Vaporization and Combustion.* American Institute of Aeronautics and Astronautics Journal, 1982. **20**(4): p. 522-527.
59. Bergeron, C.A. and W.L.H. Hallett. *Ignition Characteristics of Liquid Hydrocarbon Fuels as Single Droplets.* The Canadian Journal of Chemical Engineering 1989. **67**: p. 142-148.
60. Mawid, M. and S.K. Aggarwal. *Analysis of Transient Combustion of a Multicomponent Liquid Fuel Droplet.* Combustion and Flame, 1991. **84**(1-2): p. 197-209.
61. Hallett, W.L.H. and M.A. Ricard. *Calculations of the Auto-Ignition of Liquid Hydrocarbon Mixtures as Single Droplets.* Fuel, 1992. **71**(2): p. 225-229.
62. Sirignano, W.A. *Fluid Dynamics and Transport of Droplets and Sprays*. 1999: Cambridge University Press, Cambridge.
63. Law, C.K., S. Prakash, and W.A. Sirignano. *Theory of Convective, Transient, Multicomponent Droplet Vaporization*. in *Sixteenth Symposium (international) on combustion*, 1976. p. 605-617.
64. Landis, R.B. and A.F. Mills, *Effects of Internal Diffusional Resistance on the Evaporation of Binary Droplets* in *Fifth International Heat Transfer Conference*. 1974. p. 345-349.
65. Jin, J.D. and G.L. Borman. *A Model for Multicomponent Droplet Vaporization at High Ambient Pressures.* SAE International, Paper No.-850264, 1985.
66. Abraham, J. and V.Magi. *A Model for Multicomponent Droplet Vaporization in Sprays*. in *International Congress and Exposition* 1998, at Michigan: SAE.
67. Lara-Urraneja, P. and W.A. Sirignano. *Theory of Transient Multicomponent Droplet Vaporization in a Convective Field*. in *Eighteenth Symposium (International) on Combustion*, 1981: The Combustion Institute.
68. Prakash, S. and W.A. Sirignano. *Liquid Fuel Droplet Heating with Internal Circulation.* International Journal of Heat and Mass Transfer, 1978. **21**(7): p. 885-895.
69. Prakash, S. and W.A. Sirignano. *Theory of Convective Droplet Vaporization with Unsteady Heat Transfer in the Circulating Liquid Phase.* International Journal of Heat and Mass Transfer, 1980. **23**(3): p. 253-268.
70. Tong, A.Y. and W.A. Sirignano. *Multicomponent Droplet Vaporization in a High Temperature Gas.* Combustion and Flame, 1986. **66**(3): p. 221-235.
71. Abdel-Qader, Z. and W.L.H. Hallett. *The Role of Liquid Mixing in Evaporation of Complex Multicomponent Mixtures: Modelling Using Continuous Thermodynamics.* Chemical Engineering Science, 2005. **60**(6): p. 1629-1640.
72. Abdel-Qader, Z. and W. Hallett. *The Role of Liquid Mixing in Evaporation of Complex Multicomponent Mixtures: Modelling Using Continuous Thermodynamics - Ii*. in *Combustion Institute.*, 2000, at Canadian Section. Spring Meeting. p. 42-1 - 42-6.
73. Kim, H. and N. Sung. *The Effect of Ambient Pressure on the Evaporation of a Single Droplet and a Spray.* Combustion and Flame, 2003. **135**(3): p. 261-270.
74. Rocco, V. *Results of Quasi-Steady Evaporation Model Applied to Multi-Dimensional D.I. Diesel Combustion Simulation.* SAE International, Paper No.-930071, 1993.

75. Zhu, G.-S. and R.D. Reitz. *A Model for High-Pressure Vaporization of Droplets of Complex Liquid Mixtures Using Continuous Thermodynamics.* International Journal of Heat and Mass Transfer, 2002. **45**(3): p. 495-507.
76. Kodata, T. and H. Hiroyasu. *Evaporation of a Single Droplet at Elevated Pressures and Temperatures* Bulletin of JSME, 1976. **19**(138): p. 1515-1521.
77. Yan , C. and K.A. Suresh. *A High-Pressure Droplet Model for Spray Simulations.* Journal of Engineering for Gas Turbines and Power, 2006. **128**(3): p. 482-492.
78. Pedersen, K.S., P. Rasmussen, and A. Fredenslund. *Thermodynamics of Petroleum Mixtures Containing Heavy Hydrocarbons. 3. Efficient Flash Calculation Procedures Using the Srk Equation of State.* Ind. Eng. Chem. Proc. Des. Dev., 1985. **24**(4): p. 948-954.
79. Pedersen, K.S., P. Thomassen, and A. Fredenslund. *Thermodynamics of Petroleum Mixtures Containing Heavy Hydrocarbons 1. Phase Envelope Calculations by Use of the Soave-Redlich-Kwong Equation of State.* Industrial Engineering Chemical Process Design and Development 1984. **23**: p. 163-170.
80. Pedersen, K.S., P. Thomassen, and A. Fredenslund. *Thermodynamics of Petroleum Mixtures Containing Heavy Hydrocarbons. 2. Flash and Pvt Calculations with the Srk Equation of State.* Industrial & Engineering Chemistry Process Design and Development, 1984. **23**(3): p. 566-573.
81. Zhu, G.S. and S.K. Aggarwal. *Transient Supercritical Droplet Evaporation with Emphasis on the Effects of Equation of State.* International Journal of Heat and Mass Transfer, 2000. **43**(7): p. 1157-1171.
82. Zhu, G.S. and S.K. Aggarwal. *Fuel Droplet Evaporation in a Supercritical Environment.* Journal of Engineering for Gas Turbines and Power, 2002. **124**(4): p. 762-770.
83. Zhang, H. *Evaporation of a Suspended Droplet in Forced Convective High-Pressure Environments.* Combustion Science and Technology, 2003. **175**(12): p. 2237 - 2268.
84. Kim, H.-S., M.-S. Shin, D.-S. Jang, Y.-C. Choi, and J.-G. Lee. *Numerical Study for the Combustion Characteristics of Orimulsion Fuel in a Small-Scale Combustor.* Applied Thermal Engineering, 2005. **25**(17-18): p. 2998-3012.
85. Cotterman, R.L., R. Bender, and J.M. Prasnitz. *Phase Equilibria for Mixtures Containing Very Many Components. Development and Application of Continuous Thermodynamics for Chemical Process Design.* Industrial Engineering Chemical Process Design and Development, 1985. **24**: p. 194-203.
86. Cotterman, R.L. and J.M. Prausnitz. *Flash Calculations for Continuous or Semicontinuous Mixtures by Use of an Equation of State.* Ind. Eng. Chem. Proc. Des. Dev., 1985. **24**(2): p. 434-443.
87. Baer, U., D. Browarzik, and H. Kehlen. *Thermodynamics of Semicontinuous Mixtures Using Equations of State with Group Contributions.* Fluid Phase Equilibria, 1997. **127**(1-2): p. 29-44.
88. Zhu, G.-S. and R.D. Reitz. *Engine Fuel Droplet High Pressure Vaporization Modelling.* Journal of Engineering for Gas Turbines and Power, 2001. **123**: p. 412-418.
89. Yi, Y., G.-S. Zhu, and R.D. Reitz. *High-Pressure Spray and Combustion Modeling Using Continuous Thermodynamics for Diesel Fuels.* SAE International, Paper No.-2001-01-0998, 2001.
90. Ying, X., R. Ye, and Y. Hu. *Phase Equilibria for Complex Mixtures. Continuous-Thermodynamics Method Based on Spline Fit.* Fluid Phase Equilibria, 1989. **53**: p. 407-414.

91. Lippert, A.M. and R.D. Reitz. *Modelling of Multicomponent Fuels Using Continuous Distributions with Application to Droplet Evaporation and Sprays*. in *International Fall Fuels and Lubricants Meeting and Explosion*, 1997, at Tulsa, Oklahoma, 972882.
92. Katz, D.L. and G.G. Brown. *Vapor Pressure and Vaporization of Petroleum Fractions.* Ind. Eng. Chem., 1933. **25**(12): p. 1373-1384.
93. Du, P.C. and G.A. Mansoori. *Phase Equilibrium Computational Algorithms of Continuous Mixtures.* Fluid Phase Equilibria, 1986. **30**: p. 57-64.
94. Willman, B. and A.S. Teja. *Prediction of Dew Points of Semicontinuous Natural Gas and Petroleum Mixtures. 2. Nonideal Solution Calculations.* Ind. Eng. Chem. Res., 1987. **26**(5): p. 953-957.
95. Willman, B.T. and A.S. Teja. *Continuous Thermodynamics of Phase Equilibria Using a Multivariate Distribution Function and an Equation of State.* AIChE Journal, 1986. **32**: p. 2067-2078.
96. Angelos, C.P. and R.E. Ewing. *Continuous Thermodynamic Correlations for Thermal Simulations Using a Cubic Equation of State*. in *AIChE Symposium Series*, 1988. p. 186-190.
97. Briano, J.G. and E.D. Glandt. *Molecular Thermodynamics of Continuous Mixtures.* Fluid Phase Equilibria, 1983. **14**: p. 91-102.
98. Gualtieri, J.A., J.M. Kincaid, and G. Morrison. *Phase Equilibria in Polydisperse Fluids.* The Journal of Chemical Physics, 1982. **77**(1): p. 521-536.
99. Peng, D.Y., R.S. Wu, and J.P. Batycky. *Application of Continuous Thermodynamics to Oil Reservoir Fluid Systems Using an Equation of State.* AOSTRA Journal of Research, 1987. **3**: p. 113-122.
100. Cotterman, R.L. and J.M. Prausnitz. *Application of Continuous Thermodynamics to Natural-Gas Mixtures.* Revue de L'Imtitut Français Du Pétrole, 1990. **45**(5).
101. Hoffman, E.J. *Flash Calculations for Petroleum Fractions.* Chemical Engineering Science, 1968. **23**(9): p. 957-964.
102. Ratzsch, M.T., H. Kehlen, and J. Schumann. *Flash Calculations for a Crude Oil by Continuous Thermodynamics.* Chem. Eng. Comm., 1988. **71**: p. 113-125.
103. Kehlen, H. and M.T. Ratzsch. *Complex Multicomponent Distillation Calculations by Continuous Thermodynamics.* Chemical Engineering Science, 1987. **42**(2): p. 221-232.
104. Chou, G.F. and J.M. Prausnitz. *Adiabatic Flash Calculations for Continuous or Semicontinuous Mixtures Using an Equation of State.* Fluid Phase Equilibria, 1986. **30**: p. 75-82.
105. Ratzsch, M.T., H. Kehlen, and J. Schumann. *Computer Simulation of Complex Multicomponent Hydrocarbon Distillation by Continuous Thermodynamics.* Fluid Phase Equilibria, 1989. **51**: p. 133-146.
106. Harstad, K. and J. Bellan. *Modeling of Multicomponent Homogeneous Nucleation Using Continuous Thermodynamics.* Combustion and Flame, 2004. **139**(3): p. 252-262.
107. Kehlen, H. and M.T. Ratzsch. *Continuous Thermodynamics of Multi-Component Mixtures*. in *Proceedings Sixth International Conference on Thermodynamics*, 1980, at Merseburg(GDR). p. 41-51.
108. Kehlen, H. and M.T. Ratzsch. *Separate Treatment of Paraffins and Aromatics in Complex Hydrocarbon Mixtures by Continuous Thermodynamics*. in *Z. Phys. C'hemie.*, 1984, at Leipzig. p. 1049.
109. Kehlen, H., M.T. Ratzsch, and J. Bergmann. *Continuous Thermodynamics of Multicomponent Systems.* AIChE Journal, 1985. **31**(7): p. 1136-1148

110. Hallett, W. *A Simple Quasi-Steady Droplet Evaporation Model Using Continuous Thermodynamics*. in *Combustion Institute*, 1997, at Canadian Section. Spring Meeting p. 4-21 - 4-25.
111. Hallett, W.L.H. *A Simple Model for the Vaporization of Droplets with Large Numbers of Components.* Combustion and Flame, 2000. **121**(1-2): p. 334-344.
112. Lippert, A.M., D.W. Stanton, C.J. Rutland, W.L.H. Hallett, and R.D. Reitz. *Multidimensional Simulation of Diesel Engine Cold Start with Advanced Physical Submodels.* International Journal of Engine Research, 2000. **1**(1): p. 1-27.
113. Lippert, A.M., D.W. Stanton, R.D. Reitz, C.J. Rutland, and W.L.H. Hallett. *Investigating the Effect of Spray Targeting and Impingement on Diesel Engine Cold Start.* SAE International, Paper No.- 2002-01-0269, 2002.
114. Ra, Y. and R.D. Reitz. *A Model for Droplet Vaporization for Use in Gasoline and Hcci Engine Application.* Journal of Engineering for Gas Turbines and Power, 2004. **126**: p. 423-428.
115. Ra, Y. and R.D. Reitz. *The Application of a Multicomponent Droplet Vaporization Model to Gasoline Direct Injection Engines.* International Journal of Engine Research, 2003. **4**(3): p. 193-218.
116. Harstad, K. and J. Bellan. *Modeling Evaporation of Jet a, Jp-7, and Rp-1 Drops at 1 to 15 Bars.* Combustion and Flame, 2004. **137**(1-2): p. 163-177.
117. Harstad, K.G., P.C.L. Clercq, and J.Bellan. *Statistical Model of Multicomponent-Fuel Drop Evaporation for Many-Drop Flow Simulations.* American Institute of Aeronautics and Astronautics Journal, 2003. **41**(10): p. 1858-1874.
118. Teja, A.S. and B.T. Willman. *Phase Equilibria in Natural Gas, Crude Oil and Coal Liquid Mixtures.* Fluid Phase Equilibria, 1986. **30**: p. 247-253.
119. Radosz, M., R.L. Cotterman, and J.M. Prausnitz. *Phase Equilibria in Supercritical Propane Systems for Separation of Continuous Oil Mixtures.* Ind. Eng. Chem. Res., 1987. **26**(4): p. 731-737.
120. Vakili-Nezhaad, G.R., H. Modarress, and G.A. Mansoori. *Continuous Thermodynamics of Petroleum Fluids Fractions.* Chemical Engineering and Processing, 2001. **40**(5): p. 431-435.
121. Doué, N., Y. Biscos, G. Lavergne, and A. Berlemont. *Vaporization of Multi-Component Droplets Using Continuous Thermodynamics Model with Multiple Distribution Functions*. in *ILASS 2004*, 2004, at Nottingham (Grande Bretagne).
122. Doué, N., P.L. Clercq, and M. Aigner. *Validation of a Multicomponent-Fuel Droplet Evaporation Model Based on Continuous Thermodynamics*. in *International Congress on Liquid Atomization and Spray Systems*, 2006, at Kyoto Japan.
123. Doué, N., G. Lavergne, and A. Berlemont. *Vaporization of Gasoline, Kerosene and Diesel Droplets Using Continuous Thermodynamics Model with Multiple Distribution Functions*. in *International Symposium on Heat and Mass Transfer in Spray Systems (SPRAY 05)*, 2005, at Antalya,Turquie.
124. Banerjee, D.K., K.J. Laidler, B.N. Nandi, and D.J. Patmore. *Kinetic Studies of Coke Formation in Hydrocarbon Fractions of Heavy Crudes.* Fuel, 1986. **65**(4): p. 480-484.
125. Fang, W. and Q. Lei. *Continuous Thermodynamic Correlation and Calculation of Vapor Pressure and Vapor-Liquid Equilibrium Constant of Hydrocarbon Fuel Fractions.* Fluid Phase Equilibria, 2003. **213**(1-2): p. 125-138.
126. Dec, J.E. *Soot Distribution in a D.I. Diesel Engine Using 2-D Imaging of Laser-Induced Incandescence, Elastic Scattering, and Flame Luminosity.* SAE International, Paper No.-920115, 1992.

127. Hodges, J.T., T.A. Baritaud, and T.A. Heinze. *Planar Liquid and Gas Fuel and Droplet Size Visualization in a Dl Diesel Engine.* SAE International, Paper No.-910726, 1991.
128. Won, Y.-H., T. Kamimoto, and H. Kosaka. *A Study on Soot Formation in Unsteady Spray Flames Via 2-D Soot Imaging.* SAE International, Paper No.-920114, 1992.
129. Manuel, A., D. Gonzalez, G.L. Borman, and R.D. Reitz. *A Study of Diesel Cold Starting Using Both Cycle Analysis and Multidimensional Calculations.* SAE International, Paper No.-910180, 1991.
130. Siebers, D.L. *Liquid-Phase Fuel Penetration in Diesel Sprays.* SAE International, Paper No.-980809, 1998.
131. Siebers, D.L. *Scaling Liquid-Phase Fuel Penetration in Diesel Sprays Based on Mixing-Limited Vaporization.* SAE International, Paper No.-1999-01-0528, 1999.
132. Shiode, K., T. Kijima, and G. Fiskaa. *Ignition Properties for Marine Fuels Established on the Fuel Ignition Analyser Fia 100/2*. in *CIMAC Congress*, 1998, at Copenhagen.
133. Takeda, A., H. Nakatani, E. Shimizu, T. Ura, T. Koto, D. Suzuki, and H. Miyano, *The Ignition and the Combustion Quality by Fia (Fuel Ignition Analyzer) of Actual Mfo and the Countermeasure against the Mfo with Inferior Quality*, in *International council on combustion engines (CIMAC)*. 2007: Vienna.
134. Takasaki, K., Y. Wakuri, K. Maeda, T. Oyamada, T. Hamasaki, and F. Nakata, *Influences of Fuel Spray Impingement on Combustion in a Marine Diesel Engine (Cimac)*, in *21st Internaltional congress on combustion engines*. 1995.
135. Sarowha, S.L.S. *Determination of Molecular Weights of Petroleum Products Using Gel Permeation Chromatography.* Petroleum Science and Technology, 2005. **23**(5 - 6): p. 573-578.
136. Rahimi, P. and T. Gentzis. *The Chemistry of Bitumen and Heavy Oil Processing*. Practical Advances in Petroleum Processing. 2006. 597-634.
137. Yasar, M., F.E. Cerci, and H. Gulensoy. *Effect of Asphaltenes on Pyrolysis Kinetics of Saturates.* Journal of Analytical and Applied Pyrolysis, 2000. **56**(2): p. 219-228.
138. Vazquez, D. and G.A. Mansoori. *Identification and Measurement of Petroleum Precipitates.* Journal of Petroleum Science and Engineering, 2000. **26**(1-4): p. 49-55.
139. Farcasiu, M. *Fractionation and Structural Characterization of Coal Liquids.* Fuel, 1977. **56**(1): p. 9-14.
140. Liu, C., C. Zhu, L. Jin, R. Shen, and W. Liang. *Step by Step Modeling for Thermal Reactivities and Chemical Compositions of Vacuum Residues and Their Sfef Asphalts.* Fuel Processing Technology, 1999. **59**(1): p. 51-67.
141. Schiller, J.E. and D.R. Mathiason. *Separation Method for Coal-Derived Solids and Heavy Liquids.* Anal. Chem., 1977. **49**(8): p. 1225-1228.
142. Marquez, N., F. Ysambertt, and C. De La Cruz. *Three Analytical Methods to Isolate and Characterize Vanadium and Nickel Porphyrins from Heavy Crude Oil.* Analytica Chimica Acta, 1999. **395**(3): p. 343-349.
143. Burke, F.P., R.A. Winschel, and D.L. Wooton. *Liquid Column Fractionation: A Method of Solvent Fractionation of Coal Liquefaction and Petroleum Products.* Fuel, 1979. **58**(7): p. 539-541.
144. Mansoori, G.A., D. Vazquez, and M. Shariaty-Niassar. *Polydispersity of Heavy Organics in Crude Oils and Their Role in Oil Well Fouling.* Journal of Petroleum Science and Engineering. **In Press, Corrected Proof**.

145. Galarraga, F., G. Márquez, K. Reategui, and A. Martínez. *Comparative Study of Crude Oils from the Machete Area in the Eastern Venezuelan Basin by Pyrolysis of Asphaltenes.* Journal of Analytical and Applied Pyrolysis, 2007. **80**(2): p. 289-296.
146. Ciajolo, A. and R. Barbella. *Pyrolysis and Oxidation of Heavy Fuel Oils and Their Fractions in a Thermogravimetric Apparatus.* Fuel, 1984. **63**(5): p. 657-661.
147. McKay, J.F., P.M. Harnsberger, R.B. Erickson, T.E. Cogswell, and D.R. Latham. *Composition of Petroleum Heavy Ends. 2. Characterization of Compound Types in Petroleum >675 °C Residues.* Fuel, 1981. **60**(1): p. 17-26.
148. Aggarwal, S.K., G.-S. Zhu, and R.D. Reitz. *Quasi-Steady High-Pressure Droplet Model for Diesel Sprays.* SAE International, Paper No.-2000-01-0588, 2000.
149. Xu, G., M. Ikegami, S. Honma, K. Ikeda, X. Ma, and H. Nagaishi. *Burning Droplet of Heavy Oil Residual Blended with Diesel Light Oil -Distinction of Burning Phases.* Combustion Science and Technology, 2003. **175**: p. 1-26.
150. Singh, J., M.M. Kumar, A.K. Saxena, and S. Kumar. *Studies on Thermal Cracking Behavior of Residual Feedstocks in a Batch Reactor.* Chemical Engineering Science, 2004. **59**(21): p. 4505-4515.
151. Moszkowicz, P., L. Witzel, and G. Claus. *Modelling of Very Fast Pyrolysis of Heavy Fuel Oil Droplets.* Chemical Engineering Science, 1996. **51**(17): p. 4075-4086.
152. Ambalae, A., N. Mahinpey, and N. Freitag. *Thermogravimetric Studies on Pyrolysis and Combustion Behavior of a Heavy Oil and Its Asphaltenes.* Energy and Fuels, 2006. **20**: p. 560-565.
153. Hallett, W. *An Assessment of Quasi-Steady Models of Droplet Ignition*. in *Combustion Institute.* , 1997, at Canadian Section. Spring Meeting p. 4-6 - 4-10.
154. Al Omari, S.A.B. *Comparison between Two Droplet Heating Models under Diesel Spray-Like Conditions*. in *2003 SAE World Congress, 2003-01-1047*, at Michigan.
155. Wilms, J. and B. Weigand. *Mass Transfer in Evaporating Binary Mixture Droplets*. in *International Congress on Liquid Atomization and Spray Systems*, 2006, at Kyoto, Japan.
156. Doolan, K.R., J.C. Mackie, and R.J. Tyler. *Coal Flash Pyrolysis: Secondary Cracking of Tar Vapours in the Range 870-2000 K.* Fuel, 1987. **66**(4): p. 572-578.
157. Wallace, S., K.D. Bartle, M.P. Burke, B. Egia, S. Lu, N. Taylor, T. Flynn, W. Kemp, and W. Steedman. *Characterization of Petroleum Feedstocks for Coal-Oil Co-Processing.* Fuel, 1989. **68**(8): p. 961-967.
158. Ratzsch, M.T. and H. Kehlen. *Continuous Thermodynamics of Complex Mixtures.* Fluid Phase Equilibria, 1983. **14**: p. 225-234.
159. Sandler, S.A. *Chemical and Engineering Thermodynamics*. Second Second. 1989: John Wiley & Sons-Singapore.
160. Brandani, S. and V. Brandani. *Extension of Generalised Mixing Rules to Cubic Equations of State.* The Journal of Chemical Thermodynamics, 2004. **36**(11): p. 949-956.
161. A.C.Bajpai, L.R.Mustoe, and D.Walker. *Engineering Mathematics*. 1974, London: John Wiley & Sons.
162. Abraham, J. and S.D. Givler. *Condition in Which Vaporizing Fuel Drops Reach a Critical State in a Diesel Engines.* SAE international, Paper No-1999-01-0511, 1999.
163. Merrick, D. *Mathematical Models of the Thermal Decomposition of Coal : 2. Specific Heats and Heats of Reaction.* Fuel, 1983. **62**(5): p. 540-546.
164. Coutinho, J.A.P., G.M. Kontogeorgis, and E.H. Stenby. *Binary Interaction Parameters for Nonpolar Systems with Cubic Equations of State: A Theoretical*

Approach 1. Co2/Hydrocarbons Using Srk Equation of State. Fluid Phase Equilibria, 1994. **102**(1): p. 31-60.
165. Senda, J., T. Higaki, Y. Sagane, H. Fujimoto, A. Takagi, and M. Adachi. *Modelling and Measurement on Evaporation Process of Multicomponent Fuels.* SAE international, Paper No-2000-01-0280, 2000.
166. Avlonitis, G., G. Mourikas, S. Stamataki, and D. Tassios. *A Generalized Correlation for the Interaction Coefficients of Nitrogen---Hydrocarbon Binary Mixtures.* Fluid Phase Equilibria, 1994. **101**: p. 53-68.
167. Poling, B.E., J.H. Prausnitz, and J.P. O'connell. *The Properties of Gases and Liquids* Fifth Fifth: McGraw Hill - New York.
168. Yu, Y., S.-K. Kim, and Y.-M. Kim. *Numerical Modelling for Auto-Ignition and Combustion Processes of Fuel Sprays in High-Pressure Environment.* SAE International, Paper No.-2001-01-0253, 2001.
169. Krishna, R., Y.K. Kuchhal, G.S. Sarna, and I.D. Singh. *Visbreaking Studies on Aghajari Long Residue.* Fuel, 1988. **67**(3): p. 379-383.
170. Martinez, M.T., A.M. Benito, and M.A. Callejas. *Thermal Cracking of Coal Residues: Kinetics of Asphaltene Decomposition.* Fuel, 1997. **76**(9): p. 871-877.
171. Al-Soufi, H.H., Z.F. Savaya, H.K. Mohammed, and I.A. Al-Azawi. *Thermal Conversion (Visbreaking) of Heavy Iraqi Residue.* Fuel, 1988. **67**(12): p. 1714-1715.
172. Geng, A. and Z. Liao. *Kinetic Studies of Asphaltene Pyrolyses and Their Geochemical Applications.* Applied Geochemistry, 2002. **17**(12): p. 1529-1541.
173. Wilk, R. *The Thermal Decomposition of the Liquid Phase During the Combustion of Heavy Oil Droplets.* Fuel, 1989. **68**(3): p. 371-374.
174. Ungerer, P., F. Behar, M. Villalba, O.R. Heum, and A. Audibert. *Kinetic Modelling of Oil Cracking.* Organic Geochemistry, 1988. **13**(4-6): p. 857-868.
175. Ranjbar, M. and G. Pusch. *Pyrolysis and Combustion Kinetics of Crude Oils, Asphaltenes and Resins in Relation to Thermal Recovery Processes.* Journal of Analytical and Applied Pyrolysis, 1991. **20**: p. 185-196.
176. Urban, D.L., S.P.C. Huey, and F.L. Dryer. *Evaluation of the Coke Formation Potential of Residual Fuel Oils.* Symposium (International) on Combustion, 1992. **24**(1): p. 1357-1364.
177. Del Bianco, A., N. Panariti, M. Anelli, P.L. Beltrame, and P. Carniti. *Thermal Cracking of Petroleum Residues : 1. Kinetic Analysis of the Reaction.* Fuel, 1993. **72**(1): p. 75-80.
178. Yue, C., A.P. Watkinson, J.P. Lucas, and K.H. Chung. *Incipient Coke Formation During Heating of Heavy Hydrocarbons.* Fuel, 2004. **83**(11-12): p. 1651-1658.
179. Ebrahimi, S., J.S. Moghaddas, and M.K.R. Aghjeh. *Study on Thermal Cracking Behavior of Petroleum Residue.* Fuel, 2008. **87**(8-9): p. 1623-1627.
180. Rodríguez-Reinoso, F., M. Martínez-Escandell, P. Torregrosa, H. Marsh, C. Gómez de Salazar, and E. Romero-Palazón. *Pyrolysis of Petroleum Residues: Iii. Kinetics of Pyrolysis.* Carbon, 2001. **39**(1): p. 61-71.
181. Anthony, D.B. and J.B. Howard. *Coal Devolatilization and Hydrogasification.* AIChE Journal, 1976. **22**: p. 625-656.
182. Dec, J.E. *A Conceptual Model of Di Diesel Combustion Based on Laser-Sheet Imaging*. in *International Congress & Exposition* 1997, at Michigan: SAE.
183. *Starcd Version 3.24 Methodology*. 2004.
184. Reitz, R.D. and R. Diwakar. *Effect of Drop Breakup on Fuel Sprays.* SAE International, Paper No.-860469, 1986.

185. Baumgarten, C., H. Lettmann, and G.P. Merker. *Modelling of Primary and Secondary Break-up Processes in High Pressure Diesel Sprays*. in *CIMAC Congress*, 2004, at Kyoto.
186. Goldsworthy, L., H. Tajima, and C. Bong. *Modelling and Measurement of High Pressure Sprays, Ignition and Combustion of Heavy Fuel Oil and Marine Diesel Engine Oil*. in *ICLASS-2006*, 2006, at Kyoto, Japan.
187. Yakhot, V. and S.A. Orszag. *Renormalization Group Analysis of Turbulence. I. Basic Theory.* Journal of Scientific Computing, 1986. **1**(1): p. 3-51.
188. Takei, M., R. Weber, and T. Niioka. *Mathematical Modeling of Industrial Furnaces Considering Detailed Oil Spray Characteristics.* Combustion Science and Technology, 2003. **175**(7): p. 1237-1262.
189. Weisser, G., *Modelling of Combustion and Nitric Oxide Ormation Formedium-Speed Di Diesel Engines: A Comparison of Zero- and Three-Dimensional Approaches.* 2001, PhD Thesis, Swiss Federal Institute of Technology: Zurich.
190. Goldsworthy, L., *A Model for Ignition and Combustion Quality of Heavy Fuel Oil*, in *CIMAC Congress*. 2007: Vienna.
191. Petchers, N. *Combined Heating, Cooling & Power Handbook: Technologies & Applications*. 2003: The Fairmont press.
192. Yuan, J. and V.S.M.G. Carvalho. *Modelling and Validation of the Formation and Oxidation of Cenospheres in a Confined Spray Flame.* International Journal of Energy Research, 1997. **21**(14): p. 1331-1344.
193. Nishida, K. and H. Hiroyasu. *Simplified Three-Dimensional Modelling of Mixture Formation and Combustion in a D.I. Diesel Engine.* SAE International, Paper No.-890269, 1989.
194. Barbella, R., A. Ciajolo, A. D'Anna, and C. Bertoli. *Effect of Fuel Aromaticity on Diesel Emissions.* Combustion and Flame, 1989. **77**(3-4): p. 267-277.
195. Li, J., J.O. Chae, S.M. Lee, and J.S. Jeong. *Modeling the Effects of Split Injection Scheme on Soot and No Emissions of Direct Injection Diesel Engines by a Phenomenological Combustion Mode.* SAE International, Paper No.-962062, 1996.
196. Zannis, T.C., D.T. Hountalas, and R.G. Papagiannakis. *Experimental Study of Diesel Fuel Effects on Direct Injection (Di) Diesel Engine Performance and Pollutant Emissions.* Energy & Fuels, 2007. **21**(5): p. 2642-2654.
197. Smith, J.M. and H.C. Van Ness. *Introduction to Chemical Engineering Thermodynamics*. Fourth Fourth. 1987: McGraw-Hill Book Company-Singapore.
198. Aabo, K. *A Presentation on 'Operation on Low Sulphur Fuel and Implications for Engine Manufacturers / Operators'*. in *CIMAC* 2007, at Vienna: found at http://www.cimac.com/cimac_cms/uploads/explorer/other_events_2007/presentation_aabo.pdf (accessed on 04/06/2009)
199. Nguyen, D., D. Honnery, and J. Soria, *Magnified Digital Inline Holographic Measurement of Micro Droplets* in *Fifth Australian Conference on Laser Diagnostics in Fluid Mechanics and Combustion*. 2008: The University of Western Australia, Perth, Australia
200. Slanciauskas, A. and R. Kalpokaite. *Behaviour of a Heavy Fuel Oil Droplet on a Hot Surface.* International Journal of Heat and Mass Transfer, 2006. **49**(5-6): p. 1050-1057.
201. Juoperi, K., *Heavy Fuel Oil – Still the Dominant Fuel Quality for Diesel Engines*, Wärtsilä Finland Oy.
202. Fang, W., Q. Lei, and R. Lin. *Enthalpies of Vaporization of Petroleum Fractions from Vapor Pressure Measurements and Their Correlation Along with Pure Hydrocarbons.* Fluid Phase Equilibria, 2003. **205**(1): p. 149-161.

203. Gilyazetdinov, L.P. *Calculation of the Latent Heat of Vaporization of Petroleum Fractions.* Chemistry and Technology of Fuels and Oils, 1990. **V26**(12): p. 648-650.
204. Eckert, E. and T. Vanek. *New Approach to the Characterisation of Petroleum Mixtures Used in the Modelling of Separation Processes.* Computers & Chemical Engineering, 2005. **30**(2): p. 343-356.
205. Myrdal, P.B., J.F. Krzyzaniak, and S.H. Yalkowsky. *Modified Trouton's Rule for Predicting the Entropy of Boiling.* Ind. Eng. Chem. Res., 1996. **35**(5): p. 1788-1792.
206. Tsonopoulos, C. and D. Ambrose. *Vapor-Liquid Critical Properties of Elements and Compounds. 3. Aromatic Hydrocarbons.* J. Chem. Eng. Data, 1995. **40**(3): p. 547-558.
207. Li, F.-F., X.-q. Yao, J. Zhang, and B. Ma. *Investigation on the Chemical Composition and Structure of Daqing Vacuum Residue Narrow Fractions.* Petroleum Science & Technology, 2004. **22**(9/10): p. 1299-1308.
208. Sbaite, P., C. Batistella, A. Winter, C. Vasconcelos, M. Maciel, R. Filho, A. Gomes, L. Medina, and R. Kunert. *True Boiling Point Extended Curve of Vacuum Residue through Molecular Distillation.* Petroleum Science and Technology, 2006. **24**(3 - 4): p. 265-274.
209. Baltatu, M.E., J.F. Ely, H.J.M. Hanley, M.S. Graboski, R.A. Perkins, and E.D. Sloan. *Thermal Conductivity of Coal-Derived Liquids and Petroleum Fractions.* Ind. Eng. Chem. Proc. Des. Dev., 1985. **24**(2): p. 325-332.
210. Agroskin, A.A., E.V. Artamonova, E.I. Goncharov, V.M. Tyagunov, and G.G. Valyavin. *Thermochemical Characteristics of Petroleum Residuum Coking.* Chemistry and Technology of Fuels and Oils, 1978. **V14**(6): p. 412-415.

Appendix: Transport Properties

The present developed models require transport properties of both the liquid and vapour phases. These transport properties are usually dependent on temperature and concentration of the mixture. Therefore, these must be evaluated at some reference temperature and concentration. Vapour phase properties are calculated at the reference state as recommended in [18, 21, 71, 110, 111];

$$T_{Ref} = \frac{2}{3}T_R + \frac{1}{3}T_\infty \qquad and \qquad y_{FjRef} = \frac{2}{3}y_{FjR} + \frac{1}{3}y_{Fj\infty} \tag{110}$$

1) Density: Density of heavy fuel oil is calculated from the mass fraction X_j.

   Density of single fraction is given as;

$$\rho_j = \frac{Mass_j}{Vol_j} = \frac{X_j m_L}{Vol_j} \tag{111}$$

$$\therefore \quad Vol_j = \frac{X_j m_L}{\rho_j}$$

   Thus, the total density of the liquid (ρ) can be given as;

$$\rho = \frac{\sum_{j=1}^{J} Mass_j}{\sum_{j=1}^{J} Vol_j} = \frac{\sum_{j=1}^{J} X_j m_L}{\sum_{j=1}^{J} Vol_j} \tag{112}$$

   Now, substitute Vol_j into above equation;

$$\rho = \frac{m_L \sum_{j=1}^{J} X_j}{m_L \sum_{j=1}^{J} \frac{X_j}{\rho_j}} = \frac{\sum_{j=1}^{J} X_j}{\sum_{j=1}^{J} \frac{X_j}{\rho_j}} \qquad but, \ \sum_{j=1}^{J} X_j = 1, \quad \text{thus}$$

Density of liquid is;

$$\rho = \frac{1}{\sum_{j=1}^{J} \frac{X_j}{\rho_j}} \tag{113}$$

The density of HFO is found in the range from 970-1010 kg/m^3 in the literature [151, 200, 201], but here it is set as 995 kg/m^3 as a typically value [6, 12, 201]. To set the total density as 995 kg/m^3, densities of n-paraffins, aromatics and naphthenes are set as 980 kg/m^3 whereas the density of residue is set as 1002 kg/m^3. The total density of the HFO varies with the liquid composition.

2) Bubble point: Bubble point of a component is given by a linear relation with the component's molecular weight as [18, 21];

$$T_B(I) = a_B + b_B I \quad in\ K \tag{114}$$

3) Critical properties: Critical properties of the various components are also given by linear relations with the component's molecular weight. Critical temperature and pressure are given as follows [18, 21];

$$T_{cr}(I) = a_{cr} + b_{cr} I \quad in\ K \tag{115}$$

$$P_{cr}(I) = a_p + b_p I \quad in\ atm \tag{116}$$

4) Diffusion coefficient: Vapour phase diffusivity is given by a linear function of the component's molecular weight and its temperature dependence is given by Φ_D [18, 21];

$$D(I) = (a_D + b_D I)\Phi_D \quad where,\ \Phi_D = \frac{T^{3/2}}{T + b_\Phi} \quad in\ m^2/s \tag{117}$$

Where b_{Φ} of all components are given in transport properties table in a later part of this section.

5) Thermal conductivity: Thermal conductivity of petroleum is a weak function of molecular weight and temperature. Thermal conductivity of a component is given by a linear function of temperature and molecular weight *(I)* [18, 21];

$$\lambda(I) = a_{KC} + a_{KT}T + (b_{KC} + b_{KT}T)I \qquad in\ W/(mK) \tag{118}$$

The combined thermal conductivity of fuel vapour and pyrolysis gas is given as;

$$\lambda_V = \sum_{j=1}^{J} y_{Fj}(\lambda_j)\theta_{Fj} + y_G(\lambda_G)\theta_G \tag{119}$$

Where, y_G is determined from equation (30). Mason and Saxsena's rule is used to combine the above thermal conductivity with the conductivity of air.

6) Vapour specific heat: Heat capacities of a component in vapour phase at constant pressure is given by a function of molecular weight *(I)* and temperature as [21];

$$Cp(I) = a_{CP} + b_{CP}I \qquad in\ kJ/kmolK \tag{120}$$

Where, $a_{CP} = a_{C0} + a_{C1}T + a_{C2}T^2 + a_{C3}T^3$ and $b_{CP} = b_{C0} + b_{C1}T + b_{C2}T^2 + b_{C3}T^3$

The combined specific heat of fuel vapour and pyrolysis gas is approximated as;

$$C_{pV} = \sum_{j=1}^{J} y_{Fj}(C_{pj})\theta_j + y_G(C_{pG})\theta_G \tag{121}$$

Heat capacities of vapour phase at the constant pressure are taken from Chou & Prausnitz [104] for pure hydrocarbons.

7) Liquid specific heat: Liquid specific heat of different component is nearly independent of molecular weight, but temperature dependence is given by a second order polynomial as [21];

$$C_{pL}(I) = (a_L + b_L T + c_L T^2) I \qquad in\ kJ\ /\ kmolK \tag{122}$$

The liquid specific heat of fuel mixture is approximated as;

$$C_{pL} = \sum_{j=1}^{J} x_{Lj}(a_L + b_L T + c_L T^2)\theta_{Lj} \tag{123}$$

8) Enthalpy of evaporation: Enthalpy of evaporation is defined as the difference in the enthalpy of the vapour phase and enthalpy of the liquid phase at equilibrium pressure and temperature [202]. Enthalpy of evaporation is the sum of the enthalpy of evaporation of each individual component weighted by their molar flux. Enthalpy of evaporation at component's boiling point is nearly constant and can be approximated as [21];

$$h_{fg}(I) = (a_H + b_H I)\Phi_H \tag{124}$$

Where, Φ_H is a temperature dependence term that can be approximated from Watson's equation, based on the theory of eigenstates for the organic compounds [203] ;

$$\Phi_H = \left(\frac{T_{cr} - T}{T_{cr} - T_B}\right)^{0.38} \tag{125}$$

Enthalpy of evaporation for a mixture at quasi-steady condition is approximated as [21];

$$h_{fg} = \sum_{j=1}^{J} \Phi_{Hj} \left\{ a_{Hj}\xi_j + \frac{b_{Hj}}{B_j}[\theta_{jR} y_{FjR}(1 + B_j) - \theta_{\infty j} y_{Fj\infty}] \right\} \tag{126}$$

Coefficients of above mentioned property equations for all four components used in the current model are summarised in the table below;

Table A-1: Transport properties as a function of molecular weight *(I)* and temperature *(T)*.

Property	n-paraffins	Aromatics	Naphthenes	Residue
Density				
ρ	980	980	980	1002
Boiling Point				
$T_B(I)$	$241.4 + 1.45(I)$	$190.4+ 2.04(I)$	$348.5 + 1.17(I)$	$703+ 0.75(I)$
Critical Properties				
$T_{cr}(I)$	$440.8+ 1.21(I)$	$384.761 + 2.17(I)$	$580.085 + 1.329(I)$	$780.00 + 0.90(I)$
$P_{cr}(I)$	$40.00 - 0.08(I)$	$65.3 - 0.16(I)$	$79.5 - 0.187\ (I)$	$95.00 – 0.15(I)$
Diffusivity				
$D(I)$	$(2.89*10^{-9}-6.60*10^{-12}I)\Phi_D$	$(3.351*10^{-9}-8.620*10^{-12}I)\Phi_D$	$(2.708*10^{-9}-2.912*10^{-12}I)\Phi_D$	$(2.99*10^{-9}-5.10*10^{-12}I)\Phi_D$
Φ_D	$\frac{T^{3/2}}{T+250}$	$\frac{T^{3/2}}{T+247}$	$\frac{T^{3/2}}{T+250.5}$	$\frac{T^{3/2}}{T+250}$
Thermal Conductivity				
$\lambda(I)$	$(-2.37*10^{-2} + 1.09*10^{-4}T) + (3.47*10^{-5} -1.91*10^{-7}T)I$	$(-2.375*10^{-2} + 1.08*10^{-4}T) + (2.220*10^{-5} -1.109*10^{-7}T)I$	$(-1.412*10^{-2} + 6.137*10^{-5}T) + (-3.377*10^{-5}+1.521*10^{-7}T)I$	$(-0.0256+1.10*10^{-4}T) + (4.28*10^{-5} -1.06*10^{-7}T)I$
Vapour Specific Heat				
$Cp(I)$	$a_{CP} + b_{CP}I$	$a_{CP} + b_{CP}I$	$a_{CP} + b_{CP}I$	$a_{CP} + b_{CP}I$
a_{CP}	$2.465-1.144*10^{-2}T +1.759*10^{-5}T^2-5.972*10^{-9}T^3$	$-4.282–2.699*10^{-3}T -5.492*10^{-6}T^2+3.242*10^{-9}T^3$	$-6.985–1.106*10^{-2}T -4.485*10^{-6}T^2+3.811*10^{-9}T^3$	$-2.053+8.176*10^{-3}T -3.893*10^{-6}T^2+8.175*10^{-10}T^3$

b_{CP}	$-3.561*10^{-2}+9.367*10^{-4}T$ $-6.030*10^{-7}T^2+1.324*10^{-10}T^3$	$-6.189*10^{-3}+8.126*10^{-4}T$ $-4.703*10^{-7}T^2+1.058*10^{-10}T^3$	$-2.794*10^{-3}+8.497*10^{-4}T$ $-5.333*10^{-7}T^2+1.324*10^{-10}T^3$	$-3.557*10^{-2}+6.67*10^{-4}T$ $-4.624*10^{-7}T^2+1.169*10^{-10}T^3$
Liquid Specific Heat				
$C_{pL}(I)$	$(2.26-2.94*10^{-3}T$ $+9.46*10^{-6}T^2)I$	$(1.08+1.51*10^{-3}T$ $+2.73*10^{-6}T^2)I$	$(0.47+4.50*10^{-3}T$ $-2.5*10^{-6}T^2)I$	$(0.93+4.0*10^{-3}T$ $+0.0T^2)I$
Enthalpy of Evaporation				
$h_{fg}(I)$	$(2.07*10^7 + 1.35*10^5 I)\Phi_H$	$(8.286*10^6 + 2.606*10^5 I)\Phi_H$	$(4.733*10^7 - 1.690*10^4 I)\Phi_H$	$(6.18*10^7 + 6.6*10^4 I)\Phi_H$
Φ_H	$\frac{(T-T_{cr})^{0.38}}{6.959}$	$\frac{(T-T_{cr})^{0.38}}{7.609}$	$\frac{(T-T_{cr})^{0.38}}{8.269}$	$\frac{(T-T_{cr})^{0.38}}{7.282}$

Coefficients in property equations of n-paraffins:

Most of the transport property coefficients of n-paraffins are given by Tamim & Hallett [18], but some, such as bubble point coefficients are taken from ref. [18, 19, 75, 117] and confirmed with the data in Eckert & Vanek [204]. Diffusion and critical temperature coefficients are taken from Tamim & Hallett.[18], while critical pressure coefficients are taken from ref. [75, 88]. Entropy of evaporation is almost constant for n-paraffins which is taken from Myrda et al.[205].

Coefficients in property equations of aromatics and naphthenes:

Bubble point coefficients for aromatics and naphthenes are given in Hallett & Grimwood [19]. Critical property coefficients are taken from ref. [19, 206] and extrapolated wherever required. Entropy of evaporation for aromatics and naphthenes are almost the same as n-paraffins which is taken from Myrda et al.[205]. All other coefficients in property equations of aromatics and naphthenes are taken from Hallett & Grimwood [19].

Coefficients in property equations of residue:

Precise properties of the residual portion of HFO and their coefficients are not available in the literature due to its complex chemical nature. There is no analytical or sound database that provides characterisation of heavy petroleum residue. Therefore, the 'black oil' concept is being applied to derive the properties of heavy crude residue as suggested by Whitehead [40]. Bubble point range of heavy residue is taken from ref. [207, 208], while the critical properties are taken from Zhao et al.[40]. Entropy of evaporation is taken from Myrda et al.[205]. Diffusion coefficient of the residue is not available in the literature hence it is forced to set as; total diffusivity of HFO minus the sum of the diffusion coefficients of pure hydrocarbons.

Since the residual portion of heavy fuel oil evaporates a negligible amount, it is reasonable to approximate its vapour phase properties. Most of the literature cites the vapour phase properties only of the light hydrocarbons (molecular weight < 500). Thermal conductivity coefficients of residue are taken from Baltatu et al.[209]. Heat capacity coefficients of residue are taken from Chou & Prausnitz [104] for condensed ring hydrocarbon and it is validated with Agroskin et al.[210]. Specific heat of the heavy fuel oil is taken from Slanciauskas & Kalpokaite [200] as 2.0 kJ/kgK.

The properties of pyrolysis gas and air are taken from Poling et al.[167] and Harstad et al.[117] respectively.